

**ANTIMONY AND TELLURIUM NON-INNOCENT Z-LIGANDS FOR TRANSITION
METALS AND THEIR APPLICATION IN PHOTOREDOX CHEMISTRY AND
ELECTROPHILIC CATALYSIS**

A Dissertation

by

HAIFENG YANG

Submitted to the Office of Graduate and Professional Studies of
Texas A&M University
in partial fulfillment of the requirements for the degree of

DOCTOR OF PHILOSOPHY

| | |
|---------------------|---------------------|
| Chair of Committee, | François P. Gabbaï |
| Committee Members, | Michael B. Hall |
| | Oleg V. Ozerov |
| | Jodie L. Lutkenhaus |
| Head of Department, | Simon W. North |

August 2016

Major Subject: Chemistry

Copyright 2016 Haifeng Yang

ABSTRACT

Ligand design has been an often pursued strategy to advance the development of transition metal complexes for catalysis and activation of small molecules. In the past decade, polydentate Z-type ligands have been recognized as versatile tools to expand on the reactivity of transition metals. The interest generated by polydentate Z-type ligands mainly arises from the ability of the Lewis acidic Z site to behave as σ -acceptor, which can modulate the electronic properties of the metal and impart reactivity to the metal via flexible metal \rightarrow Z ligand interaction. Group 13 compounds, notable for their Lewis acidity, have been dominating the field of Z-type ligand chemistry, leading to a plethora of discoveries in small molecules activation and organic transformation catalysis.

In recent years, heavy main group antimony and tellurium compounds made their unique entry into the Z-type ligand family owing to their Lewis acidity and redox activity. In particular, it was demonstrated that weak donating stibine and telluroether ligands can be switched into σ -accepting Z-type ligands by post-synthetic conversion to their hyper-valent state. Although these phenomena are of fundamental importance, attempts to use these metal complexes for metal catalyzed processes or chemical transformations have not been explored. To fill this knowledge gap, it became the objective of this dissertation to investigate new versions of antimony or tellurium ligand systems and probe their use for the design of late transition metal-based catalysts

With this in mind, I chose to investigate halogen functionalized antimony ligands, with augmented Lewis acidity due to the electronegativity of the halogen atoms. The strong Lewis acidity of the halostibine antimony center, coupled with its capacity to undergo oxidation

reactions or anion exchanges, led to the isolation of trihalostiborane-gold complexes and trihalostiborane-platinum complexes, featuring magnified metal→Sb(V) interactions. These complexes have been exploited in the development of ligand-centered redox-controlled catalysis, highlighting their utility in the area of smart catalyst design. Another noteworthy result of this research includes the discovery of redox active antimony-platinum molecular platform, in which the halogenated antimony ligand is able to modulate the electron density of the coordinated platinum, thereby facilitating the two-electron redox reactions. Such redox reactions have been utilized to realize the high-quantum-yield photoreductive elimination of chlorine, which is of relevance to photocatalytic production of H₂ from HX. In parallel to the antimony chemistry, tellurium ligand chemistry has also been investigated. Our results in this area show for the first time the redox non-innocent behavior of telluroether ligand in the coordination sphere of gold.

DEDICATION

For Mom and Dad

ACKNOWLEDGEMENTS

My determination to transfer from computer science to chemistry in my second semester in college stems from my motivation to learn a little fundamental science. I never imagined I would go that far to pursue a Ph.D. years later. The five-year Ph.D. journey is long, yet short like a dream, especially when I am writing some closing words with memories flowing through my mind.

I want to express my deepest gratitude to my advisor, Prof. François P. Gabbaï, for his fundamental role in my graduate career. I have been extremely fortunate to have an advisor who is constantly supportive and inspiring. I greatly valued his thoughtful guidance and scholarly input, which made it possible for me to sail through the various stages of this five-year journey. I am deeply impressed by his wealth of knowledge as well as his precise expertise in the field of inorganic chemistry. Beyond the academic support, I am also hugely appreciative of his great personality. I just simply cannot imagine a better advisor!

I would like to acknowledge the members of my Ph.D. committee, Prof. Oleg V. Ozerov, Prof. Michael B. Hall and Prof. Jodie L. Lutkenhaus for their valuable time, insightful comments and support all the time. I also thank Prof. Oleg V. Ozerov, Prof. Michael B. Hall, Prof. Kim R. Dunbar and Prof. Timothy R. Hughbanks for their wonderful courses that I found incredibly useful in my later study.

I am deeply thankful to the past and present members of the Gabbai group. Dr. Mitsukuni Tsunoda, Dr. Min Hyung Lee, Dr. Kewei Huang, Dr. Boris Vabre, Dr. Daniel Tofan, Dr. Guillaume Bélanger-Chabot, Dr. Sikun Cheng, Dr. Kantapat Chansaenpak, Lauren Leamer, James (Stuart) Jones, Anna Marie Christianson, Srobona Sen, Chang-Hong Chen, Elham Tabei, Mengxi (Moncy) Yang, Ying-Hao Lo, Di You, Gregory Day, Christina Lollar,

Minji Kim, Xu Ye, Nilanjana Pati and Austin Williamson. Very special thank goes to Dr. Tzu-Pin Lin, Dr. Baofei Pan, Dr. Haiyan Zhao, Dr. Iou-Sheng Ke, Dr. Masato Hirai and Stuart for their mentorship, teaching me many lab techniques and guiding me through the early stage of my Ph.D. career.

I am very thankful to Dr. David Powers for the collaboration opportunity on the photochemistry work. The same respect applies to Dr. Jeffrey Miller and his group for the collaboration work on XANES measurements. I also wish to acknowledge Dr. Lisa M. Pérez who was always helpful and patient to answer my questions on theoretical calculations.

From the non-scientific part, I would like to take this opportunity to thank an organization: Organization for Cultural Diversity in Chemistry (OCDC). I was privileged to work with a group of talented, responsible, and thoughtful people, who have also become great friends of mine: Ryan Coll, Jill Ellenbarger, Sasha Chihak, Rajat Maji, Rita Silbernagel, Xuan Wang, Vishruth Gowda, Qi Wang, Kelly Nieto and our advisor Dr. Coran M. H. Watanabe . A person that deserves a special mention is Dr. Amanda David who invited me to OCDC and other student organizations. Her encouragement and friendship are like beautiful songs in my mind forever. My appreciation also goes to the Women in Science and Engineering (WISE) 2015-2016 officers and members with whom I had pleasure working with: Sarah Elmore, Rachel Chupik, Yindrila Chakrabarty, and our advisor Dr. Nancy Magnussen and Bonnie Stephen.

I thank many great friends outside the department, for all the great times we have shared. Thanks to Ying-pin Chen, Yu Shi and Xiayun Huang for sharing the apartment with me over the past years and giving me help all the time. Their unrelenting passion for pursuing academia gave me considerable encouragement as well. I am also very grateful to Fengping

Yu, Ge Li, Chen Ding, Yan Li, Guanlan Liu, Wenlong Gong, Junfeng Chen, Shu Dai, Jin Huang, Qichang Ji, Laura Bentz, Hannah Frailey, Suzanne Achgill and Bob Achgill for creating so much fun and teaching me so much in life. I have dozens of reasons to thank several special friends Huali Wu, Rongfang Ma, Feihua Wang, Mallory McCall Pearson and Brennan Bailey for being so understanding and encouraging, no matter when it is and wherever we are.

Finally, I am deeply indebted to my parents, sister and brother. Their unconditionally love and support are my constant source of strength and energy. I also thank my boyfriend, Yuachen Cui, for his love, encouragement and support.

TABLE OF CONTENTS

| | Page |
|---|------|
| ABSTRACT..... | ii |
| DEDICATION..... | iv |
| ACKNOWLEDGEMENTS..... | v |
| TABLE OF CONTENTS..... | viii |
| LIST OF FIGURES..... | xi |
| LIST OF TABLES..... | xx |
| CHAPTER I INTRODUCTION TO NON-INNOCENT Z-TYPE LIGANDS CONTAINING ANTIMONY AND TELLURIUM..... | 1 |
| 1.1 Introduction to ligand non-innocence and Z-type ligands..... | 1 |
| 1.1.1 The concept of ligand non-innocence..... | 1 |
| 1.1.2 Brief overview of Z-type ligands..... | 3 |
| 1.2 Antimony and tellurium compounds as potential non-innocent Z-ligands..... | 7 |
| 1.2.1 Lewis acidity and redox reactivity of antimony compounds..... | 7 |
| 1.2.2 Lewis acidity and redox reactivity of tellurium compounds..... | 10 |
| 1.3 Coordination chemistry of antimony polydentate ligands..... | 12 |
| 1.3.1 Background of antimony ligands in organometallic chemistry..... | 12 |
| 1.3.2 Trivalent antimony ligands as Z-type ligands..... | 14 |
| 1.3.3 Redox non-innocence of antimony(III) ligands..... | 16 |
| 1.3.4 Coordination non-innocence of antimony ligands..... | 18 |
| 1.4 Coordination chemistry of tellurium polydentate ligands..... | 23 |
| 1.4.1 Background of tellurium ligands in organometallic chemistry..... | 23 |
| 1.4.2 Telluronium as Z-type ligands..... | 24 |
| 1.4.3 Coordination non-innocence of tellurium ligands..... | 26 |
| 1.5 Application in photoreductive elimination of chlorine..... | 29 |
| 1.5.1 Background of photoreductive elimination of chlorine..... | 29 |
| 1.5.2 Photoreductive elimination of chlorine from a TePt complex..... | 30 |
| 1.6 Motivation and objectives..... | 31 |

CHAPTER II SOLUTION AND SOLID-STATE PHOTOREDUCTIVE ELIMINATION OF CHLORINE BY IRRADIATION OF A [PTSB]VII COMPLEX35

| | | |
|-----|--|----|
| 2.1 | Introduction..... | 35 |
| 2.2 | Synthesis and structure of antimony-platinum complexes | 36 |
| 2.3 | Bonding characteristics and photophysical properties..... | 40 |
| 2.4 | Photoreductive elimination of chlorine in solution..... | 43 |
| 2.5 | Photoreductive elimination of chlorine in solid-state | 46 |
| 2.6 | Conclusion | 48 |
| 2.7 | Experimental | 49 |

CHAPTER III TELLUROETHER TO TELLUROXIDE CONVERSION IN THE COORDINATION SPHERE OF A METAL: OXIDATION INDUCED UMPOLUNG OF A TE-AU BOND66

| | | |
|-----|--|----|
| 3.1 | Introduction..... | 66 |
| 3.2 | Synthesis and characterization of telluroether-gold complexes..... | 67 |
| 3.3 | Bonding analysis of the Te→Au interaction | 72 |
| 3.4 | Telluroether to telluroxide conversion in the coordination sphere of gold..... | 73 |
| 3.5 | Conclusion | 77 |
| 3.6 | Experimental | 77 |

CHAPTER IV ACTIVATION OF A HYDROAMINATION GOLD CATALYST BY OXIDATION OF A REDOX NON-INNOCENT CHLOROSTIBINE Z-LIGAND84

| | | |
|-----|---|-----|
| 4.1 | Introduction..... | 84 |
| 4.2 | Gold-chlorostibine complexes | 86 |
| 4.3 | Gold-trihalostiborane complexes | 91 |
| 4.4 | Lewis acidic behavior and electronic structures of the gold-trihalostiborane complexes | 96 |
| 4.5 | Catalytic properties of the cationic gold-trifluorostiborane salt [50][SbF ₆] | 101 |
| 4.6 | Conclusion | 102 |
| 4.7 | Experimental | 103 |

CHAPTER V SWITCHING THE REDOX STATE AND REACTIVITY OF A PLATINUM CATALYST BY ANION COORDINATION NON-INNOCENCE OF THE ANTIMONY LIGAND.....124

| | | |
|-----|--|-----|
| 5.1 | Introduction..... | 124 |
| 5.2 | Trifluorostiborane-platinum complexes..... | 126 |
| 5.3 | Cationic monofluorostiboranyl platinum complexes..... | 131 |
| 5.4 | Catalytic properties of the cationic platinum complexes..... | 137 |

| | | |
|------------------------------|--|-----|
| 5.5 | Conclusion | 140 |
| 5.6 | Experimental | 141 |
| CHAPTER VI CONCLUSION | | 156 |
| 6.1 | Photochemical activation of M-X bond..... | 156 |
| 6.2 | Redox non-innocent behavior of a telluroether ligand | 156 |
| 6.3 | Activation of an electrophilic gold catalyst | 157 |
| 6.4 | Accessing a $\text{Sb}^{\text{V}}\text{Pt}^0$ and a cationic $\text{Sb}^{\text{IV}}\text{Pt}^{\text{I}}$ complexes | 158 |
| 6.5 | Summary of halogenated antimony ligands..... | 158 |
| REFERENCES | | 160 |
| APPENDIX TO CHAPTER IV | | 176 |
| APPENDIX TO CHAPTER V | | 186 |

LIST OF FIGURES

| | Page |
|---|------|
| Figure 1. Redox non-innocence of a ditholene ligand in nickel complex. | 1 |
| Figure 2. Schematic depiction of electron exchange in redox non-innocent ligands. | 2 |
| Figure 3. Molecular orbital diagram showing a dative interaction between metal and Z- ligand. | 4 |
| Figure 4. Representative examples of unsupported M→Z ligand interactions. | 4 |
| Figure 5. Schematic representation of four coordination modes of ambiphilic L/Z ligands | 5 |
| Figure 6. An example showing the Lewis acidic site of a bis(phosphine)borane ambiphilic L/Z-ligand becoming involved in anion binding. | 6 |
| Figure 7. An example showing the Lewis acidic site of a phosphine-allane ambiphilic L/Z- ligand abstracting anion from the metal center. | 6 |
| Figure 8. Enyne cyclization catalyzed by a bis(phosphine)borane gold complex. | 7 |
| Figure 9. Left: An example showing Lewis acidic antimony (III) center; Right: σ^* orbital in stibine. | 8 |
| Figure 10. Examples of stable Lewis acidic antimony (V) compounds. | 9 |
| Figure 11. Top: General oxidation reactions converting divalent tellurium to tetravalent tellurium species. Bottom: Examples showing reversible two-electron redox chemistry of tellurium compounds. | 11 |
| Figure 12. Examples of Lewis acidic telluronium ions. | 12 |
| Figure 13. Early examples of group 10 metal complexes featuring tris-substituted polydentate antimony ligands. | 14 |
| Figure 14. Structures of 15 and 16 and NBO plot showing the Au→Sb interaction in 16. | 15 |
| Figure 15. Examples showing the conversion of stibine ligands into stiborane ligands in the coordination sphere of gold. | 17 |
| Figure 16. Scheme showing the conversion of a stibine into a stiborane in the coordination sphere of nickel. | 18 |

| | |
|--|----|
| Figure 17. View of two halostibine complexes featuring interactions between the anion and the formally neutral antimony (III) center. | 19 |
| Figure 18. Left: Synthesis of complex [24] ⁺ ; Right: Schematic representation showing how the metal coordination converts a stibine donor into a Lewis acidic acceptor, owing to the presence of Sb-M σ* orbital available for anion binding. .. | 19 |
| Figure 19. Synthesis of complexes [26] ²⁺ , [27] ⁺ and 28. | 21 |
| Figure 20. Synthesis of the stiboranyl complexes 30 and 31. | 22 |
| Figure 21. A schematic representation showing bonding electron polarization to metal can be induced by anion binding at the ligand center. | 22 |
| Figure 22. Early examples of metal complexes supported by tellurium centered pincer-style ligands. | 24 |
| Figure 23. Synthesis of complexes 34 and [35] ⁺ | 26 |
| Figure 24. Examples showing two types of coordination non-innocent behaviors of tellurium ligands. | 27 |
| Figure 25. Photocycle for the splitting of HCl mediated by a dinuclear rhodium catalyst. | 30 |
| Figure 26. Schematic representation showing the antimony-centered non-innocence behavior of early versions of antimony ligands. | 32 |
| Figure 27. Schematic representation sketching the new antimony ligand design, which couples the Z-type ligand effect with the ligand-centered non-innocence. The targeted complexes feature more electrophilic metal center, promising for photoreductive elimination of X ₂ or electrophilic catalysis. | 34 |
| Figure 28. Reported molecular platforms for chlorine photoreductive elimination. | 36 |
| Figure 29. Synthesis of complexes 42 and 43. | 37 |
| Figure 30. Structure of a stiboranyl-platinum complex. | 37 |
| Figure 31. Left: Solid state structure of 42 (top left) and 43 (bottom left). Thermal ellipsoids are drawn at the 50% probability level. Phenyl groups are drawn in wireframe. Hydrogen atoms and solvent molecules are omitted for clarity. Pertinent metrical parameters can be found in the text. NLMO plot (isovalue = 0.05) of the Sb–Pt bond in of 42 (top right) and 43 (bottom right) obtained from the NBO analysis. Hydrogen atoms are omitted for clarity. | 39 |
| Figure 32. Experimental (—) (CH ₂ Cl ₂) and calculated (---) ultraviolet–visible spectra for 42. The calculated spectra were obtained by TD–DFT calculations using the | |

| | |
|--|----|
| MPW1PW91 functional and a mixed basis set (peak half-width used for the simulation: 0.25 eV). The computed excitations are shown as thin lines with heights proportional to the calculated oscillator strengths. | 41 |
| Figure 33. Relevant resonance structures of 42. | 42 |
| Figure 34. Plots of the LUMO (−0.120 eV) and LUMO+1 (−0.106 eV) of 43 (0.03 isosurface value). | 43 |
| Figure 35. Absorption spectra (—) obtained during the photolysis of 43 in CH ₂ Cl ₂ (2.23 × 10 ^{−5} M) with monochromatic 320 nm light in the presence of 2,3-dimethyl-1,3-butadiene (7.07 × 10 ^{−4} M). The final spectrum (− −) is identical to that of 42. The inset shows the correlation between the quantum yield and the DMBD concentration. | 44 |
| Figure 36. ³¹ P NMR spectra of photolysis of 43 in the absence of 2,3-dimethyl-1,3-butadiene (in CH ₂ Cl ₂). This spectrum was recoded on Varian Unity Inova 300 FT NMR. | 45 |
| Figure 37. ³¹ P NMR spectra of photolysis of 43 in CH ₂ Cl ₂ (0.011 M) in the presence of 2,3-dimethyl-1,3-butadiene (1.77 M). | 45 |
| Figure 38. Photoreduction of 43 using a Xe lamp (75W). a) Solution photolysis in CH ₂ Cl ₂ with DMBD (1.77 M) in a glass NMR tube (complete conversion in 10 minutes). b) Solid state photolysis in a closed quartz cell with Na as a trap (conversion = 53% in 10 hours). c) Solid state photolysis in an open quartz cell (conversion =45% in 10 hours). | 46 |
| Figure 39. Ion chromatography analysis of the Na strip after the solid-state photolysis. | 47 |
| Figure 40. ³¹ P NMR spectra before and after solid state irradiation of 43 with a Xe lamp (75 W) under ambient conditions in an open quartz cell. The inset shows a schematic drawing of the experimental setup used for this open-system solid state photolysis. The spectral region marked by a “*” shows the presence of decomposition products. | 48 |
| Figure 41. ³¹ P NMR spectrum of the coproportionation product of neat SbCl ₃ and (<i>o</i> -(Ph ₂ P)C ₆ H ₄) ₃ Sb in CDCl ₃ | 56 |
| Figure 42. ¹ H NMR spectrum of 42 in CDCl ₃ | 57 |
| Figure 43. ³¹ P NMR spectrum of 42 in CDCl ₃ | 57 |
| Figure 44. ¹⁹⁵ Pt NMR spectrum of 42 in CDCl ₃ | 58 |
| Figure 45. ¹ H NMR spectrum of 43 in CDCl ₃ | 58 |

| | |
|---|----|
| Figure 46. ^{31}P NMR spectrum of 43 in CDCl_3 . | 59 |
| Figure 47. ^{195}Pt NMR spectrum of 43 in CDCl_3 . | 59 |
| Figure 48. NLMO Plot of the Sb-Pt bond in complex 42 (left) and complex 43 (right) obtained from NBO analysis (Rotated 90° from the NLMO Plot in the paper). | 60 |
| Figure 49. Absorption spectra of 42 (---) and 43 (—) in CH_2Cl_2 with DMBD (0.707 mM). The inset shows the absorption spectrum of pure DMBD (0.707 mM) in CH_2Cl_2 . | 60 |
| Figure 50. ^{31}P NMR and ^1H NMR spectra of 43 after heating at 70°C (solid state thermal stability test). | 61 |
| Figure 51. ^{31}P NMR spectrum of 43 after solid-state photolysis in a closed system in the presence of a sodium strip. | 61 |
| Figure 52. ^{31}P NMR spectrum after solid-state photolysis of 43. For this experiment, crystals of complex 43 (free of interstitial solvents) were dissolved in CH_2Cl_2 and transferred to the cuvette. Evaporation of the CH_2Cl_2 resulted in the deposition of a film which was dried thoroughly under vacuum for 1 h prior and irradiated for 8 hours using a Xe lamp. The films obtained from CH_2Cl_2 tend to be heterogenous with large crystalline particles. The heterogeneity of these films affects the reaction and lead to higher concentrations of decomposition products. The best films are obtained from THF. | 62 |
| Figure 53. GC-MS analysis of the photolyzed solution of 43 in the presence of DMBD showing the formation of DMBD“ Cl_2 ”. (a) Total GC-MS chromatogram from 0 min to 23 min. (b) Extracted GC-MS chromatogram from 8 min to 12 min. (c) and (d), Mass spectra of the DMBD“ Cl_2 ” species with retention times of 10.60 min and 10.73 min. | 63 |
| Figure 54. Reaction of Ph_2Te with $(\text{tht})\text{AuCl}$. | 67 |
| Figure 55. Synthesis of 44 and $[\text{45}][\text{Cl}]$. | 69 |
| Figure 56. (a) ^{31}P NMR spectrum of 44 in CD_2Cl_2 at 20°C (a), -40°C (b), and -80°C (c). Spectrum d was obtained by adding one equivalent of PPh_3 to the NMR tube used to measure spectra a-c. This spectrum corresponds to that of $[\text{45}][\text{Cl}]$. Spectrum e in the bottom right inset shows the ^{125}Te NMR spectrum of $[\text{45}][\text{Cl}]$. | 69 |
| Figure 57. Left: Solid state structure of 44. Thermal ellipsoids are drawn at the 50% probability level. Phenyl groups are drawn in wireframe. Hydrogen atoms and solvent molecules are omitted for clarity. Selected bond lengths (\AA) and angles ($^\circ$): Au-Te 2.874(4), Au-Cl 2.554(5), Au-P(2) 2.322(5), Au-P(1) 2.328(5), Te-C(19) 2.161(18), Te-C(1) 2.189(19); P(2)-Au-P(1) 134.40(18), P(2)-Au-Cl 113.28(17), P(1)-Au-Cl 111.07(16), P(2)-Au-Te 89.05(16), P(1)-Au-Te | |

86.56(15), Cl-Au-Te 108.75(17), C(19)-Te-C(1) 93.3(6), C(19)-Te-Au 88.3(5), C(1)-Te-Au 87.6(5). Right: NBO plot (isovalue = 0.05) showing the lp(Te)→s(Au) donor-acceptor interaction in 44. Hydrogen atoms are omitted for clarity.. 70

Figure 58. Left: Solid state structure of [45][Cl]. Thermal ellipsoids are drawn at the 50% probability level. Phenyl groups are drawn in wireframe. Hydrogen atoms and solvent molecules are omitted for clarity. Selected bond lengths (Å) and angles (°): Au-Te 2.9373(15), Au-P(1) 2.396(3), Au-P(2) 2.404(3), Au-P(3) 2.334(3), Te-C(1) 2.118(9), Te-C(19) 2.180(9), Te-Cl 3.113(3); P(3)-Au-Te 129.65(6), P(3)-Au-P(1) 120.22(9), P(3)-Au-P(2) 122.33(8), P(1)-Au-P(2) 112.10(9), P(1)-Au-Te 82.42(6), P(2)-Au-Te 77.71(6), Cl-Te-C(19) 165.4(3), C(1)-Te-C(19) 89.8(3), C(1)-Te-Au 94.3(2), C(19)-Te-Au 85.8(3). Right: NBO plot (isovalue = 0.05) showing the lp(Te)→s(Au) donor-acceptor interaction in [45]⁺. Hydrogen atoms are omitted for clarity. 72

Figure 59. Synthesis of complex 46..... 74

Figure 60. Top and bottom left: Solid state structure of 46 with thermal ellipsoids drawn at the 50% probability level. The phenyl groups are drawn in wireframe. Hydrogen atoms and solvent molecules are omitted for clarity. The top view shows the dimer under two perpendicular orientations. The bottom left view shows the monomeric unit. Selected bond lengths (Å) and angles (°): Au-Te 2.9864(5), Te-O: 1.857(3), Au-Cl 2.524(2), Au-P(2) 2.301(2), Au-P(1) 2.318(2), Te-C(19) 2.167(6), Te-C(1) 2.154(7); Au-Te-O 175.9(1), P(2)-Au-P(1) 136.71(6), P(2)-Au-Cl 113.90(7), P(1)-Au-Cl 108.59(7), P(2)-Au-Te 85.29(4), P(1)-Au-Te 82.74(4), Cl-Au-Te 117.05(5), C(19)- Te-C(1) 92.5(2), C(19)-Te-Au 88.9(1), C(1)-Te-Au 85.6(2). Bottom right: NBO plot of 46 (monomer) (isovalue = 0.05) showing the lp(Au)→σ*(Te=O) donor-acceptor interaction in 46. Hydrogen atoms are omitted for clarity. 76

Figure 61. (a) ³¹P spectrum of 44 in CDCl₃ at 20 °C (b) Spectrum was obtained by adding one equivalent of PPh₃ to the NMR tube used to measure spectra (a). This spectrum corresponds to that of [45][Cl]. Picture in the top left inset shows the crystals of 44 used for NMR experiment. 81

Figure 62. ¹H, ¹³C, ³¹P, and ¹²⁵Te NMR spectra of [45][Cl] at ambient temperature in CDCl₃. 82

Figure 63. ¹H, ¹³C, ³¹P, and ¹²⁵Te NMR spectra of 46 at ambient temperature in CDCl₃. 83

Figure 64. Oxidation of coordinated stibine ligands..... 85

Figure 65. Representation of possible catalyst structures..... 86

Figure 66. Synthesis of 47-Cl and [47][SbF₆]. 87

| | |
|--|-----|
| Figure 67. Solid state structure of 47-Cl (top) and [47][SbF ₆] (bottom). Thermal ellipsoids are drawn at the 50% probability level. Phenyl groups are drawn in wireframe. Hydrogen atoms and solvent molecules are omitted for clarity. Relevant metrical parameters can be found in the text or the experimental section..... | 88 |
| Figure 68. NBO plots of the major Sb-Au bonding interactions in 47-Cl (left) and [47][SbF ₆] (right) (isodensity value = 0.05). Hydrogen atoms are omitted. | 90 |
| Figure 69. Side by side comparison showing [47] ⁺ and a recently reported boron complex of type [48] ⁺ . ²⁴³ | 90 |
| Figure 70. Model hydroamination reaction used to evaluate [47][SbF ₆]..... | 91 |
| Figure 71. Synthesis of 49-Cl, 50-Cl and [50][SbF ₆]. | 93 |
| Figure 72. Solid state structure of 49-Cl. Thermal ellipsoids are drawn at the 50% probability level. Phenyl groups are drawn in wireframe. Hydrogen atoms are omitted for clarity. Relevant metrical parameters can be found in the text or in the experimental section..... | 93 |
| Figure 73. Resonances observed in the ¹⁹ F NMR spectrum of 50-Cl measured in CDCl ₃ | 94 |
| Figure 74. Solid state structure of 50-Cl (top) and [50][SbF ₆] (bottom). Thermal ellipsoids are drawn at the 50% probability level. Phenyl groups are drawn in wireframe. Hydrogen atoms and solvent molecules are omitted for clarity. Relevant metrical parameters can be found in the text or in the experiment section..... | 96 |
| Figure 75. Structure of [51] ⁺ | 97 |
| Figure 76. Formation of [50-OH ₂][SbF ₆]..... | 98 |
| Figure 77. Solid state structure of [50-OH ₂][SbF ₆]. Thermal ellipsoids are drawn at the 50% probability level. Phenyl groups are drawn in wireframe. Hydrogen atoms and solvent molecules are omitted for clarity. Relevant metrical parameters can be found in the text or in the experimental section. | 98 |
| Figure 78. NBO plots of the major Sb-Au bonding interactions [50] ⁺ (isodensity value = 0.05). Hydrogen atoms are omitted. The same donor acceptor interactions are also observed for 50-Cl and [50-OH ₂] ⁺ | 99 |
| Figure 79. Resonance structures for [50] ⁺ to [50-OH ₂] ⁺ and 50-Cl..... | 100 |
| Figure 80. ¹ H NMR spectra of 47-Cl and [47]SbF ₆ in CDCl ₃ | 108 |
| Figure 81. ³¹ P NMR spectra of 47-Cl and [47]SbF ₆ in CDCl ₃ | 109 |

| | |
|--|-----|
| Figure 82. ^{13}C NMR spectra of 47-Cl and $[\text{47}]\text{SbF}_6$ in CDCl_3 | 110 |
| Figure 83. ^1H NMR spectra of 49-Cl in CDCl_3 | 110 |
| Figure 84. ^{13}P NMR spectra of 49-Cl in CDCl_3 | 111 |
| Figure 85. ^1H NMR spectra of 50-Cl in CDCl_3 | 111 |
| Figure 86. ^{13}C NMR spectra of 50-Cl in CDCl_3 | 112 |
| Figure 87. ^{31}P NMR spectra of 50-Cl in CDCl_3 | 112 |
| Figure 88. ^{19}F NMR spectra of 50-Cl in CDCl_3 | 113 |
| Figure 89. ^1H NMR spectra of $[\text{50}]\text{SbF}_6$ in CDCl_3 | 113 |
| Figure 90. ^{13}C NMR spectra of $[\text{50}]\text{SbF}_6$ in CDCl_3 | 114 |
| Figure 91. ^{31}P NMR spectra of $[\text{50}]\text{SbF}_6$ in CDCl_3 | 114 |
| Figure 92. ^{19}F NMR spectra of $[\text{50}]\text{SbF}_6$ in CDCl_3 | 115 |
| Figure 93. ^{31}P NMR spectra of CH_2Cl_2 solutions (0.75 mL) containing the cationic gold complex (0.010 mmol) and tri(phenyl)phosphine oxide (0.011 mmol, 3.3 mg)... | 116 |
| Figure 94. ^1H NMR spectra for the hydroamination of phenylacetylene with <i>p</i> -toluidine. (a) ^1H NMR spectra collected for the purpose of reaction monitoring. (b) ^1H NMR spectrum of the isolated product. | 118 |
| Figure 95. ^1H NMR spectra for the hydroamination of phenylacetylene with 2,6-diisopropylaniline. (a) ^1H NMR spectra collected for the purpose of reaction monitoring. (b) ^1H NMR spectrum of the isolated product..... | 120 |
| Figure 96. ^1H NMR spectra for the hydroamination of phenylacetylene with pentafluoroaniline..... | 121 |
| Figure 97. ^1H NMR spectra for the hydroamination of phenylacetylene with phenylhydrazine. a) ^1H NMR spectra collected for the purpose of reaction monitoring. (b) ^1H NMR spectrum of the isolated product..... | 122 |
| Figure 98. ^1H NMR spectra for the hydroamination of 1-hexyne with <i>p</i> -toluidine..... | 123 |
| Figure 99. Anion-induced internal redox event. | 125 |
| Figure 100. Schematic representation showing chloride-to-fluoride exchange reaction of a fully chlorinated antimony-metal complex. | 126 |
| Figure 101. Synthesis of 52 and 53..... | 127 |

| | |
|--|-----|
| Figure 102. Solid state structure of 52 (left) and 53 (right). Thermal ellipsoids are drawn at the 50% probability level. Phenyl groups are drawn in wireframe. Hydrogen atoms and solvent molecules are omitted for clarity. Relevant metrical parameters can be found in the text or the experimental section. | 128 |
| Figure 103. NBO plots of the major Sb-Pt bonding interactions in 52 (left) and 53 (right) (isodensity value = 0.04). Hydrogen atoms are omitted. | 130 |
| Figure 104. Reported examples showing a zero valent platinum center forms dative bonds with Lewis acids. Complex 52 and 53 features a similar dative bonding to the Lewis acidic antimony site. | 131 |
| Figure 105. Side by side comparison showing complex 52 or 53 and recently reported $[\text{Au} \rightarrow \text{Z}]^+$ complexes of type $[\text{C}]^+$ and $[\text{D}]^+$ | 131 |
| Figure 106. Hypothesized ligand post-synthetic modification through acid binding to the fluorine atoms, in order to enhance the Lewis acidity at the metal center. | 132 |
| Figure 107. Reaction of complexes 52 and 53 with HBF_4 . The insert shows the crystals of 54. | 133 |
| Figure 108. Top: Solid state structure of 54 (Top left) and 55 (Top right). Thermal ellipsoids are drawn at the 50% probability level. Phenyl groups are drawn in wireframe. Hydrogen atoms and solvent molecules are omitted for clarity. Relevant metrical parameters can be found in the experimental section. Bottom: NBO plots of the major Sb-Pt bonding interactions in 54 (Bottom left) and 55 (Bottom right). (isodensity value = 0.05). Hydrogen atoms are omitted. | 136 |
| Figure 109. ^1H NMR spectrum of 52 in CD_2Cl_2 | 144 |
| Figure 110. ^{13}C NMR spectrum of 52 in CD_2Cl_2 | 145 |
| Figure 111. ^{31}P NMR spectrum of 52 in CD_2Cl_2 | 145 |
| Figure 112. ^{19}F NMR spectrum of 52 in CD_2Cl_2 | 145 |
| Figure 113. ^1H NMR spectrum of 53 in CD_2Cl_2 | 146 |
| Figure 114. ^{13}C NMR spectrum of 53 in CD_2Cl_2 | 146 |
| Figure 115. (above) ^{31}P NMR spectrum of 53 in CD_2Cl_2 . (below) Magnified spectrum corresponding to 53. | 146 |
| Figure 116. ^{19}F NMR spectrum of 53 in CD_2Cl_2 | 147 |
| Figure 117. ^1H NMR spectrum of 54 in CD_2Cl_2 | 147 |

| | |
|---|-----|
| Figure 118. ^{31}P NMR spectrum of 54 in CD_2Cl_2 . | 148 |
| Figure 119. ^{19}F NMR spectrum of 54 in CD_2Cl_2 . | 148 |
| Figure 120. ^1H NMR spectrum of 55 in CD_2Cl_2 . | 149 |
| Figure 121. ^{31}P NMR spectrum of 55 in CD_2Cl_2 . | 149 |
| Figure 122. ^{19}F NMR spectrum of 55 in CD_2Cl_2 . | 150 |
| Figure 123. ^{31}P NMR spectra for reaction of 53 with excess HBF_4 or two equivalents of $\text{B}(\text{C}_6\text{F}_5)_3$ in CH_2Cl_2 , showing the same resonance at 48.5 ppm, $J_{\text{pt-p}}=2239$ Hz. | 150 |
| Figure 124. ^{19}F NMR spectrum for reaction of 53 with two equivalents of $\text{B}(\text{C}_6\text{F}_5)_3$ in CH_2Cl_2 , showing one set of signals corresponding to the formation of $[\text{FB}(\text{C}_6\text{F}_5)_3]^-$. | 151 |
| Figure 125. ^{31}P NMR spectra for reaction of 53 with $\text{SbCat}^{\text{Cl}}(\text{C}_6\text{F}_5)_3$ in CH_2Cl_2 . The addition of 1.25 equivalents of $\text{SbCat}^{\text{Cl}}(\text{C}_6\text{F}_5)_3$ results in one resonance at 63.7 ppm, $J_{\text{pt-p}}=2607$ Hz. | 151 |
| Figure 126. ^{19}F NMR spectra for reaction of 53 with $\text{SbCat}^{\text{Cl}}(\text{C}_6\text{F}_5)_3$ in CH_2Cl_2 . The addition of 1 or 1.25 equivalents of $\text{SbCat}^{\text{Cl}}(\text{C}_6\text{F}_5)_3$ result in the same signals corresponding to the formation of $[\text{SbFCat}^{\text{Cl}}(\text{C}_6\text{F}_5)_3]^-$. | 152 |
| Figure 127. Comparative ^1H NMR spectra of enyne cyclization catalysis. | 153 |
| Figure 128. Structure of complex $[\text{50-DMAP}][\text{SbF}_6]$. | 176 |
| Figure 129. Structure of complex $[\text{50-}p\text{-toluidine}][\text{SbF}_6]$. | 178 |
| Figure 130. Structure of complex $[\text{50-THF}][\text{SbF}_6]$. | 179 |
| Figure 131. Structure of a zwitterionic complex 50-F. | 181 |
| Figure 132. ^{31}P NMR spectrum of zwitterionic complex 50-F in CH_2Cl_2 . | 183 |
| Figure 133. ^{19}F NMR spectrum of zwitterionic complex 50-F in CH_2Cl_2 . | 183 |
| Figure 134. Structure of complex 56. | 184 |
| Figure 135. Synthesis and crystal structure of complex $[\text{52-Cl}]\text{N}^n\text{Bu}_4$. | 186 |
| Figure 136. ^{31}P NMR spectrum of complex $[\text{52-Cl}]\text{N}^n\text{Bu}_4$ in CH_2Cl_2 . | 186 |
| Figure 137. ^{19}F NMR spectrum of complex $[\text{52-Cl}]\text{N}^n\text{Bu}_4$ in CH_2Cl_2 . | 187 |
| Figure 138. Synthesis and crystal structure of complex $[\text{52-Cl}]\text{Tl}$. | 188 |

LIST OF TABLES

| | Page |
|--|------|
| Table 1. Selected bond lengths (Å) and angles (°) for complexes 42 and 43 as determined crystallographically and optimized computationally. | 64 |
| Table 2. TD-DFT calculation output showing the nature of the low energy excitations for 43. | 64 |
| Table 3. Selected bond lengths (Å) for complexes 44, [45] ⁺ and 46 as determined crystallographically and computationally. | 74 |
| Table 4. Results obtained in the hydroamination of terminal alkynes with aromatic amines with [50]SbF ₆ as a catalyst. | 102 |
| Table 5. Selected bond lengths (Å) and angles (°) for complexes 52-CH ₃ CN and 53 as determined crystallographically. | 129 |
| Table 6. Selected bond lengths (Å) for complexes 54 and 55 as determined crystallographically. | 136 |
| Table 7. 1,6-Enyne cyclization catalysis. | 139 |
| Table 8. Selected bond lengths (Å) and angles (°) for complexes 52 and 53 as determined crystallographically and optimized computationally. | 153 |
| Table 9. Selected bond lengths (Å) and angles (°) for complexes 54 and 55 as determined crystallographically and optimized computationally. | 154 |
| Table 10. Crystal data collection and refinement parameters for complex [50-DMAP][SbF ₆]. | 177 |
| Table 11. Crystal data collection and refinement parameters for complex [50- <i>p</i> -toluidine][SbF ₆]. | 178 |
| Table 12. Crystal data collection and refinement parameters for complex [50-THF][SbF ₆]. | 179 |
| Table 13. Crystal data collection and refinement parameters for complex 50-F. | 182 |
| Table 14. Crystal data collection and refinement parameters for complex 56. | 184 |
| Table 15. Crystal data collection and refinement parameters for complex [52-Cl]N ⁿ Bu ₄ . .. | 187 |

Table 16. Crystal data collection and refinement parameters for complex [52-Cl]Tl. 189

CHAPTER I

INTRODUCTION TO NON-INNOCENT Z-TYPE LIGANDS CONTAINING ANTIMONY AND TELLURIUM

1.1 Introduction to ligand non-innocence and Z-type ligands

1.1.1 The concept of ligand non-innocence

The “non-innocent” terminology was introduced in 1966 in a review by Jørgensen ¹ who explained that “ligands are innocent when they allow oxidation states of the central atom to be defined”. Since the 1960’s, examples of complexes that did not comply with this rule started to surface. One of the first families of such complexes are nickel dithiolene complexes for which an assignment of the nickel oxidation state proved to be problematic as summarized in Figure 1. ² Careful analysis of the structure and bonding of such complexes reveals that oxidation changes occurs at the ligand rather than at the metal center. Calculations also showed that the frontier orbitals of such complexes are ligand-based rather than the metal-based.³ That is, the ligands of these complexes may become involved in redox processes thus suggesting their possible use as electron reservoir. ⁴

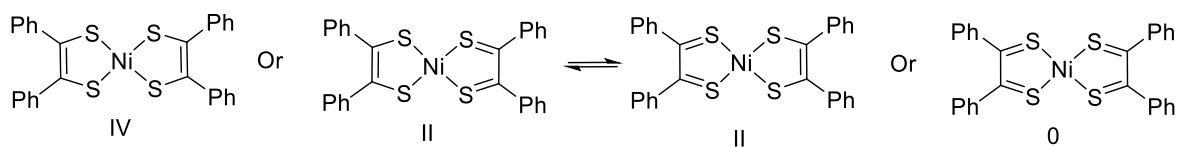


Figure 1. Redox non-innocence of a dithiolene ligand in nickel complex.

In the past few years, this possibility has attracted a great deal of interest, with several research groups succeeding in exploiting ligand-centered redox processes for the discovery of new reactions and catalytic processes. Prototypical ligand platforms that support such ligand centered redox processes include catecholate, imiopyridine, amidophenolate and their analogs.

⁵⁻¹² During the redox process, the electrons were shuttled between the single bond (C-X, X= N, O, S⁻) and double bond (C=X) within the π conjugated ligand backbone, transforming the X type donor into L type donor upon oxidation, while the oxidation state of the metal center can remain intact (Figure 2).

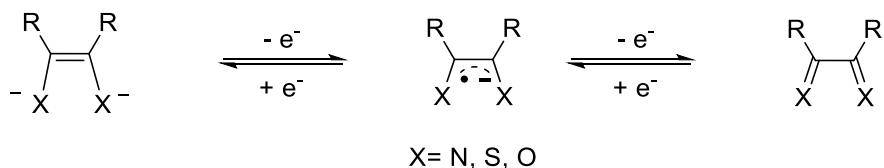


Figure 2. Schematic depiction of electron exchange in redox non-innocent ligands.

While this type of redox non-innocent ligand design remains popular and continues to present new discoveries, it is interesting to note a different type of redox non-innocent ligands, which incorporates redox active elements into the ligand platforms. In such ligand systems, the electrons can be preferentially exchanged between different oxidation states E^n and E^{n+2} in the presence of oxidants, while the formal oxidation state of the metal center does not change. In such cases, antimony based non-innocent ligands ($M^n\text{-Sb}^{\text{III}}$ and $M^n\text{-Sb}^{\text{V}}$) will be briefly reviewed in Section 1.3.3.

In addition to redox non-innocent ligands, recent investigations into the coordination behavior of heavy main group ligands suggests that a ligand can also become non-innocent by participating in anion exchange or coordination. This ligand-centered coordination event was shown to induce oxidation changes in the complex, making the assignment of oxidation states to individual metal atom and ligand difficult. Specific examples showing coordination non-innocence will be elaborated in Section 1.3.4 and Section 1.4.3.

1.1.2 Brief overview of Z-type ligands

In coordination chemistry, ligands are generally classified as X, L and Z type ligands on the basis of two-center interactions involving the metal and the coordinated ligand.¹³⁻¹⁴ X type ligands could be viewed as one electron donor in the formation of M-X bond, which means both the transition metal and ligand contributes one electron to the M-X bond. L type ligands are considered as two electron donors because they possess a pair of non-bonding valence electrons available for donation to the transition metal. The resulting donor-acceptor interaction can be formulated as L→M. While these two types of ligands are prevailing in coordination chemistry, the complementary Z-type ligands have spurred much fundamental interest due to their unique coordination behavior. Owing to the presence of vacant orbitals, a Z-type ligand is capable of drawing d-electrons away from transition metals, resulting in the formation of a metal to ligand dative bond M→Z.¹³⁻¹⁵ As illustrated by the molecular diagram in Figure 3, the electron pair from the metal dz^2 orbital donates to the vacant p orbital of the Z ligand in a σ donating fashion. It can be inferred from this bonding formalism that metal complexes bearing a Z-type ligand, would draw the electron density from the metal center; or alternatively, an electron rich, low-valent metal center can be stabilized by Z-type ligands. These electronic benefits were first seen with a variety of unsupported M→Z interactions involving simple Lewis acids, such as $AlCl_3$, $GaCl_3$, $AlPh_3$, and SO_2 (Figure 4).¹⁶⁻¹⁹

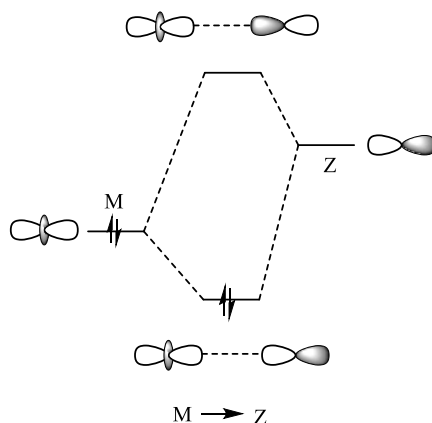


Figure 3. Molecular orbital diagram showing a dative interaction between metal and Z-ligand.

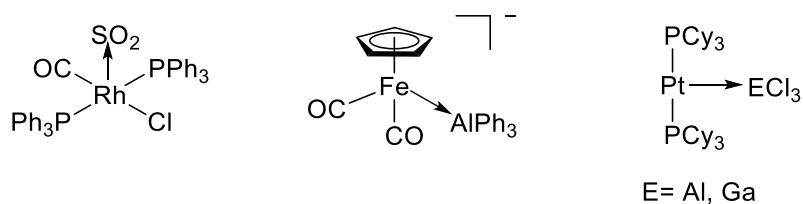


Figure 4. Representative examples of unsupported $M \rightarrow Z$ ligand interactions.

Over the past decade, Z-type ligands have become very popular at least in part due to the introduction of new ambiphilic ligand platforms combining both L-type and Z-type ligands. The presence of the L ligands helps to stabilize the complex and bring the metal ion or atom in close proximity to the Lewis acidic Z-type ligand site. Efforts from multiple laboratories have led to a large collection of such complexes now described in several comprehensive reviews.²⁰⁻²¹ As depicted in Figure 5, four coordination modes can be extracted, according to the role that the Lewis acid moiety plays in the coordination sphere of the transition metal. These four coordination modes may appear as isolated complexes or as intermediates during catalysis.

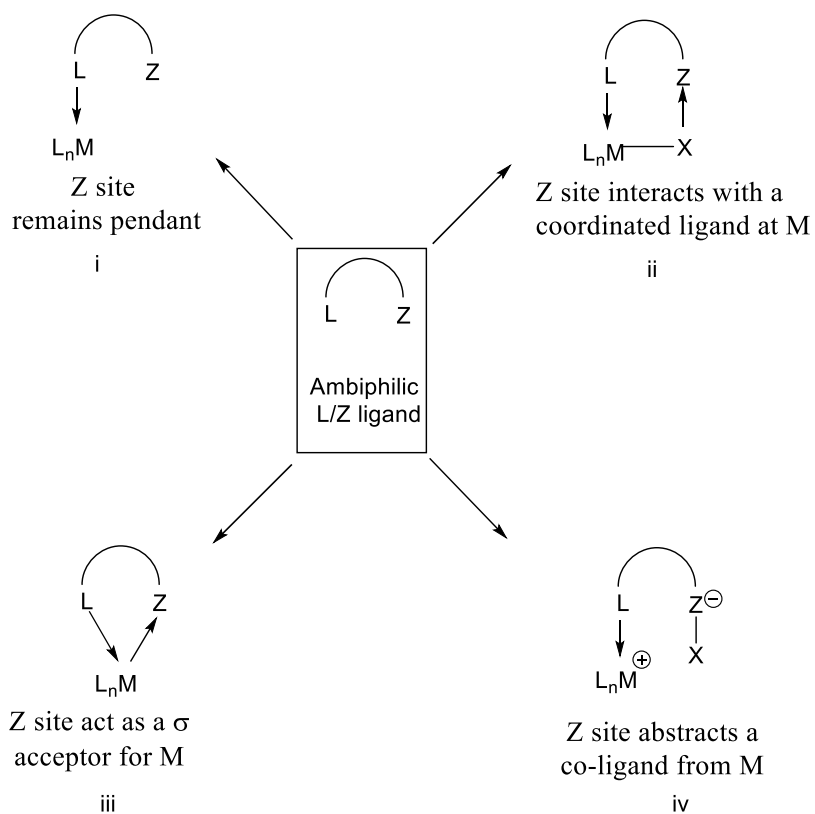


Figure 5. Schematic representation of four coordination modes of ambiphilic L/Z ligands

Ambiphilic L/Z-ligands containing group 13 or group 14 elements as Lewis acidic sites are the most studied. In particular, phosphine-boranes and related ambiphilic ligands have been shown to possess rich and unusual coordination properties, as evidenced by their unique ability to support metal-ligand cooperation in reactions involving small molecules such as N_2 and H_2 . For the latter, these cooperative effects facilitate addition of H_2 across the metal-boron interaction, resulting in the formation of a borohydride and a metal hydride moiety.²²⁻²⁶ For example, the bis(phosphine)borane nickel complex **1** reacts with H_2 reversibly to form the borohydride/nickel hydride complex (Figure 6). This complex also catalyzes the hydrogenation of styrene and 3,3-dimethylbutene. Collectively, these results show that the Lewis acidity of the boron center is not necessarily neutralized by donation from the metal

center. Instead, when the structure is sufficiently flexible, the metal-boron interaction can cleave and participate in the activation of small molecules while also exposing a catalytically active metal center.

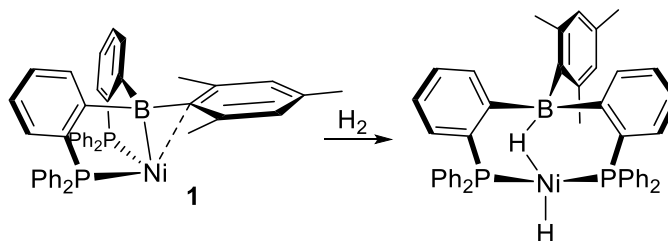


Figure 6. An example showing the Lewis acidic site of a bis(phosphine)borane ambiphilic L/Z-ligand becoming involved in anion binding.

The same general principle has been applied for the Lewis acid activation of the gold center in complex **2** (Figure 7).²⁷ The reaction of the L^{Al/P} ligand with (tht)AuCl results in chloride transfer to the aluminum center, resulting in the formation of the zwitterionic gold complex. The latter is catalytically active, and carbophilic catalyst and readily promotes the cyclization of propargylamides. The phenomenon of a zwitterion formation has been observed for other ambiphilic ligand gold complexes containing strongly Lewis acidic group 13 compounds.²⁸⁻³¹

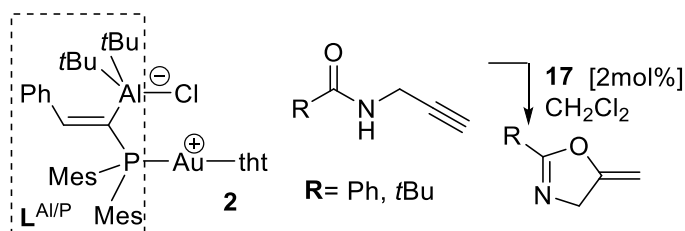


Figure 7. An example showing the Lewis acidic site of a phosphine-allane ambiphilic L/Z-ligand abstracting anion from the metal center.

In another example illustrating the impact of a Z-ligand in catalysis, the Mukai group has recently investigated cationic complexes of type $[3]^+$ for the carbophilic activation of alkynes (Figure 8).³² The group found that these complexes are much more efficient catalysts for enyne cyclizations than their simpler analog $[(PPh_3)_2Au][SbF_6]$. The authors proposed that this enhanced catalytic activity results from the strong σ -accepting, electron-withdrawing effect of the Lewis acidic boron atom *trans* from the reactive site. This result suggests that Z-ligands can be used for what we term “the perpendicular activation of bis(phosphine)gold complexes.”

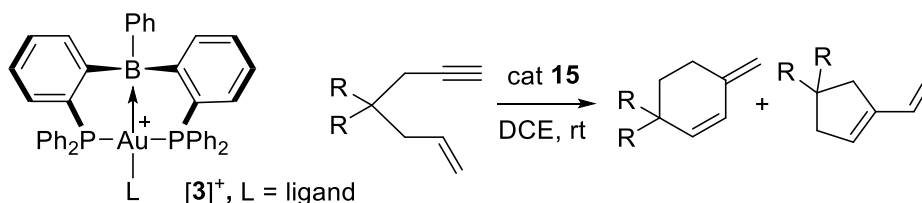


Figure 8. Enyne cyclization catalyzed by a bis(phosphine)borane gold complex.

1.2 Antimony and tellurium compounds as potential non-innocent Z-ligands

1.2.1 Lewis acidity and redox reactivity of antimony compounds

Main group 15 elements, with ns^2np^3 electron configuration, tend to form trivalent compounds with one electron lone pair. Owing to the presence of electron lone pair, it has been well accepted that main group 15 compounds, such as phosphine, are nucleophiles or Lewis bases in the +III oxidation state. However, organoantimony (III) species were known to be Lewis acidic when substituted by electronegative ligands, which affords a low-lying σ^* orbital at the central atom. In agreement with this argument, various organoantimony (III) species have been shown to display strong Lewis acidity. As indicated in compounds **4**,³³⁻³⁴,

5³⁵ and **6**³⁶ (Figure 9), the halogenated Lewis acidic antimony (III) center exhibits Lewis acidity by accepting electron donation from the Lewis basic nitrogen.

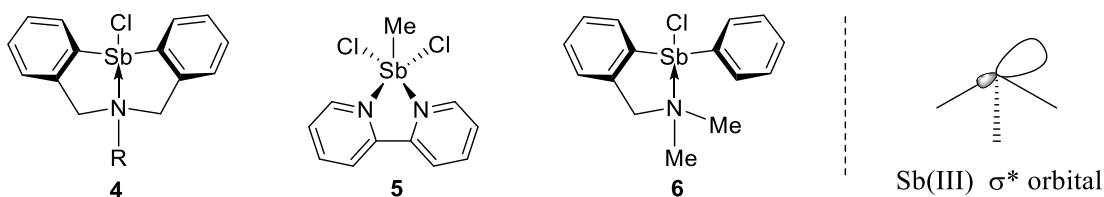


Figure 9. Left: An example showing Lewis acidic antimony (III) center; Right: σ^* orbital in stibine

In the context of coordination chemistry, an elegant contribution by Reid also demonstrated that halogenated organoantimony(III) compound of general formula $\text{SbMe}_{3-n}\text{Br}_n$ display increased π -acceptor properties as the number of bromine atoms increases. The electron accepting low-lying σ^* orbital of such antimony(III) species are depicted in Figure 9 (Right). For comparative purposes, an early investigation into the electron accepting ability of a series halogenated compounds established their Lewis acidity in the following order.³⁷



This seminal result reinforces our understanding that antimony (III) species can behave as Lewis acids, whose acidity could be enhanced by introducing electronegative substituents. In the meantime, this report also pointed towards an important conclusion that a fully halogenated organoantimony(V) species SbCl_5 is among the most potent of Lewis acids. In a parallel work, Gutmann and his group proved that SbCl_5 is indeed the strongest Lewis acid among all, followed by AlCl_3 , BCl_3 , and PCl_5 .³⁸

While the halogenated inorganic derivatives SbCl_3 and SbCl_5 are corrosive, and thus not suitable for convenient use, the Lewis acidity displayed by them bodes well for their incorporation into Lewis acidic molecules and ligands. This idea has been explored extensively by the Gabbai group in the past decade. These efforts have resulted in the Lewis acidic neutral stiborane, and cationic stibonium, a few examples of which are shown in Figure 10. It is reported that the Lewis acidic stiborafluorene-alizarin derivative **7**³⁹ and tetraarylstibonium **8**⁺⁴⁰ can be used as effective anion sensors for detecting fluoride at ppm levels in water. Further, the idea of achieving a stable and highly Lewis acidic antimony (V) compound by using electron withdrawing ligands was nicely embodied by compound **9**⁺, which was obtained by reaction of $\text{C}_6\text{F}_5\text{Li}$ with SbCl_5 followed by chloride abstraction with $[\text{Et}_3\text{SiHSiEt}_3][\text{B}(\text{C}_6\text{F}_5)_4]$.⁴¹

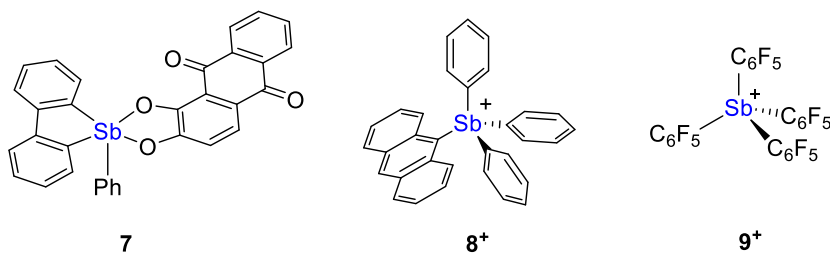


Figure 10. Examples of stable Lewis acidic antimony (V) compounds.

Based on the findings described above, it can be inferred that the Lewis acidity in conjugation with the redox activity of antimony compounds, may allow antimony species to act as redox non-innocent Z-type ligands.

1.2.2 Lewis acidity and redox reactivity of tellurium compounds

Tellurium, with $5s^25p^4$ electron configuration, forms many divalent compounds with two electron lone pairs. In the presence of oxidants, such as halogen and peroxide, divalent organotellurium compounds can be readily converted into tetravalent and hexavalent tellurium compounds, illustrating their rich redox chemistry (Figure 11).⁴²⁻⁴⁶ In particular, some tellurium compounds can even sustain reversible two-electron redox chemistry. In 1992, Furukawa and co-workers first reported that the dinuclear tellurium compound, 1,5-ditelluracyclooctane, can react with halogens to give the $\text{Te}^{\text{IV}}\text{-Te}^{\text{IV}}$ product, which can be reduced back to the starting compound in the presence of reducing reagents (Figure 11, Bottom (a)).⁴⁷ The similar reversible redox chemistry was further observed with π -conjugated tellurapyrylium dyes, which are prone to oxidative addition and thermal reductive elimination of chlorine (Figure 11, Bottom(b)).⁴⁸ Recently, Seferos and co-workers showed that dibromotellurophenes can undergo facile reductive elimination of bromine under irradiation (Figure 11, Bottom(c)).⁴⁹⁻⁵¹ The reversible redox chemistry displayed by these examples suggested that tellurium compounds are promising candidates to be introduced in the family of redox active ligands in coordination chemistry.

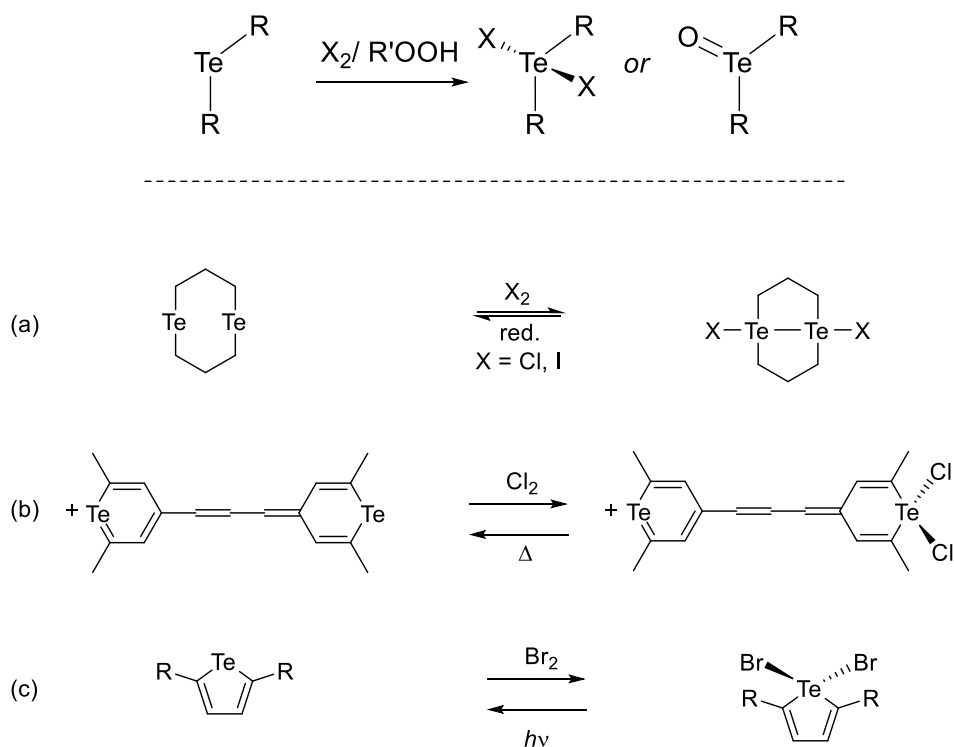


Figure 11. Top: General oxidation reactions converting divalent tellurium to tetravalent tellurium species. Bottom: Examples showing reversible two-electron redox chemistry of tellurium compounds.

Although tetravalent tellurium species retain one electron lone pair, they have been identified to be Lewis acidic. Neutral tetravalent tellurium compounds, which could be formulated as $\text{TeR}_{4-n}\text{X}_n$ (R refers to organic substrate, X refers to halogen), possess increased Lewis acidity when the number of electronegative halogen increases.⁵² This phenomenon, which is similar to that of halogenated antimony compounds, originates from the availability of the low-lying σ^* orbital. In a quantitative respect, Satchell and coworkers carried out a comparative study on the acidity for a series of Lewis acids, including TeCl_4 . Judged by the equilibrium constant along with the stoichiometric values, for adduct formation between the Lewis base and Lewis acids, the strength of the acidity was found to follow the sequence $\text{ZrCl}_4 > \text{TeCl}_4 > \text{SnCl}_4$.⁵³ Provided that the acidity of SnCl_4 has been demonstrated to be greater than

that of ZnCl_2 , SbCl_3 and PCl_5 , this result suggested that tellurium compounds might be superb Lewis acids, and potential candidates for incorporation in Z-type ligands. Further, cationic tetravalent tellurium species ($\text{R}_{3-n}\text{X}_n\text{Te}^+$), termed as telluronium ions, are predicted to possess even stronger Lewis acidity because of the positive charge. As illustrated by the structure of **10** and $[\mathbf{11}]^+$ (Figure 12), the Lewis acidic tellurium sites readily form strong interactions with Lewis bases, with $\text{O} \rightarrow \text{Te}$ and $\text{N} \rightarrow \text{Te}$ dative bonds of $2.613(3) \text{ \AA}$ ⁵⁴ and $2.31(2) \text{ \AA}$ ⁵⁵ respectively.

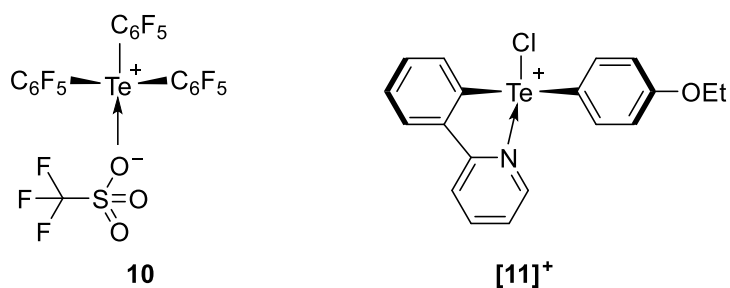


Figure 12. Examples of Lewis acidic telluronium ions.

In parallel to the hypothesis that the Lewis acidity and redox property of antimony compounds makes them well-suited for the design of redox non-innocent Z-ligands, the same hypothesis could be made here for tellurium compounds. Compared to the group 13 Z-type ligands, the redox property and Lewis acidity represent noteworthy features for group 15 and group 16 Z-type ligands. This idea forms the basis of my dissertation work.

1.3 Coordination chemistry of antimony polydentate ligands

1.3.1 Background of antimony ligands in organometallic chemistry

The number of complexes with stibine ligands represents a tiny fraction compared to the number of phosphine complexes reported. Tertiary stibines SbR_3 are soft and weak donor

ligands, due to the diffuseness of the antimony orbitals. They have been used as ligands for transition metals of the group 3-12.⁵⁶ In particular, SbPh₃ is the most frequently used tertiary stibine ligand, due to its availability and air stability.⁵⁷⁻⁷³ SbPh₃ often serves as a labile ligand in substitution reactions⁵⁹ or as a weak donor that can be displaced by incoming substrate during catalysis, as evidenced by its use in olefin polymerization.⁷¹⁻⁷²

From a structural point of view, tertiary stibines typically bind to the transition metal in the η^1 coordination mode, with the electron lone pair donation from antimony to the metal center. With a majority of metal complexes, stibines act as unsupported spectator ligands. Slightly different coordination behavior was observed with halogenated stibine ligands, such as R₂SbX, or RSbX₂. Complexes with halogenated stibine ligands are relatively rare, presumably because of the poor donating ability of these ligands. Among the very few examples of such complexes, the halogenated stibines were shown to display non-spectator behavior by interacting with counter anions.⁷⁴⁻⁷⁵ This phenomenon could be assigned to the increased Lewis acidity of halogenated stibines, as noted in Section 1.2.1.

Tertiary stibine ligands have also been incorporated in multi-dentate ligands design, featuring a combination of antimony atoms and one, two or three other donor arms. Coordination complexes containing such multidentate stibine ligands are very rare, presumably because of the synthetic difficulty. Notable examples of such complexes were the five-coordinate group nickel complexes, obtained by chelation of the metal salt with tris(o-diphenylphosphinophenyl) or tris(o-diphenylarsinophenyl) antimony ligands developed by McAuliffe and co-workers.⁷⁶ As shown in Figure 13, the resulting complexes **12** and **13** were assigned as trigonal bipyramidal, with a well stabilized metal-antimony interaction. Spectroscopic study on a series of chelated complexes, achieved by changing the apical donor

atom to P and As, indicated that antimony tetradentate ligand afforded an anomalous ligand field strength in the order of $P > As < Sb$, which was different from the order found in complexes with their monodentate ligands, $P > As > Sb$. The increased ligand field strength was attributed to the compression and stabilization of the metal-antimony interaction by chelation, which were further confirmed with an analogous palladium complex **14** (Figure 13).⁷⁷ These interesting and at time intriguing results constitutes the basis of our current research work on antimony ligands.

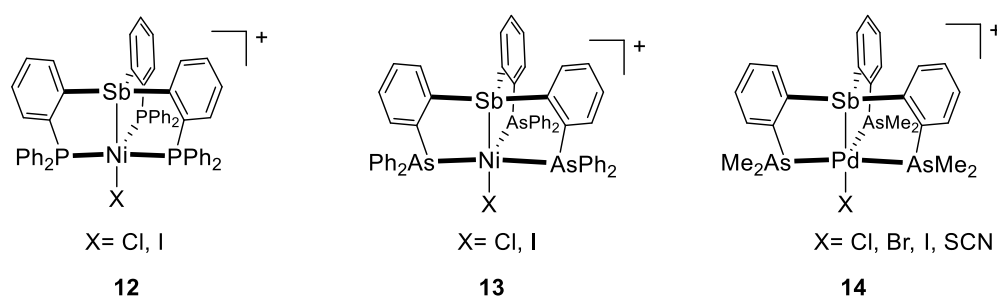


Figure 13. Early examples of group 10 metal complexes featuring tris-substituted polydentate antimony ligands.

To a large extent, the above-described chemistry of stibine ligands, including that of the monodentate and multidentate ligands, is limited to their use as ancillary ligands. Although the potential of a stibine ligand to have dual functions as a Lewis base and a Lewis acid has been put forward, such potential was not fully explored for stibine ligands, as means to modify the coordination geometry and reactivity of a neighboring transition metal. As such, research on stibine ligands seems to be destined for bright developments.

1.3.2 Trivalent antimony ligands as Z-type ligands

While often regarded as heavy phosphine analogues, stibine ligands possess a number of unusual characteristics, including soft donor properties^{56, 78-84} combined with increased

accepting properties^{74-75, 85} These characteristics are illustrated by some of our recent investigations in the chemistry of $L_2^{Ph}AuCl$ (**15**) and $L_2^{Cl}AuCl$ (**16**), two gold complexes which we synthesized from the corresponding ligands (o -(iPr_2P) C_6H_4) $_2$ SbPh) (L_2^{Ph}) and (o -(iPr_2P) C_6H_4) $_2$ SbCl) (L_2^{Cl}) (Figure 14).⁸⁶

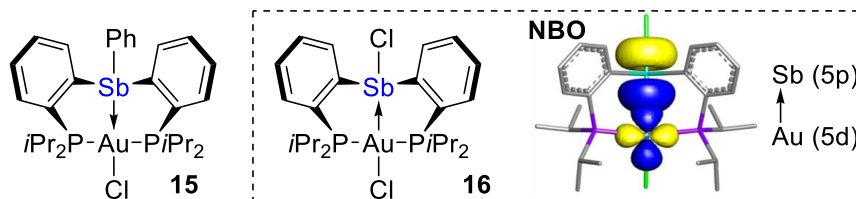


Figure 14. Structures of **15** and **16** and NBO plot showing the Au→Sb interaction in **16**.

As suggested by the structure of these complexes and in agreement with the results of Natural Bond Orbital (NBO) calculations, the gold and antimony atoms of **15** and **16** are involved in Au→Sb donor acceptor interactions. The magnitude of this interaction is higher in complex **16** which possesses a chlorinated and thus more Lewis acidic antimony center.⁸⁶ In the case of **15**, NBO calculations find that the antimony center is also involved in a more classical Sb→Au interaction. The bonding ambiguity led us to introduce the concept of “ σ -donor/acceptor-confused ligands.”⁸⁶ Another important outcome of this work comes from a computational comparison of $L_2^{Cl}AuCl$ (**16**) with the phenylboron analog $L_2^{PhB}AuCl$ ($L_2^{PhB} = o$ -(iPr_2P) C_6H_4) $_2$ BPh). NBO analyses performed on both complexes found that the strength of the Au→Sb and Au→B interactions are similar, suggesting that the boron and antimony moieties in these complexes display comparable σ -accepting properties toward gold.

1.3.3 Redox non-innocence of antimony(III) ligands

In the past few years, we have observed that when a $\text{Sb} \rightarrow \text{M}$ interaction is present in the stibine form of a complex, the dative interaction can be switched by oxidation of the antimony atom. This phenomenon is illustrated by conversion of the stibine-gold chloride complex **15** into **17** by reaction with *o*-chloranil;⁸⁶ as well as the conversion of complex **18** into **19** upon treatment with PhICl_2 (Figure 15)⁸⁷ In both cases, the dinuclear core of the structure shows a clear response to oxidation of the antimony center. In particular, the Au-Sb distances (2.6833(3) Å for **17**; 2.7086(9) Å for **19**) are shorter than those measured for the reduced complexes (2.8669(4) Å for **15**; 2.8374(4) Å for **18**). Changes are also observed in the coordination geometries of the gold centers, which shift from distorted trigonal pyramidal in **15** and **18** to square planar in **17** and **19**. These changes, in particular the square planar geometry of the gold atom, indicate that the latter is affected by oxidation as it transitions from a monovalent form in **15** and **18** to a trivalent form in **17** and **19**. NBO analysis of **19** confirms this view and shows that the gold $d_{x^2-y^2}$ orbital acts as a donor toward a $\sigma^*(\text{Sb-Cl})$ orbital.⁸⁷ Altogether, these results show that oxidation of the antimony center induces an umpolung of the Sb-Au dative bond, which switches from $\text{Au} \leftarrow \text{Sb}$ in the reduced state to $\text{Au} \rightarrow \text{Sb}$ in the oxidized state.

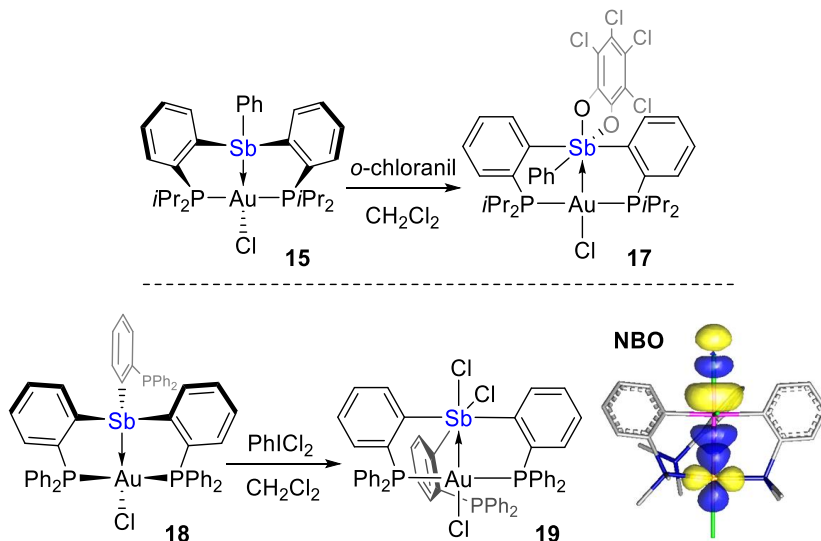


Figure 15. Examples showing the conversion of stibine ligands into stiborane ligands in the coordination sphere of gold.

Another related situation is encountered in the stibine nickel complex **20**, which can be converted into the stiborane nickel complex **21** by a formal two-electron oxidation reaction (Figure 16). The conversion of **20** into **21** is accompanied by an umpolung of the Ni-Sb interaction, which switches from $\text{Ni} \leftarrow \text{Sb}$ in **20** to $\text{Ni} \rightarrow \text{Sb}$ in **21**. This umpolung shows that oxidation of the antimony center induces a L to Z (or σ -donor to σ -acceptor) switch in the ligand type of the antimony atom. We find this transformation to be interesting because it suggests that the redox state of the antimony atom could be used to alter the electron density and thus reactivity of the adjacent transition metal center.

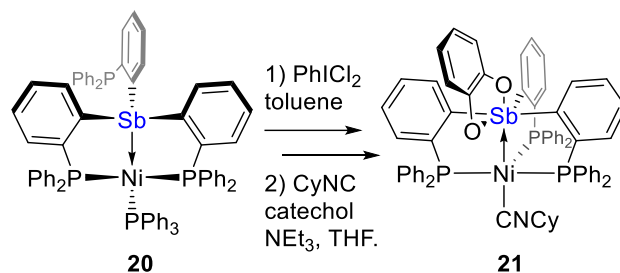


Figure 16. Scheme showing the conversion of a stibine into a stiborane in the coordination sphere of nickel.

1.3.4 Coordination non-innocence of antimony ligands

Beyond the above-noted Z-ligand property and redox behavior of stibine ligands, another prominent coordination characteristic of stibine ligands relates to their ability to engage in secondary bonding interactions. This phenomenon, termed as coordination non-innocence, could be rationalized by the ability of low-lying Sb-M σ^* orbitals to act as Lewis acidic accepting site. Such phenomenon has appeared in first row carbonyl metal complexes, involving unsupported halogenated stibine ligands $\text{SbMe}_{3-n}\text{Br}_n$.⁷⁴⁻⁷⁵ As mentioned in section 1.2.2, these halogenated stibine ligands displayed increased Lewis acidity as the number of halogen atoms increases. Due to the increased Lewis acidity, unusual secondary interactions $\text{O}\cdots\text{Sb}$ were observed in the coordination sphere of complexes **22** and **23**, with O-Sb bond distance of 2.696(5) Å and 2.59-2.65 Å respectively.

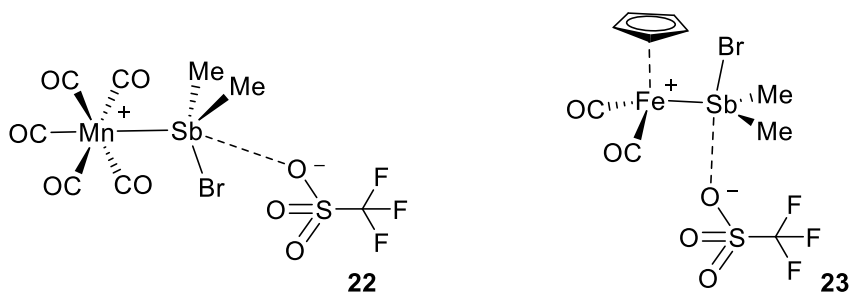


Figure 17. View of two halostibine complexes featuring interactions between the anion and the formally neutral antimony (III) center.

In 2012, this phenomenon was also confirmed in the case of a cationic trisphosphanystibine-palladium complex $[24]^+$, which was obtained from complexation of the trisphosphanystibine ligand $(o\text{-(Ph}_2\text{P)C}_6\text{H}_4)_3\text{Sb}$ followed by the addition of NaBPh_4 (Figure 18, left). As indicated by its crystal structure, the cationic complex $[24]^+$ displays a four-coordinate antimony center, which readily binds fluoride and generates the corresponding fluorostiboranyl unit.⁸⁵ This Lewis acidity ‘turn on’ effect could be summarized in a model, where the stibine donor becomes a Lewis acidic center upon coordination of the metal fragment, due to the presence of $\text{Sb-M } \sigma^*$ orbital available for anion binding, as shown in Figure 18 (right).

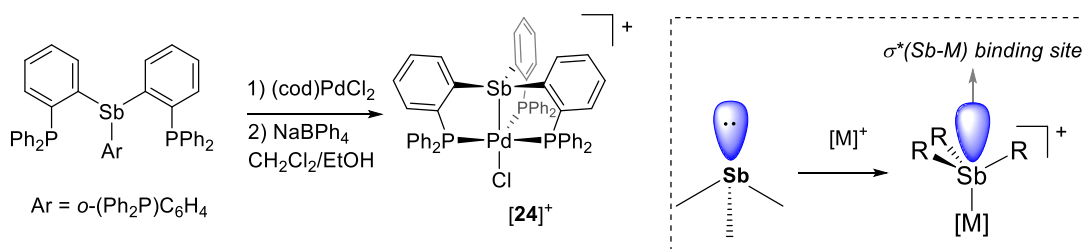


Figure 18. Left: Synthesis of complex $[24]^+$; Right: Schematic representation showing how the metal coordination converts a stibine donor into a Lewis acidic acceptor, owing to the presence of $\text{Sb-M } \sigma^*$ orbital available for anion binding

The phenomenon of coordination non-innocence was further demonstrated in a more recent paper dealing with a series of platinum complexes. Starting from a stibine trisphosphine lantern complex **25**, a dicationic stibine platinum complex $[\mathbf{26}]^{2+}$ was prepared by abstraction of two chloride ligands, as shown in Figure 19. The dicationic complex undergoes coordination of a stoichiometric amount of fluoride, affording the monofluoro-antimony analogue $[\mathbf{27}]^+$. Alternatively, a difluoroantimony complex **28** was also obtained by anion abstraction and exchange. The complexes $[\mathbf{26}]^{2+}$, $[\mathbf{27}]^+$ and **28** are related by the stepwise coordination of two fluoride anions to the Lewis acidic antimony center. Inspection of the Sb-Pt bonding distances of the complexes revealed an increase across the series (2.4706(5) for $[\mathbf{26}]^{2+}$, 2.6236(3) for $[\mathbf{27}]^+$, and 2.6568(6) for **28**, indicating a weakening of the Sb-Pt interaction. This trend shows that the Lewis acidity of the antimony center is decreased upon stepwise coordination of fluoride anions. Computational studies by using both the QTAIM and NBO method show that the anion coordination also leads to a polarization of the Sb-Pt bond, with more electron density shifting towards the platinum center upon successive coordination of fluoride anions. This polarization trend suggests the platinum center become more reduced upon fluoride coordination at the antimony center.

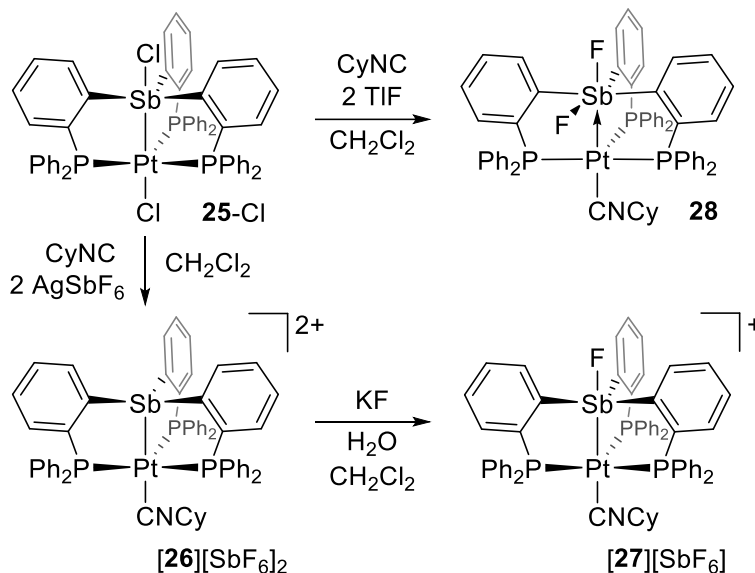


Figure 19. Synthesis of complexes $[\mathbf{26}]^{2+}$, $[\mathbf{27}]^+$ and $\mathbf{28}$.

In addition, the so-called coordination non-innocence behavior was also elaborated in stiboranyl metal complexes. In case of the tetravalent platinum complex $\mathbf{29}$, the antimony center can be subjected to two-electron oxidation by *o*-chlorianil, which gives rise to complex $\mathbf{30}$. The *o*-chlorianil decorated antimony moiety displays coordination non-innocence by readily binding fluoride, leading to a fluorostibane unit. Concurrent with this coordination event, a chloride is automatically eliminated from the platinum center, resulting into a neutral stiborane platinum complex $\mathbf{31}$, which could be viewed as a consequence of anion exchange reaction.⁸⁸ Examination of the coordination geometry and valence of the metal unit of this resulting complex suggested that the anion exchange also induces internal redox changes, with the $\text{Sb}^{\text{IV}}\text{-Pt}^{\text{III}}$ being converted into a $\text{Sb}^{\text{V}}\text{-Pt}^{\text{II}}$ complex based on formal oxidation state assignments.

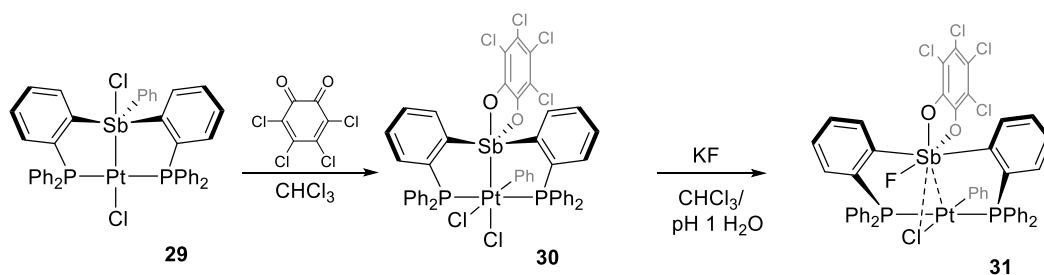


Figure 20. Synthesis of the stiboranyl complexes **30** and **31**.

Collectively, it can be inferred from these results that the antimony ligand, despite being coordinated to the metal, has strong affinity for fluoride, which allows for anion coordination, exchange and redistribution in the coordination sphere. As a consequence, this coordination non-innocence would significantly affect the Sb-M interaction and the electron density distribution for individual metal centers; or specifically, the coordination of fluoride to the coordinated antimony site, would polarize more electron density towards the metal site, resulting into a more reduced metal center, as summarized in Figure 21.

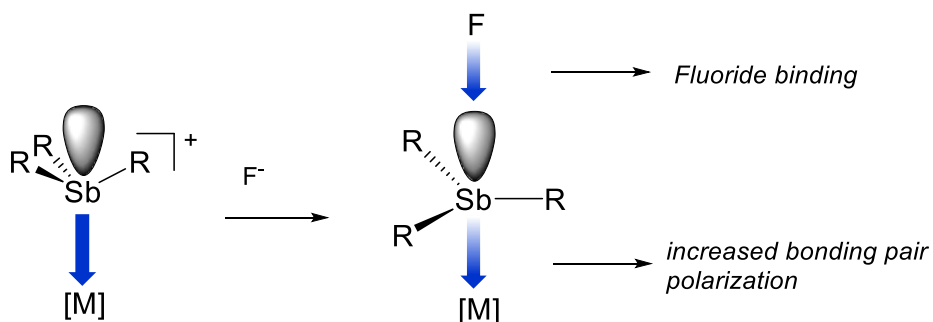


Figure 21. A schematic representation showing bonding electron polarization to metal can be induced by anion binding at the ligand center.

1.4 Coordination chemistry of tellurium polydentate ligands

1.4.1 Background of tellurium ligands in organometallic chemistry

Although tellurium, and tellurium derivatives have been exploited extensively in material science, including their use in nanocrystals⁸⁹⁻⁹¹ and semiconducting polymers,⁹²⁻⁹⁸ the coordination chemistry of tellurium ligands remains relatively under developed. In coordination chemistry, divalent tellurium ligands have been given more attention than the tetravalent tellurium species, due to their electron donating ability. Telluroethers act as weak and soft σ donor ligands. They are noticeably labile, as evidenced by early reports that TeR_2 ligands tend to undergo dissociation or displacement in the presence of even modest σ donors, such as DMSO and CO.⁹⁹⁻¹⁰⁰ The lability of these ligands can be circumvented by their incorporation in polydentate or hybrid ligands. For example, hybrid ligands combining a soft tellurium(II) donor and a hard donor such as N or O, have been shown to form a large range of complexes.¹⁰¹⁻¹⁰⁷ Particularly, rare examples of tellurium-centered pincer style ligands were also reported¹⁰⁸⁻¹¹⁰ and their metal complexes have been isolated, as shown by the palladium complex **32** which features a NTeN chelating motif,¹⁰⁹ and the titanium complex **33** supported by OTO pincer-style ligands¹¹⁰. In these prominent examples, the auxiliary supporting hard donors effectively bring the metal center into close proximity to the tellurium atom, allowing for the observation of the Te-M interaction. While these metal complexes are limited to their structural novelty, the idea revealed by such ligand design is remarkably useful for the latter development of tellurium coordination chemistry.

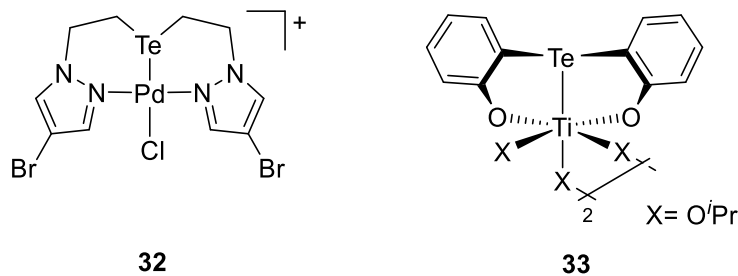


Figure 22. Early examples of metal complexes supported by tellurium centered pincer-style ligands.

1.4.2 Telluronium as Z-type ligands

Despite the presence of one electron lone pair, tetravalent tellurium ligands have not yet been successfully explored as donor ligands for transition metals, presumably because the donicity of the remaining electron lone pair is largely confined by the increased electrostatic effects in the higher oxidation state. Tetravalent tellurium species are also found to react with low valent transition metals, which oxidatively inserts in tellurium-ligand bonds.¹¹¹

In an effort to expand the chemistry of tellurium ligands, the Gabbai group set out to design tetravalent tellurium ligands starting from TeCl_4 . Such an effort led to the isolation of a telluronium ligand featuring three 8-quinolinyl donor arms, and a neutral tetravalent tellurium ligand containing two 8-quinolinyl donor arms and two bromine atoms. These two ligands represent a successful implementation of the hybrid ligand approach, with the ancillary nitrogen donors flanking the central tellurium. Further reaction of the cationic telluronium ligands with Na_2PdCl_4 afforded the telluronium palladate complex **34**, while complexation of the neutral tetravalent tellurium ligand with Na_2PdCl_4 in the presence of NaOH led to the formation of complex **[35]⁺**, featuring a cationic telluronium hydroxide ligand. These two

complexes are fully characterized, including their crystal structures. As indicated by the Pd-Te-C ($157.40(12)^\circ$) and Pd-Te-O ($169.3(2)^\circ$) angles in complex **34** and **[35]⁺**, the palladium atoms assume positions trans to the vector of Te-C or Te-O, respectively. Interestingly, the Pd-Te bond length of $2.9201(8)$ Å found for complex **34** is notably longer than the distance found for complex **[35]⁺** ($2.7823(8)$ Å). This difference indicates a stronger Pd→Te interaction in complex **[35]⁺**. In addition to the strengthened Pd→Te bonding, the coordination sphere of the palladium center in complex **[35]⁺** was found to be pseudooctahedral because of an interaction with a chloride from the neighboring molecule. This observation, suggesting a tetravalent character of the palladium, further supports the view of an enhanced Pd→Te donor-acceptor interaction in complex **[35]⁺**, because of the presence of telluronium moiety. A comparative study of the Pd→Te interaction was also carried out by natural bond orbital (NBO) analyses for both complexes. A donor-acceptor interaction was found in both cases, involving electron donation from the palladium d orbital to the Te-X σ^* orbital, with stabilization energies of 22.5 kcalmol⁻¹ for complex **34** and 69.8 kcalmol⁻¹ for complex **[35]⁺**, which correlate very well with the experimentally determined Pd-Te bond length.

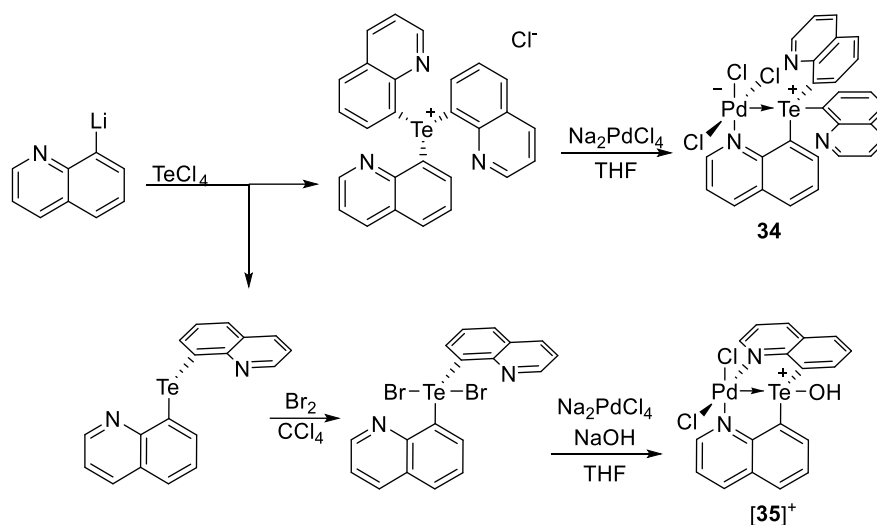


Figure 23. Synthesis of complexes **34** and **[35]⁺**.

1.4.3 Coordination non-innocence of tellurium ligands

Telluroethers are often considered as spectator ligands in the coordination chemistry. However, recent efforts have revealed the non-spectator behavior of such ligands, as evidenced by their ability to engage secondary interactions with the surrounding Lewis bases.^[Ref] This phenomenon is reminiscent to the coordination non-innocence that was defined in a number of our recent publications on antimony ligand coordination chemistry,^{88,112} owing to the presence of the low lying Sb-M or Sb-X σ^* orbitals or electrostatic forces. An example of tellurium-centered coordination non-innocence can be observed upon conversion of **[36]Cl** into **37** (Figure 24). Both complex **[36]Cl** and complex **37** are structurally characterized. As indicated by its crystal structure, complex **[36]Cl** features telluroether ligand, with the tellurium center weakly binding a chloride at a distance of 3.1759(12) Å. While telluroethers tend to behave as σ donors, the weak accepting behavior displayed in this case might be imparted by the strong Te-Pt (2.5281(5) Å) interaction, which affords an available Te-Pt σ^* orbital available for anion

coordination. Interestingly, the oxidized complex **37** possesses an octahedral platinum center, which is characteristic of the tetravalent state. Although oxidation occurs at the platinum center, the coordinated tellurium center is also affected, as indicated by the substantial contraction of the Te-Cl bond to 2.712(3) Å. This shortening suggests an increased Lewis acidity at the tellurium center, which might be attributed to the increased σ donation from the tellurium to the highly electron deficient platinum center. Alternatively, this σ donation effect could be described by a “chloride-push/platinum-pull” effect, where the tellurium serves as a relay. Natural bond orbital analyses were also carried out for these two complexes to probe such effect by an investigation on the nature of Te-Pt bonds. In complex **[36]Cl**, the Te-Pt bond was found to bear larger electron contribution from tellurium than platinum (Te:57%/Pt:39%). A different situation was identified for complex **37**, in which the bonding was polarized towards platinum (Te:35%/Pt:63%), in support of the view that a greater σ -donation occurred from tellurium to platinum in response to the oxidation reactions.

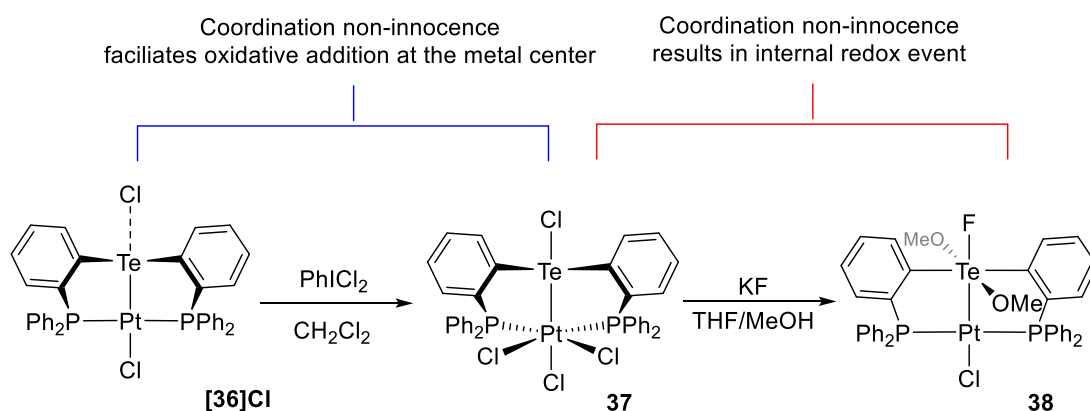


Figure 24. Examples showing two types of coordination non-innocent behaviors of tellurium ligands.

Noting the Lewis acidity of the coordination non-innocent tellurium center is strongly correlated with the oxidation state of the metal center, it was questioned if the tellurium centered anion exchange event would also cause changes at the transition metal. This speculation was substantiated by the anion exchange chemistry for complex **37**. Treatment of complex **37** with KF in THF/MeOH, led to the formation of complex **38**, which was fully characterized by multinuclear NMR and X-ray crystallography. As indicated by the crystal structure, the platinum center displays square planar geometry characteristic of divalent state. Compared to the original structure of complex **37**, the resulting complex clearly shows that three chlorides were exchanged with one fluoride and two methoxide anions, which are all bound to the tellurium center in an octahedral environment, indicative of the hexavalent state. Formal oxidation state assignment to this complex suggests a $\text{Te}^{\text{VI}}\text{Pt}^{\text{II}}$ core, which could be viewed as a result of anion-induced internal redox reaction in which the platinum is reduced while the tellurium is oxidized. Due to this internal redox event, the resulting Te-Pt bond becomes strongly covalent, with a bond length of 2.5238(5) Å which is comparable to that in complex **[36]Cl** (2.5281(5) Å). This covalent bonding was also reflected by a marked increase in the $^1J_{\text{Te-Pt}}$ value from 1112 Hz to 9044 Hz. Similar to the non-innocent behavior displayed by a coordinated antimony ligand,¹¹³ the anion-induced internal redox event on Te-Pt could also be assigned to the propensity of Lewis acidic tellurium center to bind harder anions such as fluoride and methoxide.

1.5 Application in photoreductive elimination of chlorine

1.5.1 Background of photoreductive elimination of chlorine

As reiterated by the Intergovernmental Panel on Climate Change (IPCC Fifth Assessment Report summary released on November 2 in Copenhagen), tackling growing CO₂ emissions will necessitate that fossil fuels be phased out as the main energy source in the next few decades. While it is difficult to predict which energy production technologies will surface as the most practical and economical alternatives, the conversion of solar energy into chemical fuels will undoubtedly play a major role. Water splitting into hydrogen and oxygen is one of the most elegant solutions but its realization is based on a complex redox process that involves four electrons. The splitting of hydrohalic acids such as HCl into H₂ and Cl₂ is also a viable energy storage reaction;¹¹⁴ it involves an inherently less complex two electron redox process and has become an attractive target.¹¹⁵⁻¹¹⁸ The successful implementation of the photo-driven splitting of HCl hinges on the discovery of a suitable catalyst. In an ideal cycle, a transition metal-based catalyst will oxidatively add HCl and undergo reductive elimination of H₂ and Cl₂ upon irradiation with sunlight. Despite the simplicity of its formulation, this approach has been exceedingly challenging to implement, especially with mononuclear complexes.¹¹⁹ A class of derivatives that have shown the most promise are binuclear rhodium complexes¹²⁰⁻¹²¹ such as complex **39** which features a Rh(0)-Rh(II) core held by two bridging tfepma (tfepma=CH₃N[P(OCH₂CF₃)₂]₂) ligands (Figure 25).¹²²⁻¹²³ The core of these complexes and in particular the Rh(0) center is electron-rich and prone to HCl oxidative addition. More importantly, when the reaction is carried out under irradiation in the presence of a chlorine radical trap, the complex behaves as a catalyst to produce hydrogen and the chlorinated trap molecule. The reaction can be decomposed into a series of steps. The first step involves

oxidative addition of HCl and formation of **40** (Figure 25). Upon photolysis, compound **40** reacts with HCl to produce one equivalent of H₂ as well as the tetrachloro Rh(II)-Rh(II) form of the catalyst, complex **41s**. The catalytic cycle is completed by the photoreduction of **41s** in the presence of a trap. The low quantum efficiency of this photoreduction reaction indicates that this last step is likely the bottleneck of the overall catalytic process. Because designing a more efficient photocatalyst will depend on facilitating this photoreduction step, improving the quantum yield for halogen elimination and exploring the mechanism by which the halogen elimination step proceeds have come to the forefront of this research field.

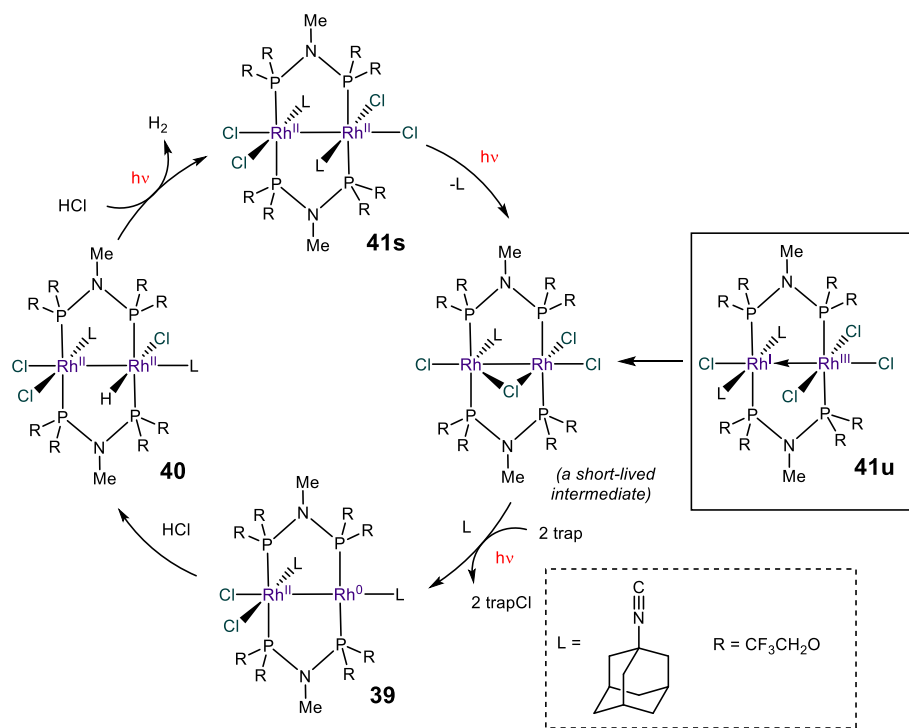


Figure 25. Photocycle for the splitting of HCl mediated by a dinuclear rhodium catalyst.

1.5.2 Photoreductive elimination of chlorine from a TePt complex

As noted above, photoreductive elimination of halogen is a challenging step in the HX-splitting photocatalytic cycle, a series of binuclear complexes, such as Pt-Pt, Pt-Au and Au-Ir,

¹²⁴⁻¹²⁶ have been developed for photoreductive elimination of chlorine by Nocera and coworkers. These complexes, featuring two metal centers in close proximity via ligand linkers, can be readily oxidized by addition of an equivalent of chlorine in the reduced form and photo-reduced back into their original states in the presence of radical trap. By analogy with their two-electron redox chemistry, the late transition metal complexes supported by heavy main group ligands were also speculated to have this capacity, due to their established two-electron redox activity. This speculation was first tested in the case of an aforementioned complex **[36]**⁺, which can be oxidized into complex **37** by addition of an equivalent of Cl₂ to the platinum. In the presence of radical trap 2,3-dimethyl-1,3-butadiene (DMBD), photolysis of complex **37** with 350 nm light results in elimination of a chlorine equivalent from the platinum center, with a maximum quantum yield of 4.4% in CH₂Cl₂ solution.

Although the quantum yield is relatively low compared to the reported value for Pt-Pt system (38%)¹²⁵ and Au-Ir systems,(10%)¹²⁴ the successful photoreduction of halogen from the tellurium-platinum complex validated the speculation that redox active main group transition metal complexes indeed have a potential in this area.

1.6 Motivation and objectives

The Lewis acidity and redox chemistry of antimony and tellurium compounds have been well established for a long time, as mentioned in Section 1.2. However, in the development of antimony and tellurium ligand chemistry, these properties are under-tapped in their coordination chemistry, as evidenced by the fact that antimony and tellurium ligands were normally used as ancillary donor ligands, mainly in the form of SbR₃ or TeR₂, respectively. Although several reports presented polydentate ligand design, which can benefit from

chelation to stabilize the metal-ligand interaction M-E (E= antimony or tellurium), most studies are limited to structural and spectroscopic analysis (See Section 1.3.1 and 1.4.1). In the past decade, inspired by the chemistry of ambiphilic L/Z boron ligands, a few versions of polydentate antimony or tellurium ligands were developed, and presented rich and unusual coordination properties.¹²⁷⁻¹²⁸ It was demonstrated that the Lewis acidity and redox properties of the antimony ligands are not quenched upon coordination with the transition metal. Specifically, the metal-ligand interactions can be altered by the propensity of antimony to sustain redox reactions and anion coordination in the coordination sphere of transition metals (Figure 26).

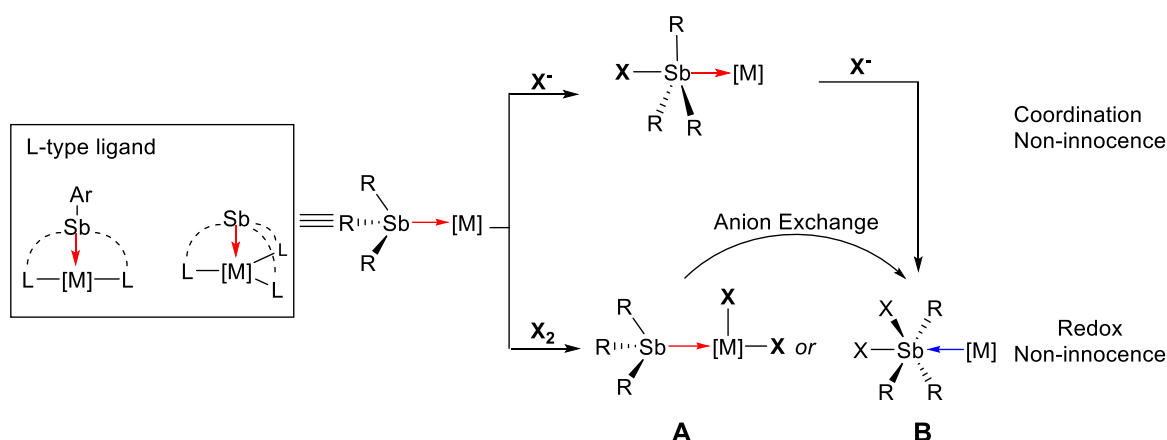


Figure 26. Schematic representation showing the antimony-centered non-innocence behavior of early versions of antimony ligands.

These ligand-centered behaviors, referred to ‘redox-non-innocence’ and ‘coordination non-innocence’, indicated accessible and tunable metal \rightarrow Z ligand interactions may be of importance in ligand-mediated catalysis. To explore this possibility, it has become the objective of this thesis to (i) define how strongly acidic antimony and tellurium ligand can be;

(ii) define new applications for late transition metal-antimony and late transition metal-tellurium complexes in catalysis.

With respect to the first idea, we note that all complexes investigated so far are derived from a triaryl stibine ligands. Even after oxidation, the σ -accepting stiborane ligand is not able to impart reactivity to the neighboring metal, presumably because the Lewis acidity is reduced by the presence of an aryl group, as in the complex **17** (See Section 1.3.3). This issue becomes more acute in the case of the classical tripodal ligand platform (SbP_3 , $\text{P} = o$ -phosphinophenylene), in which the presence of a third supporting group will donate more electron density to the metal center, offsetting the σ -accepting effect of the Z-ligand, as in the complex **19**, **21** and (See Section 1.3.3).

To overcome these possible limitations, I have set out to optimize the Z-ligand effect by introducing electron withdrawing functionalities at antimony. As explained in Section 1.2 and 1.3.2, that halogenated antimony(III) species tend to show Lewis acidity, despite the presence of electron lone pair. Why not couple such built-in Lewis acidity with the ligand-centered redox non-innocence and coordination non-innocence, to achieve an overall more Lewis acidic Z-ligand? It is important to note the parallel that exists in the example of a chlorostibine-gold complex, in which the trivalent chlorostibine behaves as a σ -accepting ligand rather than a donating ligand (See Section 1.3.2). This seminal result further confirmed the feasibility of the idea of increasing Lewis acidity of antimony ligands by relying on electron withdrawing groups, even in the coordination sphere of transition metal.

As sketched in Figure 27, it can be proposed that starting from a σ -accepting stibine ligand, followed by oxidation or anion exchange, distinctly stronger σ -accepting Z-ligands can be obtained in the coordination sphere of transition metal. In these **A-D** model complexes, the

metal \rightarrow Z ligand interaction will be stabilized by two supporting donors by using a chelating framework.

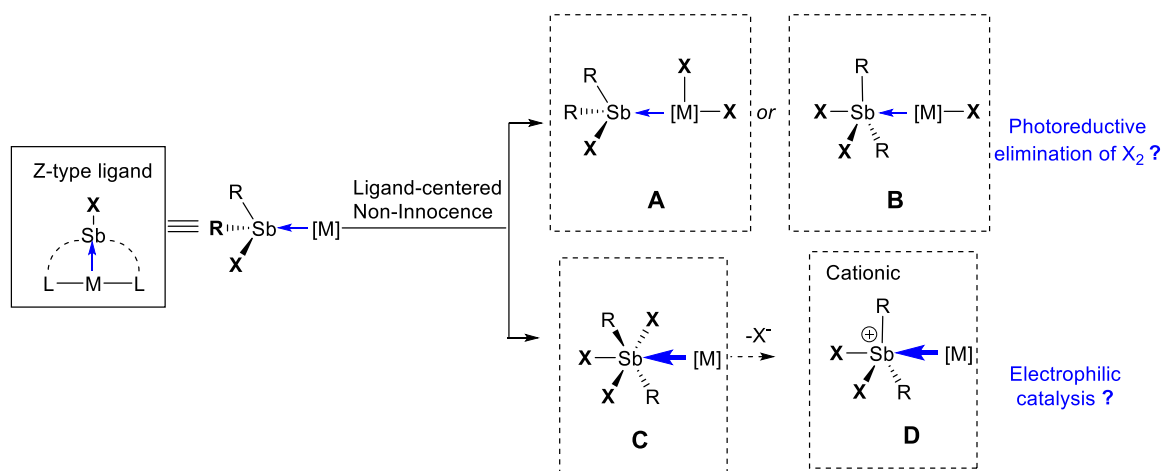


Figure 27. Schematic representation sketching the new antimony ligand design, which couples the Z-type ligand effect with the ligand-centered non-innocence. The targeted complexes feature more electrophilic metal center, promising for photoreductive elimination of X₂ or electrophilic catalysis.

Provided that Lewis acidic Z-type ligands can draw electron density from the metal center via metal \rightarrow Z ligand interaction, it can be assumed that the electrophilic nature of the metal center will increase. This assumption led to our investigation on two types of reactivity that an electrophilic metal center may favor, namely reductive elimination reactions and electrophilic catalysis. With respect to the former, it was decided to focus on developing Sb-M molecular platforms for the photo-reductive elimination of chlorine (**A** or **B**, Figure 27), which is relevance to a key step in the photocatalytic splitting of HX. For the latter, I targeted electrophilic gold and platinum catalysts for organic transformation (**C** or **D**, Figure 27). A description of these efforts constitute the bulk of this dissertation.

CHAPTER II

SOLUTION AND SOLID-STATE PHOTOREDUCTIVE ELIMINATION OF CHLORINE BY IRRADIATION OF A [PTSB]VII COMPLEX*

2.1 Introduction

The photoreductive elimination of halogens from transition metal complexes is a thermodynamically difficult process which necessitates the activation of strong metal-halides bonds. Given the relevance of such reactions to the photo-induced splitting of hydrohalic acids,^{120-121, 129-135} a great deal of effort has been devoted to identifying molecular platforms that support such transformations.^{123, 125-126, 136-142} Most platforms identified to date contain a late transition metal such as platinum,¹²⁵ iridium¹²⁶ or gold.¹²⁶ These systems can be either mononuclear as in the case of *trans*-Pt(PEt₃)₂(Br)₃Ar (**A**, Ar = *o*-(CF₃)C₆H₄, Figure 28) which eliminates bromine with a very high quantum yield (Φ) of 82%.¹⁴³ Chlorine photo-elimination has also been actively pursued because of its relevance to HCl splitting. Some of the best platforms reported to date for chlorine elimination are the Au^{II}-Ir^{II} complex (**B**, maximum Φ = 10%, Figure 28)¹²⁶ and the Pt^{III}-Pt^{III} complex (**C**, maximum Φ = 38%, Figure 28).¹²⁵ A common element of design uniting these different systems is the use of electron withdrawing ligands which destabilize the high valent metal centers thus favoring reductive elimination.

* Reprinted in part with permission from Yang, H.; Gabbai, F. P. *J. Am. Chem. Soc.* **2014**, 136, 10866. Copyright 2014 American Chemical Society.

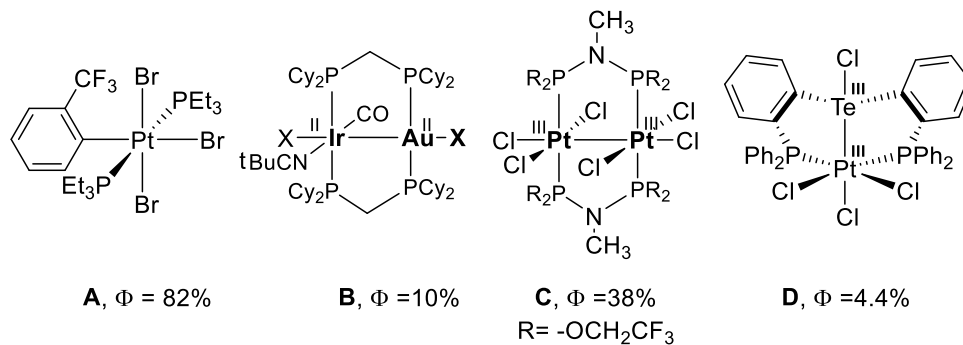


Figure 28. Reported molecular platforms for chlorine photoreductive elimination.

In a recent paper, we have shown that the heterobimetallic $\text{Te}^{\text{III}}\text{-Pt}^{\text{III}}$ complex **D** (Figure 28) supports the photoreductive elimination of chlorine with a maximum quantum yield of 4.4%.¹¹⁶ Although the quantum yield of this reaction is relatively low, these results suggest that poorly exploited heavy main group elements could be considered in lieu of noble metals.⁵⁰

2.2 Synthesis and structure of antimony-platinum complexes

On the basis of the above considerations, we have now chosen to broaden the scope of our approach by testing the use of antimony. Our choice of this element was prompted by the realization that: i) antimony displays a rich III/V redox chemistry making it well suited for the targeted application,^{86, 113, 144} and, ii) the extra valence of tri- or pentavalent antimony when compared to di- or tetra-valent tellurium offers an opportunity for a greater degree of electronic control through the incorporation of an extra ligand. This logic led us to consider [*o*-(Ph_2P) C_6H_4] $_2\text{SbCl}$], a ligand derived from [*o*-(Ph_2P) C_6H_4] $_2\text{Te}$] by replacement of the Te atom by a less electron releasing SbCl moiety. This ligand could be accessed by comproportionation of neat SbCl_3 and [*o*-(Ph_2P) C_6H_4] $_3\text{Sb}$ at 100 °C.⁸⁶ Reaction of [*o*-(Ph_2P) C_6H_4] $_2\text{SbCl}$] with $(\text{Et}_2\text{S})_2\text{PtCl}_2$ afforded complex **42** (Figure 29). This complex displays a ^{31}P NMR signal at

50.9 ppm and a ^{195}Pt NMR signal at -5164 ppm. The presence of ^{195}Pt satellites in the ^{31}P NMR spectrum as well as the multiplicity of the ^{195}Pt NMR resonance (triplet, $^1J_{\text{Pt-P}} = 2566$ Hz) confirm the expected coordination of the phosphine arms to the platinum.

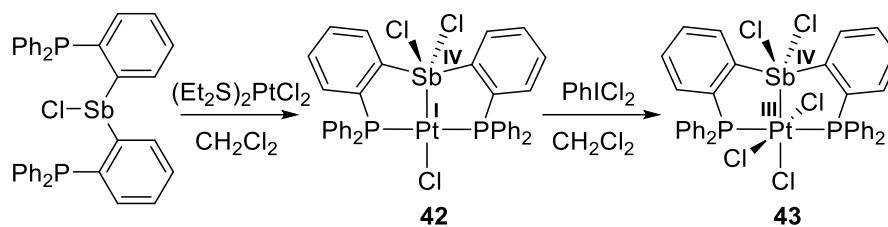


Figure 29. Synthesis of complexes **42** and **43**.

These spectroscopic features are close to those observed for the stiboranyl complex [(*o*-(Ph_2P) C_6H_4) $_2\text{SbClPh}$] PtCl (**E**, $\delta(^{31}\text{P}) = 53.9$ ppm, $\delta(^{195}\text{Pt}) = -5019$ ppm, $^1J_{\text{Pt-P}} = 2706$ Hz),¹¹³ suggesting the possible insertion of the antimony atom into one of the Pt-Cl bonds.

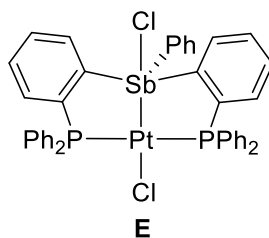


Figure 30. Structure of a stiboranyl-platinum complex.

This proposal was confirmed by a determination of the crystal structure of **42** which shows a divalent square planar platinum center with a dichlorodiarlylstiboranyl ligand positioned trans from the chloride ligand ($\text{Sb-Pt-Cl}(3) = 175.25(3)^\circ$, $\text{P}(1)\text{-Pt-P}(2) = 169.86(5)^\circ$) (Figure 31). The Sb-Pt bond of 2.4407(5) Å is notably shorter than that observed in **E** (2.5380(8) Å),¹¹³ a complex also formed by insertion of the antimony atom into a Pt-Cl bond. The shorter bond observed in **42** most likely originates from the geometry adopted by

the pentavalent antimony atom. In **E**, one of the antimony-bound chloride ligands is located directly opposite from the platinum center, thus lengthening the Sb-Pt bond via a trans-effect. In **42**, we observe a very different situation with the two antimony-bound chloride ligands projecting in an direction oblique to the Pt-Sb bond (Pt-Sb-Cl(1) = 99.22(4)°, Pt-Sb-Cl(2) = 107.51(4)°). The coordination geometry at antimony is best described as square pyramidal with the two chlorine atom Cl(1) and Cl(2) and the two carbon atom C(1) and C(2) defining the base (Cl(1)-Sb-Cl(2) = 153.24(5)°, C(1)-Sb-C(2) = 153.7(2)°). With three electron-withdrawing ligands decorating its core, it became important to verify whether **42** would be amenable to oxidation. While no reaction was observed with HCl in CH₂Cl₂/Et₂O mixtures, **42** quickly reacted with PhICl₂ in CH₂Cl₂ to afford complex **43** as a deep yellow solid. The ³¹P NMR spectrum of **43** displays a signal at 43.3 ppm with ¹⁹⁵Pt satellites (¹J_{Pt-P} = 1842 Hz) as well as a ¹⁹⁵Pt NMR resonance at -3473 ppm. When compared to **42**, the ¹J_{Pt-P} coupling constant of **43** is notably reduced and its ¹⁹⁵Pt NMR resonance is shifted downfield, consistent with oxidation of the platinum center.¹⁴⁵⁻¹⁴⁶ Although tetravalent platinum complexes are known to thermally eliminate halogens,^{143, 147-150} ³¹P and ¹H NMR spectroscopy show that **43** remains intact when heated to 70°C in the solid state for 12 hours.

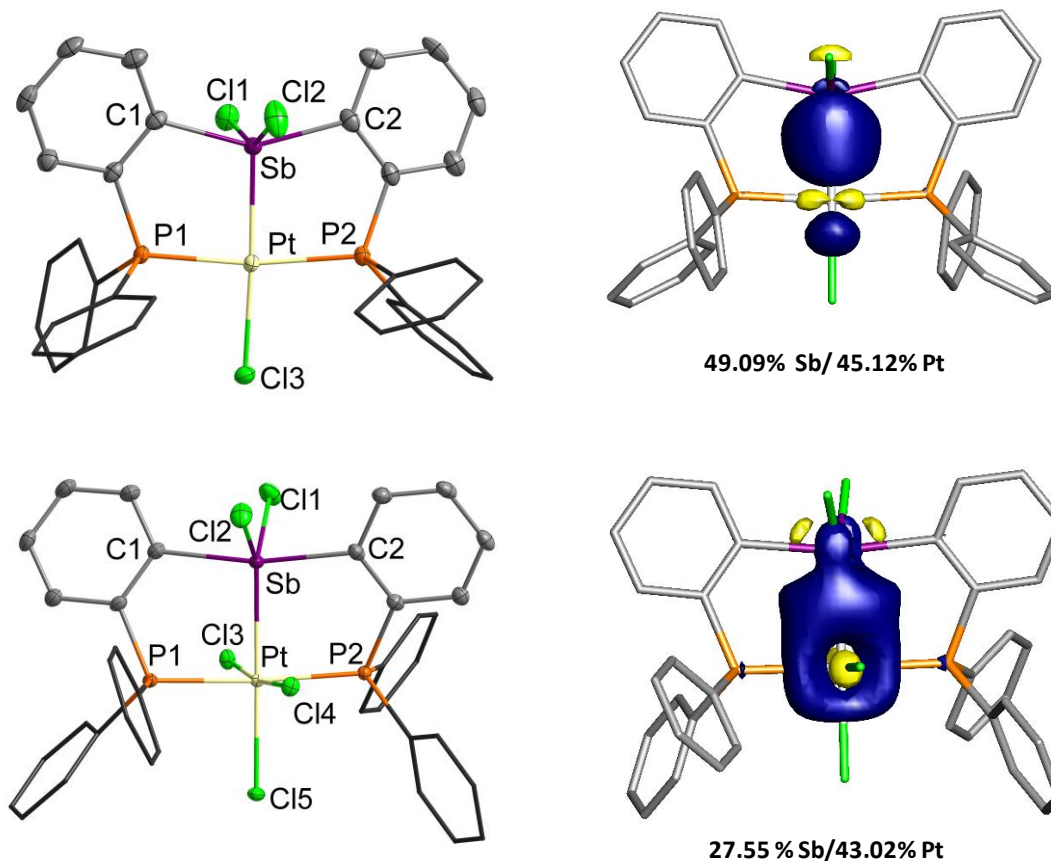


Figure 31. Left: Solid state structure of **42** (top left) and **43** (bottom left). Thermal ellipsoids are drawn at the 50% probability level. Phenyl groups are drawn in wireframe. Hydrogen atoms and solvent molecules are omitted for clarity. Pertinent metrical parameters can be found in the text. NLMO plot (isovalue = 0.05) of the Sb–Pt bond in of **42** (top right) and **43** (bottom right) obtained from the NBO analysis. Hydrogen atoms are omitted for clarity.

X-ray diffraction confirms Cl₂ addition to the platinum center, which now exhibits an octahedral geometry with three chloride ligands arranged in a meridional fashion (Figure 31). It is interesting to note that the bond distance of 2.4405(6) Å separating the platinum atom and the chlorine atom (Cl(5)) trans from the antimony atom is longer than the Pt–Cl bond distances involving the chlorine atoms trans from each other (Pt–Cl(2) = 2.3429(5) Å, Pt–Cl(4) = 2.3231(5) Å). This noticeable difference suggests that the antimony ligand is a stronger σ -donor than a chloride ligand. Oxidation of the platinum center also induced some changes at

antimony including: i) a important shortening of the Sb–Cl bond from 2.494(3) Å (av.) in **42** to 2.402(2) Å (av.) in **43**; ii) an contraction of the Cl(1)–Sb–Cl(2) angle from 153.24(5)° in **42** to 118.67(2)° in **43**. As a result, the antimony atom displays a slightly distorted trigonal bipyramidal geometry, with Cl(1)–Sb–Pt and Cl(2)–Sb–Pt angles of 119.99(2)° and 121.33(2)°, respectively. Finally, the increase in the coordination number of the platinum center is accompanied by a detectable lengthening of the Sb–Pt bond from 2.4407(5) Å in **42** to 2.560(2) Å in **43**.

2.3 Bonding characteristics and photophysical properties

The UV-vis spectrum of **43** displays an intense low energy band centered at 320 nm ($\epsilon = 30,005 \text{ M}^{-1} \text{ cm}^{-1}$) which tails into the visible part of the spectrum (Figure 32). A Natural Bond Orbital analysis of **42** and **43** carried out at the DFT optimized geometry (Gaussian 09 program, functional: BP86;¹⁵¹⁻¹⁵² mixed basis set: Sb/Pt: cc-pVTZ-PP; P/Cl: 6-31g(d'); C/H: 6-31g)¹⁵³⁻¹⁵⁴ shows that the Sb–Pt σ -bond is largely covalent for both complexes (see NLMO plots in Figure 31). For **42**, the orbital contributions from antimony and platinum (Sb: 49.09% / Pt: 45.12%) are almost identical indicating that the bond is essentially non-polar. Because of the covalent character of this bond and by analogy with formal oxidation state assignments¹⁵⁵ in complexes with metal-metal bonds such as **B** and **C**,¹²⁵⁻¹²⁶ we describe **42** as a $\text{Sb}^{\text{IV}}\text{Pt}^{\text{I}}$ complex. In **43**, the orbital contributions (Sb: 27.55% / Pt: 43.02%) show that the bonding pair is significantly shifted toward the oxidized and thus more electron demanding platinum center. This shift of the bonding density shows that oxidation impacts the core electronic distribution of this heterobimetallic platform. The polarization of the Sb–Pt bond in **43** is best reconciled by invoking the two resonance structures (**a** and **b**) shown in Figure 33. Resonance structure

a which corresponds to a $\text{Sb}^{\text{IV}}\text{Pt}^{\text{III}}$ complex is the most important contributor to the actual electronic structure of the complex. The second resonance structure (**b**), which allows to account for the polarization of the Sb-Pt bonding pair toward platinum, corresponds to a platinate (Pt^{II}) complex stabilized by a Z-type or σ -accepting stibonium (Sb^{V}) ligand.^{14, 21, 156-}

167

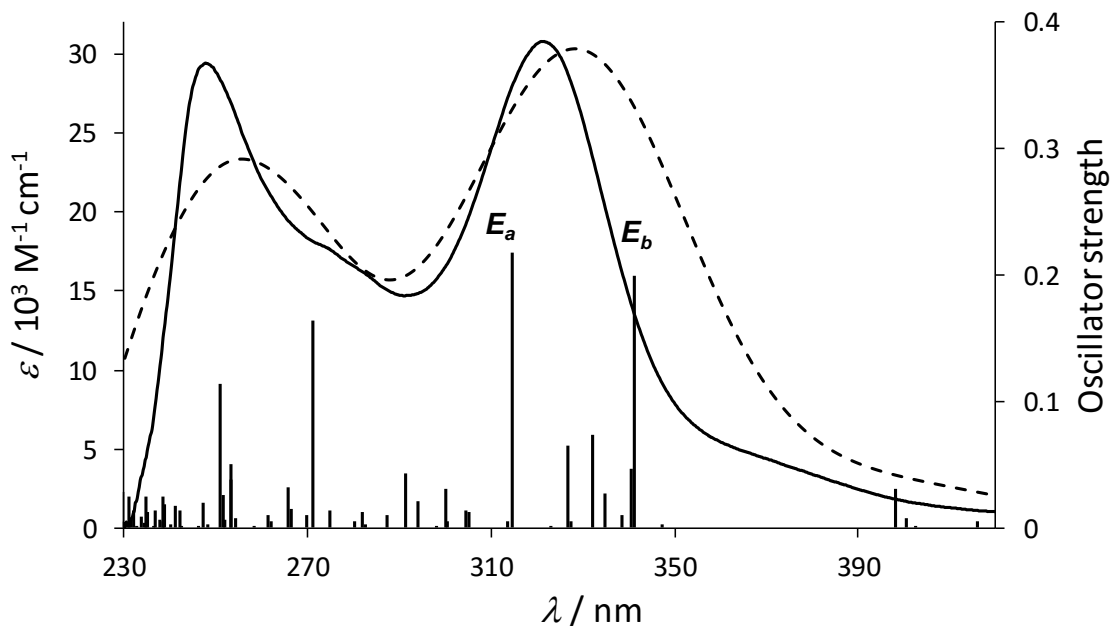


Figure 32. Experimental (—) (CH_2Cl_2) and calculated (---) ultraviolet–visible spectra for **42**. The calculated spectra were obtained by TD–DFT calculations using the MPW1PW91 functional and a mixed basis set (peak half–width used for the simulation: 0.25 eV). The computed excitations are shown as thin lines with heights proportional to the calculated oscillator strengths.

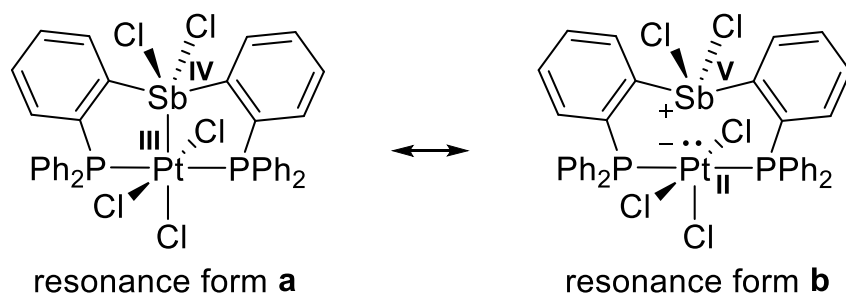


Figure 33. Relevant resonance structures of **42**.

Computational methods have also been used to simulate the UV-vis spectrum of **43** using time-dependent density functional theory (TD-DFT). A good match with the experimental data is obtained when the spectrum is simulated using the MPW1PW91 functional (mixed basis set: Sb, Pt: cc-pVTZ-PP; P, Cl: 6-31g(d⁺); C, H: 6-31g) and the SMD implicit solvation model with CH₂Cl₂ as a solvent (Figure 32).¹⁶⁸ According to these calculations, the high oscillator strength excitations labeled as E_a and E_b contribute to the 320 nm band and involve the LUMO and LUMO+1 as the accepting orbitals (Table 2). As could be expected for an octahedrally coordinated platinum species, these two orbitals have e_g^* character and are antibonding with respect to the Pt-Cl bonds (Figure 34).

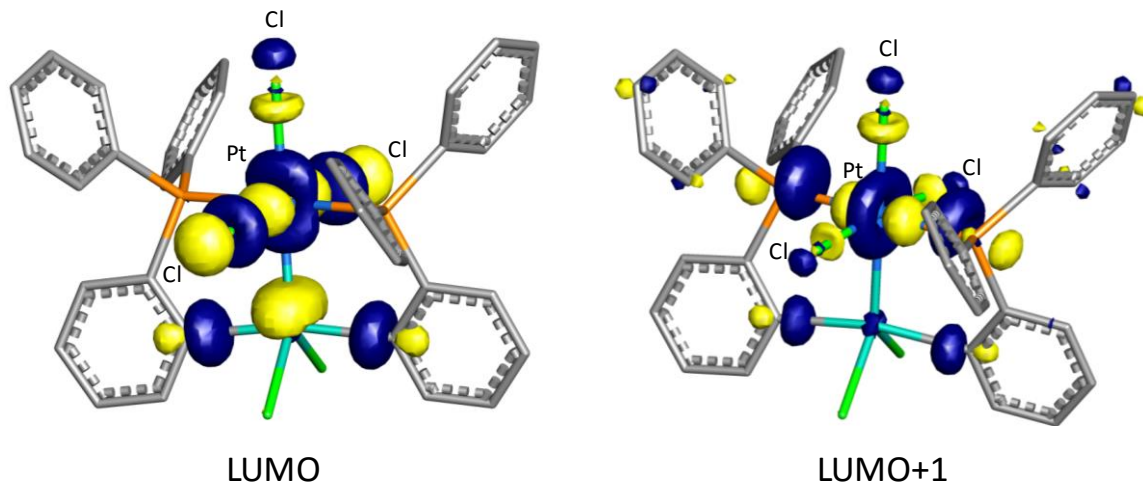


Figure 34. Plots of the LUMO (−0.120 eV) and LUMO+1 (−0.106 eV) of **43** (0.03 isosurface value).

2.4 Photoreductive elimination of chlorine in solution

In agreement with this spectroscopic assignment, irradiation of **43** in CH_2Cl_2 results in a rapid quenching of the band at 320 nm suggesting photoreduction of the complex (Figure 35). This photoreduction can be monitored by ^{31}P NMR spectroscopy. When carried out in neat CH_2Cl_2 , the reaction affords **42** in a ~85% yield, with some decomposition products detected in the 10–37 ppm range (Figure 36). The presence of these decomposition products can be assigned to side reactions between the ligand and the chlorine generated by photolysis. As documented in the literature, chlorine atoms can also be trapped by reaction with the CH_2Cl_2 solvent.¹⁶⁹ Addition of 2,3–dimethyl–1,3–butadiene (DMBD, 1.77 M) as a chlorine scavenger to the solution makes the photolysis significantly cleaner, with **42** as the sole phosphorus–containing species (Figure 37).^{125–126, 136, 138–141} This photoreductive elimination of chlorine is efficient, with a maximum quantum yield of 13.8% measured at a DMBD concentration of 4.4

M, using potassium ferrioxalate as a standard actinometer.¹⁷⁰⁻¹⁷² The high quantum yield of this photoreductive elimination, which exceeds that of the tellurium complex **D**,¹¹⁶ is correlated to the destabilizing effect of the five electron withdrawing chlorine ligands on the oxidized core of **43**. This situation is reminiscent of that described for the hexachloro diplatinum complex **C**, for which a maximum quantum efficiency of 38% has been reported.¹³⁷ It is also interesting to note that the quantum yield measured for the photoreduction of **43** is comparable to the value of 19% measured for the photoaquation of $[\text{PtCl}_6]^{2-}$ ($\lambda = 313 \text{ nm}$), a reaction that proceeds through formation of a Pt(III) intermediate via extrusion of a $\text{Cl}\cdot$ radical.¹⁷³

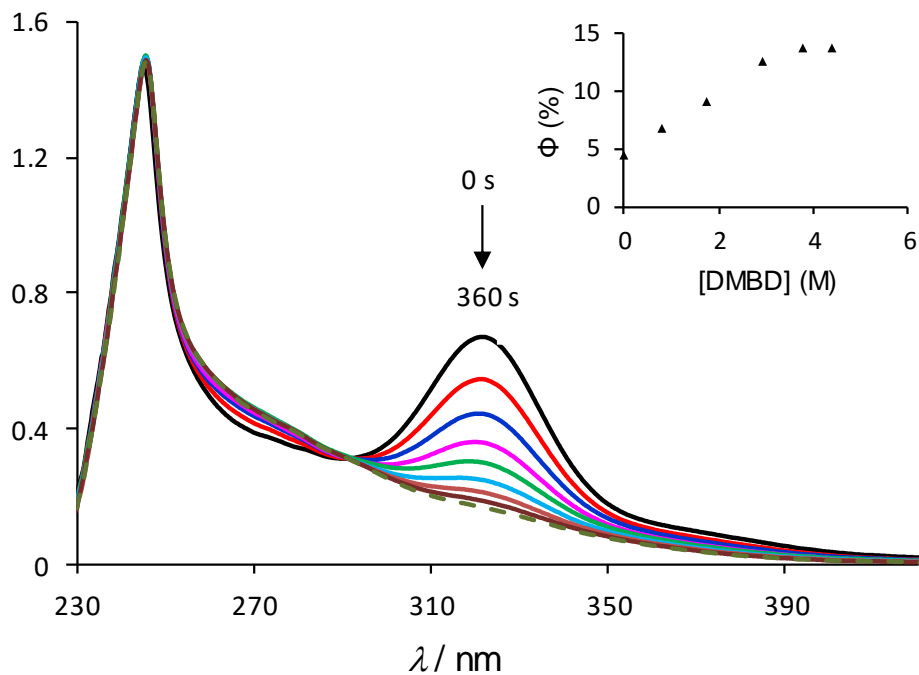


Figure 35. Absorption spectra (—) obtained during the photolysis of **43** in CH_2Cl_2 ($2.23 \times 10^{-5} \text{ M}$) with monochromatic 320 nm light in the presence of 2,3-dimethyl-1,3-butadiene ($7.07 \times 10^{-4} \text{ M}$). The final spectrum (---) is identical to that of **42**. The inset shows the correlation between the quantum yield and the DMBD concentration.

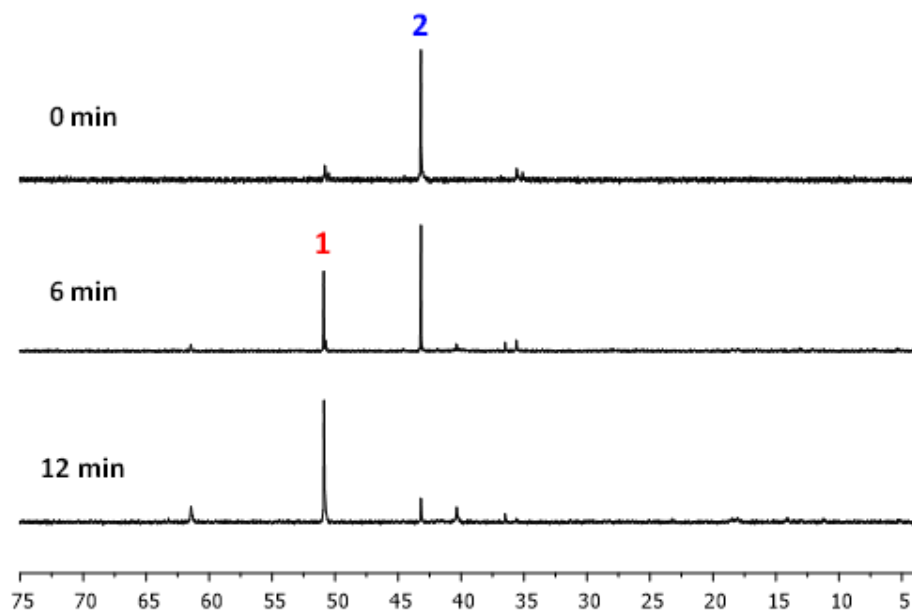


Figure 36. ^{31}P NMR spectra of photolysis of **43** in the absence of 2,3-dimethyl-1,3-butadiene (in CH_2Cl_2). This spectrum was recorded on Varian Unity Inova 300 FT NMR.

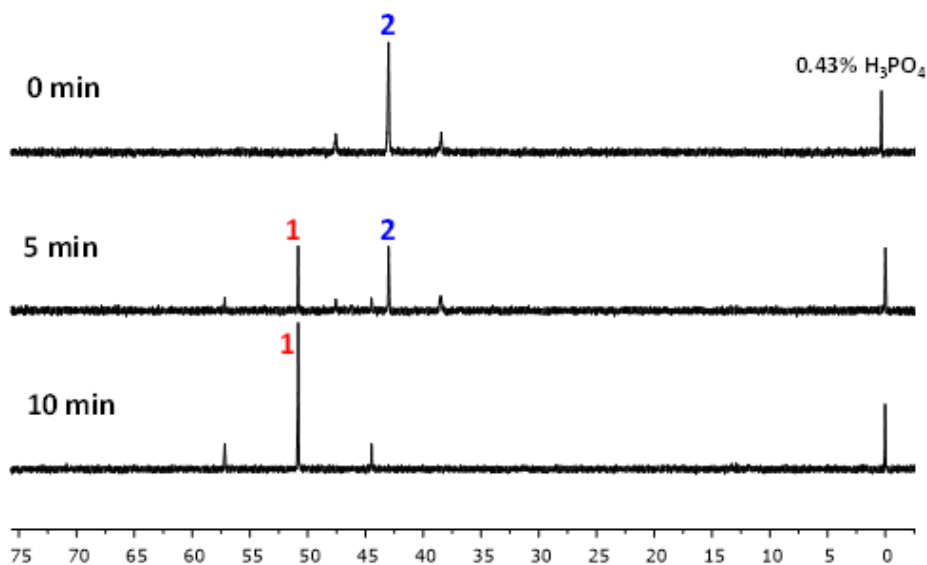


Figure 37. ^{31}P NMR spectra of photolysis of **43** in CH_2Cl_2 (0.011 M) in the presence of 2,3-dimethyl-1,3-butadiene (1.77 M).

2.5 Photoreductive elimination of chlorine in solid-state

To conclude these studies, we decided to test whether **43** would behave like **C** and evolve chlorine in the solid state.¹²⁵ To this end, a sample of **43** was loaded into a quartz cell at atmospheric pressure, under nitrogen. A small sodium strip, whose base was covered with Teflon tape in order to prevent contact with **43**, was placed inside the cell. The cell was tightly closed and irradiated with a Xe lamp for 10 h (Figure 38). The temperature of the sample, which was monitored with a mercury thermometer directly adjoined to the cell was kept below 32 °C using a high velocity fan during photolysis. After 10 h, the photolysis was stopped. The solid sample showed noticeable sign of discoloration, in agreement with the conversion of deep yellow **43** into pale yellow **42**. The surface of the sodium strip had tarnished significantly suggesting chlorine oxidation. In line with these observations, ¹H and ³¹P NMR analysis of the photolyzed solid indicated a 53% conversion of **43** into **42**.

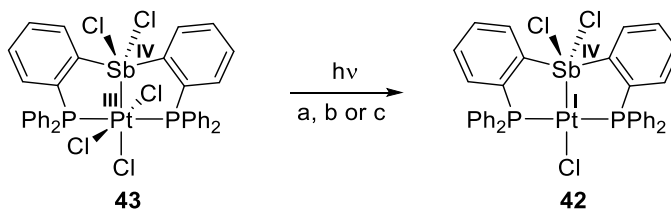


Figure 38. Photoreduction of **43** using a Xe lamp (75W). a) Solution photolysis in CH₂Cl₂ with DMBD (1.77 M) in a glass NMR tube (complete conversion in 10 minutes). b) Solid state photolysis in a closed quartz cell with Na as a trap (conversion = 53% in 10 hours). c) Solid state photolysis in an open quartz cell (conversion = 45% in 10 hours).

The evolution of chlorine was confirmed by dissolution of the sodium strip in water and subsequent chloride analysis using ion chromatography. The latter indicated that 72% of

the expected chlorine had been captured by sodium during the photolysis experiment (Figure 39).

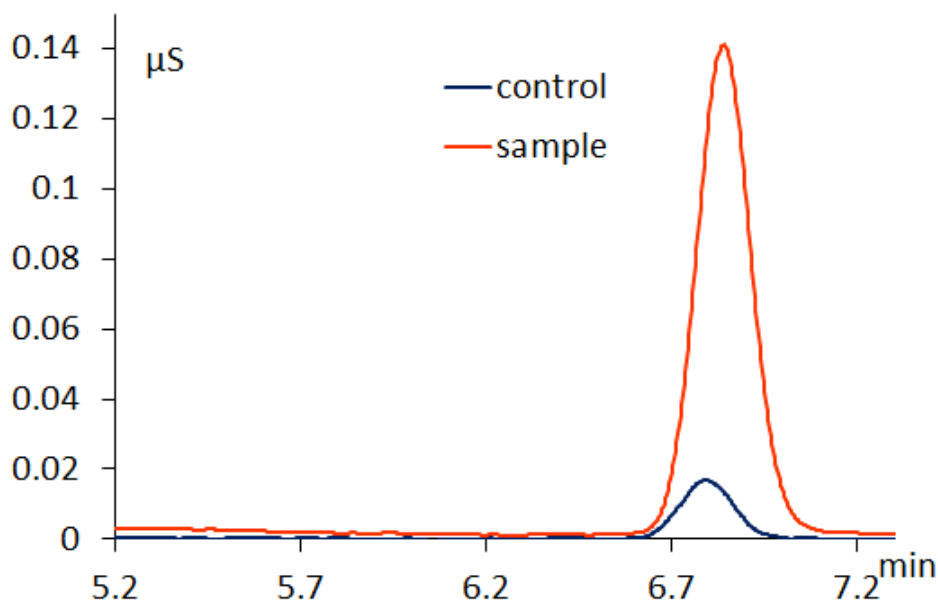


Figure 39. Ion chromatography analysis of the Na strip after the solid-state photolysis.

We propose that the rest of the chlorine is incorporated in the decomposition products observed by ^{31}P NMR spectroscopy in the 5 ppm to 25 ppm range. Using single point energy calculations carried out with the B3LYP functional and a mixed basis set (C, H, P, Cl: 6-311+g(2d,p); Sb, Pt: cc-pVTZ-PP), we estimate that the photoreduction of **43** into **42** is endothermic by ~ 544 kJ/mol assuming the formation of two $\text{Cl}\cdot$ radicals or ~ 300 kJ/mol assuming the formation of Cl_2 . These values provide a measure of the energy storing potential of this reaction. Finally, the solid state photolysis of **43** into **42** can be carried out with the cell open to air without sodium as a chemical trap (Figure 40, conversion of 45% after 10 h). The evolution of chlorine under such conditions shows that the title SbPt complex is able to evolve chlorine on its own, without the thermodynamic bias associated with a trap. To our knowledge,

no other bimetallic complexes have been tested under such conditions. Complex **C** also evolves chlorine when irradiated in the solid state, albeit under vacuum, with the chlorine photoproduct captured in a low-temperature trap.¹²⁵

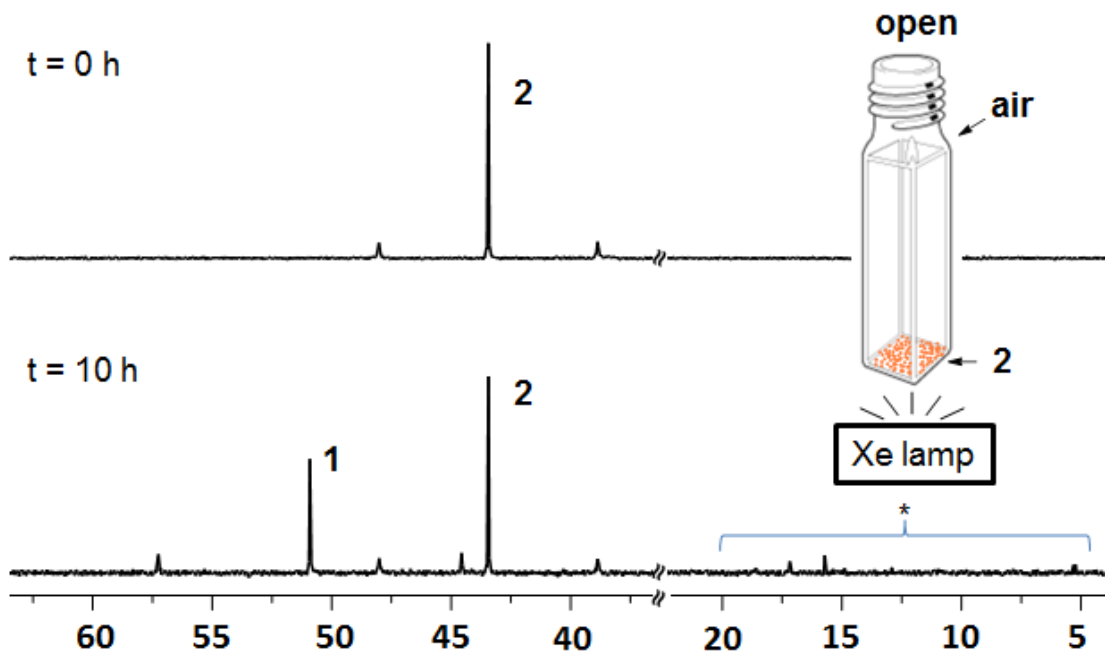


Figure 40. ^{31}P NMR spectra before and after solid state irradiation of **43** with a Xe lamp (75 W) under ambient conditions in an open quartz cell. The inset shows a schematic drawing of the experimental setup used for this open-system solid state photolysis. The spectral region marked by a “*” shows the presence of decomposition products.

2.6 Conclusion

In summary, we describe a new SbPt platform for the high quantum yield photoevolution of chlorine. The photoreduction quantum yield of **43** is more than three times greater than that measured for the TePt complex **D** previously investigated by our group.¹¹⁶ This increase validates the notion that replacement of the TeCl unit in **D** by a less electron releasing SbCl₂ unit in **43** destabilizes the oxidized complex and facilitates its photoreduction. Another unique feature of the title SbPt platform is its ability to support this reaction in the

solid-state, in the absence of a trap. We propose that such platforms may become useful for the production of halogens as solar fuels. We are currently investigating the mechanism of this solid state reaction and whether chlorine is evolved as Cl• or Cl₂.¹⁷⁴

2.7 Experimental

General considerations. SbCl₃ was purchased from Alfa Aesar and used as received. The ligand [(*o*-(Ph₂P)C₆H₄)₃Sb],¹⁷⁵ *cis*-PtCl₂(Et₂S)₂¹⁷⁶ and PhICl₂¹⁷⁷ were prepared as described in the literature. All air and moisture sensitive experiments were carried out under an atmosphere of dry N₂ employing either a glove box or standard Schlenk techniques. Solvents were dried by passing through an alumina column (CH₂Cl₂) or by reflux under N₂ over Na/K (Et₂O). All other solvents were used as received. Ambient temperature NMR spectra were recorded on a Varian Unity Inova 500 FT NMR (499.42 MHz for ¹H, 125.58 MHz for ¹³C, 202.18 MHz for ³¹P) spectrometer. Chemical shifts (δ) are given in ppm and are referenced against residual solvent signals (¹H, ¹³C) or external 85% H₃PO₄ (³¹P). Elemental analyses were performed at Atlantic Microlab (Norcross, GA). Electrospray mass spectra were obtained with a SciexQstarr Pulsar and a Protana Nanospray ion source.

Generation of [(*o*-(Ph₂P)C₆H₄)₂SbCl]. *o*-(Ph₂P)C₆H₄)₃Sb (527 mg, 0.582 mmol) and SbCl₃ (66.4 mg, 0.291 mmol) were combined neat in a Schlenk tube. Five drops of toluene (or 250 μL) were added to the mixture which was subsequently heated to 100 °C and stirred for 16 h. The solid obtained upon cooling was analyzed by ³¹P NMR spectroscopy which indicated formation of (Ph₂P)C₆H₄)₂SbCl (-11.39 ppm) in a 92% yield. The other species

detected at -6.35 ppm is unreacted *o*-(Ph₂P)C₆H₄)₃Sb. The comproportionation product was used without further purification.

Synthesis of 42. A solution of PtCl₂(Et₂S)₂ (0.28 g, 0.62 mmol) in CH₂Cl₂ (8 mL) was added to a solution of [(*o*-(Ph₂P)C₆H₄)₂SbCl] (corrected amounts: 0.42 g, 0.62 mmol) in CH₂Cl₂ (10 mL) at ambient temperature. The resulting clear yellow solution was stirred for 12 h and subsequently evacuated to dryness under reduced pressure. The resulting residue was washed with Et₂O (3 × 5 mL) to afford crude **42** as a light yellow solid. Single crystals (square in habits) were obtained by slow diffusion of Et₂O into a CH₂Cl₂ solution (0.50 g, 85% yield). ¹H NMR (499.42 MHz; CDCl₃): δ = 8.34 (d, 2H, *o*-P(Sb)C₆H₄, ³J_{H-H} = 7.99 Hz), 7.69–7.75 (m, 8H), 7.52 (d of t, 2H, *o*-P(Sb)C₆H₄, ³J_{H-H} = 7.99 Hz, ³J_{H-P} = 3.99 Hz), 7.40–7.47 (m, 16H). ¹³C{¹H} NMR (125.58 MHz; CDCl₃): δ = 134.0 (t, -C₆H₅, CH, J_{C-P} = 6.66 Hz), 131.5 (s, -C₆H₅, CH), 128.8 (t, -C₆H₅, CH, J_{C-P} = 5.52 Hz), 134.5 (t, J_{C-P} = 3.27 Hz), 134.2 (s), 130.9 (d, J_{C-P} = 9.29 Hz), 130.5 (t, J_{C-P} = 4.14 Hz), 129.4 (s), 129.1 (s), 128.2 (s). ³¹P{¹H} NMR (202.16 MHz; CDCl₃): δ = 50.9 (s, J_{Pt-P} = 2566 Hz). Elemental analysis calculated (%) for **1** (C₃₆H₂₈Cl₃P₂PtSb): C, 45.72; H, 2.98; found C, 45.72; H, 3.01.

Synthesis of 43. To a CH₂Cl₂ (10 mL) solution of **42** (0.35 g, 0.37 mmol) was added a CH₂Cl₂ (10 mL) solution of PhICl₂ (0.10 g, 0.37 mmol) at ambient temperature. The mixture turned from light yellow to deep yellow-orange. After stirring for 2 h, the solvent was removed under reduced pressure. The residue was washed with Et₂O (10 mL), leaving behind compound **43** as a yellow solid. Compound **43**, in a crude form, was collected by filtration and dried under vacuum (0.35 g, 92% yield). Yellow crystals of **43** were obtained by diffusion of pentane into

a CH₂Cl₂ solution. ¹H NMR (499.42 MHz; CDCl₃): δ = 8.53 (d, 2H, *o*-P(Sb)C₆H₄, ³J_{H-H} = 7.99 Hz), 7.72–7.82 (m, 10H), 7.35–7.52 (m, 16H). ¹³C{¹H} NMR (125.58 MHz; CDCl₃): 135.3 (t, -C₆H₅, CH, J_{C-P} = 5.02 Hz), 131.9 (s, -C₆H₅, CH), 127.9 (t, -C₆H₅, CH, J_{C-P} = 5.02 Hz), 134.1 (s), 133.3 (d, J_{C-P} = 8.79 Hz), 133.1 (t, J_{C-P} = 5.02 Hz), 130.1 (t, J_{C-P} = 3.77 Hz), 125.1 (t, J_{C-P} = 30.83 Hz). Two of the ten resonances are not detected. ³¹P{¹H} NMR (202.16 MHz; CDCl₃): δ = 43.3 (J_{Pt-P} = 1842 Hz). Elemental analysis calculated (%) for **43** (C₃₆H₃₀Cl₅P₂PtSb): C, 42.45; H, 2.97; found C, 42.57; H, 2.79.

Computational Details. Density functional theory (DFT) structural optimizations were performed on the solid state structures of complexes **42** and **43** using Gaussian 09 suite of programs with effective core potentials on all heavy atoms (functional: BP86;¹⁵¹⁻¹⁵² mixed basis set: Sb/Pt: cc-pVTZ-PP; P/Cl: 6-31g(d'); C/H: 6-31g).^{39,40} Frequency calculations were also performed on the optimized geometry, showing no imaginary frequencies. The optimized structures, which are in good agreement with the solid state structures (Table 1), were subjected to a NBO analysis. The resulting Natural Localized Molecular Orbitals (NLMOs) were visualized and plotted using the Jimp 2 program.¹⁷⁸⁻¹⁷⁹ In addition, the optimized structure of **2** was subjected to time-dependent density functional theory (TD-DFT) calculations (functional: MPW1PW91; mixed basis set: Sb/Pt: cc-pVTZ-PP; P/Cl: 6-31g(d'); C/H: 6-31g) using the SMD implicit solvation model with CH₂Cl₂ as a solvent.¹⁶⁸

Thermochemistry calculation

Benchmarking of the method using for $\text{PtCl}_6^{2-} \rightarrow \text{PtCl}_4^{2-} + \text{Cl}_2$

DFT structural optimizations were first performed for PtCl_6^{2-} , PtCl_4^{2-} , and Cl_2 species using Gaussian 09 suite of programs (functional: BP86,¹⁵¹⁻¹⁵² mixed basis set: Pt: cc-pVTZ-PP; Cl: 6-31g(d')).^{39,40} Single point calculations were subsequently conducted for the three species (Gaussian 09, functional: B3LYP, mixed basis set: Pt: cc-pVTZ-PP; Cl: 6-311+g(2d, p)). With thermal correction to enthalpy considered, the enthalpy change for $\text{PtCl}_6^{2-} \rightarrow \text{PtCl}_4^{2-} + \text{Cl}_2$ was obtained as follows:

$$\text{PtCl}_6^{2-} \qquad \qquad \qquad \Delta H_{\text{HF}} = -2881.120581 \text{ Hartrees} \qquad (1)$$

$$\text{PtCl}_4^{2-} \qquad \qquad \qquad \Delta H_{\text{HF}} = -1960.628706 \text{ Hartrees} \qquad (2)$$

$$\text{Cl}_2 \qquad \qquad \qquad \Delta H_{\text{HF}} = -920.3540324 \text{ Hartrees} \qquad (3)$$

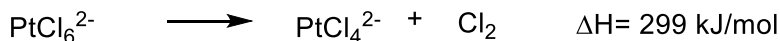
$$(1)-(2)-(3)$$



To compare the above computed value to other estimates from the literature, we also calculated the enthalpy change for $\text{PtCl}_6^{2-} \rightarrow \text{PtCl}_4^{2-} + \text{Cl}_2$ using the published atomization for PtCl_6^{2-} (1) and PtCl_4^{2-} (2).¹⁸⁰ We also considered the dissociation energy of Cl_2 (3) which was obtained from thermodynamic tables.



$$(4)-(5)-(6)$$



Application of the method to **43** → **42** + Cl₂

Single point energy calculations for **43**, **42** and Cl₂ were carried out with the B3LYP functional and a mixed basis set (C, H, P, Cl: 6-311+g(2d,p); Sb, Pt: cc-pVTZ-PP). With thermal correction to enthalpy considered, the enthalpy change for **43** → **42** + Cl₂ was obtained as follows:

$$\mathbf{43} \qquad \qquad \qquad \Delta H_{\text{HF}} = -4732.441481 \text{ Hartrees} \qquad (7)$$

$$\mathbf{42} \qquad \qquad \qquad \Delta H_{\text{HF}} = -3811.972728 \text{ Hartrees} \qquad (8)$$

$$\text{Cl}_2 \qquad \qquad \qquad \Delta H_{\text{HF}} = -920.3540324 \text{ Hartrees} \qquad (9)$$

$$(7)-(8)-(9)$$



Crystallographic Measurements. The crystallographic measurements were performed at 110(2) K using a Bruker APEX-II CCD area detector diffractometer (Mo-K_α radiation, λ = 0.71069 Å). In each case, a specimen of suitable size and quality was selected and mounted onto a nylon loop. The structures were solved by direct methods, which successfully located most of the non-hydrogen atoms. Semi-empirical absorption corrections were applied. Subsequent refinement on *F*² using the SHELXTL/PC package (version 6.1) allowed location of the remaining non-hydrogen atoms.

UV-vis Absorption Measurements. UV-vis spectra were recorded at room temperature on an Ocean Optics USB4000 spectrometer with an Ocean Optics ISS light source.

Quantum yield measurements for the photolysis of 2 in CH₂Cl₂. Photolysis experiments were performed using the 75 W xenon light source. Broad spectrum irradiation experiments were carried out with a Carl Zeiss Photomicroscope III 75W XBO Lamp. For monochromatic irradiation, the light source of a PTI QuantaMaster 40 fluorescence spectrometer was used. The built-in monochromator (PTI model 101) was used for wavelength selection (320 nm). Potassium ferrioxalate was freshly prepared as a standard actinometer to determine the photon flux.¹⁸¹⁻¹⁸³ The quantum yield of the photolysis reaction (Φ_2) was determined according to Equation (10):

$$\Phi_u = \Phi_s \times (\Delta C_2 \times V_2 \times t_s) / (\Delta C_s \times V_s \times t_2) \quad \text{Eq. (10)}$$

where Φ_s is the quantum yield of the standard; ΔC_s and ΔC_2 are the concentration differences before and after irradiation at 320 nm over a period of t_s and t_2 seconds, respectively; V_s and V_2 are volumes of the standard and sample (compound **43**), respectively. The solutions of the standard and sample used in these measurements are sufficiently concentrated ([standard] = 6 mM, [**43**] = 22 μ M) to assume 100% absorption of the incident light ($\epsilon_{\text{standard}} = 11100 \text{ M}^{-1} \text{ cm}^{-1}$, $\epsilon_2 = 30005 \text{ M}^{-1} \text{ cm}^{-1}$ at 320 nm). ΔC_s and ΔC_2 could be calculated based on the absorbance differences (ΔA_s and ΔA_2) after arbitrary dilutions. These experiments were repeated at various DMBD concentrations.

Thermal stability test: Before performing solid state photolysis experiment, the thermal stability of **2** was tested. A powdered sample of **43** (7.0 mg) was loaded into a vial and kept at 70 °C in an oil bath for 12 hours. The sample was then analyzed by ³¹P NMR and ¹H NMR.

Solid-state photolysis: Solid state photolysis experiments were carried out in a quartz cuvette. In a typical experiment, a powdered sample of **43** (7.0 mg) was suspended in THF and transferred to the cuvette. Evaporation of the THF resulted in the deposition of a film of **43** at the bottom of quartz cuvette. The film was dried thoroughly under vacuum for 1 h prior to irradiation using the Xe lamp. The temperature during irradiation was kept below 35 °C. These experiments were carried out under different conditions (open system, closed system with a sodium strip to trap the evolved chlorine). After irradiation, the sample was analyzed by ³¹P NMR and ¹H NMR in CDCl₃. For experiments carried out in the presence of a sodium, the cell was transferred to a N₂ glove box and loaded with a sodium strip (0.2 g). A direct contact between the sodium strip and the sample was prevented with Teflon tape that we used to dress the base of the sodium strip. At the end of the photolysis, the sodium strip was carefully removed from the cell, transferred to a beaker. The beaker was placed over dry ice and treated with deionized water, dropwise (*Caution: water must be added slowly to prevent a sodium fire; cooling of the sodium by placing the beaker over dry ice is also absolutely necessary*). Ion chromatography was used to measure the Cl⁻ concentration of the resulting solution. The final value was adjusted to account for the low chloride content that we also determined for the unreacted sodium metal alone.

Gas Chromatography–Mass Spectrometry. GC–MS was performed on Ultra GC/DSQ (ThermoElectron, Waltham, MA). Rxi–5ms was used as a gas chromatographic column with dimensions of 60 m length, 0.25 mm i.d., and 0.25 μm film thickness (Restek; Bellefonte, PA). Helium was used as a carrier gas at constant flow of 1.5 ml/min. Splitless and split (1:10) injection were used. Transfer line and ion source were held at 250°C. The column temperature

was maintained at 50°C for 5 min and raised to 320°C at 20°C/min. Mass spectra were acquired in full scan mode in the range of 30–500 m/z.

Ion Chromatography. Ion Chromatography was performed at room temperature on Dionex ICS- 900 Ion Chromatography System with MMS™ 300 membrane suppressor module (Thermo Fisher Scientific Inc.). 9.0 mM sodium carbonate and 75 mM sulfuric acid were used as eluent and regenerant respectively.

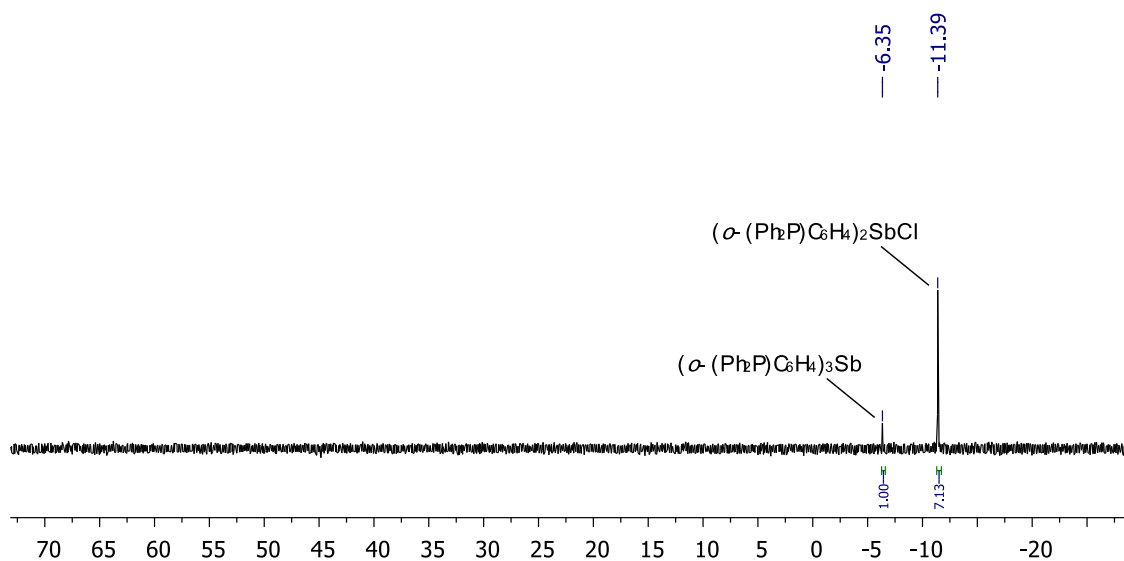


Figure 41. ^{31}P NMR spectrum of the coproportionation product of neat SbCl_3 and $(o\text{-(Ph}_2\text{P)C}_6\text{H}_4)_3\text{Sb}$ in CDCl_3 .

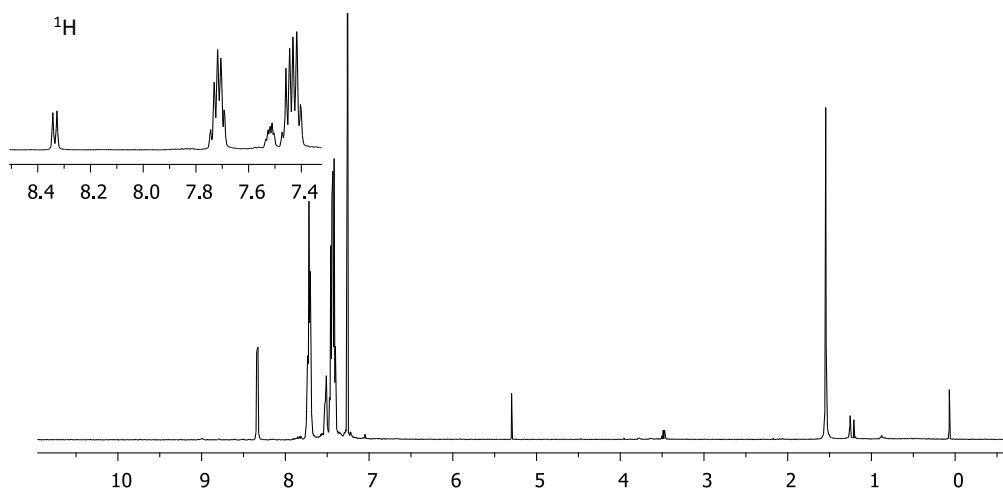


Figure 42. ^1H NMR spectrum of **42** in CDCl_3 .

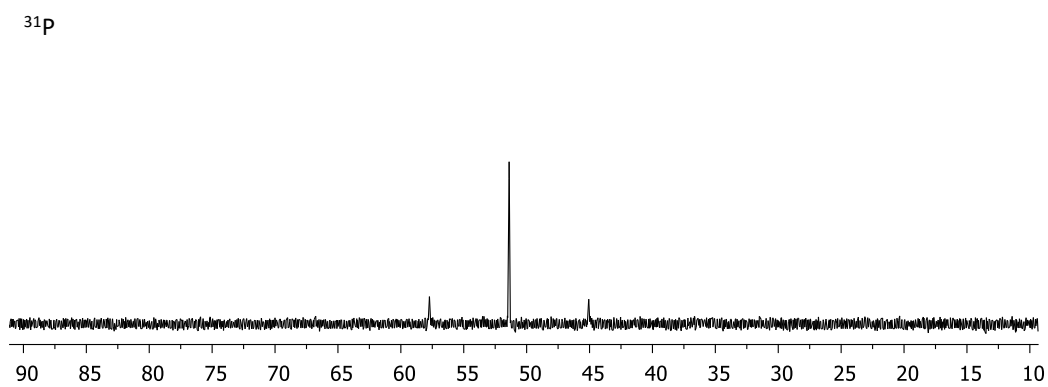


Figure 43. ^{31}P NMR spectrum of **42** in CDCl_3 .

^{195}Pt

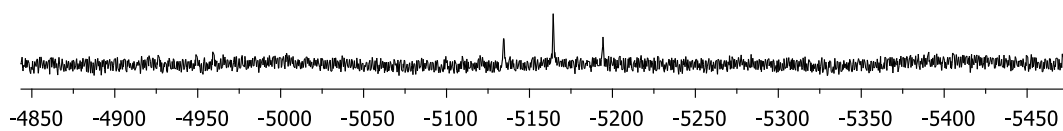


Figure 44. ^{195}Pt NMR spectrum of **42** in CDCl_3 .

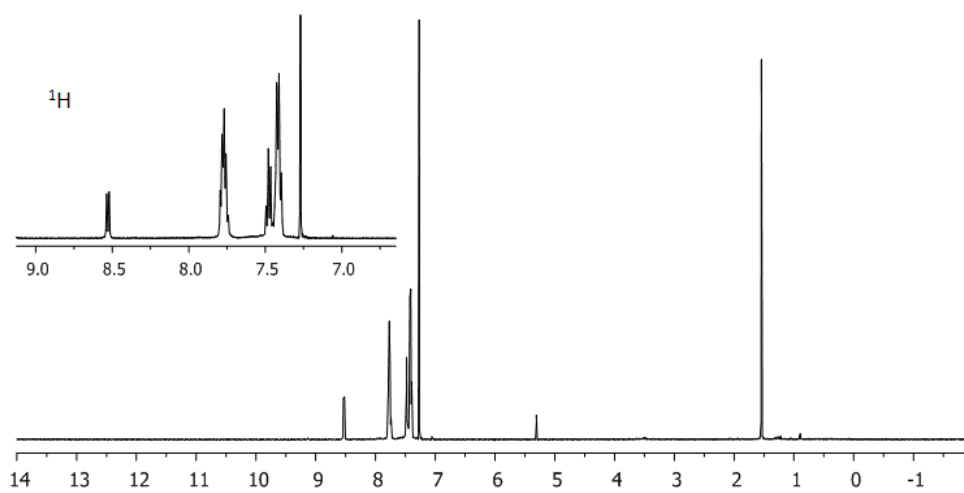


Figure 45. ^1H NMR spectrum of **43** in CDCl_3 .

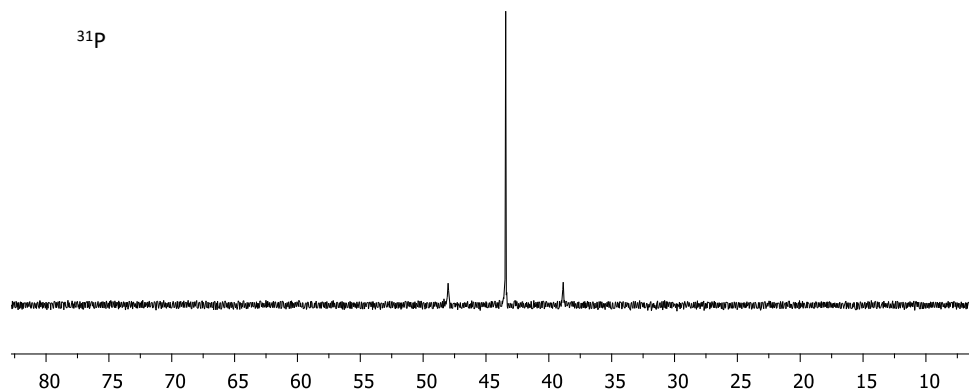


Figure 46. ^{31}P NMR spectrum of **43** in CDCl_3 .

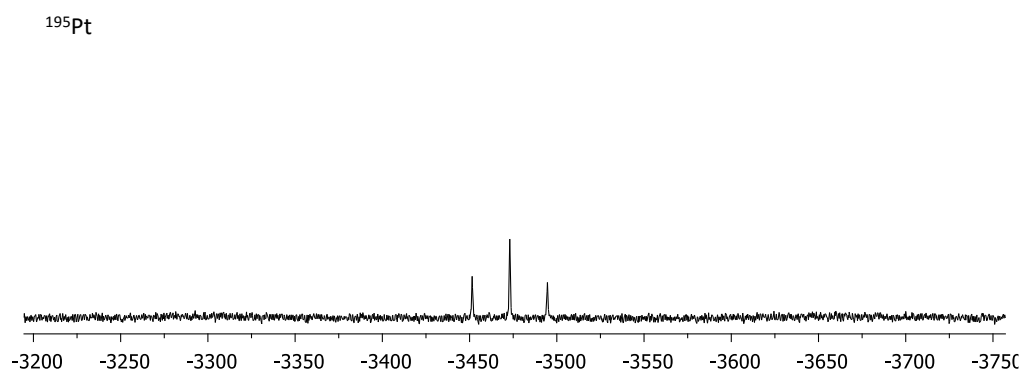


Figure 47. ^{195}Pt NMR spectrum of **43** in CDCl_3 .

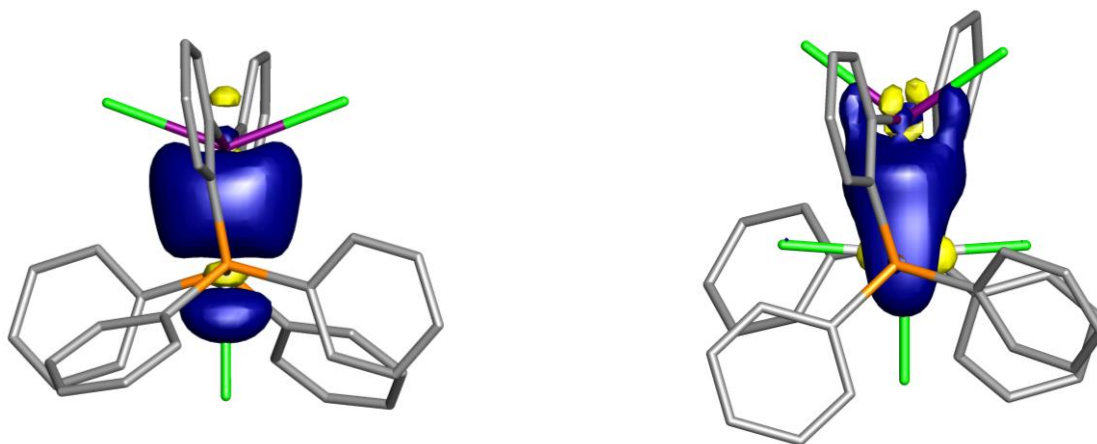


Figure 48. NLMO Plot of the Sb-Pt bond in complex **42** (left) and complex **43** (right) obtained from NBO analysis (Rotated 90° from the NLMO Plot in the paper).

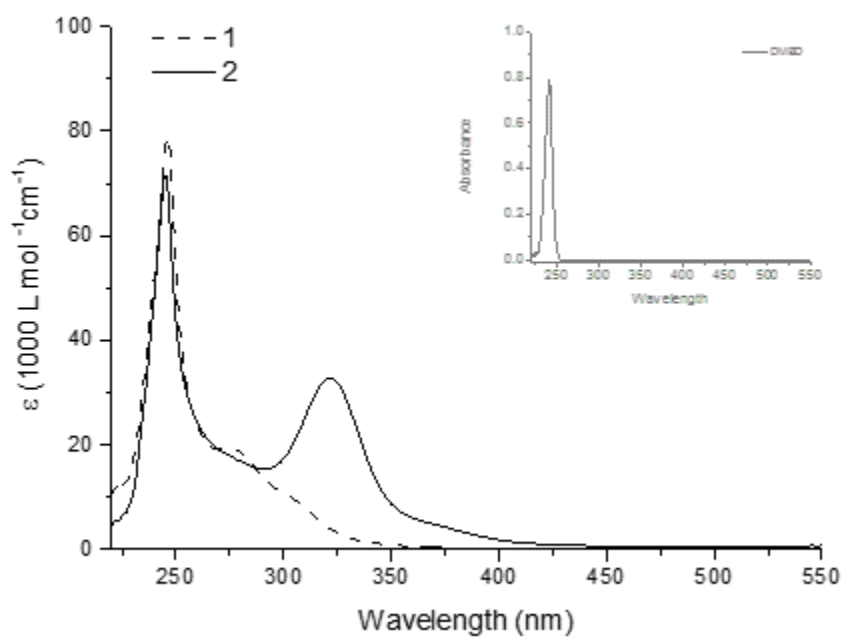


Figure 49. Absorption spectra of **42** (---1) and **43** (—2) in CH₂Cl₂ with DMBD (0.707 mM). The inset shows the absorption spectrum of pure DMBD (0.707 mM) in CH₂Cl₂.

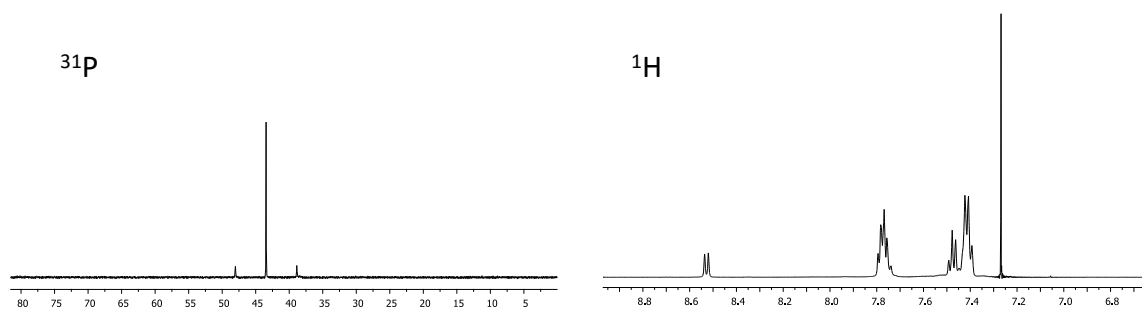


Figure 50. ^{31}P NMR and ^1H NMR spectra of **43** after heating at 70 °C (solid state thermal stability test).

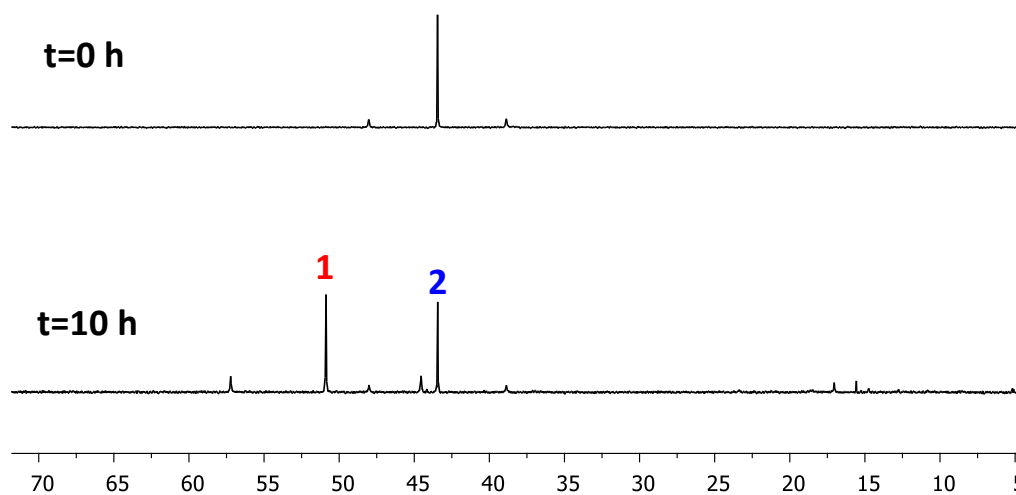


Figure 51. ^{31}P NMR spectrum of **43** after solid-state photolysis in a closed system in the presence of a sodium strip.

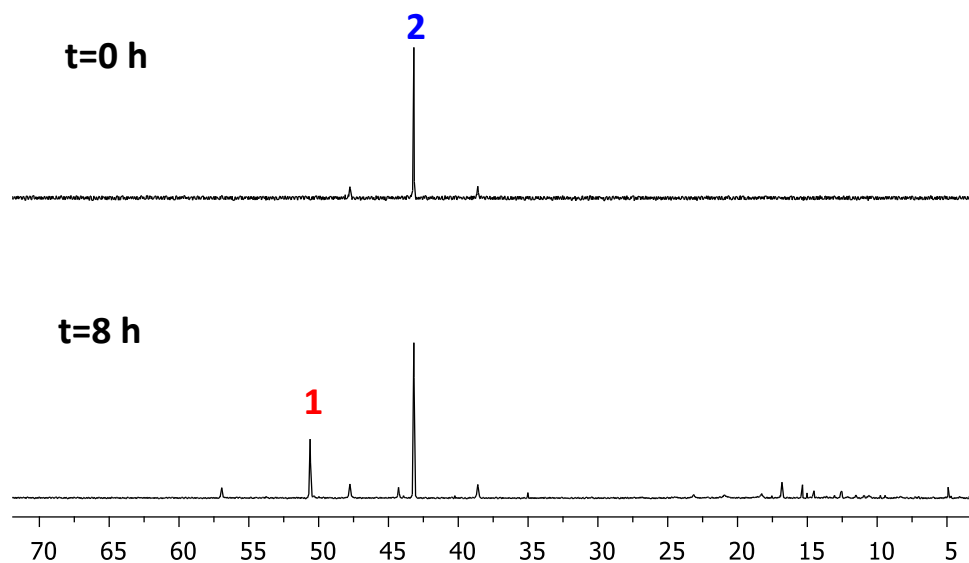


Figure 52. ^{31}P NMR spectrum after solid-state photolysis of **43**. For this experiment, crystals of complex **43** (free of interstitial solvents) were dissolved in CH_2Cl_2 and transferred to the cuvette. Evaporation of the CH_2Cl_2 resulted in the deposition of a film which was dried thoroughly under vacuum for 1 h prior and irradiated for 8 hours using a Xe lamp. The films obtained from CH_2Cl_2 tend to be heterogenous with large crystalline particles. The heterogeneity of these films affects the reaction and lead to higher concentrations of decomposition products. The best films are obtained from THF.

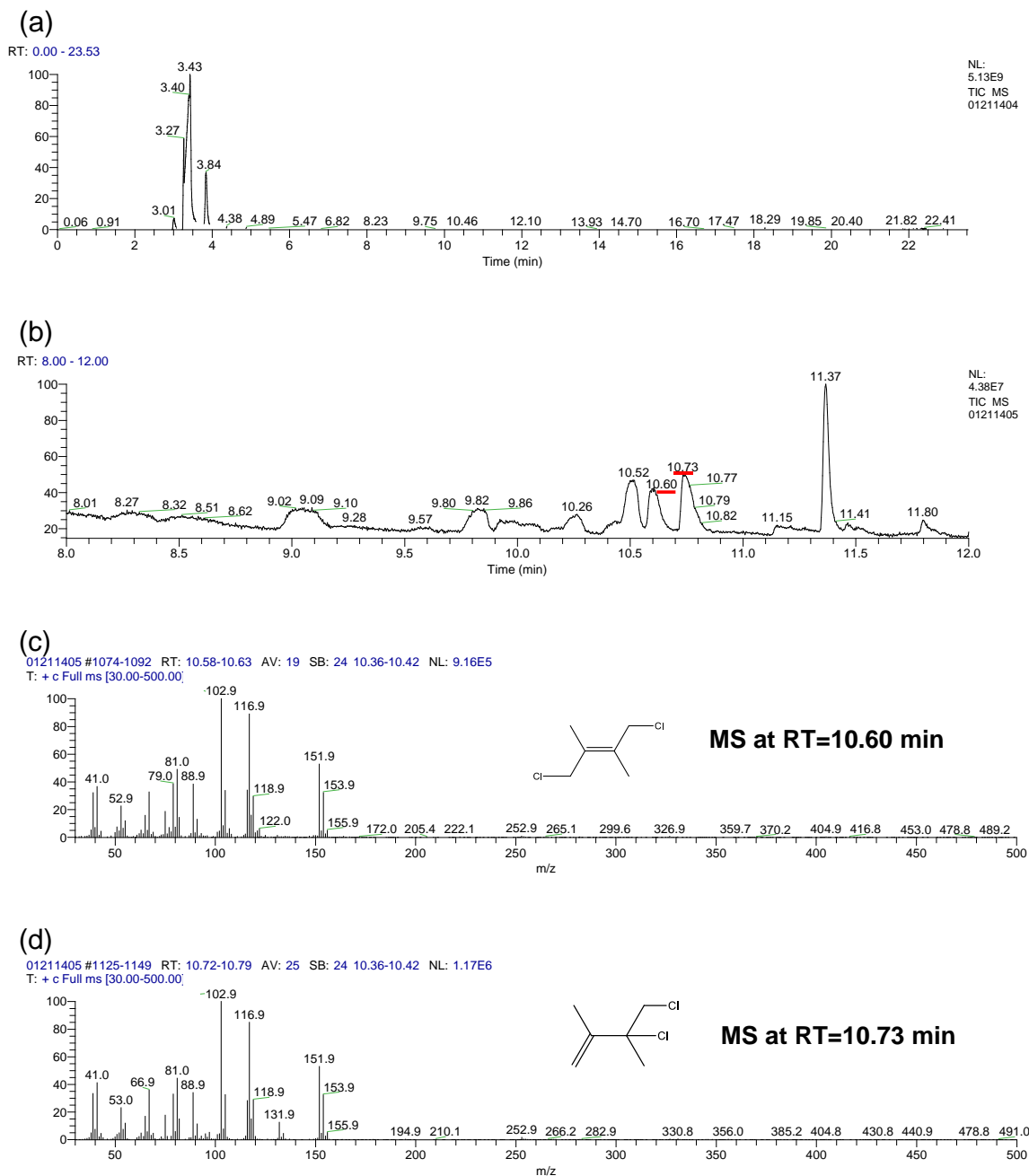


Figure 53. GC-MS analysis of the photolyzed solution of **43** in the presence of DMBD showing the formation of DMBD“Cl₂”. (a) Total GC-MS chromatogram from 0 min to 23 min. (b) Extracted GC-MS chromatogram from 8 min to 12 min. (c) and (d), Mass spectra of the DMBD“Cl₂” species with retention times of 10.60 min and 10.73 min.

Table 1. Selected bond lengths (Å) and angles (°) for complexes **42** and **43** as determined crystallographically and optimized computationally.

| | 42 | | 43 | |
|--------------------|--------------|------------|--------------|------------|
| | X-Ray | DFT | X-Ray | DFT |
| Sb-Pt | 2.4407(5) | 2.5089 | 2.560(2) | 2.6163 |
| Sb-Cl ^a | 2.494(2) | 2.5089 | 2.401(6) | 2.4443 |
| Pt-P ^a | 2.300(1) | 2.3214 | 2.3569(6) | 2.3880 |
| Pt-Cl ^b | 2.349(1) | 2.3931 | 2.4405(6) | 2.4804 |
| Cl-Sb-Cl | 153.24(5) | 139.86 | 118.67(2) | 112.22 |
| Sb-Pt-Cl | 175.25(3) | 179.99 | 178.99(1) | 180.00 |
| P-Pt-P | 169.86(5) | 173.35 | 174.83(2) | 178.51 |

^a An average value.

^b The platinum-bound chloride ligand trans from antimony

Table 2. TD-DFT calculation output showing the nature of the low energy excitations for **43**.

| Excitations ^a | Energy | Oscillator strength | MO→MO transition ^b | Contributions |
|--------------------------|--------------------------|---------------------|-------------------------------|---------------|
| E_a | 3.6331 eV (341.27 nm) | 0.1617 | 187→201 | 0.12039 |
| | | | 188→201 | -0.13975 |
| | | | 190→201 | -0.23380 |
| | | | 190→202 | 0.13232 |
| | | | 191→201 | 0.17455 |
| | | | 191→202 | -0.16884 |
| | | | 193→201 | -0.19148 |
| | | | 196→201 | 0.14029 |
| | | | 196→202 | -0.16641 |
| | | | 200→202 | 0.46813 |

Table 2 Continued.

| Excitations ^a | Energy | Oscillator strength | MO→MO transition ^b | Contributions |
|--------------------------|--------------------------|---------------------|-------------------------------|---------------|
| E_b | 3.9468 eV (314.14 nm) | 0.1252 | 187→201 | 0.23814 |
| | | | 187→202 | -0.14590 |
| | | | 188→201 | 0.27785 |
| | | | 190→202 | -0.18051 |
| | | | 191→202 | 0.10587 |
| | | | 196→202 | 0.34958 |
| | | | 197→202 | -0.32301 |
| | | | 200→202 | 0.20520 |

^a The excitations labeled as E_a and E_b are the main contributors to the low-energy absorption band (see Figure 32).

^b 201 = LUMO, 202 = LUMO + 1.

CHAPTER III

**TELLUROETHER TO TELLUROXIDE CONVERSION IN THE COORDINATION
SPHERE OF A METAL: OXIDATION INDUCED UMPOLUNG OF A TE-AU
BOND***

3.1 Introduction

While gold combines with tellurium to form a variety of binary minerals,¹⁸⁴ the chemistry of organotellurium gold species is remarkably underdeveloped and largely limited to a few gold tellurolates (RTe^-) derivatives in which the R-Te unit can act as a terminal or bridging ligand.¹⁸⁵⁻¹⁹⁰ Another interesting class of gold tellurium species are polyaurated telluronium cations of general formula $[(\text{R}_3\text{PAu})_3\text{Te}]^+$ which have been obtained by reaction of disilyltelluroether with $[(\text{R}_3\text{PAu})_3\text{O}]^+$.¹⁹¹ A much less well documented class of compounds are telluroether-gold complexes which have never been isolated. This phenomenon lies in marked contrast to the lighter chalcogen analogues (R_2S and R_2Se) which are frequently reported as donor ligands for gold(I) centers.¹⁹²⁻¹⁹⁴ To the best of our knowledge, Me_2TeAuBr constitutes the only reported example of a gold-telluroether complex.¹⁹⁵ This complex was observed in solution but it was not isolated.

As part of our exploratory interest in the chemistry of redox active heavy main group ligands,^{86, 113, 116, 144, 196-197} we have now decided to investigate the synthesis and oxidation of gold telluroether complexes. In this paper, we report the synthesis and isolation of a gold

* Reprinted in part with permission from Yang, H.; Lin, T.-P.; Gabbai, F. P. *Organometallics*. **2014**, 33, 4368. Copyright 2014 American Chemical Society. Complexes 44 and [45]Cl were first synthesized and characterized by Dr. T.-P. Lin.

telluroether complex. We also report that this complex can be oxidized into the corresponding telluroxide derivative without dissociation of the gold atom.

3.2 Synthesis and characterization of telluroether-gold complexes

In a first attempt to isolate a telluroether-gold complex, Ph₂Te was mixed with (tht)AuCl (tht = tetrahydrothiophene) in dry CH₂Cl₂ at ambient temperature in the absence of air (Figure 54). This reaction can be conveniently monitored by ¹²⁵Te NMR spectroscopy which indicates the instantaneous formation of a new species resonating at 909 ppm, a chemical shift more downfield than that of Ph₂Te (688 ppm).¹⁹⁸ While it is tempting to assign the product as the coordination complex Ph₂TeAuCl, we noticed the concomitant formation of metallic gold on the inner surface of the flask. In turn, the product is identified as Ph₂TeCl₂.¹⁹⁹ Upon optimizing the reaction by adding 2 equivalent of (tht)AuCl, Ph₂TeCl₂ was isolated in 96% yield. The above reaction demonstrates that telluroethers may act as reducing reagents toward gold(I) species. This redox reaction, albeit never documented,²⁰⁰ may be responsible for the fact that gold-telluroether complexes have not been previously reported.

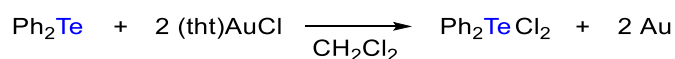


Figure 54. Reaction of Ph₂Te with (tht)AuCl.

Next, we speculated that the coordination of a telluroether to gold could be supported by the presence of ancillary ligands.²⁰¹⁻²⁰² With this in mind, we turned our attention to (*o*-(Ph₂P)C₆H₄)₂Te (hereafter denoted as **L**^{TeP2}), a ligand that we have recently described and used in divalent and tetravalent platinum complexes.¹¹⁶ This telluroether ligand features two

phosphine arms which, we envisioned, could help stabilize the gold(I) center and prevent reduction. The ligand L^{TeP2} was allowed to react with (tht)AuCl in CH_2Cl_2 (Figure 55). Remarkably, this reaction proceeds cleanly to afford complex **44** as a light yellow solid. Complex **44** has been characterized by elemental analysis as well as ESI mass spectrometry (m/z for $[M-Cl]^+$: 849.0371). Using a sample whose purity was confirmed by elemental analysis, we attempted to measure the ^{31}P NMR spectrum of **44** in CD_2Cl_2 . The room temperature spectrum was surprisingly unresolved with broad features centered between 30 and 65 ppm (Figure 56). Sharper resonances were observed upon cooling to $-80\text{ }^\circ\text{C}$ but the multitude of resonances observed at this temperature could not be rationalized on the basis of a simple fluxional behavior. To rule out a possible decomposition of the complex during the NMR measurement, we treated the NMR tube containing the solution of **1** in CD_2Cl_2 with an equivalent of PPh_3 . Addition of the phosphine resulted in the quantitative formation of a new species identified as $[45][Cl]$ and characterized by two well resolved ^{31}P resonances (Figure 55 and Figure 56). The use of $CDCl_3$, THF, and CD_3CN did not afford a better spectral resolution and no ^{125}Te resonance could be detected, even at low temperature. These results, together with the observation of broad 1H and ^{13}C resonances, suggest that the solution structure of **44** is affected by a complex fluxional process that we are unable to rationalize. Although a clear understanding of the solution structure of this complex could not be derived from the NMR studies, we observed that slow diffusion of Et_2O into a THF solution of **44** at $-30\text{ }^\circ\text{C}$ affords yellow crystals of the complex as a bis(THF) solvate.

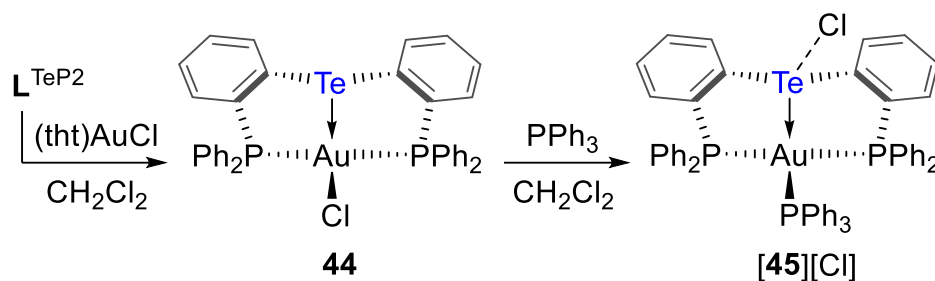


Figure 55. Synthesis of **44** and **[45][Cl]**.

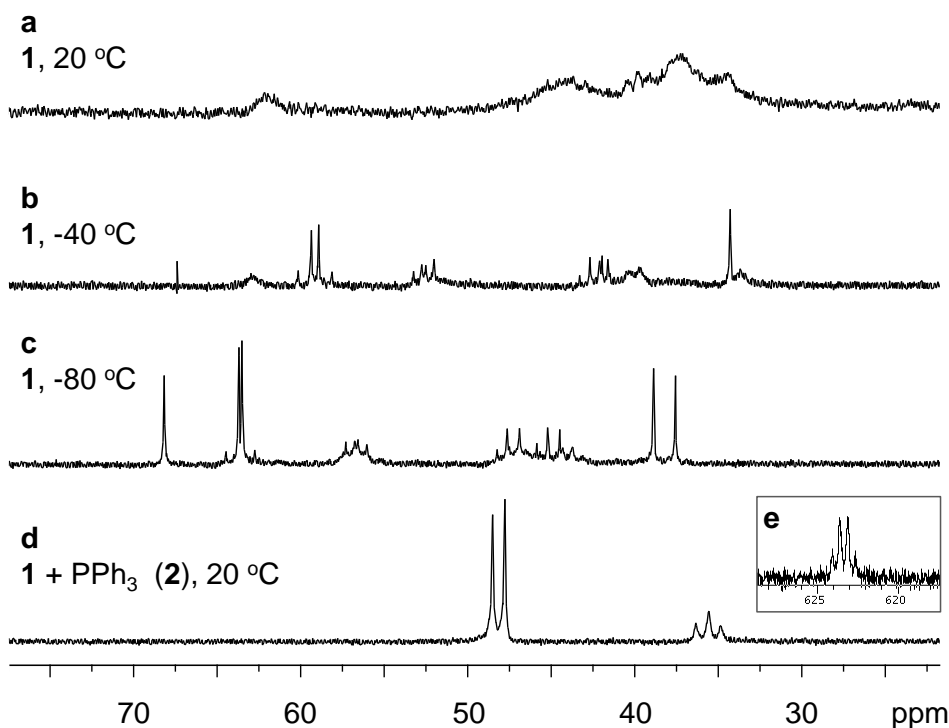


Figure 56. (a) ³¹P NMR spectrum of **44** in CD₂Cl₂ at 20 °C (a), -40 °C (b), and -80 °C (c). Spectrum d was obtained by adding one equivalent of PPh₃ to the NMR tube used to measure spectra a-c. This spectrum corresponds to that of **[45][Cl]**. Spectrum e in the bottom right inset shows the ¹²⁵Te NMR spectrum of **[45][Cl]**.

As indicated by a single crystal X-ray diffraction analysis, the solid state structure of **44** shows coordination of the L^{TeP2} ligand to the AuCl unit. Interestingly, with the sum of the

P-Au-P and P-Au-Cl angles equal to 358.75° , the two phosphine arms and the chloride anion are arranged around the gold atom in a trigonal planar fashion. The tellurium atom is positioned along a direction that is essentially perpendicular to the P-Au bonds (P(2)-Au-Te 89.05(16), P(1)-Au-Te 86.56(15)) leading to a trigonal pyramidal geometry at gold. Another important structural aspect of this complex is the long Te-Au distance of 2.874(4) Å which exceeds the sum of covalent radii of the two elements (2.60-2.74 Å)²⁰³⁻²⁰⁴ by 4.7-9.5%. This distance is also significantly longer than that observed in gold telluroate derivatives. Taken collectively, the coordination geometry of the gold center as well as the long Te-Au separation indicates the formation of a relatively weak Te→Au coordination bond. This conclusion is consistent with the observation that the Au-Cl bond distance in **44** (2.554(5) Å) is close to that measured in the three-coordinate gold complex (Ph₃P)₂AuCl (2.54 Å)²⁰⁵ and significantly shorter than that in the four-coordinate gold complex (Ph₃P)₃AuCl (2.71 Å).²⁰⁶

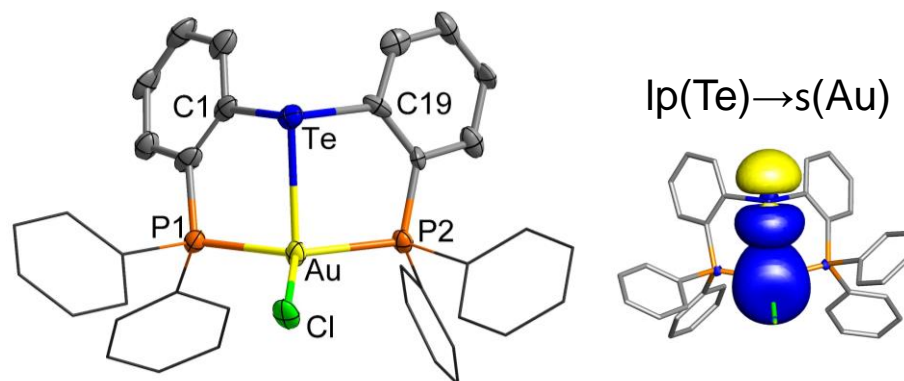


Figure 57. Left: Solid state structure of **44**. Thermal ellipsoids are drawn at the 50% probability level. Phenyl groups are drawn in wireframe. Hydrogen atoms and solvent molecules are omitted for clarity. Selected bond lengths (Å) and angles (°): Au-Te 2.874(4), Au-Cl 2.554(5), Au-P(2) 2.322(5), Au-P(1) 2.328(5), Te-C(19) 2.161(18), Te-C(1) 2.189(19); P(2)-Au-P(1) 134.40(18), P(2)-Au-Cl 113.28(17), P(1)-Au-Cl 111.07(16), P(2)-Au-Te 89.05(16), P(1)-Au-Te 86.56(15), Cl-Au-Te 108.75(17), C(19)-Te-C(1) 93.3(6), C(19)-Te-Au 88.3(5), C(1)-Te-Au 87.6(5). Right: NBO plot (isovalue = 0.05) showing the lp(Te)→s(Au) donor-acceptor interaction in **44**. Hydrogen atoms are omitted for clarity.

Complex [45][Cl] observed by NMR spectroscopy upon treatment of 44 with PPh₃ has also been isolated (Figure 55). The cationic complex [45]⁺ present in this salt is characterized by two coupled ³¹P resonances (Figure 56d) at 35.6 ppm (triplet, ²J_{P-P} = 122.5 Hz) and 48.1 ppm (doublet, ²J_{P-P} = 122.5 Hz) flanked by ¹²⁵Te satellites (²J_{Te-P} = 55.4 Hz). The ¹²⁵Te resonance of [45][Cl] appears as a *pseudo* quartet indicating an accidental degeneracy of the coupling constant between the tellurium nucleus and the two different types of phosphorus nuclei (²J_{Te-P} = 55.4 Hz) (Figure 56e). The ¹²⁵Te chemical shift of [45][Cl] (623 ppm) is more downfield than that of L^{TeP2} (580 ppm, ³J_{Te-P} = 416 Hz), in accordance with the formation of a Te→Au dative bond. As confirmed by X-ray crystallography, the L^{TeP2} and Ph₃P ligands present in [45][Cl] are coordinated to the gold atom. Coordination of the L^{TeP2} to the gold center results in a Te-Au bond distance of 2.9373(15) Å which is slightly elongated when compared to that in 44 (2.874(4) Å). The constraints imposed by the rigidity of the L^{TeP2} ligand as well as the bulk of the Ph₃P ligand lead to a distorted tetrahedral geometry around the gold atom. Of note is the sum of the P-Au-P angles of 354.65° which indicates that the three primary phosphine ligands are arranged around the gold center to generate a slightly pyramidal AuP₃ unit. The gold atom of this unit is capped by the tellurium ligand leading to somewhat acute P(1)-Au-Te and P(2)-Au-Te angles of 82.42(6)° and (77.71(6)° angles and a wide P(3)-Au-Te angle of 129.65(6)°. The chloride anion is weakly bound to the tellurium center via a long interaction of 3.113(3) Å.

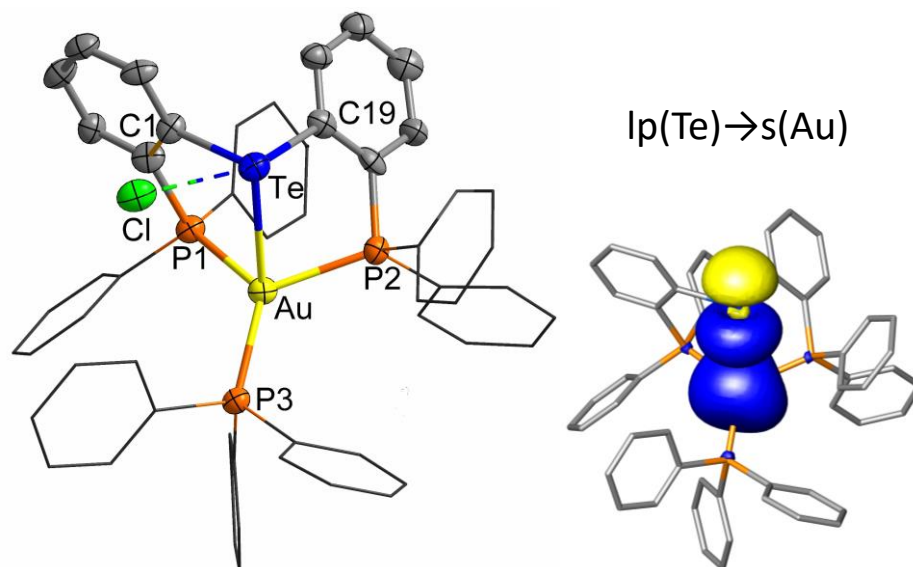


Figure 58. Left: Solid state structure of **[45][Cl]**. Thermal ellipsoids are drawn at the 50% probability level. Phenyl groups are drawn in wireframe. Hydrogen atoms and solvent molecules are omitted for clarity. Selected bond lengths (Å) and angles (°): Au-Te 2.9373(15), Au-P(1) 2.396(3), Au-P(2) 2.404(3), Au-P(3) 2.334(3), Te-C(1) 2.118(9), Te-C(19) 2.180(9), Te-Cl 3.113(3); P(3)-Au-Te 129.65(6), P(3)-Au-P(1) 120.22(9), P(3)-Au-P(2) 122.33(8), P(1)-Au-P(2) 112.10(9), P(1)-Au-Te 82.42(6), P(2)-Au-Te 77.71(6), Cl-Te-C(19) 165.4(3), C(1)-Te-C(19) 89.8(3), C(1)-Te-Au 94.3(2), C(19)-Te-Au 85.8(3). Right: NBO plot (isovalue = 0.05) showing the lp(Te)→s(Au) donor-acceptor interaction in **[45]⁺**. Hydrogen atoms are omitted for clarity.

3.3 Bonding analysis of the Te→Au interaction

When compared to documented gold-tellurolates¹⁸⁵⁻¹⁹⁰ which possess Au-Te bonds in the range of the sum of the covalent radii of the two elements (2.60-2.74 Å),²⁰³⁻²⁰⁴ the Te-Au bond distances of the gold telluroether complexes described in this paper are significantly longer (2.874(4) Å for **44** and 2.937(2) Å for **[45][Cl]**). To probe the nature of this bond, we decided to analyze these two compounds using the Natural Bond Orbital (NBO) method. The structure of the complexes was first optimized with the Gaussian program²⁰⁷ using DFT methods (functional: BP86,¹⁵¹⁻¹⁵² mixed basis set: Te/Au: cc-pVTZ;^{153, 208-209} The optimized geometries are in good agreement with those experimentally determined (Table 3) with the

largest deviation observed for the Te-Au bonds. We believe that these deviations originate from the inability of DFT methods to account for dispersion forces. Such forces are especially important for heavy nuclei such as gold, which is affected by intense relativistic effects.²¹⁰⁻²¹² An NBO bonding analysis was subsequently carried out at the optimized geometry of each complex.²¹³ For both complexes, the Te-Au bond is described as a donor-acceptor interaction involving a tellurium lone pair of 5p-character and the gold 6s orbital as the accepting orbital (Figure 57 and Figure 58). The second-order stabilization energy of 38.3 and 50.7 kcal/mol calculated for the lp(Te)→s(Au) interactions in **44** and **[45]⁺**, respectively, show that coordination of tellurium to gold is indeed stabilizing. These calculations also indicate that the Te→Au coordination bond in **[45]⁺** is stronger than in **44**, a result assigned to the cationic nature of the gold center in **[45]⁺**.

3.4 Telluroether to telluroxide conversion in the coordination sphere of gold

Since both tellurium and gold can engage in a two electron redox couples (II/IV for and I/III for Au), we decided to complete this work by testing the behaviour of **44** under oxidative conditions. Treatment of **44** with PhICl₂ in CH₂Cl₂ resulted in a complex mixture of products, the identity of which could not be established. By contrast, we observed that **44** cleanly reacts with 1 eq. of H₂O₂ in CH₂Cl₂ or THF to afford the bis(phosphine)telluroxide gold chloride complex **46** (Figure 59). The bis(phosphine)telluroxide ligand present in **46** is an heavy main group analog of *o*-(Ph₂P)C₆H₄)₂S=O, a ligand which has been incorporated in group 9 and 10 transition metal complexes.²¹⁴ We also note a parallel with complexes containing the (*o*-(iPr₂P)C₆H₄)₂P(=O)Ph ligand recently described by Bourissou.²¹⁵⁻²¹⁶

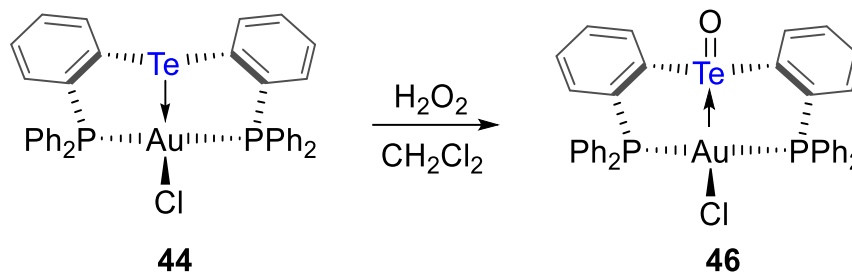


Figure 59. Synthesis of complex **46**.

Table 3. Selected bond lengths (Å) for complexes **44**, **[45]⁺** and **46** as determined crystallographically and computationally.

| | 44 | | [45]⁺ | | 46 | |
|---------------------|-----------|------------------|-------------------------|------------------|-----------|------------------|
| | X-Ray | DFT ^a | X-Ray | DFT ^a | X-Ray | DFT ^a |
| Te-Au | 2.874(4) | 3.073 | 2.937(2) | 3.085 | 2.986(1) | 3.106 |
| Te-C ^b | 2.18(4) | 2.168 | 2.15(3) | 2.152 | 2.16(2) | 2.216 |
| Au-P ^b | 2.33(1) | 2.358 | 2.38(1) | 2.468 | 2.31(1) | 2.355 |
| Au-Cl | 2.554(5) | 2.528 | - | - | 2.524(2) | 2.530 |
| Te-O | - | - | - | - | 1.857(3) | 1.933 |
| Au-PPh ₃ | - | - | 2.334(3) | 2.399 | - | - |

^a BP86/cc-pVTZ(Te/Au), 6-31g(d')(P/Cl:), 6-31g(C/H). ^bAverage values.

Complex **46** has been characterized by ³¹P, ¹H and ¹³C NMR spectroscopy. The ³¹P NMR spectrum shows a single resonance at 40.6 ppm, with ¹²⁵Te satellites (²J_{Te-P} = 290 Hz). The ¹²⁵Te NMR resonance gives rise to a broad, unresolved signal at 1074 ppm (w_{1/2} = 1072 Hz), a chemical shift close to that reported for Ph₂Te=O (1035 ppm).²¹⁷ A single crystal X-ray diffraction analysis confirms conversion of **44** into the corresponding telluroxide derivative **46**, without dissociation of the gold atom. The Te-Au bond of 2.9864(5) Å in **3** is slightly elongated when compared to **44** (2.874(4) Å), signaling a possible change in the nature of the Te-Au interaction. The coordination sphere of the tellurium center is completed by the two *ortho*-phenylene groups as well as an oxygen atom provided by a neighboring molecule. This

last interaction leads to the formation of centrosymmetrical dimers organized around a Te₂O₂ ring. As found in the dimer of Ph₂Te=O,²¹⁸ this Te₂O₂ ring is unsymmetrical with a short intramolecular Te=O bond of 1.857(3) Å and a long Te---O intermolecular contact of (2.508(5) Å). The resulting coordination geometry at tellurium is that of a square pyramid with the gold atom positioned trans from the oxo ligand (Au-Te-O = 175.91°). Although the gold atom remains coordinated to its three primary ligand in an essentially trigonal planar fashion ($\angle P(1)\text{-Au-P}(2) + \angle P(1)\text{-Au-Cl} + \angle P(2)\text{-Au-Cl} = 359.2^\circ$), we note that the Te–Au–Cl angle in **46** (117.05(5)°) is larger than in **44** (108.75(17)°). The trans location of the gold atom with respect to the tellurium-bound oxo ligand and the increase noted in the Te–Au–Cl angle suggest the presence of a donor acceptor interaction involving the gold atom as a donor and the tellurium as the acceptor. To probe this unusual Au→Te interaction, we optimized the structure of dimeric **46** using DFT methods (functional: BP86;¹⁵¹⁻¹⁵² mixed basis set: Te/Au: cc-pVTZ;^{153, 208} P/Cl: 6-31g(d'); C/H: 6-31g). NBO analysis carried out at the optimized geometry shows that instead of a Te→Au coordination bond as found in **44** and [45]⁺, **46** possesses a Au→Te interaction involving a d orbital from gold as the donor and the σ*(Te=O) orbital as the acceptor, with a second-order stabilization energy (E^2) of 9.0 kcal/mol. This stabilization energy indicates that the Au→Te interaction of **46** is weaker than the Te→Au bonds observed in **44** and [45]⁺ ($E^2 = 38.3$ kcal/mol for **44** and 50.7 kcal/mol for [45]⁺). More importantly, these results show that oxidation of the tellurium center switches its ligand type from L-type in **44** to Z-type in **46**.^{14, 21, 156-167} The σ-acidic properties of the tellurium atom in **46** result in an umpolung of the Te-Au bond. These σ-acidic properties are also reminiscent of those observed in related late transition metal complexes featuring hypervalent tellurium

ligands.^{116, 219-220} A parallel can also be drawn between the σ -acidic properties of the telluroxide unit in **46** and the documented Z-type behaviour of the SO_2 ligand^{14, 16}

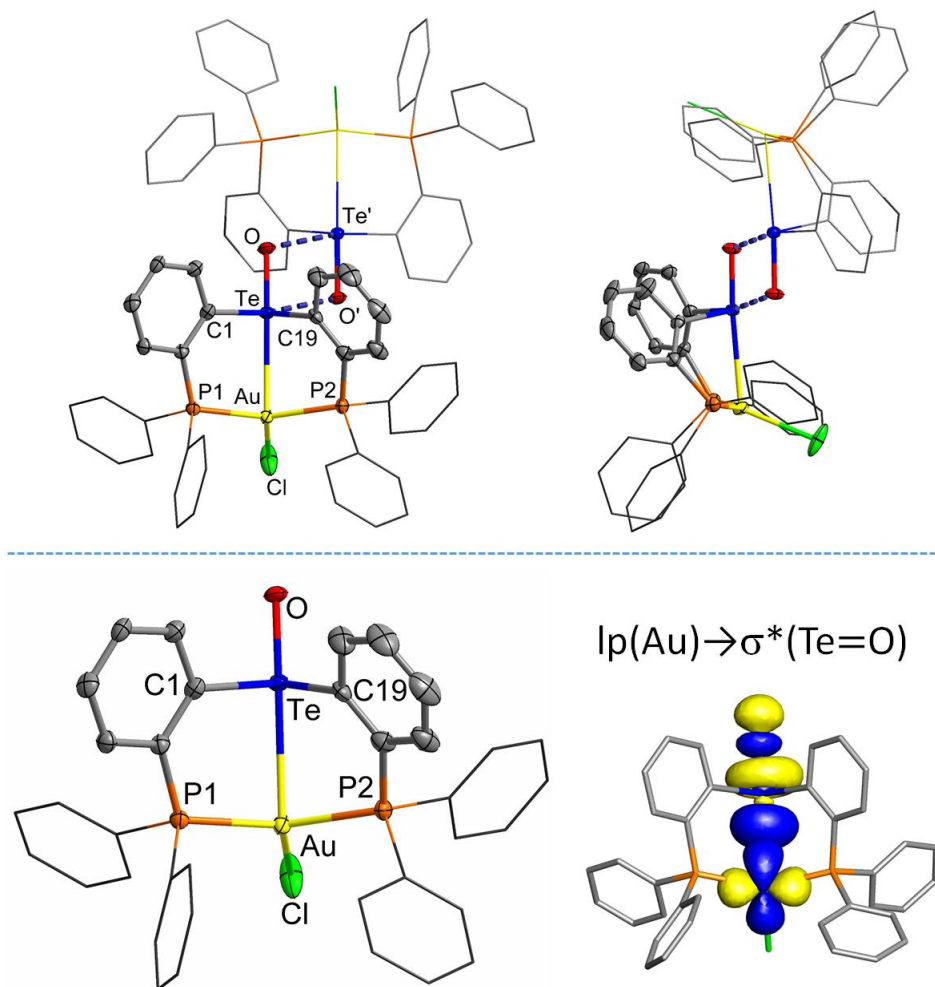


Figure 60. Top and bottom left: Solid state structure of **46** with thermal ellipsoids drawn at the 50% probability level. The phenyl groups are drawn in wireframe. Hydrogen atoms and solvent molecules are omitted for clarity. The top view shows the dimer under two perpendicular orientations. The bottom left view shows the monomeric unit. Selected bond lengths (\AA) and angles ($^\circ$): Au-Te 2.9864(5), Te-O: 1.857(3), Au-Cl 2.524(2), Au-P(2) 2.301(2), Au-P(1) 2.318(2), Te-C(19) 2.167(6), Te-C(1) 2.154(7); Au-Te-O 175.9(1), P(2)-Au-P(1) 136.71(6), P(2)-Au-Cl 113.90(7), P(1)-Au-Cl 108.59(7), P(2)-Au-Te 85.29(4), P(1)-Au-Te 82.74(4), Cl-Au-Te 117.05(5), C(19)-Te-C(1) 92.5(2), C(19)-Te-Au 88.9(1), C(1)-Te-Au 85.6(2). Bottom right: NBO plot of **46** (monomer) (isovalue = 0.05) showing the $\text{lp}(\text{Au}) \rightarrow \sigma^*(\text{Te}=\text{O})$ donor-acceptor interaction in **46**. Hydrogen atoms are omitted for clarity.

3.5 Conclusion

Complexes **44** and **[45]Cl** constitute the first isolated examples of gold-telluroether complexes. The Te→Au coordination bonds present in these complexes is supported by two ancillary phosphine ligands which immobilize the gold atom in proximity to the tellurium atom. Despite the inherent lability of the Te-Au bond present in these complexes, we observe that **44** is cleanly oxidized into **46** when treated with H₂O₂. This oxidation, which does not induce dissociation of the gold unit, results in a conversion of the telluroether functionality into a telluroxide functionality. The latter behaves as a Z-type ligand and engages the gold atom of complex **46** into a Au→Te interaction.

3.6 Experimental

General considerations. L^{TeP2} and (tht)AuCl were prepared according to the reported procedures.^{116, 221} Solvents were dried by passing through an alumina column (CH₂Cl₂ and Et₂O). All other solvents were used as received. Ph₃P was purchased from Aldrich and used as received. Ambient temperature NMR spectra were recorded on a Varian Unity Inova 400 FT NMR (399.59 MHz for ¹H, 100.45 MHz for ¹³C, 161.74 MHz for ³¹P, 126.14 MHz for ¹²⁵Te) spectrometer. Chemical shifts (δ) are given in ppm and are referenced against residual solvent signals (¹H, ¹³C) or external Ph₃P (³¹P) and Ph₂Te₂ (¹²⁵Te). Elemental analyses were performed at Atlantic Microlab (Norcross, GA). Electrospray mass spectra were obtained with a SciexQstarr Pulsar and a Protana Nanospray ion source.

Reaction of Ph₂Te and (tht)AuCl. To a CH₂Cl₂ solution (0.5 mL) of Ph₂Te (9.4 mg, 0.033 mmol) was added a CH₂Cl₂ solution (0.5 mL) of (tht)AuCl (21.4 mg, 0.066 mmol) at ambient

temperature in the absence of air. After stirring for two hours, the colorless solution was separated from metallic gold by filtration. Removal of the solvent under reduced pressure afforded a white solid of Ph_2TeCl_2 (11.3 mg, 96%). This product was identified on the basis of its ^{125}Te NMR resonance at 909 ppm in CH_2Cl_2 which is close to the value of 917 ppm reported in CDCl_3 .¹⁹⁹

Synthesis of 44. To a CH_2Cl_2 solution (2 mL) of L^{TeP_2} (190 mg, 0.292 mmol) was added a CH_2Cl_2 solution (2 mL) of $(\text{tht})\text{AuCl}$ (93.7 mg, 0.292 mmol) at ambient temperature. After stirring for 12 hours, Et_2O (15 mL) was added to the mixture, resulting in a yellow precipitate which was collected by filtration. The resulting solid was dried under vacuum to afford **44** as a yellow solid (235 mg, 91% yield). Yellow crystals of **44**-2THF suitable for single crystal diffraction analysis were obtained by slowly diffusing Et_2O into a THF solution of **44** at -30°C . ^1H NMR (399.59 MHz; CDCl_3): δ 6.5-7.8 (broad). $^{13}\text{C}\{^1\text{H}\}$ NMR (100.45 MHz; CDCl_3): δ 129.14 (bs), 132.58 (bs), 134.04 (bs), 134.76 (bs), $^{31}\text{P}\{^1\text{H}\}$ NMR (161.74 MHz; CDCl_3): δ 34.9 (bs), 37.0 (bs), 42.1 (bs), 62.8 (bs). The ^{125}Te NMR resonance of this compound could not be detected. HRMS (ESI⁺) calcd for $[\mathbf{44}\text{-Cl}]^+$ ($\text{C}_{36}\text{H}_{28}\text{AuP}_2\text{Te}^+$): 849.0392, found: 849.0371. Elemental analysis calculated (%) for **44**: C, 48.99; H, 3.20; found C, 49.20; H, 3.90. When the elemental analysis was carried out using **44** recrystallized from THF, the following results are obtained: calculated (%) for **44**-THF: C, 50.32; H, 3.80; found C, 50.31; H, 4.26. These last results show partial loss the two interstitial THF molecules found in the structure of **44**.

Synthesis of [45][Cl]. To a CH₂Cl₂ solution (2 mL) of **44** (100 mg, 0.113 mmol) was added Ph₃P (29.7 mg, 0.113 mmol) at ambient temperature. After stirring for 15 min, Et₂O (15 mL) were added to the mixture, resulting in a light yellow precipitate which was collected by filtration. The resulting solid was dried under vacuum to afford [45][Cl] as a light yellow solid (110 mg, 85% yield). Yellow crystals of [45][Cl]-CH₂Cl₂ suitable for single crystal diffraction analysis were obtained by slowly diffusing Et₂O into a CH₂Cl₂ solution of [45][Cl] at ambient temperature. ¹H NMR (399.59 MHz; CDCl₃): δ 6.69-6.75 (m, 8H), 6.93-7.34 (m, 31H), 7.38 (t, 2H, ³J_{H-H} = 7.57 Hz, ³J_{H-H} = 4.62 Hz), 8.34 (d, 2H, ³J_{H-H} = 7.53 Hz, ³J_{Te-H} = 82.78 Hz). ¹³C{¹H} NMR (100.45 MHz; CDCl₃): δ 126.27 (t, J_{C-P} = 21.68 Hz), 128.81 (d, J_{C-P} = 3.18 Hz), 128.88, 128.92, 130.57, 130.64, 130.85, 131.99, 132.46, 133.05, 133.53 (d, J_{C-P} = 14.28 Hz), 134.99, 140.41 (t, J_{C-P} = 23.74 Hz), 141.51 (t, J_{C-P} = 4.80 Hz). ³¹P{¹H} NMR (161.74 MHz; CDCl₃): δ 35.6 (1P, t, ²J_{P-P} = 122.5 Hz, ²J_{Te-P} = 55.4 Hz), 48.1 (2P, d, ²J_{P-P} = 122.5 Hz, ²J_{Te-P} = 55.4 Hz). ¹²⁵Te{¹H} NMR (126.14 MHz; CDCl₃): δ 623 (pseudo q, ²J_{Te-P} = 55.4 Hz). Elemental analysis calculated (%) for [2][Cl]-CH₂Cl₂: C, 53.72; H, 3.69; found C, 53.21; H, 3.69.

Synthesis of 46. Mixing a THF solution (3 mL) of L^{TeP2} (134 mg, 0.2 mmol) with a THF solution (2 mL) of (tht)AuCl (66 mg, 0.2 mmol) at ambient temperature resulted in the progressive precipitation of complex **44**. After 4 hours, the resulting solution, which contained complex **44** as a yellow precipitate, was treated with an aqueous solution of hydrogen peroxide (30%, 0.1 mL). Bright yellow complex **44** which remained suspended in the solution progressively converted in a pale yellow precipitate. After 20 min of stirring, this precipitate was isolated by filtration and washed with Et₂O (2 × 2 mL). The precipitate was dried under

vacuum to afford **46** as pale yellow powder (165 mg, 89% yield). Light yellowish crystals of **46** were obtained by slow diffusion of Et₂O into a CH₂Cl₂ solution. ¹H NMR (499.42 MHz; CDCl₃): δ = 8.59 (d, 2H, *o*-P(Te)C₆H₄, ³J_{H-H} = 7.49 Hz), 7.85 (q, 4H), 7.75 (t, 2H, *o*-P(Te)C₆H₄, ³J_{H-H} = 7.49 Hz), 7.48–7.57 (m, 16H), 7.43 (t, 2H, *o*-P(Te)C₆H₄, ³J_{H-H} = 7.49 Hz), 7.07 (m, 2H, *o*-P(Te)C₆H₄). ¹³C{¹H} NMR (125.58 MHz; CDCl₃): δ = 134.7 (t, J_{C-P} = 26 Hz), 134.3 (d of t, -C₆H₅, CH), 133.1 (s), 132.5 (s), 131.9 (s), 131.8 (s), 130.7 (t, J_{C-P} = 3.5 Hz), 129.6 (t, -, -C₆H₅, CH, J_{C-P} = 5.7 Hz), 129.3 (t, -, -C₆H₅, CH, J_{C-P} = 5.7 Hz), 129.2 (d, J_{C-P} = 7 Hz). ³¹P{¹H} NMR (202.16 MHz; CDCl₃): δ = 40.6 (s, J_{P-Te} = 290 Hz). ¹²⁵Te{¹H} NMR (126.14 MHz; CDCl₃): 1074 ppm (w_{1/2} = 1072 Hz). Elemental analysis calculated (%) for **46**-CH₂Cl₂ (C₃₇H₃₀AuCl₃OP₂Te): C, 45.18; H, 3.07; found C, 46.90; H, 3.12. These EA results can be reconciled by invoking a 50% loss of CH₂Cl₂. Elemental analysis calculated (%) for **46**-0.5(CH₂Cl₂) (C_{36.5}H₂₉AuCl₂OP₂Te): C, 46.59; H, 3.11. The presence of 0.5 eq. CH₂Cl₂ is confirmed by integration of the ¹H NMR spectrum.

Crystallographic measurements. The crystallographic measurements were performed at 110(2) K using a Bruker APEX-II CCD area detector diffractometer (Mo-K_α radiation, λ = 0.71073 Å). In each case, a specimen of suitable size and quality was selected and mounted onto a nylon loop. The structures were solved by direct methods, which successfully located most of the non-hydrogen atoms. Semi-empirical absorption corrections were applied.²²² Subsequent refinement on *F*² using the SHELX/PC package (version 6.1) allowed location of the remaining non-hydrogen atoms.²²³

Computational details. Complexes **44**, **[45]⁺** and **46** were optimized using the Gaussian program²⁰⁷ with DFT methods (functional: BP86;¹⁵¹⁻¹⁵² mixed basis set: Te/Au: cc-pVTZ;^{153,}²⁰⁸ P/Cl: 6-31g(d'); C/H: 6-31g). The NBO analysis was performed at the same level of theory using the NBO 5.9 program.²¹³ Visualizations of the NBO orbitals were performed using the Jimp 2 program.¹⁷⁹

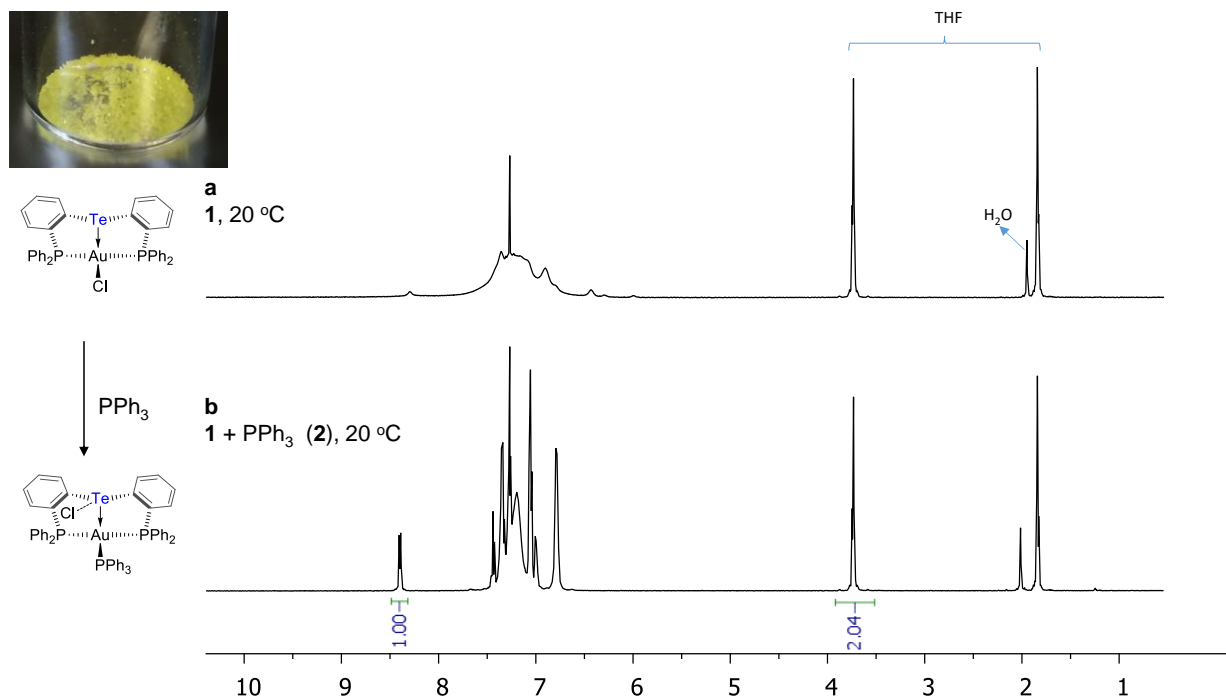


Figure 61. (a) ³¹P spectrum of **44** in CDCl₃ at 20 °C (b) Spectrum was obtained by adding one equivalent of PPh₃ to the NMR tube used to measure spectra (a). This spectrum corresponds to that of **[45][Cl]**. Picture in the top left inset shows the crystals of **44** used for NMR experiment.

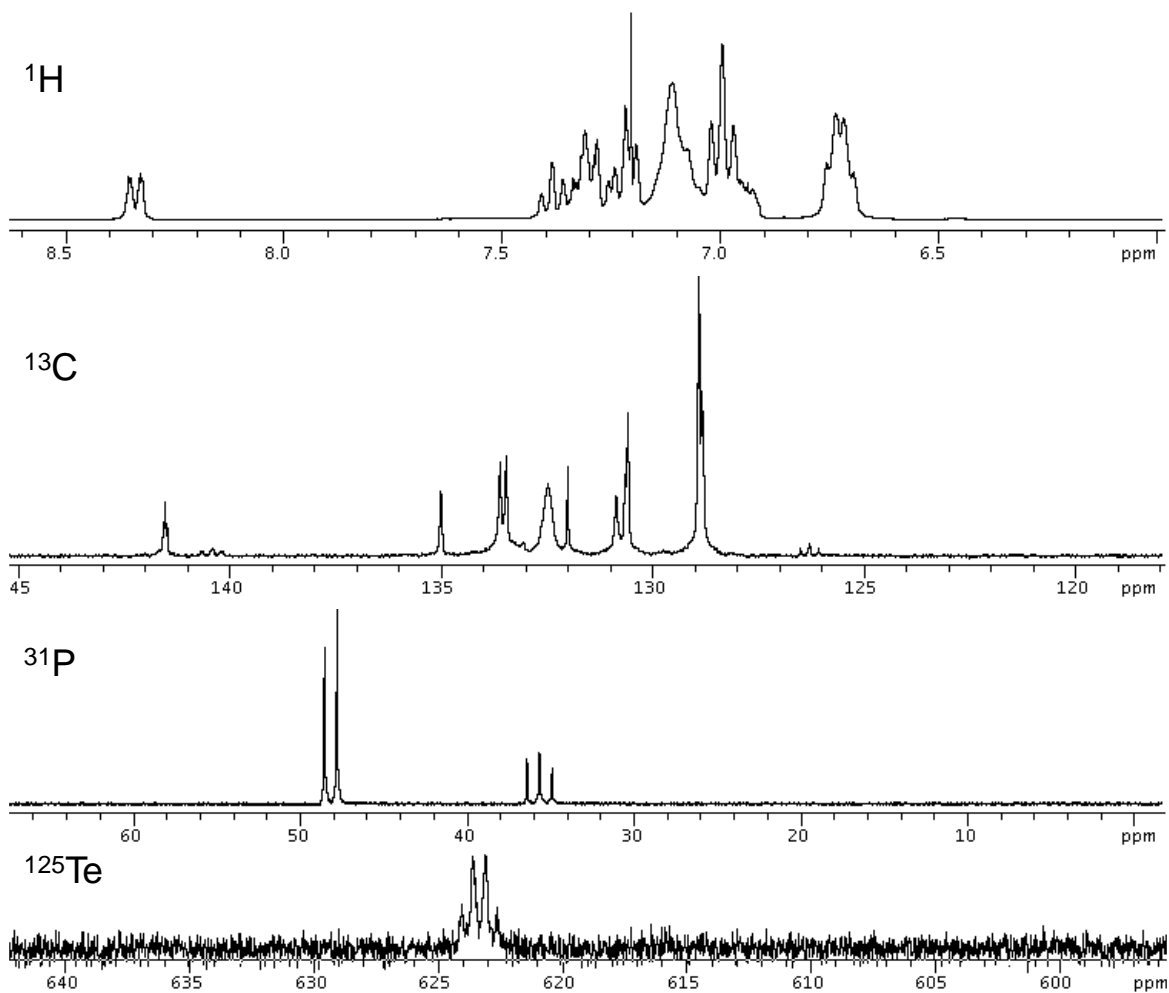


Figure 62. ¹H, ¹³C, ³¹P, and ¹²⁵Te NMR spectra of [45][Cl] at ambient temperature in CDCl₃.

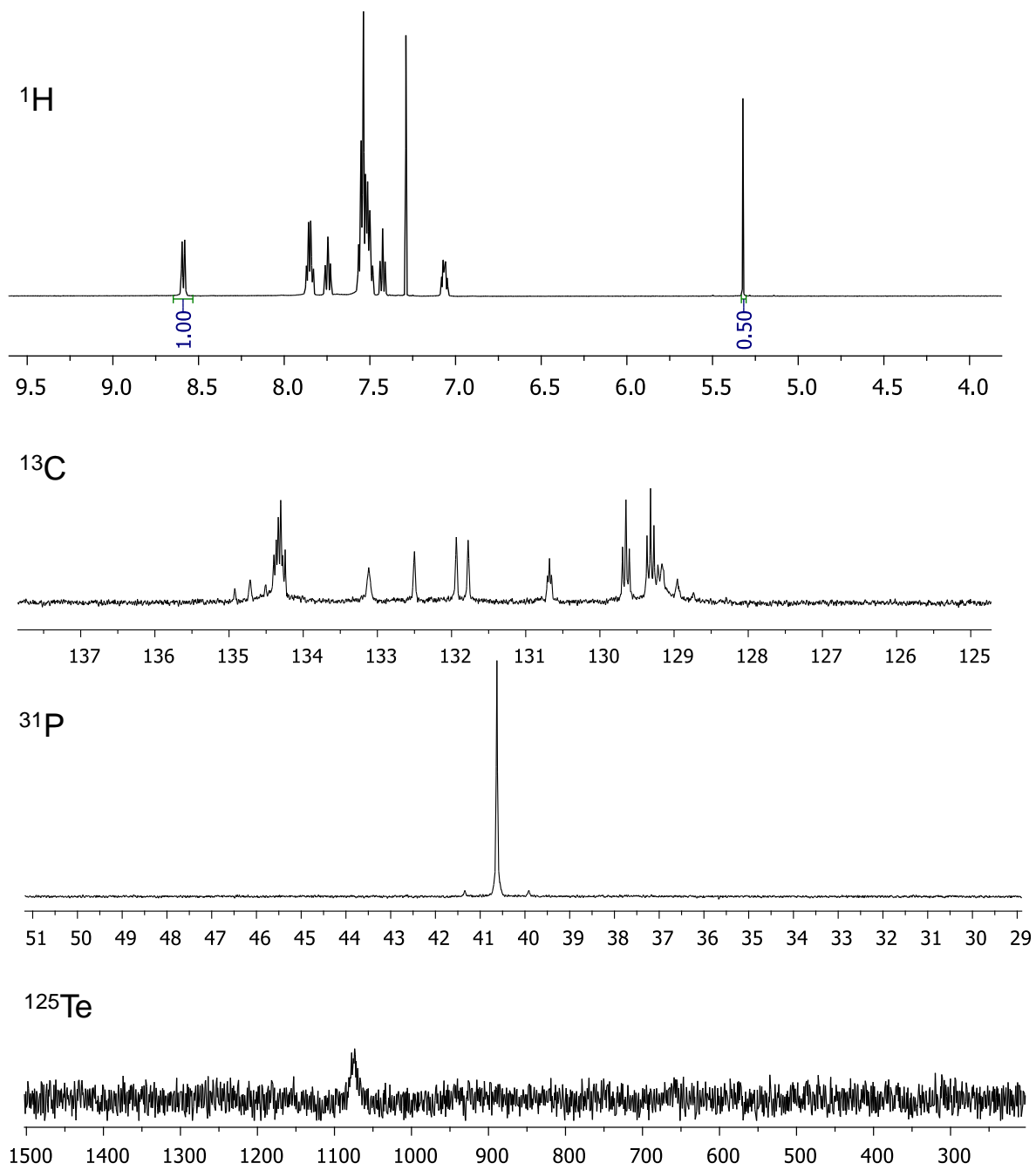


Figure 63. ¹H, ¹³C, ³¹P, and ¹²⁵Te NMR spectra of **46** at ambient temperature in CDCl₃.

CHAPTER IV

ACTIVATION OF A HYDROAMINATION GOLD CATALYST BY OXIDATION OF A REDOX NON-INNOCENT CHLOROSTIBINE Z-LIGAND*

4.1 Introduction

While often regarded as heavy phosphine analogues, stibine ligands possess a number of unusual characteristics, including softer donor properties^{56, 79-81, 84, 224-227} combined with increased accepting properties.⁷⁴⁻⁷⁵ We have also demonstrated that triarylstibine ligands are redox non-innocent and can be converted from L-type (**A**) to Z-type ligands^{14, 21, 156-167} (**B**) via oxidation (Figure 64).^{113, 144, 196, 228} Oxidation proceeds without dissociation of the metal, provided that ancillary ligands are employed. This redox process has been shown to induce an umpolung of the M-Sb bond which switches from Sb→M in the reduced state to M→Sb in the oxidized state.¹⁴⁴ Interestingly, σ -accepting properties are also observed with halostibine ligands (**C**).⁸⁶ In this case, oxidation of the antimony simply increases the Lewis acidity of the antimony center, making it a stronger σ -acceptor and thus a harder Z-ligand. While we have previously focused on the impact of oxidation on the nature of the metal-antimony bond, it occurred to us that such ligand-centered processes may provide control over the Lewis acidity and reactivity of the adjoining metal center.²²⁹

* Reprinted in part with permission from Yang, H.; Gabbai, F. P. *J. Am. Chem. Soc.* **2015**, 137, 13425. Copyright 2015 American Chemical Society.

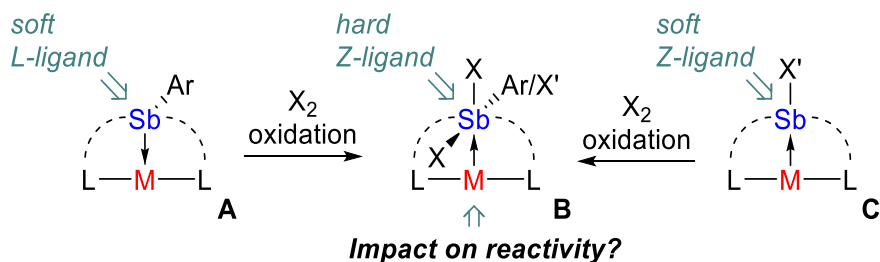


Figure 64. Oxidation of coordinated stibine ligands.

The hydroamination of alkynes is a powerful synthetic method which provides access to a diverse array of nitrogen-containing organic compounds. These hydroamination reactions are efficiently catalyzed by late transition metal complexes²³⁰⁻²³¹ including gold complexes.²³²⁻²⁴² To date, most of the gold catalysts used are mono-ligated gold(I) complexes of the type $[\text{LAu}]^+$ in which the exposed and thus Lewis acidic metal ion is readily available for substrate activation. Two coordinate gold(I) complexes of the type $[\text{L}_2\text{Au}]^+$ are not active, presumably because of the lack of Lewis acidity of the gold center. Inspired by a recent report describing the use of a gold boron complex of the type $[\text{L}_2\text{Au} \rightarrow \text{BAr}_3]^+$ as a catalyst for enyne cyclization,²⁴³ we questioned whether the use of a redox active Z-ligand such as a halostibine could afford a complex whose catalytic properties are controlled by the redox state of the Z-ligand (Figure 65). In this work, we describe a chlorostibine gold complex whose catalytic activity for the hydroamination of alkynes is turned on by oxidation of the antimony center. These results add to the growing repertoire of redox controlled catalytic processes²⁴⁴⁻²⁴⁵ and illustrate the role that Z-ligands can play in the activation of otherwise inactive catalytic centers.^{23, 27, 229, 243, 246-247}

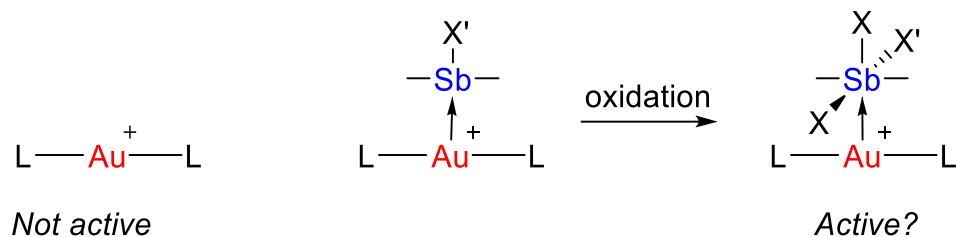


Figure 65. Representation of possible catalyst structures.

4.2 Gold-chlorostibine complexes

The chlorostibine-gold complex **47**-Cl was synthesized from the known ligand $(\text{L}^{\text{Cl}})^{248}$ and $\text{Au}(\text{tht})\text{Cl}$ (Figure 66). This complex, which is an analog of the known complex $[(o\text{-}(i\text{Pr}_2\text{P})\text{C}_6\text{H}_4)_2\text{SbCl}]\text{AuCl}$,⁸⁶ reacts with AgSbF_6 in dichloromethane to afford the air stable salt $[\mathbf{47}][\text{SbF}_6]$. The ^{31}P NMR spectrum of $[\mathbf{47}][\text{SbF}_6]$ features a signal at 50.3 ppm, significantly downfield from that of **47**-Cl at 38.4 ppm. Complexes **47**-Cl and $[\mathbf{47}][\text{SbF}_6]$ have been fully characterized and their structures have been determined using single crystal X-ray diffraction (Figure 67). In both complexes, the antimony atom adopts a distorted seesaw geometry with a Cl(1)-Sb-Au angle close to linearity ($177.00(3)^\circ$ for **47**, $177.16(3)^\circ$ for $[\mathbf{47}][\text{SbF}_6]$) and a compressed C(1)-Sb-C(19) angle ($99.89(15)^\circ$ for **47**-Cl, $98.08(13)^\circ$ for $[\mathbf{47}][\text{SbF}_6]$). The gold center of **47**-Cl displays a distorted square-planar geometry, with the chloride bending away from the Sb-Au vector by $26.10(3)^\circ$. The primary ligands of $[\mathbf{47}][\text{SbF}_6]$ are arranged about the gold atom in a distorted T-shaped geometry with P(1)-Au-Sb(1), P(2)-Au-Sb(1) and P(1)-Au-P(2) angles of $83.00(2)^\circ$, $81.39(3)^\circ$ and $159.46(4)^\circ$, respectively. The coordination sphere of the gold atom is completed by the SbF_6^- anion which is engaged in a long secondary Au-F contact of $2.931(3)$ Å. Conversion of **47**-Cl into $[\mathbf{47}][\text{SbF}_6]$ induces a shortening of the Sb-Cl bond from $2.4829(13)$ in **47**-Cl to $2.4106(11)$ in $[\mathbf{47}][\text{SbF}_6]$. This contraction reflects the

increased Lewis acidity of the cationic antimony-gold complex. It also results in a lengthening of the Au-Sb bond from 2.8527(6) in **47-Cl** to 2.9318(5) Å in [**47**][SbF₆] which suggest a weakening of the Au-Sb interaction.

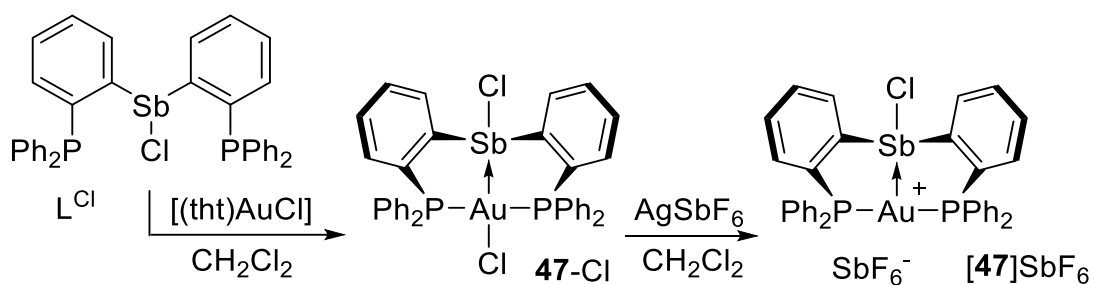


Figure 66. Synthesis of **47-Cl** and [**47**][SbF₆].

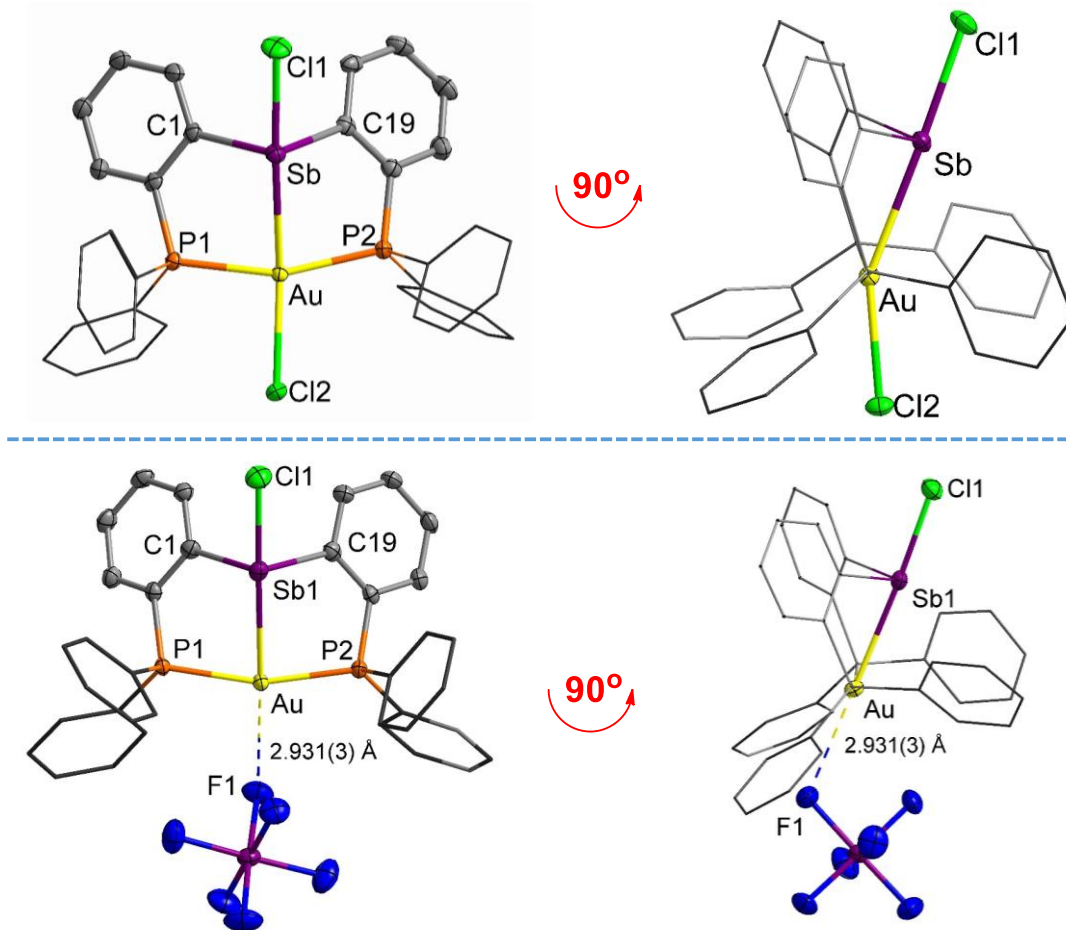


Figure 67. Solid state structure of **47-Cl** (top) and **[47][SbF₆]** (bottom). Thermal ellipsoids are drawn at the 50% probability level. Phenyl groups are drawn in wireframe. Hydrogen atoms and solvent molecules are omitted for clarity. Relevant metrical parameters can be found in the text or the experimental section.

To better understand the nature of these changes, both **47-Cl** and **[47]⁺** have been studied computationally using DFT methods (Gaussian program,²⁰⁷ functional: BP86;¹⁵¹⁻¹⁵² mixed basis set: Sb/Au: cc-pVTZ;^{153, 208} P/Cl: 6-31g(d'); C/H: 6-31g). The structure optimizations reproduce the trend observed experimentally, with **47-Cl** displaying a shorter computed Au-Sb bond (2.911 Å) than **[47]⁺** (2.955 Å). Analyses of these structures using the Natural Bond Orbital method (NBO) suggest that the Au-Sb interactions are weak and best

described as donor-acceptor interactions (Figure 68). As observed for other chlorostibine gold complexes investigated by us,⁸⁶ the NBO analysis shows that **47**-Cl possesses a Au→Sb rather than a Sb→Au interaction. In turn, we conclude that the accepting properties of the chlorostibine moiety dominate its ligative characteristics, as observed for related chlorobismuthine complexes.²⁴⁹⁻²⁵⁰ This interaction, which has lp(Au)→lp*(Sb) character is associated to a deletion energy (or stabilization energy) E_{del} of 70.79 kcal/mol. The donicity of the gold center toward antimony is notably decreased in [**47**]⁺ which possesses a lp(Au)→σ*(Sb-Cl) interaction associated to a deletion energy E_{del} of only 28.29 kcal/mol. This decrease directly results from the removal of the gold-bound chloride anion positioned trans from the antimony atom. The removal of this ligand leads to a decreased electron density on the gold atom which becomes a weaker donor toward antimony. Such effects have been previously discussed by Bourissou who showed that conversion of the gold boratrane (*o*-iPr₂P-(C₆H₄)₃B)AuCl into its cationic counterpart [(*o*-iPr₂P-(C₆H₄)₃B)Au]⁺ is accompanied by a weakening of the Au→B interaction present in these complexes.²⁵¹

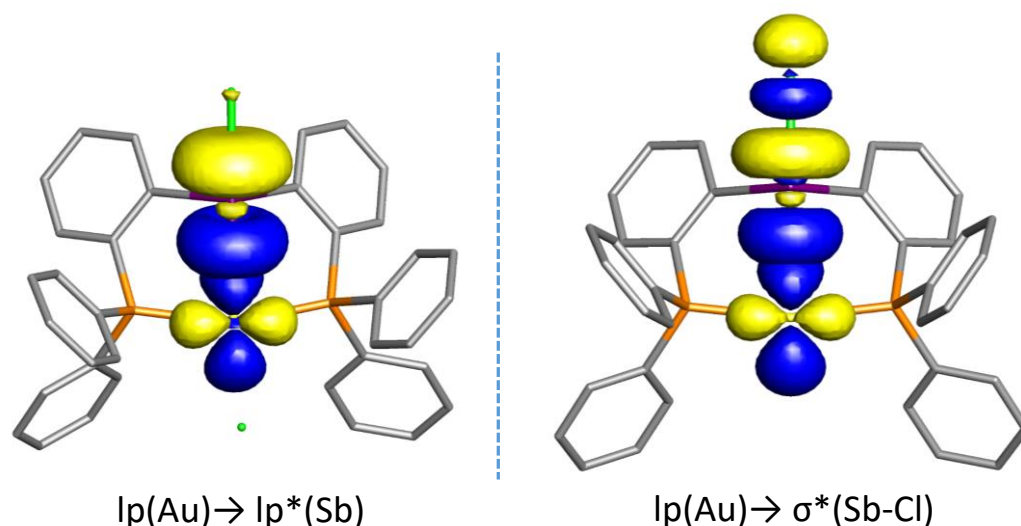


Figure 68. NBO plots of the major Sb-Au bonding interactions in **47-Cl** (left) and **[47][SbF₆]** (right) (isodensity value = 0.05). Hydrogen atoms are omitted.

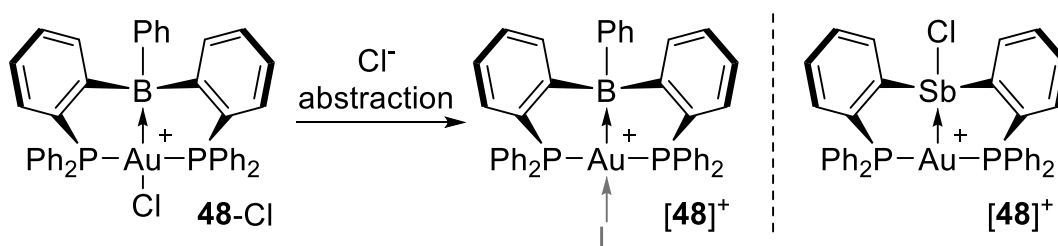


Figure 69. Side by side comparison showing **[47]⁺** and a recently reported boron complex of type **[48]⁺**.²⁴³

The electronic structure of **[47]⁺** is reminiscent of that displayed by cations of type **[48]⁺** (Figure 69).²⁴³ These cations, which are derived from the corresponding gold chloride complex **48-Cl**,²⁴⁷ have been reported as competent catalysts for reactions that necessitate alkyne activation. Because the chlorostibine moiety of **[47]⁺** mimics the σ -acceptor properties of boron,⁸⁶ we decided to determine whether **[47]⁺** could also be used for the activation of alkynes. To test this idea, we chose to study the hydroamination of alkynes, not only because of the synthetic importance of this reaction but also because of its simplicity. A test reaction

involving *p*-toluidine and phenylacetylene was carried out in CDCl₃ under ambient conditions, with a catalyst loading of 3.5 mol% (Figure 70). Catalysts [47][SbF₆] displayed a non-negligible but very low activity, with only 2.7% conversion into the Markovnikov imine product after 3 hours. When the same reaction was repeated with [(Ph₃P)₂Au]SbF₆ as a catalyst, no measurable conversion was observed. These results suggest that the chlorostibine moiety of [47]⁺ plays an activating role, albeit a very weak one. This prompted us to question whether oxidation of the antimony atom could be used to strengthen the Au→Sb interaction, leading to a more acidic and thus more catalytically active gold center.

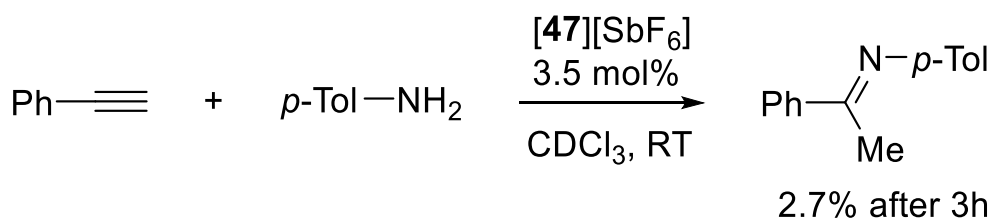


Figure 70. Model hydroamination reaction used to evaluate [47][SbF₆].

4.3 Gold-trihalostiborane complexes

With oxidation of the antimony center as a goal, complex **47** was allowed to react with PhICl₂ in CH₂Cl₂ (Figure 71). This reaction afforded the trichlorostiborane complex **49-Cl** as a pale yellow precipitate. The ³¹P NMR spectrum of **49-Cl** shows a signal at 72.0 ppm, which is significantly downfield from that of complex **49-Cl**. Crystals of **49-Cl** were grown from CH₂Cl₂. Inspection of the structure confirms oxidation of the antimony center and formation of a trichlorostiborane unit that directly engages the gold atom in a Au→Sb interaction of 2.6985(14) (Figure 72). The Au-Sb bond is notably shorter than that in **47-Cl** (2.8527(6) Å) indicating that oxidation of the antimony center increases its Lewis acidity leading to a stronger

Au→Sb dative interaction. The gold atom displays a square planar geometry which, as indicated by the Cl-Au-Sb angle ($177.88(5)^\circ$ in **49-Cl** vs. $153.90(3)^\circ$ in **49-Cl**), is much less distorted than in **47-Cl**. This square planar geometry points to the trivalent character of the gold atom, providing further support for the increased Au→Sb dative interaction upon oxidation of the antimony center. Lastly, the antimony center adopts an octahedral geometry which shows little distortion as indicated by the values of the Cl1-Sb-Au ($167.95(11)^\circ$), Cl2-Sb-Cl3 ($175.75(10)^\circ$) and Cl1-Sb-C19 angles ($169.6(4)^\circ$). Complex **49-Cl** is poorly soluble in most organic solvents, including CH_2Cl_2 and CHCl_3 which complicated an exploration of its chemical reactivity. Confronted with this difficulty, we decided to explore the generation of a more soluble analog. Gratifyingly, we observed that **49-Cl** could be easily converted into the more soluble trifluoride complex **50-Cl** by reaction with TBAF or TASF in CH_2Cl_2 (Figure 71). The ^{31}P NMR resonance of **50-Cl** at 83.5 ppm is split into a doublet, indicating coupling to the axial antimony-bound fluorine atom ($J_{\text{P-Fax}} = 16$ Hz). The ^{19}F NMR spectrum shows two signals (Figure 73). The two equatorial fluorine atom give rise to a doublet at -72 ppm with $J_{\text{Fax-Feq}} = 17$ Hz. The axial fluorine resonance appears as a pseudo-quintet at -133 ppm because of the near degeneracy of $J_{\text{P-Fax}}$ (16 Hz) and $J_{\text{Fax-Feq}}$ (17 Hz). The absence of coupling between the phosphorus and equatorial fluorine nuclei is certainly noteworthy and may be rationalized by invoking the Karplus rule and the orthogonality of the F-Sb-F and P-Au-P vector. Crystals of **50-Cl** were readily obtained through Et_2O diffusion into a CH_2Cl_2 solution. The structure of **50-Cl** is very similar to that of **49-Cl**. The Sb-Au bond of 2.7069(7) in **50-Cl** is almost identical to that in **49-Cl** (2.6985(14)) suggesting little change in the Au→Sb interaction. As in **49-Cl**: i) the gold atom of **50-Cl** adopts a square planar geometry with a Cl-Au-Sb angle close to linearity ($176.37(7)^\circ$); ii) the antimony atom, now at the center of a trifluorostiborane

unit, retains an octahedral geometry ($F1-Sb1-Au1 = 178.3(2)^\circ$, $F2-Sb1-F3 = 179.2(3)^\circ$ and $C1-Sb1-C19 = 173.7(3)^\circ$).

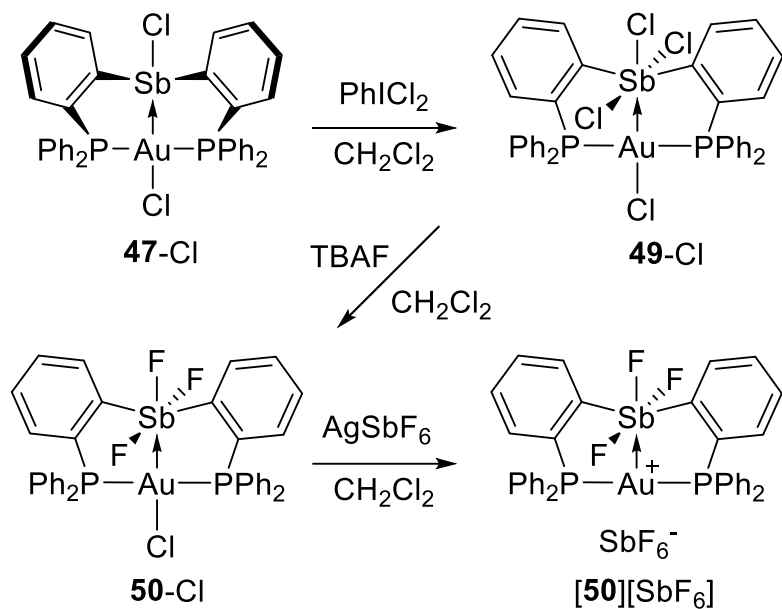


Figure 71. Synthesis of **49-Cl**, **50-Cl** and **[50][SbF₆]**.

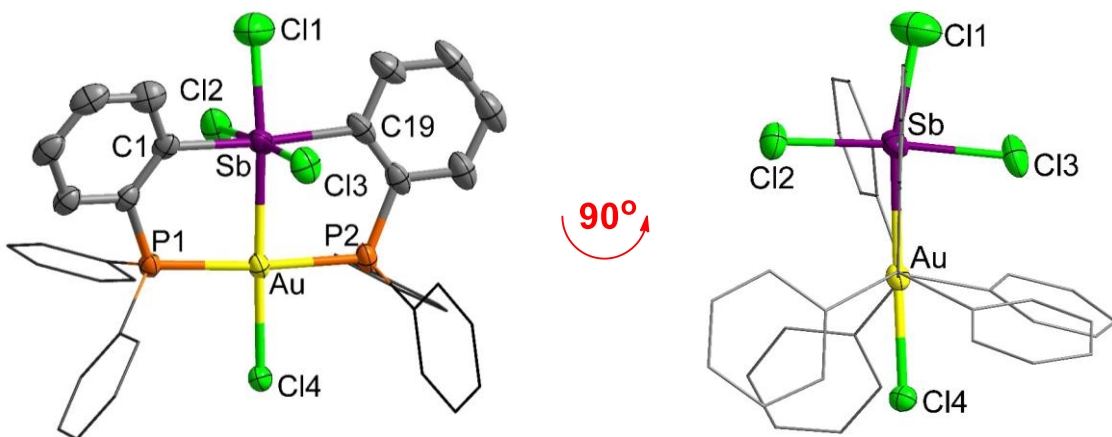


Figure 72. Solid state structure of **49-Cl**. Thermal ellipsoids are drawn at the 50% probability level. Phenyl groups are drawn in wireframe. Hydrogen atoms are omitted for clarity. Relevant metrical parameters can be found in the text or in the experimental section.

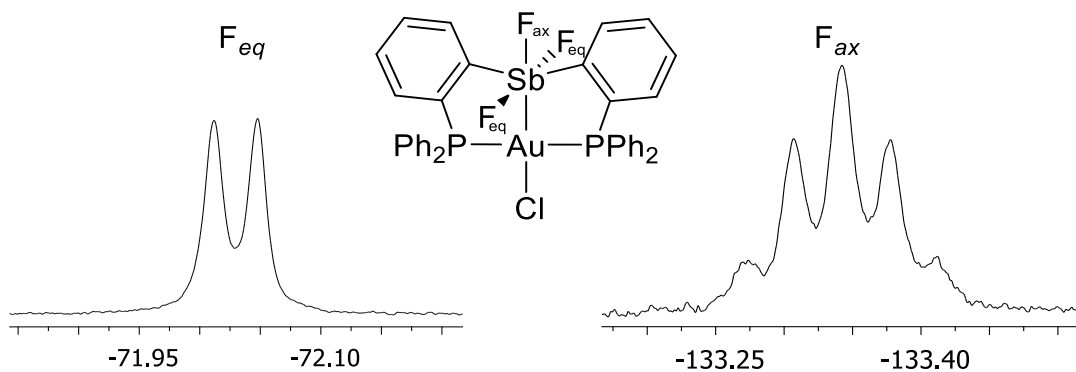


Figure 73. Resonances observed in the ^{19}F NMR spectrum of **50-Cl** measured in CDCl_3 .

With the intent of accessing a well-defined alkyne activation catalyst, complex **50-Cl** was treated with AgSbF_6 in CH_2Cl_2 which resulted in the clean formation of the corresponding cationic complex $[\mathbf{50}]^+$ as a hexafluoroantimonate salt (Figure 71). A similar reaction could not be cleanly carried out with **49-Cl** which gave an intractable product mixture when treated with AgSbF_6 . Salt $[\mathbf{50}][\text{SbF}_6]$ has been characterized by ^{31}P NMR spectroscopy which shows a resonance at 66.3 ppm. The ^{19}F NMR spectrum displays two new resonances corresponding to the axial (-147.1 ppm) and equatorial fluorine ligands (-55.1 ppm). In addition to chemical shift changes, these resonances are all singlets indicating that the F-F and P-F scalar coupling has become too small to observe. The weakening of the Sb-Au bond upon conversion of **50-Cl** into $[\mathbf{50}][\text{SbF}_6]$ (*vide infra*) may be responsible for the disappearance of the P-F scalar coupling. The disappearance of the F-F coupling is more difficult to rationalize but is nevertheless firmly established based on the spectra. Crystals of $[\mathbf{50}][\text{SbF}_6]$ could be obtained through Et_2O diffusion into a CH_2Cl_2 solution of the complex under moisture-free conditions. The main distinguishing feature in the structure of $[\mathbf{50}][\text{SbF}_6]$ is a Au-Sb bond of 2.8196(4) Å which is significantly elongated when compared to that in **50-Cl** (2.7069(7) Å) (Figure 74). As argued in the case of $[\mathbf{47}][\text{SbF}_6]$, the removal of the chloride anion from the gold center

decreases the metallobasicity of the latter, leading to a weaker Au→Sb.²⁵¹ This weaker Au→Sb dative bond also impacts the length of the Sb-F bonds, which are notably shorter in **[50][SbF₆]** (Sb-F_(axial) = 1.942(7) Å in **50-Cl** vs. 1.897(4) Å in **[50][SbF₆]**; and Sb-F_(eq.) = 1.961(6) Å in **50-Cl** vs. 1.942(2) Å in **[50][SbF₆]**). The P(1)-Au-Sb, P(2)-Au-Sb and P1-Au-P2 angles of 86.689(18)°, 86.689(18)° and 173.38(4)°, respectively, suggest that the gold coordination geometry is best described as T-shaped. The structure of **[50][SbF₆]** can also be compared with that of **[47][SbF₆]**. Comparison of the Au-Sb distance (2.9318(5) Å in **[47][SbF₆]** vs. 2.8196(4) Å in **[50][SbF₆]**) illustrates the higher acidity of the oxidized antimony center and the comparatively stronger Au→Sb dative interaction. Finally, the vacant site trans from the antimony is flanked by the SbF₆⁻ counter anion with which it forms an Au---F contact of 2.728(4) Å. The presence of this contact, which is shorter than that observed in **[47][SbF₆]** (2.931 (3) Å), attests to the greater Lewis acidity of the gold atom. In turn, these comparisons show that oxidation of the antimony center in **[50][SbF₆]** translates into a stronger Au→Sb dative interaction and a harder gold atom.

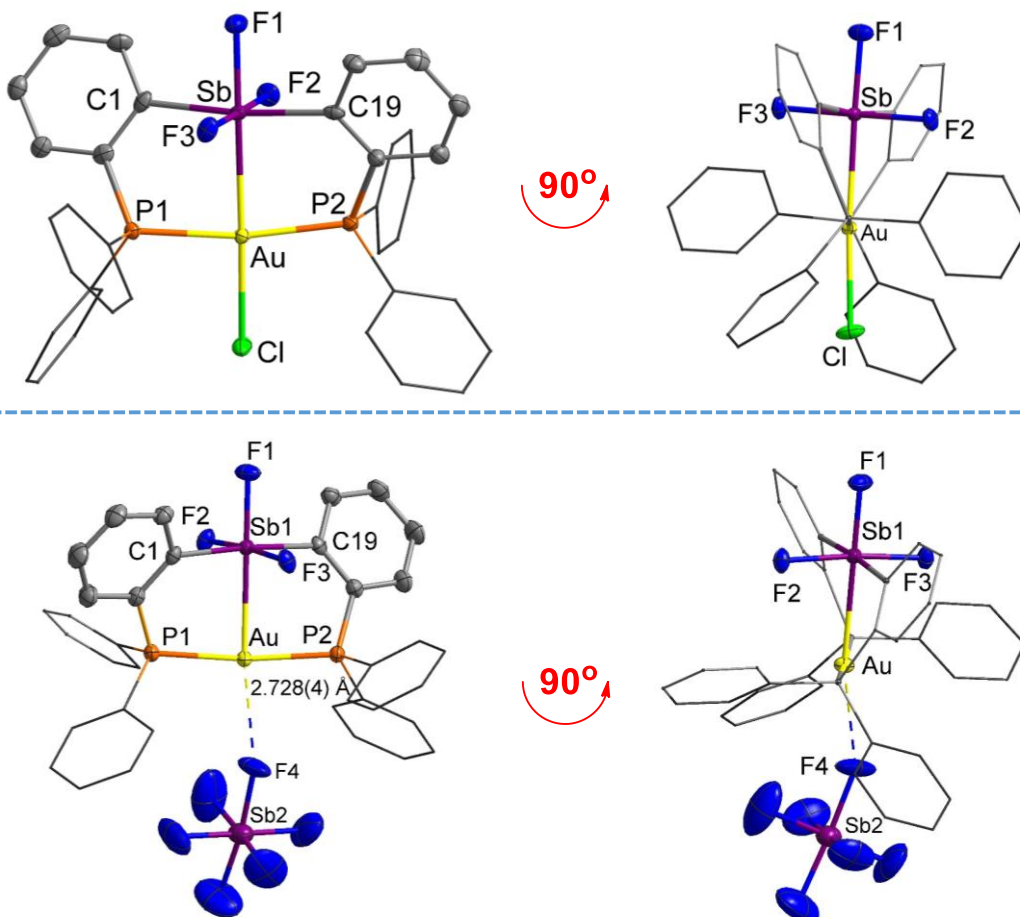


Figure 74. Solid state structure of **50-Cl** (top) and **[50][SbF₆]** (bottom). Thermal ellipsoids are drawn at the 50% probability level. Phenyl groups are drawn in wireframe. Hydrogen atoms and solvent molecules are omitted for clarity. Relevant metrical parameters can be found in the text or in the experiment section.

4.4 Lewis acidic behavior and electronic structures of the gold-trihalostiborane complexes

The increased hardness of the gold atom in **[50]⁺** is reminiscent of the mercury stibonium complex **[51]⁺** in which the Lewis acidity of the d¹⁰ ion is enhanced by juxtaposition with a strongly Lewis acidic pentavalent antimony moiety (Figure 75).²⁵²⁻²⁵³ Complex **[51]⁺** forms adducts with both neutral and anionic donors (D), which coordinate to the mercury center in a direction perpendicular to the two primary ligands. The Lewis acidity enhancement

observed for $[50]^+$ has the same origin, namely the presence of an adjoining and highly acidic pentavalent antimony center.

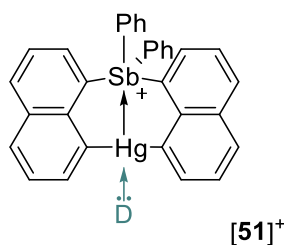


Figure 75. Structure of $[51]^+$.

In support of this analogy, we observe formation of the water adduct $[50-OH_2][SbF_6]$ which was isolated as a byproduct in small quantities due to the presence of adventitious water (Figure 76). X-ray analysis of this adduct shows that the water ligand is coordinated to the gold center via a bond of 2.383(3) Å. The Au-Sb bond of 2.7775(6) Å is intermediate between that of $50-Cl$ (2.7069(7) Å) and $[50][SbF_6]$ (2.837(4) Å). Accordingly, the Sb-F bonds in the water adduct $[50-OH_2][SbF_6]$ ($Sb-F_{(axial)} = 1.914(3)$ Å and $Sb-F_{(eq)} = 1.947(3)$ Å) > 1.942(2) Å) also fall between those in $50-Cl$ and $[50][SbF_6]$ (*vide supra*). These structural features can be assigned to the donor strength of the water ligand which is weaker than that of the chloride anion in $50-Cl$ and yet stronger than that of the weakly coordinating SbF_6^- anion in $[50][SbF_6]$. The ability of the gold center of $[50]^+$ to coordinate water bears a parallel with some recently described triorganogold(III) complexes which engage water among other hard donors.²⁵⁴ A further measure of the Lewis acidity of $[50]^+$ is provided by a simple Gutmann-Beckett measurement using $Ph_3P=O$ ($\delta = 27.3$, CH_2Cl_2) as a Lewis base. When mixed 1:1 with a $[Au(PPh_3)_2]^+$ salt in CH_2Cl_2 , no shift of the $Ph_3P=O$ ^{31}P NMR resonance is observed indicating that coordination does not occur. When the same experiment is repeated with $[47][SbF_6]$ and

[50][SbF₆], the resonance shifts downfield to 30.6 and 32.9 ppm, respectively. These changes speak to the increased acidity of the gold atom imparted by the presence of a chlorostibine unit in [47]⁺ and an oxidized trifluorostiborane unit in [50]⁺.

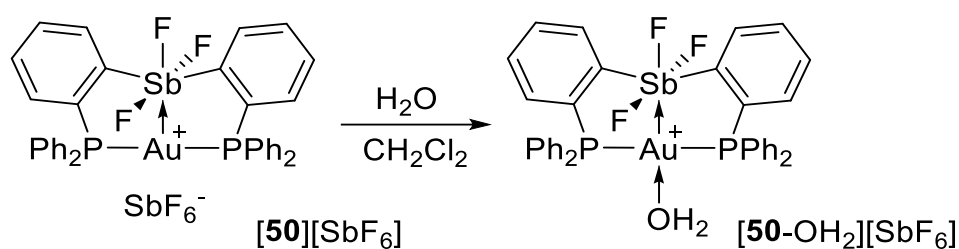


Figure 76. Formation of [50-OH₂][SbF₆].

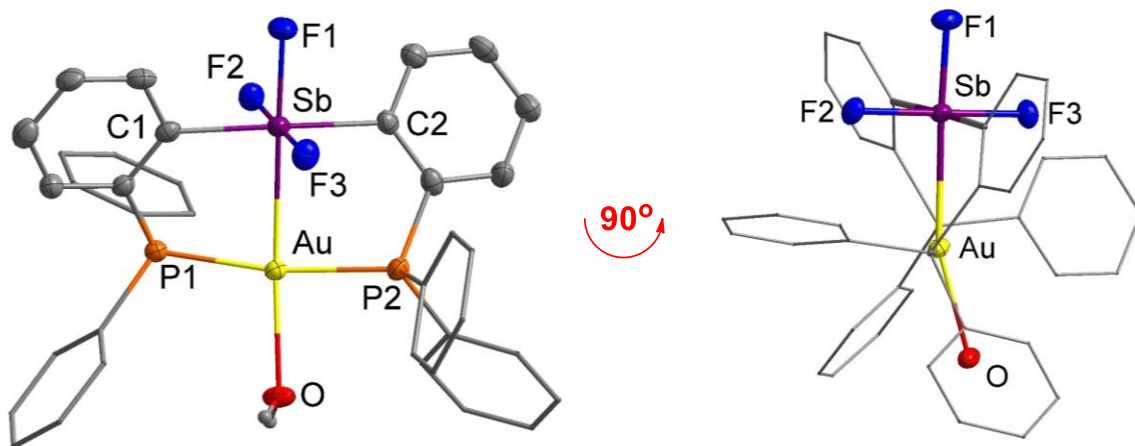


Figure 77. Solid state structure of [50-OH₂][SbF₆]. Thermal ellipsoids are drawn at the 50% probability level. Phenyl groups are drawn in wireframe. Hydrogen atoms and solvent molecules are omitted for clarity. Relevant metrical parameters can be found in the text or in the experimental section.

The ligand push/antimony pull effects observed in these complexes can also be analyzed computationally. The structure of 50-Cl, [50-OH₂][SbF₆] and [50][SbF₆] have been optimized computationally at the same level of theory as that used for 47-Cl and [47]⁺ (basis

set for F: : 6-31+g(d')) (Figure 78). The lengthening of the Sb-Au bond observed experimentally on going from **50**-Cl to [**50**-OH₂]⁺ and [**50**]⁺ is nicely reproduced computationally with distances of 2.76(6) Å, 2.82(4) Å and 2.87(1) Å for these three compounds, respectively. The NBO analyses support the dative nature of the Au-Sb interaction (Figure 78). In addition to lp(Au)→σ*(Sb-F) interactions, each complex also feature lp(Au)→σ*(Sb-C) donor acceptor interactions that make an important contribution to the stability of the complexes. This is confirmed by deletion calculations which afford $E_{\text{del}} = 148.52, 91.18$ and 59.18 kcal/mol for the in **50**-Cl, [**50**-OH₂]⁺ and [**50**]⁺, respectively. These energies correlate with the donor strength of the ligand bound to gold and provide a further illustration of the ligand push/antimony pull effect at play in these complexes. A comparison of the Au→Sb stabilization energies in [**47**]⁺ (28.29 kcal/mol) and [**50**]⁺ (59.18 kcal/mol) illustrates the increased σ-accepting properties of the trifluorostiborane which behaves as a Z-type ligand.

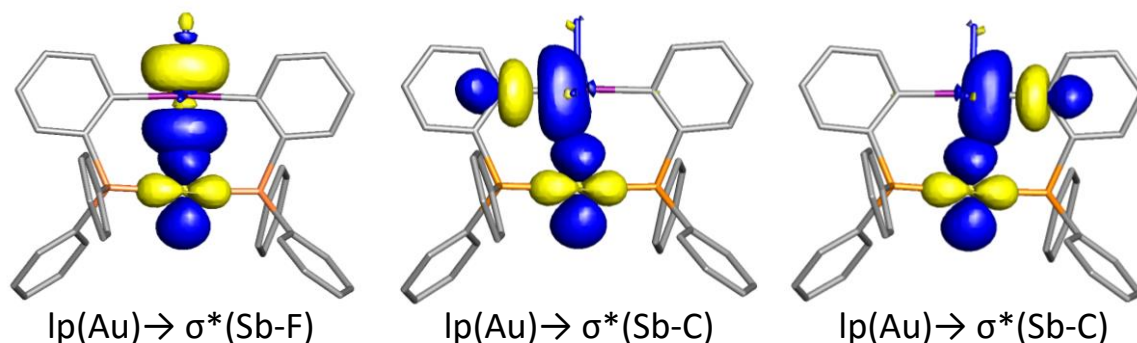


Figure 78. NBO plots of the major Sb-Au bonding interactions [**50**]⁺ (isodensity value = 0.05). Hydrogen atoms are omitted. The same donor acceptor interactions are also observed for **50**-Cl and [**50**-OH₂]⁺.

The increasing transfer of electron density from gold to antimony observed on going from [**50**]⁺ to [**50**-OH₂]⁺ and **50**-Cl can also be depicted based on the resonance structures

shown in Figure 79. Structures of type **a** correspond to Au(I)-Sb(V) species with the gold atom in the monovalent state. Resonance structures of type **b**, which account for the donation of an electron pair from gold to antimony, correspond to Au(II)-Sb(IV) species. Remembering that valence and formal oxidation states are different concepts,¹⁵⁵ the gold atom in structures of type **b** is in the trivalent state. While both resonance structures contribute to the electronic structures of all three complexes, the structural and computational results described above show that the importance of structure **b** increases on going from $[\mathbf{50}]^+$ to $[\mathbf{50-OH}_2]^+$ and $\mathbf{50-Cl}$. This smooth transition illustrates the dynamic and adaptive nature of the Au-Sb interaction which increases in strength when the gold atom accepts a donor ligand.

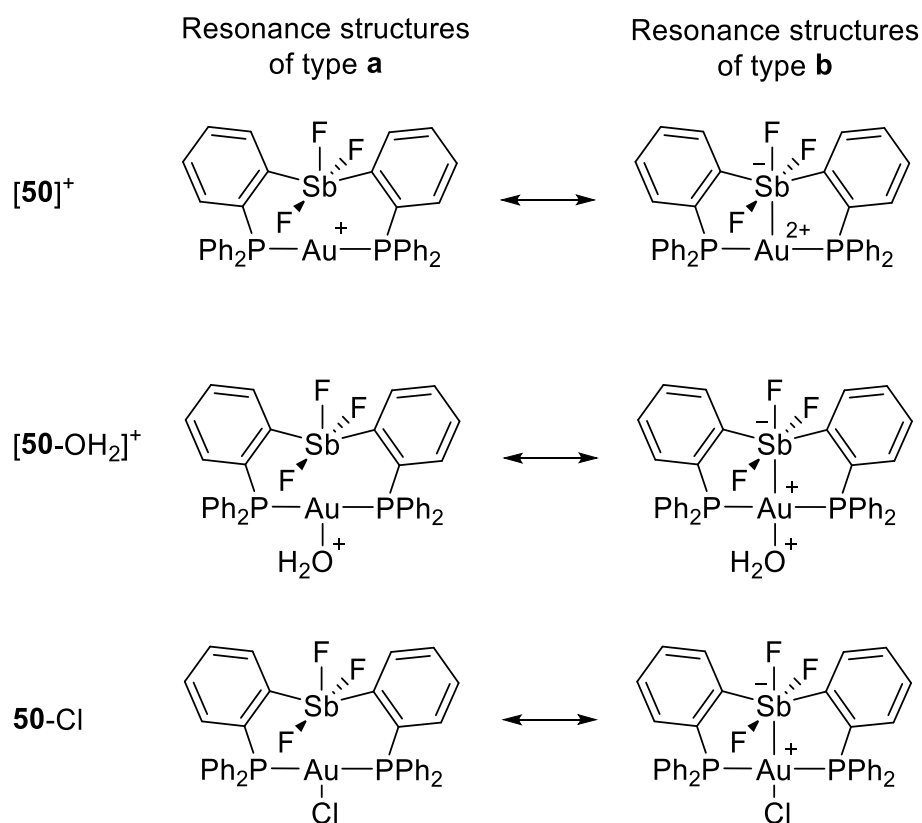
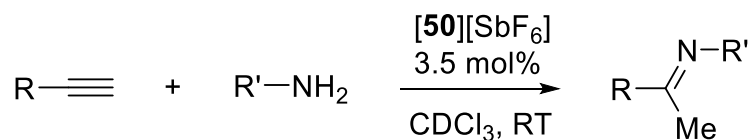


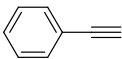
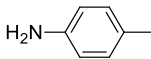
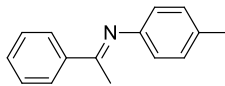
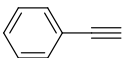
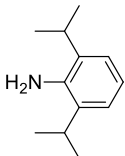
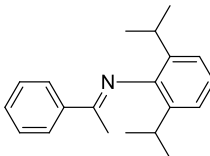
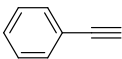
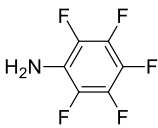
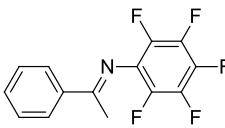
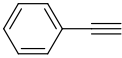
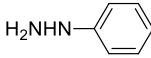
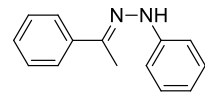
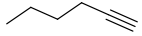
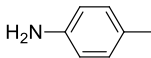
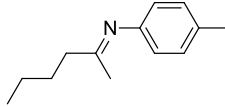
Figure 79. Resonance structures for $[\mathbf{50}]^+$ to $[\mathbf{50-OH}_2]^+$ and $\mathbf{50-Cl}$.

4.5 Catalytic properties of the cationic gold-trifluorostiborane salt [50][SbF₆]

With [50][SbF₆] in hand, we became eager to test whether the stronger Au→Sb interaction would indeed correlate with a higher catalytic activity in reactions involving alkynes. While the reaction of *p*-toluidine and phenylacetylene was very poorly catalyzed by [47][SbF₆], we found [50][SbF₆] to be a very competent catalyst for this reaction, with an essentially complete conversion after 40 min at room temperature in CDCl₃, with a catalyst loading of 3.5 mol%. Since many late transition metals^{230-231, 255-259} including gold²³²⁻²⁴² hydroamination catalysts often necessitate an inert atmosphere, high temperature and relatively long reaction time, the fact that [50][SbF₆] catalyzes the reactions under mild conditions is noteworthy. We have also carried out this reaction on a larger scale (6.5 mmol), with a lower catalyst loading (0.5 mol%). Full conversion was also observed but necessitated a longer reaction time of 6 hours. We have studied the scope of this reaction with bulky, electron rich and/or electron poor amines. As shown in Table 4, hydroamination of phenyl acetylene with the bulky 2,6-diisopropylaniline gave 93% of the desired products in 70 min at ambient condition (Entry 2).^{239, 256} The reaction proceeded more slowly with the electron poor pentafluoroaniline, affording a 68% yield after 48 hours (Entry 3). The low yield of this reaction is caused by partial hydrolysis of the imine product and formation of acetophenone. The reaction also proceeded quickly with phenylhydrazine (Entry 4) but failed with alkyl amines such as cyclohexylamine, which may bind to the gold center thus preventing alkyne activation. We also examined the hydroamination reactions of the less activated terminal aliphatic alkyne. 1-Hexyne reacted with *p*-toluidine to produce the desired imine within 60 minutes (Entry 5).

Table 4. Results obtained in the hydroamination of terminal alkynes with aromatic amines with [50]SbF₆ as a catalyst.



| Entry | R-C≡C | H ₂ N-R' | R-C(=N-R') | t | Conv. (Yield) ^a |
|-------|---|---|--|--------|----------------------------|
| 1 |  |  |  | 40 min | 98 % (92%) |
| 2 |  |  |  | 70 min | 93% (83%) |
| 3 |  |  |  | 48 h | 68% |
| 4 |  |  |  | 30 min | 86% (72%) |
| 5 |  |  |  | 60 min | 61% |

^aThe conversion (conv.) was measured by ¹H NMR spectroscopy using an internal standard. The yield given in parentheses corresponds to the isolated yield.

4.6 Conclusion

In this work, we show that the σ -accepting properties of chlorostibine ligands can be greatly enhanced by oxidative conversion into the corresponding trihalostiboranes. This increase leads to a strengthening of the Au→Sb interaction. As a result of this strengthening,

the gold center acquires a trivalent character, making it a harder Lewis acid as confirmed by the isolation of a water adduct. More importantly, these changes also impact the catalytic properties of the gold complex which becomes a competent catalyst for the hydroamination of alkynes in the oxidized state.

4.7 Experimental

General considerations. [(tht)AuCl] (tht = tetrahydrothiophene)²²¹ and PhICl₂¹⁷⁷ were prepared according to the reported procedures. Solvents were dried by passing through an alumina column (n-pentane and CH₂Cl₂) or by reflux under N₂ over Na/K (Et₂O and THF). All other solvents were used as received. Commercially available chemicals were purchased and used as provided (Commercial sources: Aldrich for SbCl₃ and Bu₄NF; Strem chemicals for AgSbF₆). Ambient temperature NMR spectra were recorded on a Varian Unity Inova 500 FT NMR (499.42 MHz for ¹H, 125.58 MHz for ¹³C, 469.89 MHz for ¹⁹F, 202.16 MHz for ³¹P). Chemical shifts δ are given in ppm and are referenced against residual solvent signals (¹H, ¹³C) or external BF₃-Et₂O (¹⁹F) and 85% H₃PO₄ (³¹P).

Synthesis of 47. A CH₂Cl₂ solution (8 mL) of (tht)AuCl (250 mg, 0.78 mmol) was slowly added to a CH₂Cl₂ solution (10 mL) of L^{Cl} (530 mg, 0.78 mmol) at ambient temperature. After stirring for 12 hours, the solvent was removed under vacuum, affording an oily residue. This residue was treated with Et₂O (10 mL) leading to the precipitation of **47**-Cl as a yellow solid. Compound **47**-Cl was dried under vacuum and obtained in a 93% yield (660 mg). Crystals of **47**-Cl-(CH₂Cl₂)₂ suitable for X-ray diffraction were obtained by slow diffusion of Et₂O into concentrated CH₂Cl₂ solution of **47** at low temperature (2~8 °C). ¹H NMR (499.42 MHz;

CDCl₃): δ 7.01 (m, 2 H, *o*-P(Sb)C₆H₄), 7.35 (t, 2 H, *o*-P(Sb)C₆H₄, ³J_{H-H} = 7.49 Hz), 7.45–7.54 (m, 16 H), 7.64 (t, 2 H, *o*-P(Sb)C₆H₄, ³J_{H-H} = 7.49 Hz), 7.86 (m, 4 H), 8.59 (d, 2 H, *o*-P(Sb)C₆H₄, ³J_{H-H} = 7.49 Hz). ¹³C{¹H} NMR (125.58 MHz; CDCl₃): δ 128.5 (q, J_{C-P} = 28.9 Hz), 129.3 (t, J_{C-P} = 4.0 Hz), 129.4 (t of d, -C₆H₅, CH, J_{C-P} = 42.7 Hz, J = 5.9 Hz), 131.9 (d, -C₆H₅, CH, J_{C-P} = 4.9 Hz), 132.7 (s), 133.5 (t, J_{C-P} = 2.8 Hz), 134.2 (t of d, -C₆H₅, CH, J_{C-P} = 24.6 Hz, J = 7.2 Hz), 135.3 (t, J_{C-P} = 8.5 Hz), 137.7 (t, J_{C-P} = 29.1 Hz), 149.3 (t, J_{C-P} = 17.7 Hz). ³¹P{¹H} NMR (202.16 MHz; CDCl₃): δ 38.4 (s). Mp: 186 °C dec. Anal. Calcd for **47**-Cl·2CH₂Cl₂ (C₃₈H₃₂Cl₆P₂AuSb): C, 42.18; H, 2.98. Found: C, 43.25; H, 3.15. These elemental analysis results may suggest partial loss of the interstitial CH₂Cl₂. Anal. Calcd for **47**-Cl·1.5CH₂Cl₂ (C_{37.5}H₃₁Cl₅P₂AuSb): C, 43.33; H, 3.01. For additional information on the purity of this compound, please see the NMR spectra.

Synthesis of [47][SbF₆]. A CH₂Cl₂ (1 mL) solution of AgSbF₆ (15.5 mg, 45 μ mol) was slowly added to a CH₂Cl₂ solution (2 mL) of complex **47**-Cl (41 mg, 45 μ mol). The resulting cloudy solution was stirred for 15 min, filtered and analyzed by ³¹P NMR spectroscopy which confirmed full conversion of **47**-Cl into [47][SbF₆]. Salt [47][SbF₆] was purified by evaporation of the solvent and washing with two portions of Et₂O (2 mL). Salt [47][SbF₆] was obtained in 56% yield (38 mg) as a pale yellow powder. Light yellow plates of [47][SbF₆](CH₂Cl₂) were obtained by slow diffusion of Et₂O into a concentrated CH₂Cl₂ solution of [47][SbF₆] at room temperature. ¹H NMR (499.42 MHz; CDCl₃): δ 7.15 (q, 2 H, *o*-P(Sb)C₆H₄, ³J_{H-H} = 6.49 Hz), 7.51 (q, 6 H, ³J_{H-H} = 7.49 Hz), 7.60 (t, 4 H, ³J_{H-H} = 7.49 Hz), 7.64–7.66 (m, 12 H), 7.72 (t, 2 H, ³J_{H-H} = 7.99 Hz), 8.48 (d, 2 H, *o*-P(Sb)C₆H₄, ³J_{H-H} = 7.49 Hz). ¹³C{¹H} NMR (125.58 MHz; CDCl₃): δ 125.0 (t, J_{C-P} = 30.9 Hz), 125.8 (t, J_{C-P} = 30.1 Hz), 130.3 (t of

d, -C₆H₅, CH, $J_{C-P} = 37.7$ Hz, $J = 6.0$ Hz), 131.1 (t, $J_{C-P} = 4.5$ Hz), 133.3 (s, -C₆H₅, CH), 133.6 (s), 133.9 (t, $J_{C-P} = 4.2$ Hz), 134.1 (t of d, -C₆H₅, CH, $J_{C-P} = 27.9$ Hz, $J = 7.4$ Hz), 135.3 (t, $J_{C-P} = 7.8$ Hz), 148.8 (t, $J_{C-P} = 16.1$ Hz). ³¹P{¹H} NMR(202.16 MHz; CDCl₃): δ 50.3 (s). Mp: 255 °C dec. Anal. Calcd for [47][SbF₆]·CH₂Cl₂ (C₃₇H₃₀Cl₃F₆P₂AuSb₂): C, 37.11; H, 2.53. Found: C, 37.58; H, 2.53. For additional information on the purity of this compound, please see the NMR spectra.

Synthesis of 49-Cl. A CH₂Cl₂ solution (5 mL) of PhICl₂ (151 mg, 0.55 mmol) was slowly added to a CH₂Cl₂ solution (8 mL) of 47-Cl (387 mg, 0.42 mmol) at ambient temperature, resulting in the slow precipitation of the product. After 2 hours, the resulting mixture was evacuated to dryness and the resulting pale yellow residue was washed with ether. This procedure afforded 49-Cl in 94% yield (390 mg). Complex 49-Cl is only slightly soluble in CHCl₃ and CH₂Cl₂. Single crystals of 49-Cl were obtained by slow evaporation of the CH₂Cl₂ solution. ¹H NMR (499.42 MHz; CDCl₃): δ 7.41 (t of d, 2 H, *o*-P(Sb)C₆H₄, ³J_{H-H} = 6.49 Hz, ³J_{H-P} = 4.00 Hz), 7.47 (t 10 H, ³J_{H-H} = 7.49 Hz), 7.54 (t, 4 H, *o*-P(Sb)C₆H₄, ³J_{H-H} = 7.49 Hz), 7.65 (q 8 H, ³J_{H-H} = 6.99 Hz), 7.74 (t, 2 H, ³J_{H-H} = 8.49 Hz), 9.44 (d, 2 H, *o*-P(Sb)C₆H₄, ³J_{H-H} = 7.99 Hz). ³¹P{¹H} NMR (202.16 MHz; CDCl₃): δ 79.2 (s). The poor solubility of this product did not allow for a satisfactory ¹³C NMR spectrum to be collected. Mp: 220 °C dec. Anal. Calcd for 49-Cl (C₃₆H₂₈Cl₄P₂AuSb): C, 43.98; H, 2.87. Found: C, 43.30; H, 2.81. For additional information on the purity of this compound, please see the NMR spectra.

Synthesis of 50-Cl. TBAF·3H₂O (530 mg, 1.68 mmol) dissolved in CH₂Cl₂ (6 mL) was added within 1 minute to a CH₂Cl₂ (10 mL) suspension of 49-Cl (460 mg, 0.47 mmol).

The yellowish suspension of **49**-Cl became immediately clear and colorless. After stirring for 2 hours, the solvent was removed under vacuum. The white residue was washed with three portions of methanol (4 mL) and dried under vacuum affording **50**-Cl in 91% yield (397 mg). Colorless crystals of **50**-Cl-(CH₂Cl₂) were easily obtained by slow diffusion of ether into a CH₂Cl₂ solution. ¹H NMR (499.42 MHz; CDCl₃): δ =7.40–7.48 (m, 12H), 7.53 (t, 4 H, *o*-P(Sb)C₆H₄, ³J_{H-H} = 7.00 Hz), 7.60 (q 8 H, ³J_{H-H} = 7.00 Hz), 7.70 (q, 2 H, ³J_{H-H} = 8.00 Hz), 8.74 (d, 2 H, *o*-P(Sb)C₆H₄, ³J_{H-H} = 8.00 Hz). ¹³C{¹H} NMR (125.58 MHz; CDCl₃): δ 121.8 (broad, weak, t, J_{C-P} = 29.5 Hz), 127.0 (t, J_{C-P} = 31.0 Hz), 127.4 (t, J_{C-P} = 31.3 Hz), 129.0 (t of d, -C₆H₅, CH, J_{C-P} = 7.8 Hz, J_{C-F} = 5.9 Hz) 130.9 (t of d, J_{C-P} = 11.8 Hz, J_{C-F} = 3.1 Hz), 132.3 (d, -C₆H₅, CH, J_{C-P} = 3.6 Hz), 133.3 (d, J_{C-P} = 17.1 Hz), 133.8 (broad), 134.0 (t of d, -C₆H₅, CH, J_{C-P} = 9.4 Hz, J_{C-F} = 6.4 Hz), 134.9 (m). ³¹P{¹H} NMR (202.16 MHz; CDCl₃): δ = 83.5 (d, J_{p-Fa} = 16.2 Hz). ¹⁹F{¹H} NMR (469.89 MHz; CDCl₃): δ -72.0 (d, 2F_{eq}, J_{Feq-Fa} = 17.0 Hz), -133.3 (pseudo-quintet, 1F_a, J_{Fa-Feq} = 17.0 Hz, J_{Fa-p} = 16.2 Hz). Mp: 238 °C dec. Anal. Calcd for **50**-Cl (C₃₆H₂₈ClF₃P₂AuSb): C, 46.31; H, 3.02. Found: C, 46.01; H, 3.22. For additional information on the purity of this compound, please see the NMR spectra.

Synthesis of [50][SbF₆]. A CH₂Cl₂ (2 mL) solution of AgSbF₆ (73.6 mg, 0.21 mmol) was slowly added to a CH₂Cl₂ solution (3 mL) of complex **50**-Cl (200 mg, 0.21 mmol). The resulting cloudy solution was stirred for 1 hour, filtered and analyzed by ³¹P NMR spectroscopy which confirmed full conversion of **50**-Cl into [50][SbF₆]. Salt [50][SbF₆] was isolated by evaporation of the solvent and washing with two portions of Et₂O (2mL). Salt [50][SbF₆] was obtained in 75% yield (184 mg) as a colorless powder. Crystals of [50][SbF₆] were obtained by slow diffusion of pentane into a concentrated CH₂Cl₂ solution at room

temperature under an inert atmosphere using a glovebox. ^1H NMR (499.42 MHz; CDCl_3): δ 7.37 (q, 2 H, $^3J_{\text{H-H}} = 5.99$ Hz), 7.54–7.66 (m, 22H), 7.79 (t, 2 H, $^3J_{\text{H-H}} = 7.99$ Hz), 8.42 (d, 2 H, *o*-P(Sb) C_6H_4 , $^3J_{\text{H-H}} = 7.99$ Hz) $^{13}\text{C}\{^1\text{H}\}$ NMR (125.58 MHz; CDCl_3): δ 124.7 (t, $J_{\text{C-P}} = 30.8$ Hz), 130.1 (t, $-\text{C}_6\text{H}_5$, CH, $J_{\text{C-P}} = 6.03$ Hz), 132.2 (t, $J = 4.02$ Hz), 133.5 (s, $-\text{C}_6\text{H}_5$, CH), 134.1 (t, $-\text{C}_6\text{H}_5$, CH, $J_{\text{C-P}} = 7.16$ Hz), 134.1 (s), 135.7 (s), quaternary carbon nuclei not detected. $^{31}\text{P}\{^1\text{H}\}$ NMR (202.16 MHz; CDCl_3): δ 66.3 (s). $^{19}\text{F}\{^1\text{H}\}$ NMR (469.89 MHz; CDCl_3): δ -55.1 (s, 2 F_{eq}), -147.1 (s, 1 F_a), -121.5 (broad, SbF_6). Mp: 205 °C dec. Anal. Calcd for [**50**][SbF_6] ($\text{C}_{36}\text{H}_{28}\text{F}_9\text{P}_2\text{AuSb}$): C, 38.13; H, 2.49. Found: C, 37.86; H, 2.44. For additional information on the purity of this compound, please see the NMR spectra.

General procedure for catalytic hydroamination reactions. Catalytic reactions were carried out in air. In a typical reaction, the alkyne (~0.5 mmol) was mixed with the amine (~0.55 mmol) in CDCl_3 (2 mL). After addition of the catalyst (3.5 mol% loading), conversion was estimated using ^1H NMR spectroscopy with 1,4-di-(*t*-butyl)benzene..

Computational Details. Density functional theory (DFT) structural optimizations were carried with the Gaussian 09 suite of programs with effective core potentials on all heavy atoms (functional: BP86; mixed basis set: Sb/Au: cc-pVTZ-PP; P/Cl: 6-31g(d); C/O/H: 6-31g, F: 6-31+g(d')). The optimized structures were subjected to a NBO analysis.²⁶⁰ The resulting NBOs were visualized and plotted using Jimp 2 program.¹⁷⁹

Crystallographic Measurements. The crystallographic measurements were performed at 110(2) K using a Bruker APEX-II CCD area detector diffractometer (Mo- $\text{K}\alpha$ radiation, $\lambda =$

0.71069 Å). In each case, a specimen of suitable size and quality was selected and mounted onto a nylon loop. The structures were solved by direct methods, which successfully located most of the non-hydrogen atoms. Semi-empirical absorption corrections were applied. Subsequent refinement on F^2 using the SHELXTL/PC package (version 6.1) allowed location of the remaining non-hydrogen atoms.

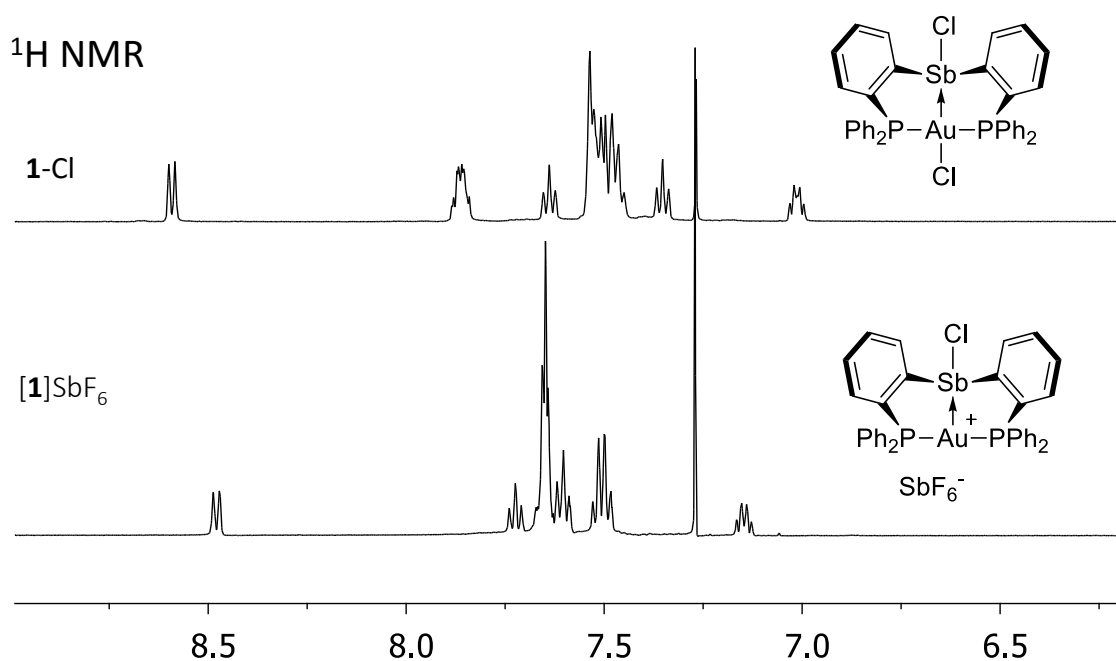


Figure 80. $^1\text{H NMR}$ spectra of **47-Cl** and **[47]SbF₆** in CDCl_3 .

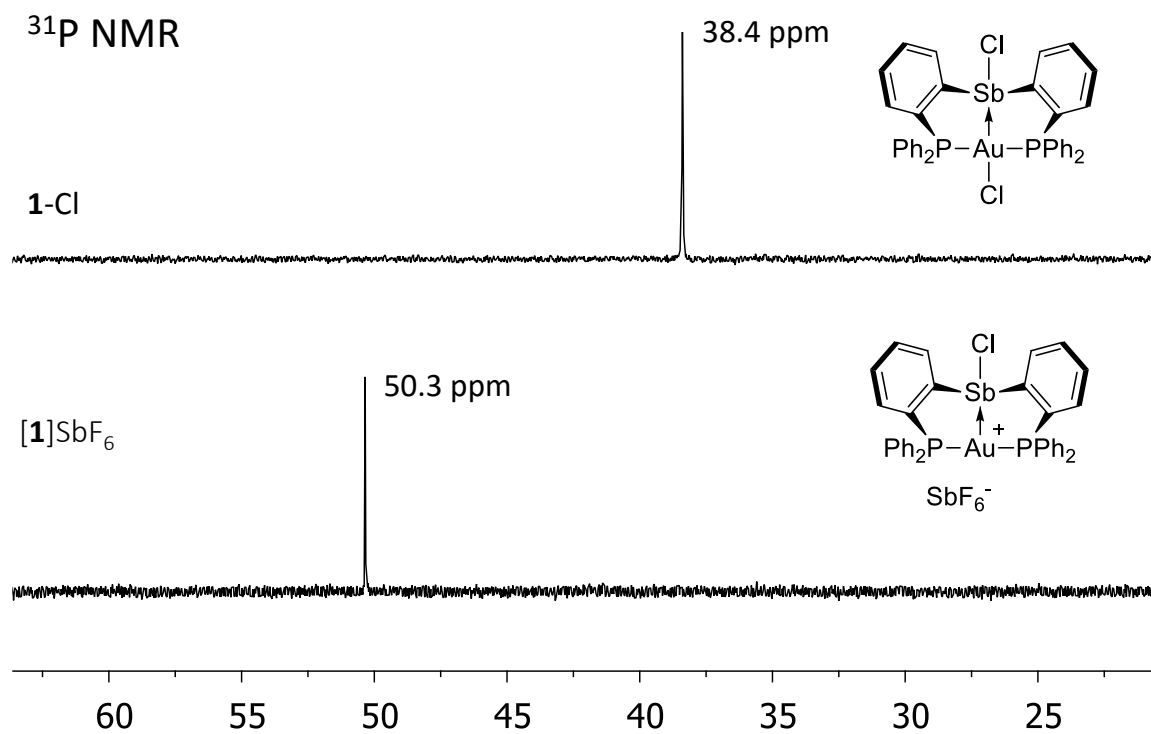


Figure 81. ³¹P NMR spectra of **47-Cl** and [**47**]SbF₆ in CDCl₃.

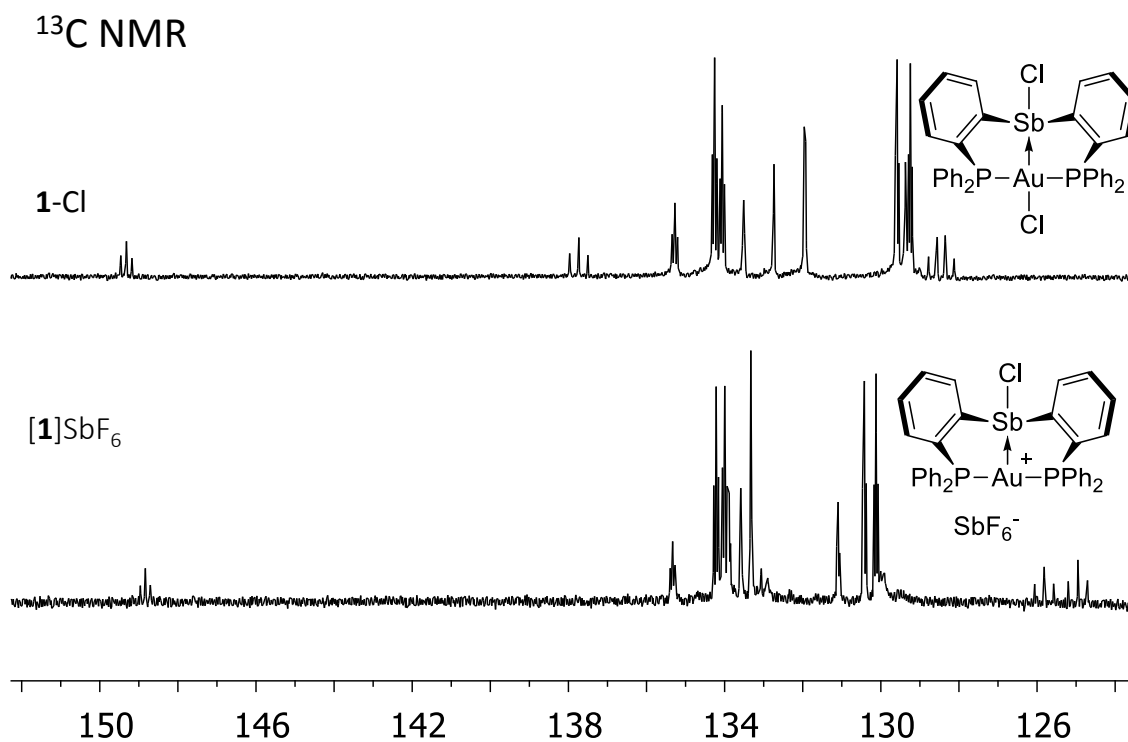


Figure 82. ^{13}C NMR spectra of **47-Cl** and **[47]SbF₆** in CDCl_3 .

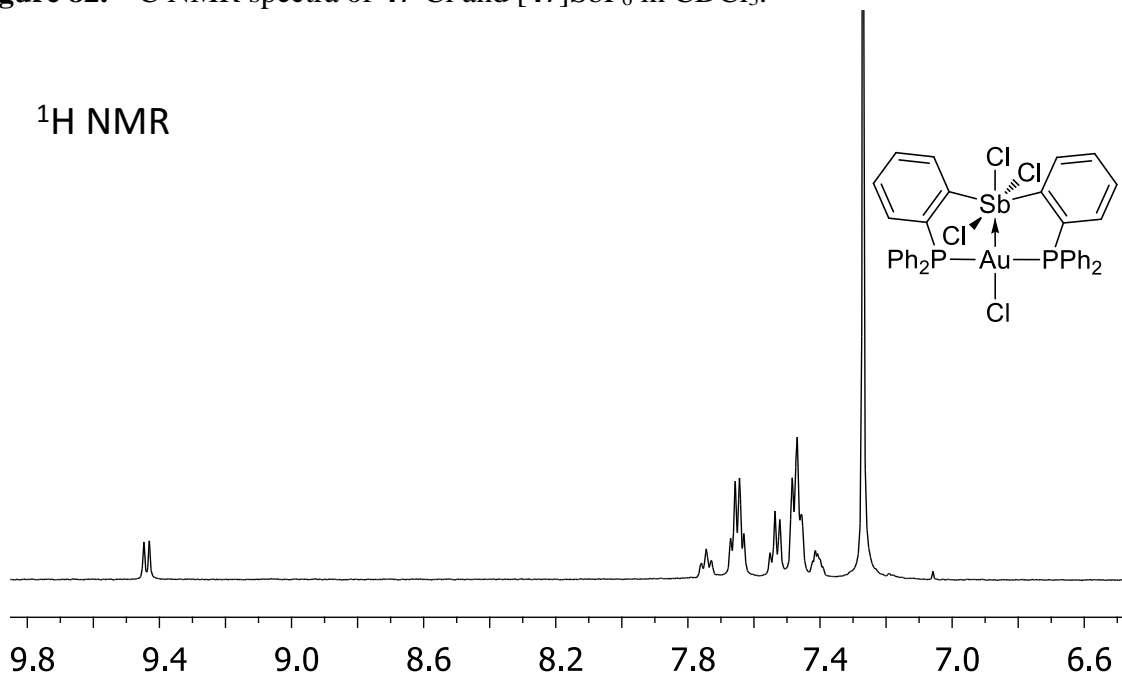


Figure 83. ^1H NMR spectra of **49-Cl** in CDCl_3 .

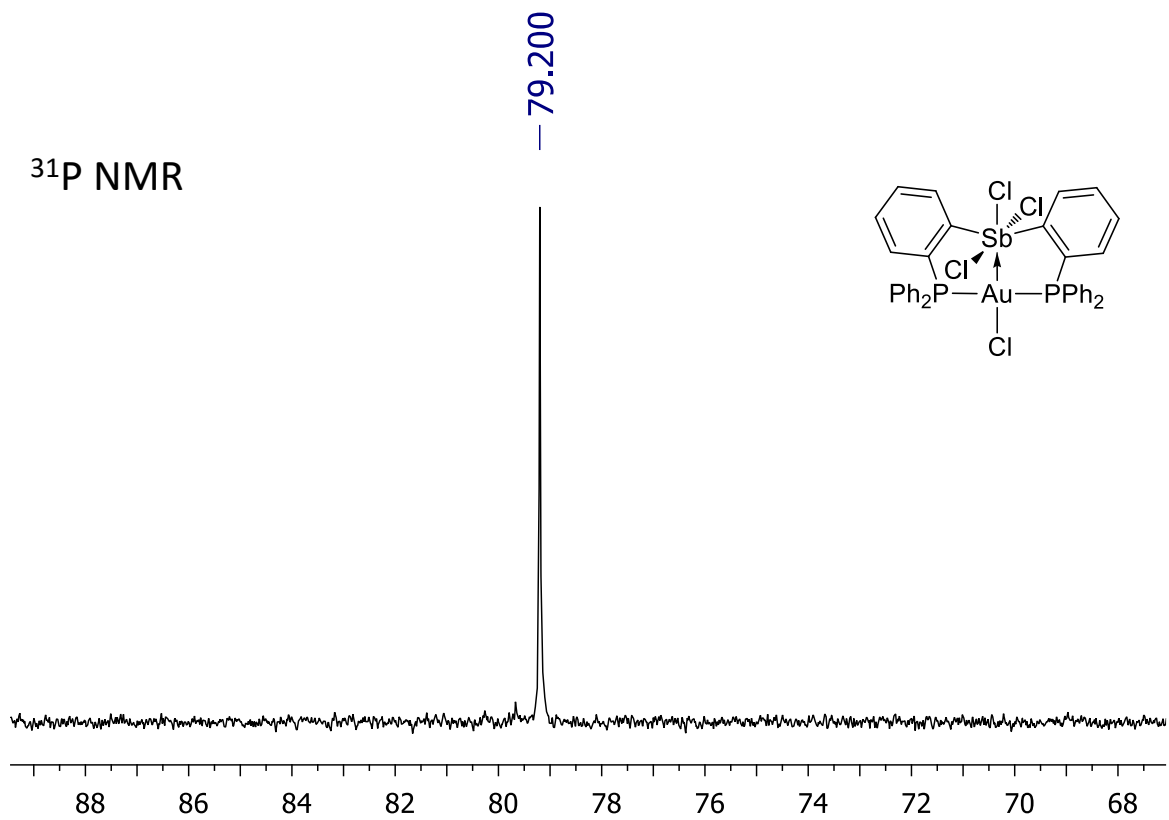


Figure 84. ³¹P NMR spectra of **49-Cl** in CDCl₃.

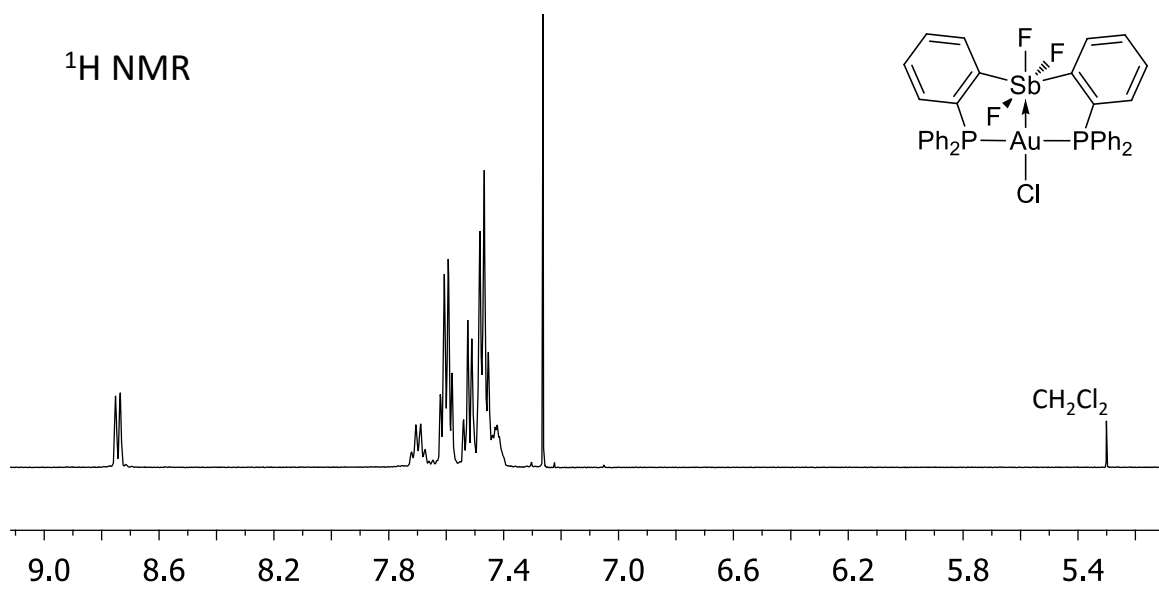


Figure 85. ¹H NMR spectra of **50-Cl** in CDCl₃.

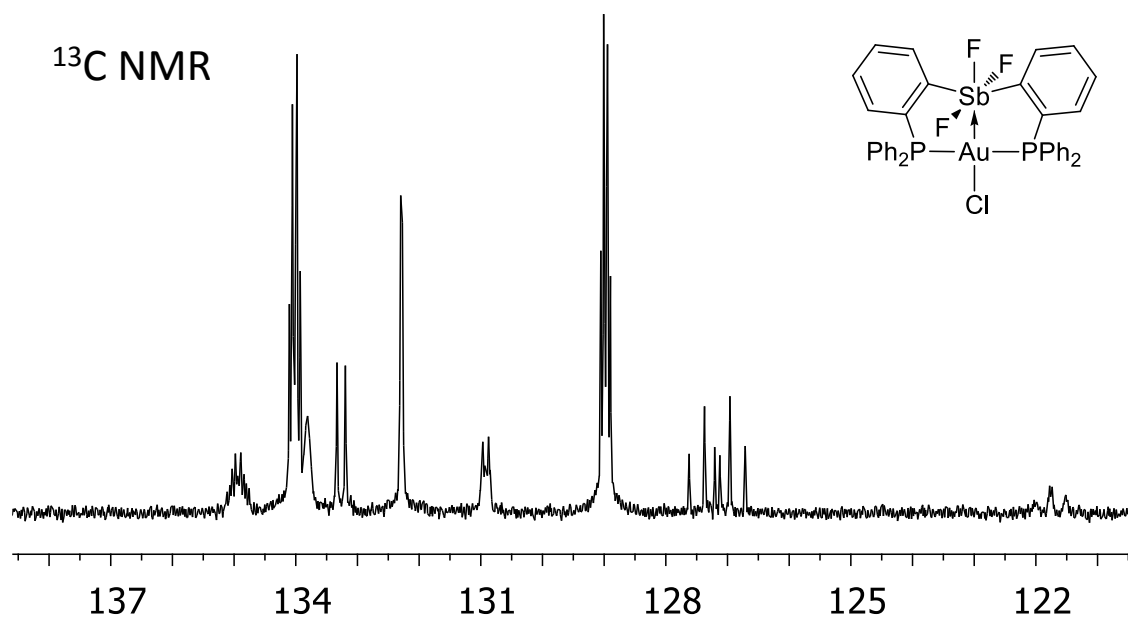


Figure 86. ¹³C NMR spectra of **50-Cl** in CDCl₃.

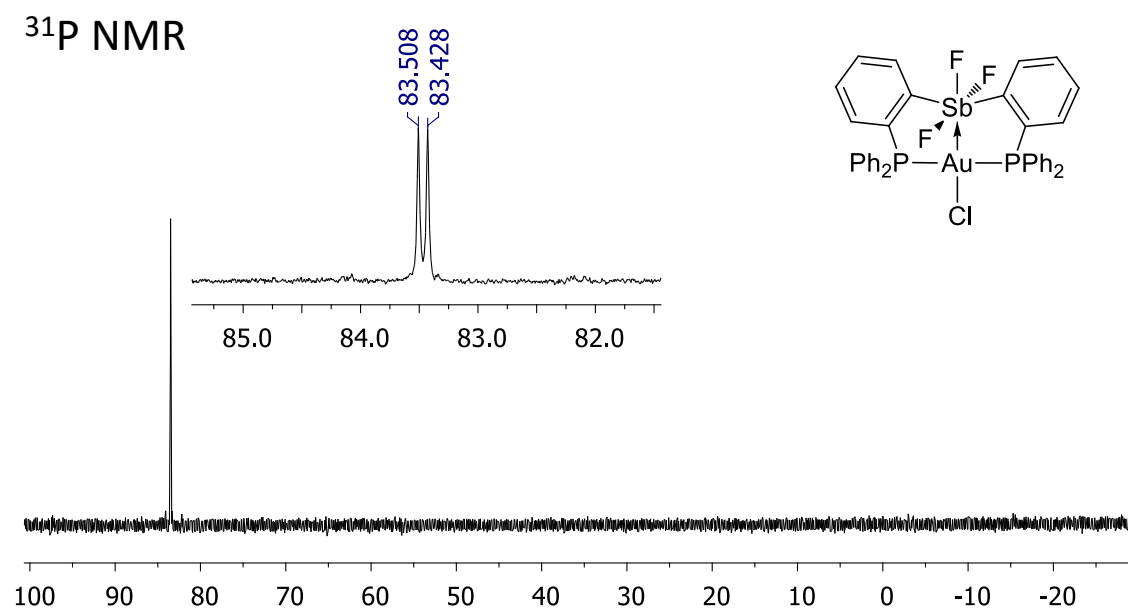


Figure 87. ³¹P NMR spectra of **50-Cl** in CDCl₃.

^{19}F NMR

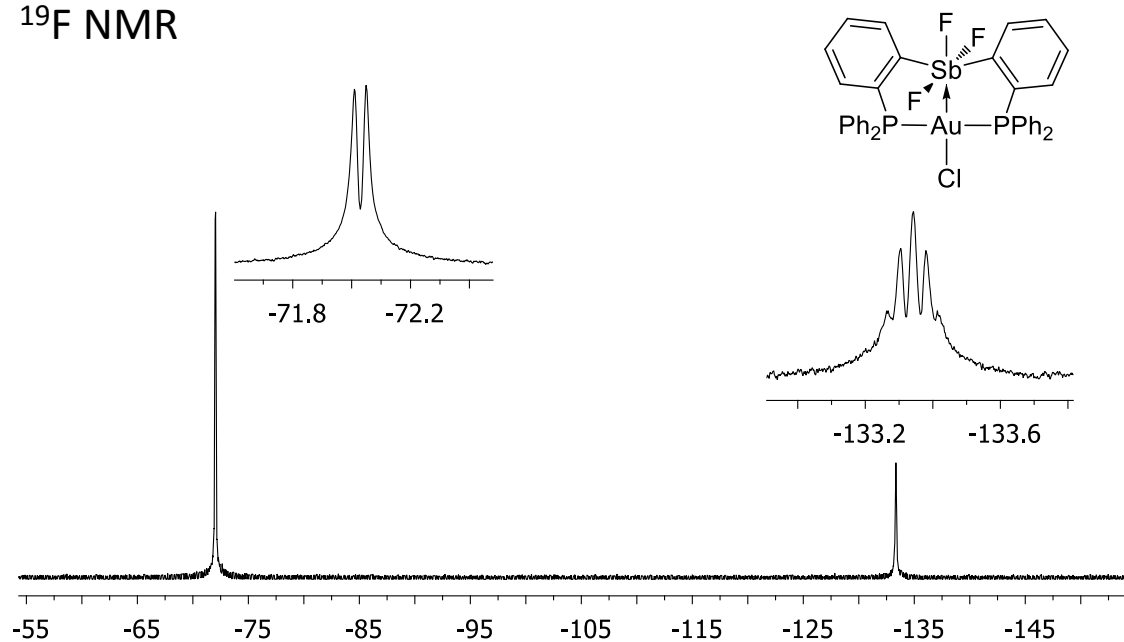


Figure 88. ^{19}F NMR spectra of **50-Cl** in CDCl_3 .

^1H NMR

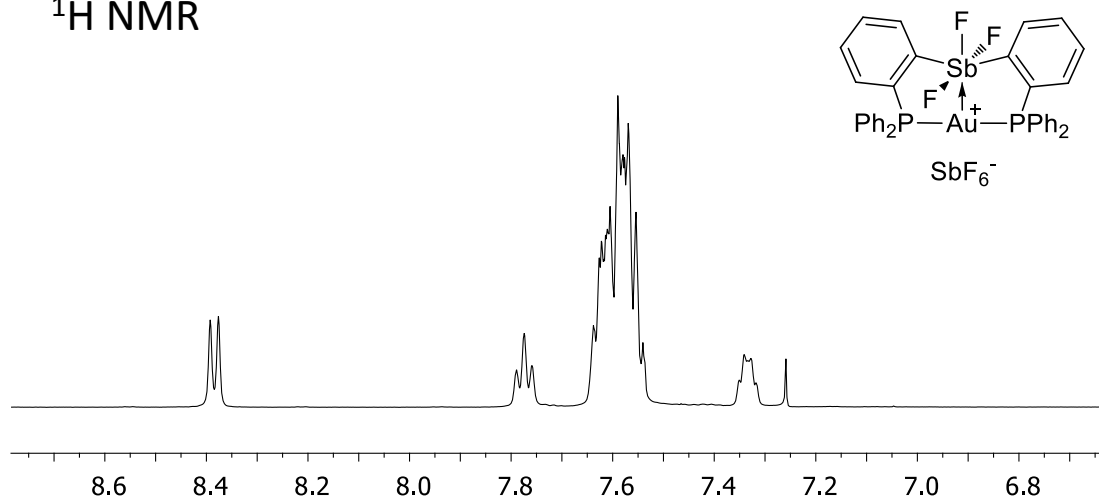


Figure 89. ^1H NMR spectra of $[\mathbf{50}]\text{SbF}_6$ in CDCl_3 .

^{13}C NMR

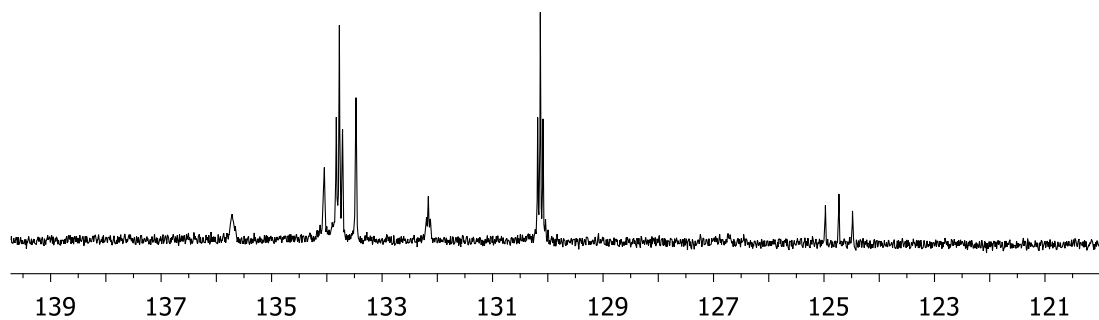
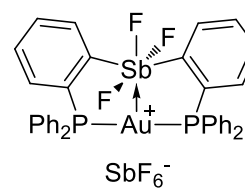


Figure 90. ^{13}C NMR spectra of **[50]** SbF_6 in CDCl_3 .

^{31}P NMR

66.343

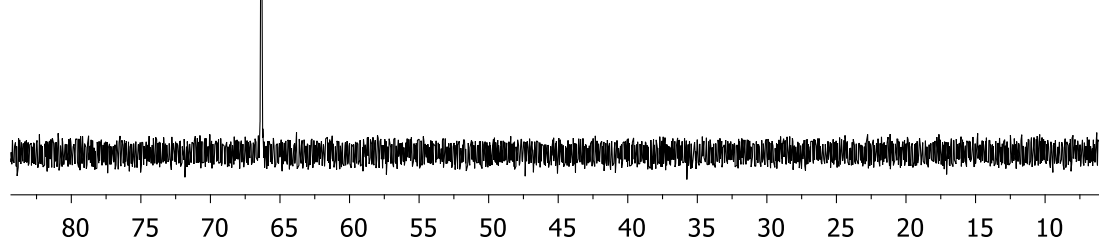
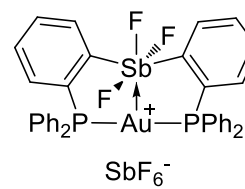


Figure 91. ^{31}P NMR spectra of **[50]** SbF_6 in CDCl_3 .

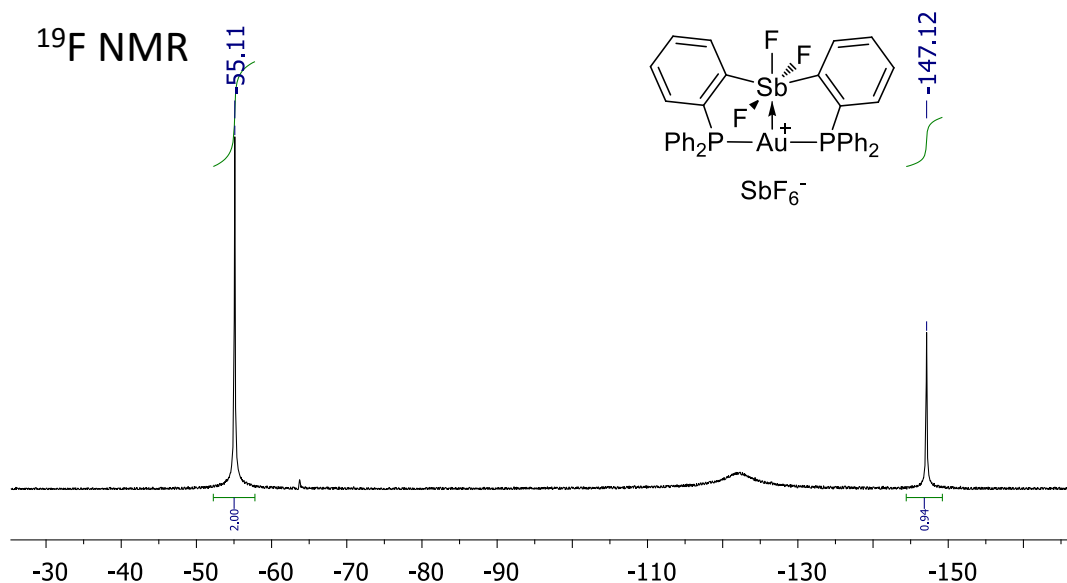


Figure 92. ^{19}F NMR spectra of $[\mathbf{50}]\text{SbF}_6$ in CDCl_3 .

Estimation of the Lewis acidity of cationic $[(\text{Ph}_3\text{P})_2\text{Au}]\text{SbF}_6$ and $[\mathbf{3}]\text{SbF}_6$ complexes by the Gutmann-Beckett method:²⁶¹ To a vial containing the desired gold complexes (0.010 mmol) was added CH_2Cl_2 (500 μL). A 250 μL CH_2Cl_2 solution of triphenylphosphine oxide (0.011 mmol, 3.3 mg) was then slowly added the gold complex solutions. The reaction mixture was transferred to NMR tube. The chemical shift of the coordination complex was measured by ^{31}P NMR, and noted relative to triphenylphosphine oxide (27.30 ppm).

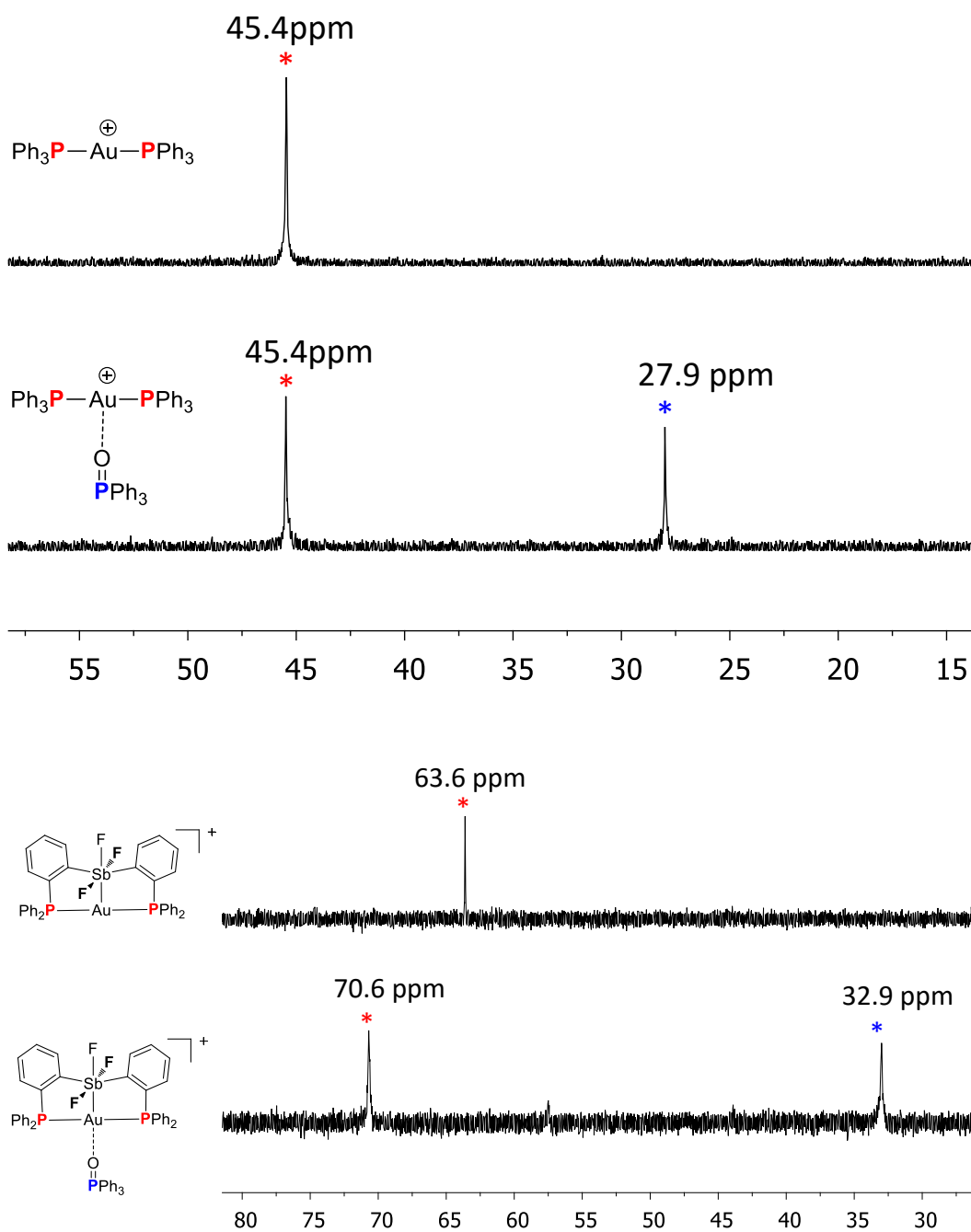


Figure 93. ^{31}P NMR spectra of CH_2Cl_2 solutions (0.75 mL) containing the cationic gold complex (0.010 mmol) and tri(phenyl)phosphine oxide (0.011 mmol, 3.3 mg).

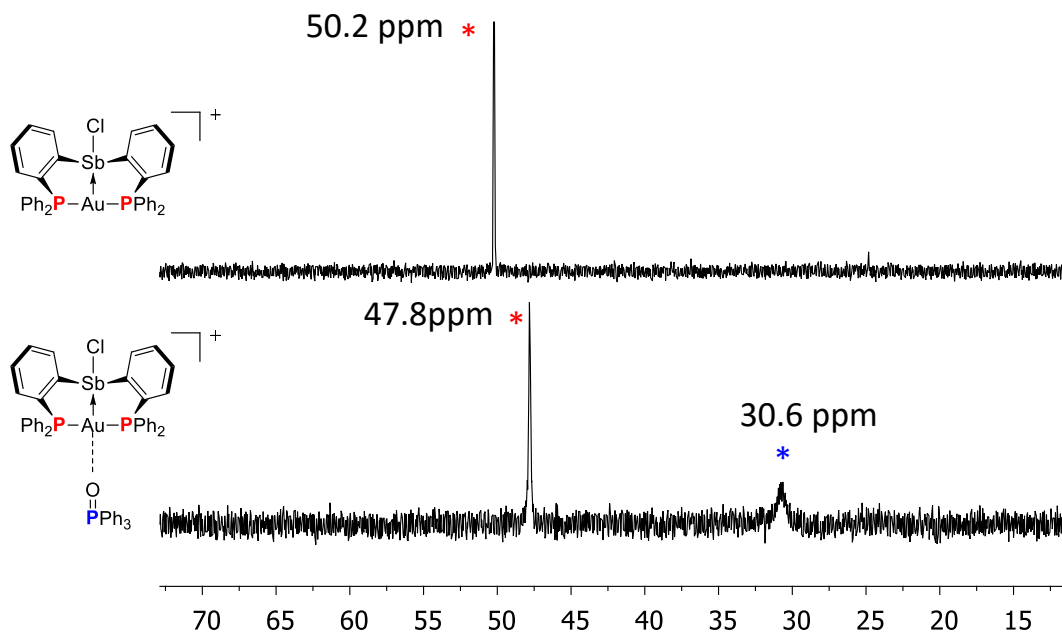
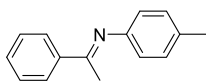


Figure 93. Continued

General procedure for catalytic hydroamination reactions. Catalytic reactions were carried out in air. In a typical reaction, the alkyne (0.5 mmol) was mixed with the amine (0.55 mmol) in CDCl_3 (2 mL). After addition of the catalyst (3.5 mol% loading), conversion was estimated using ^1H NMR spectroscopy with 1,4-di-(*t*-butyl)benzene. Other reaction conditions including scaled-up reactions carried out for product isolation are described hereafter.

N-(1-phenylethylidene)-4-methylaniline



Yellow oil. Loading: phenylacetylene (2.5g, 24.5mmol), *p*-toluidine (2.5g, 23.4 mmol), catalyst (40mg, 0.3mol %). Reaction time 6 hr. Conversion 98%. Isolation: After evaporation of the solvent under vacuum, the product was extracted with pentane and purified by vacuum distillation. Isolated yield 92%. ^1H NMR (499.42 MHz; CDCl_3): δ =7.98–8.00 (m, 2H), 7.49–

7.44 (m, 3H), 7.18 (d, $^3J_{\text{H-H}} = 8.49$, 2H, Tol), 6.73 (d, $^3J_{\text{H-H}} = 8.49$, 2H, Tol), 2.38 (s, 3H, CH₃), 2.26 (s, 3H, CH₃).

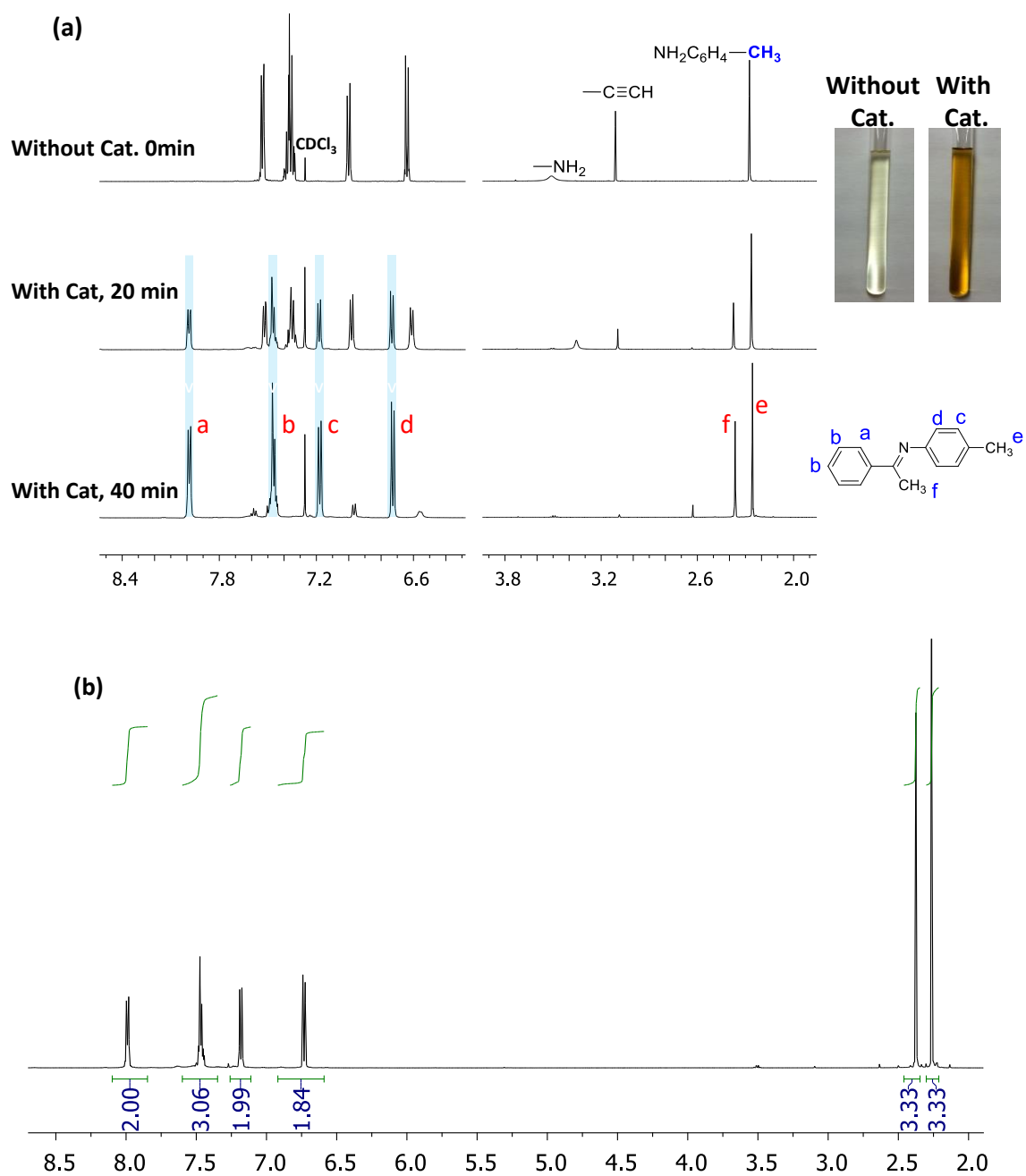
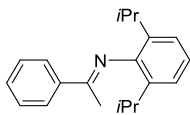


Figure 94. ^1H NMR spectra for the hydroamination of phenylacetylene with p-toluidine. (a) ^1H NMR spectra collected for the purpose of reaction monitoring. (b) ^1H NMR spectrum of the isolated product.

2,6-diisopropyl-N-(1-phenylethylidene)aniline



Light yellow solid, m.p. 69-71°C. Loading: phenylacetylene (276 mg, 2.7mmol), 2,6-diisopropylaniline (430 mg, 2.45 mmol), catalyst (9.0 mg, 0.3mol %). Reaction time 6hr. Conversion 93%. Isolation: After evaporation of the solvent under vacuum, the product was purified by recrystallization with ethanol and dried under vacuum. Isolated yield 83%. ¹H NMR (499.42 MHz; CDCl₃): δ = 8.06-8.08 (m, 2H), 7.49-7.53 (m, 3H), 7.17-7.20 (m, 2H), 7.10-7.13 (m, 1H), 2.78 (hept, *J* = 6.99 Hz, 2H), 2.14 (s, 3H), 1.17 (t, *J* = 6.99 Hz, 12H).

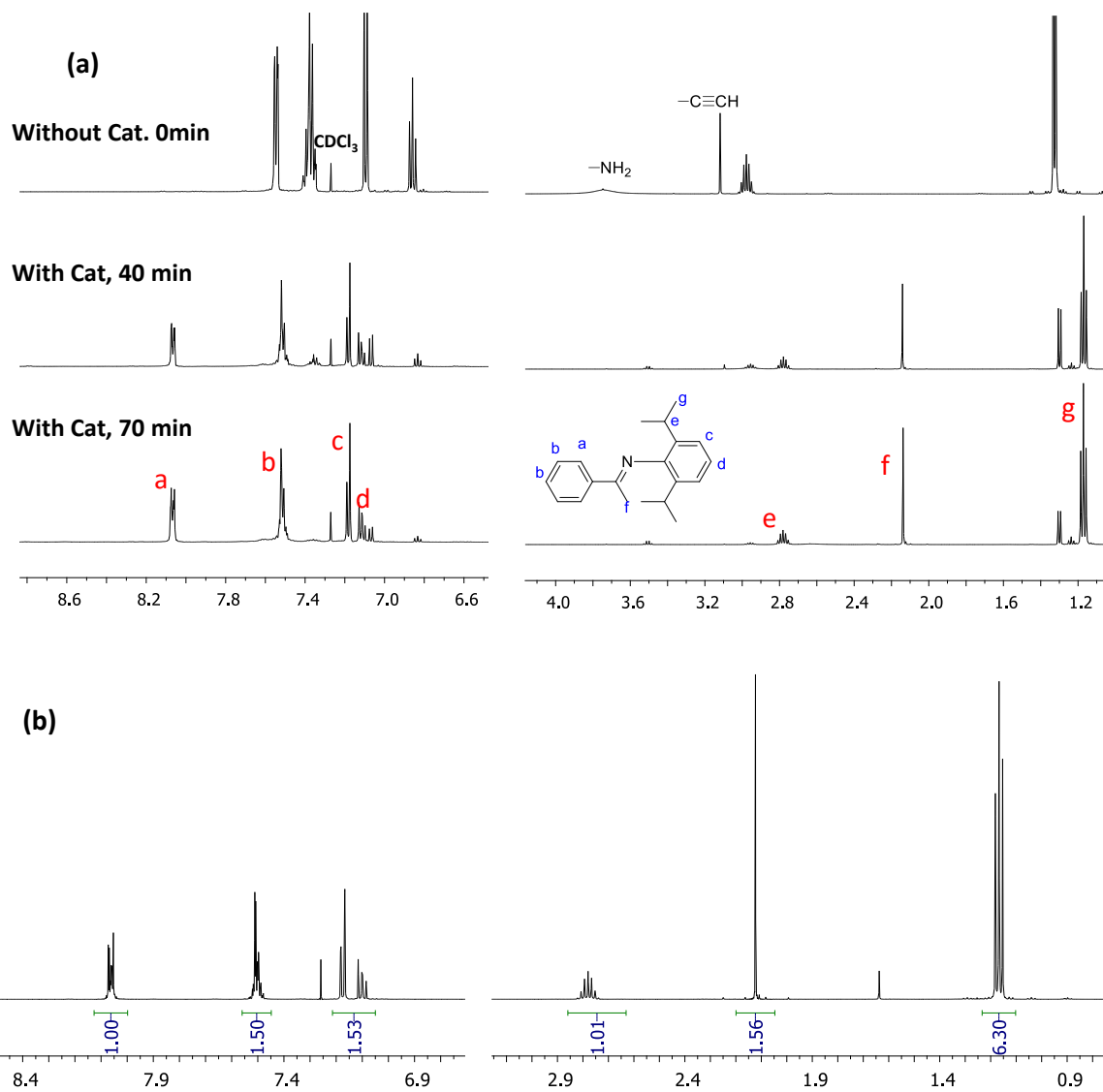
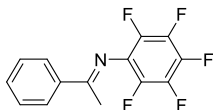


Figure 95. ^1H NMR spectra for the hydroamination of phenylacetylene with 2,6-diisopropylaniline. (a) ^1H NMR spectra collected for the purpose of reaction monitoring. (b) ^1H NMR spectrum of the isolated product.

2,3,4,5,6-pentafluoro-N-(1-phenylethylidene)aniline



Loading: phenylacetylene (18.1mg, 0.18mmol), 2,3,4,5,6-pentafluoroaniline (29.2mg, 0.16 mmol). Reaction time 48h. NMR yield 68%. ^1H NMR (499.42 MHz; CDCl_3): $\delta = 8.02\text{-}8.04$ (m, 2H), 7.46-7.51 (m, 3H), 2.33 (s, 3H).

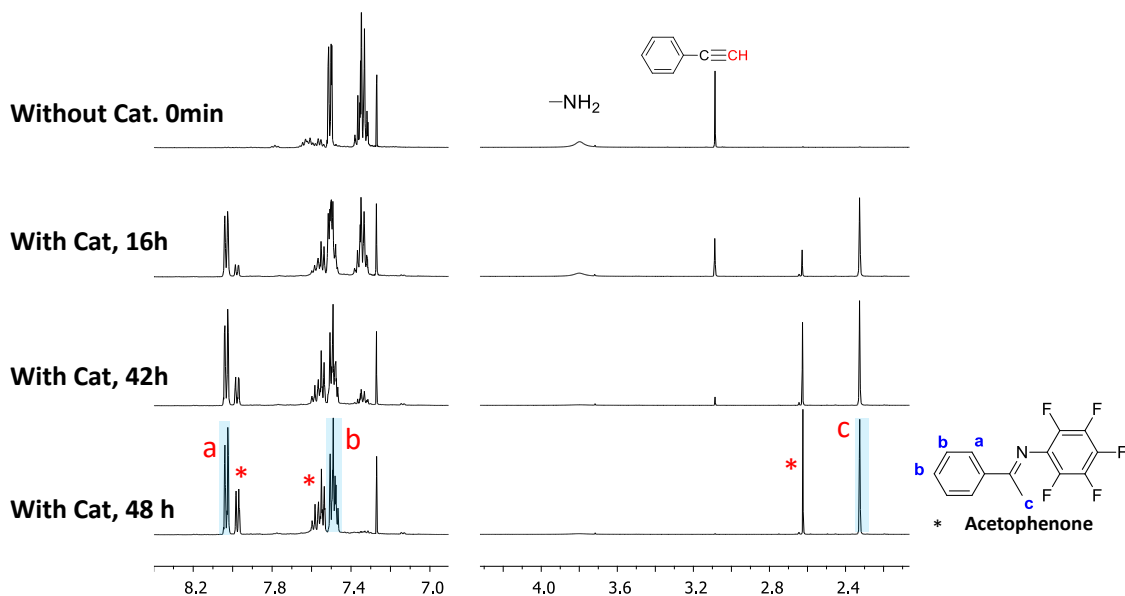
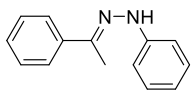


Figure 96. ^1H NMR spectra for the hydroamination of phenylacetylene with pentafluoroaniline.

1-phenyl-2-(1-phenylethylidene)hydrazine



Yellow solid, m.p. 102-104°C. Loading: phenylacetylene (168mg, 1.64mmol), phenylhydrazine (170mg, 1.57 mmol), catalyst (9.5 mg, 0.3mol %). Reaction time 2 hr. Conversion 86%. Isolation: After evaporation of the solvent under vacuum, the product was extracted with diethyl ether. After evaporation of the diethyl ether, the product was purified washed with methanol (2x 2mL) on a frit. Isolated yield 72%. ^1H NMR (499.42 MHz; CDCl_3):

$\delta = 7.81-7.83$ (m, 2H), $7.42-7.21$ (m, 8H, ArH and NH), 6.91 (t, $J = 6.99$ Hz, 1H, *p*-CH of Ph), 2.26 (s, 3H, CH₃).

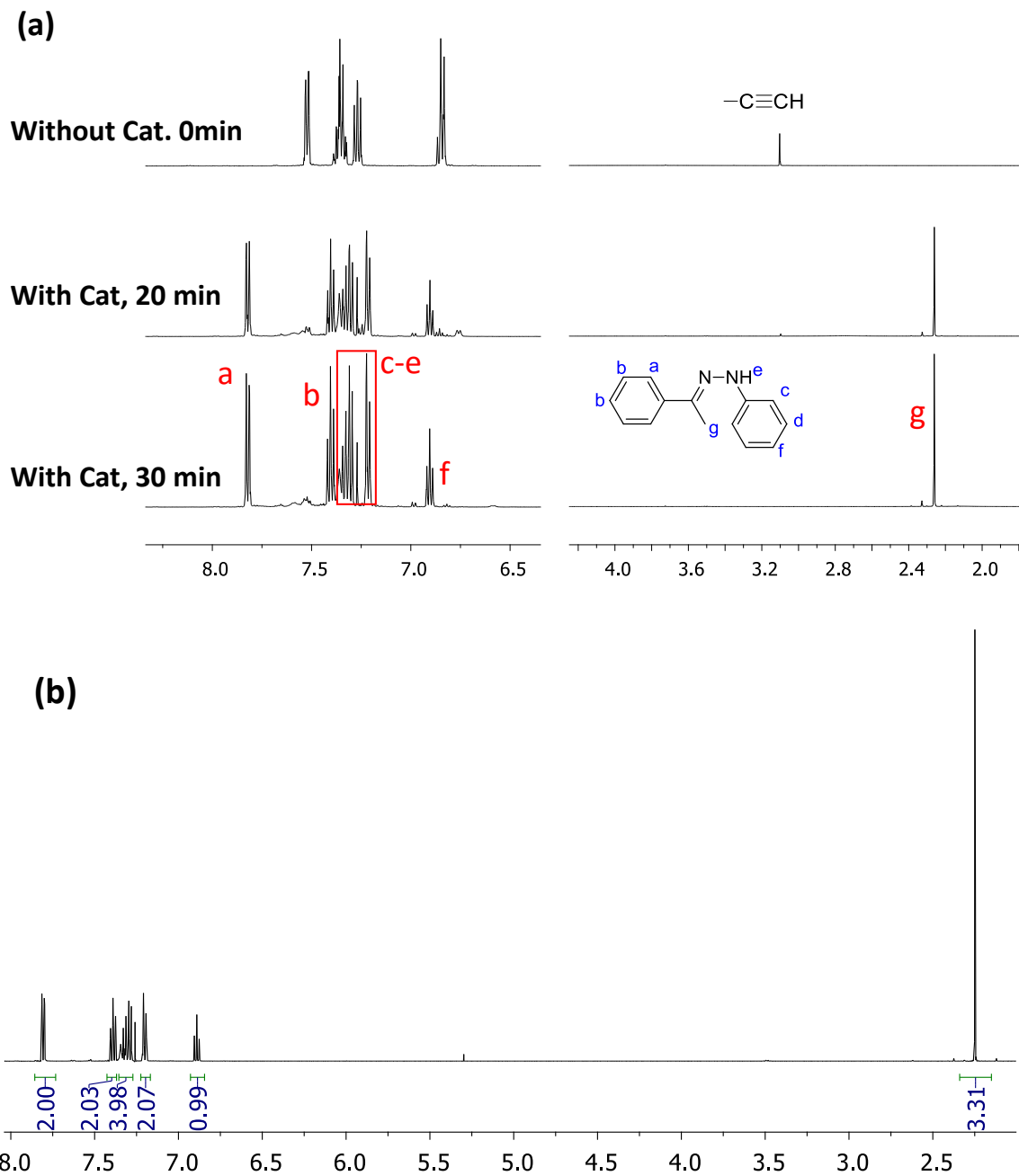
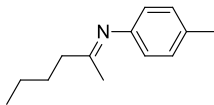


Figure 97. ¹H NMR spectra for the hydroamination of phenylacetylene with phenylhydrazine. a) ¹H NMR spectra collected for the purpose of reaction monitoring. (b) ¹H NMR spectrum of the isolated product.

N-(hexan-2-ylidene)-4-methylaniline



Loading: 1-hexyne (19.0mg, 0.23mmol), *p*-toluidine (24.8mg, 0.23 mmol), catalyst (9 mg, 3.4 mol%). Reaction time 60 min. NMR yield 61%. ^1H NMR (499.42 MHz; CDCl_3): δ = 7.10 (d, 2H), 6.60 (d, 2H), 2.32 (s, 3H, CH_3), 1.78 (s, 3H, CH_3), 1.66 (m, 2H, CH_2), 1.42 (m, 2H, CH_2), 1.22 (m, 2H, CH_2), 0.97 (t, 3H, CH_3).

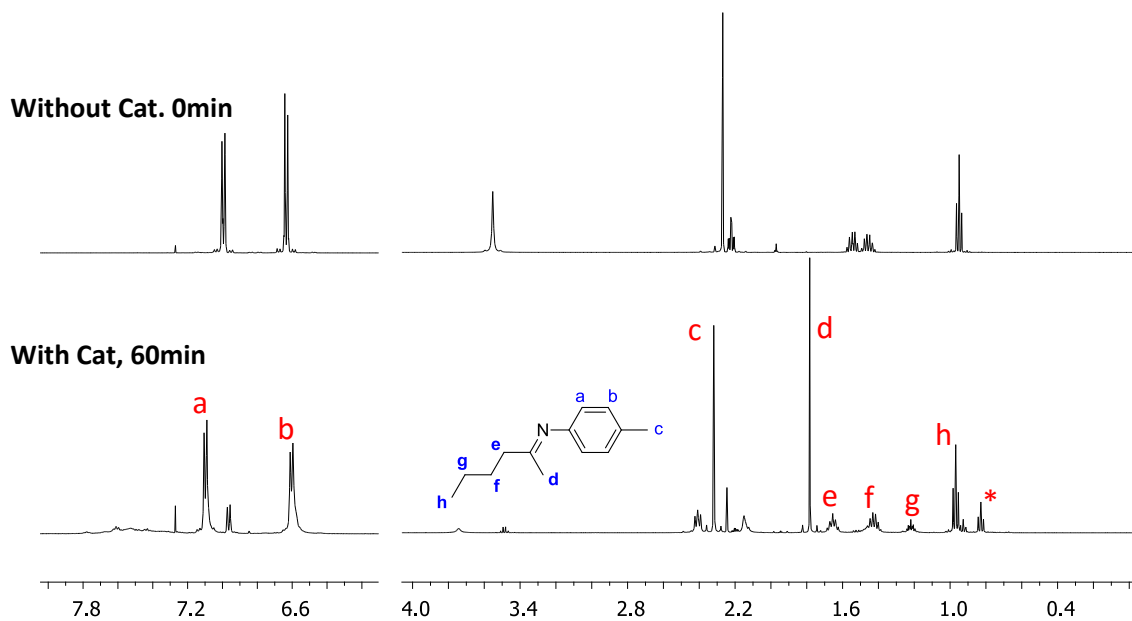


Figure 98. ^1H NMR spectra for the hydroamination of 1-hexyne with *p*-toluidine.

CHAPTER V

**SWITCHING THE REDOX STATE AND REACTIVITY OF A PLATINUM
CATALYST BY ANION COORDINATION NON-INNOCENCE OF THE
ANTIMONY LIGAND**

5.1 Introduction

Non-innocent ligands have emerged as versatile tools in modern organometallic chemistry where their unique redox properties have been used to open new vista in catalysis.^{4, 8, 262} In contrast to the conventional spectator ligands, the so-called non-innocent ligands can participate in redox processes in the coordination sphere of the transition metal. They act as electron reservoirs and shuttle electrons to and from the metal during reactions, including catalytic ones. Examples of non-innocent ligands include, among others, the well-known dithiolene, diiminopyridine and their derivatives.^{6, 8, 10-11, 263-265} Recent efforts in coordination chemistry has shown that non-innocence is also displayed by heavy main group ligands, in particular those containing antimony.^{86-88, 112, 127, 196, 266-267} Indeed, it has been demonstrated that complexes featuring Sb-M cores are prone to oxidation at the antimony center, leading to the formation of a hypervalent antimony species which remains connected to the transition metal.^{86-87, 196, 266-267} As a consequence of this ligand-centered oxidation, the Lewis acidity of the main group element is greatly enhanced, resulting in a strengthening of the metal ligand donor-acceptor interaction which develops a strong M→Sb character. Another consequence of this antimony-centered interaction is the formation of a more electrophilic metal atom.

The non-innocent behavior of antimony ligands is also reflected by their ability to participate in anion exchange or coordination events.^{88, 113, 127} While such events are centered on the antimony atom, they also affect the Sb-M interaction and can thus serve to modulate the

electron density at the metal center and possibly its reactivity. The behavior of the trigonal bipyramidal complex **A** shown in Figure 99 nicely illustrates some of these concepts. Using TlF, the two axial chloride ligands bound to both the antimony and platinum centers can be exchanged with fluoride to afford the difluorostiborane platinum complex **B**.⁸⁸ The harder fluoride ligands preferentially locate to the Lewis acidic and harder antimony (V) center. More importantly, the anion exchange/redistribution reaction leads to a change in the polarization of the Sb-Pt bonding pair. This pair becomes more polarized towards the platinum, which is thus in a more reduced form as confirmed by NMR studies and DFT calculations.⁸⁸ The results point to the ability of halogenated antimony ligands to behave as coordination non-innocent ligands, and to modulate the electron density of the metal center.

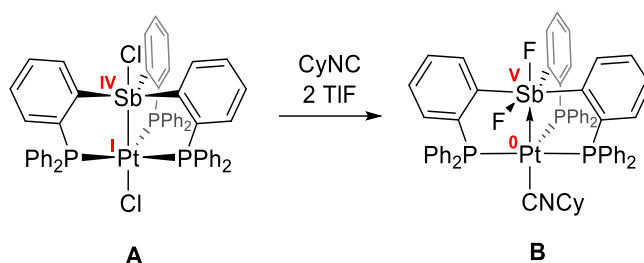


Figure 99. Anion-induced internal redox event.

Compared to the classical tris(phosphino)antimony ligand used in complex **A**, we were motivated to question if a bis(phosphino)antimony ligand could achieve the maximum possibility for anion exchange. Further, if all metal bound chlorides can be exchanged with fluorides and then located to the antimony center, would this lead to the formation of a trifluorostiborane and an unsaturated metal atom, stabilized by the M→Sb dative interaction? If so, we could envisage that the vacant site generated around the metal would be accessible for incoming substrates, making the metal complex suitable for electrophilic catalysis.

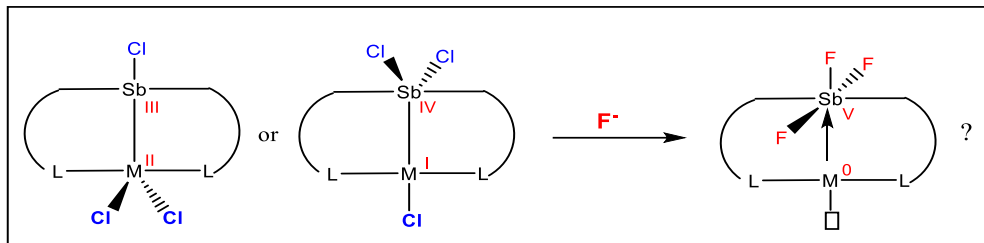


Figure 100. Schematic representation showing chloride-to-fluoride exchange reaction of a fully chlorinated antimony-metal complex.

In this work, we report the successful implementation of this idea by describing the synthesis of a zero valent platinum complex bearing a trifluorostiborane ligand. The zero valent platinum is stabilized by the σ -accepting Sb(V) atom *trans* to a coordinating solvent molecule, such as acetonitrile. While this coordination mode indicates an electrophilic metal center, the electrophilicity is not sufficient for alkyne activation towards nucleophilic attack. Further attempts to increase the Lewis acidity at the antimony site were successful by fluoride abstraction using Lewis acids or Brønsted acids. As a result, a cationic monofluorostibine platinum complex formed, with a more oxidized platinum center. This resulting platinum complex displays an improved ability to activate alkynes towards alkene or other nucleophile addition.

5.2 Trifluorostiborane-platinum complexes

To put the hypothesis into practice, we started from a previously reported dichlorostiboranyl platinum complex **42**,²⁶⁸ which features three chlorides decorating the central core. Treatment of complex **42** with three equivalents of TIF in the presence of donating solvent CH₃CN or ligand CNCy, afforded complexes **52** and **53** quantitatively at

room temperature. Isolated complexes **52** and **53** are very soluble in organic solvents CH_2Cl_2 , CHCl_3 and moderately soluble in CH_3CN .

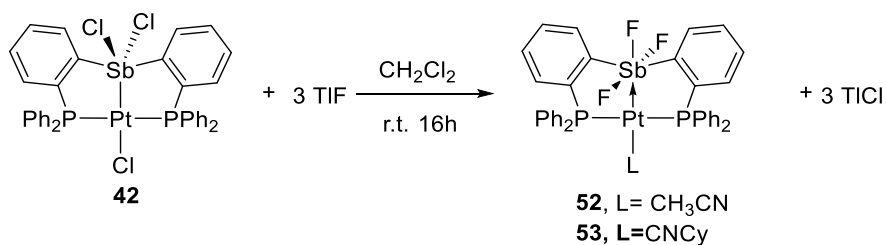


Figure 101. Synthesis of **52** and **53**.

The ^{31}P NMR spectrum of **52** and **53** displays a doublet at 71.8 ppm, with a $J_{\text{F-P}}$ of 11.7 Hz and a $J_{\text{Pt-P}}$ of 3462 Hz. Similar signal pattern was observed with **53**, showing a resonance at 75.9 ppm, with a $J_{\text{F-P}}$ of 14.8 Hz and a $J_{\text{Pt-P}}$ of 3131 Hz. For both complexes, the $J_{\text{Pt-P}}$ coupling constants are relatively high, comparable to the values found for zero valent complexes forming adducts with a variety of Lewis acids.^{18-19, 269-271} The reduced platinum center may be induced upon fluoride coordination to the antimony center, a phenomenon consistent with the above mentioned case of complex **B**. ^{19}F NMR spectra further supported the coordination of three fluorides to antimony. In complex **52**, two signals in a 2:1 intensity ratio were observed with the chemical shifts of -79.5 ppm and -113.4 ppm, respectively, which could be assigned to the two equatorial fluorine atoms and one axial fluorine atom bound to antimony. The same assignment applies to complex **53**, which features two resonances at -85.1 and -11.5 ppm.

The crystal structures of complexes **52** and **53** were obtained and subjected to X-ray single crystal diffraction analysis. The results confirmed that the three chloride ligands have been fully exchanged with three fluoride ligands, with two fluorine atoms trans from each other

and one fluorine atom trans from the platinum atom. As a result, the antimony atom is in an octahedral geometry in both structures, as shown by the F(1)-Sb-Pt, F(2)-Sb-F(3) and C(1)-Sb-C(19) angles which are close to linearity (Table 5). The platinum centers of these two complexes retained a square planar environment, with the difference being the replacement of the chloride ligand by acetonitrile or cyclohexylisocyanide. This square planar geometry is also evidenced by the Sb-Pt-(N1 for **52**, C37 for **53**) and P(1)-Pt-P(2) angles which are close to linearity. The most notable features of these structures are the Sb-Pt bond distances of 2.57974(19) in **52**, and 2.6215(11) in **53**, which are significantly longer than that found in complex **42** (2.4408(5) Å). While the Sb-Pt bond in complex **42** has been described as a covalent bond, the lengthening of the Sb-Pt bond distances in **52** and **53** suggests a polarized bonding situation, reminiscent to the polarization of Sb-Pt bonding towards platinum encountered in **B**.

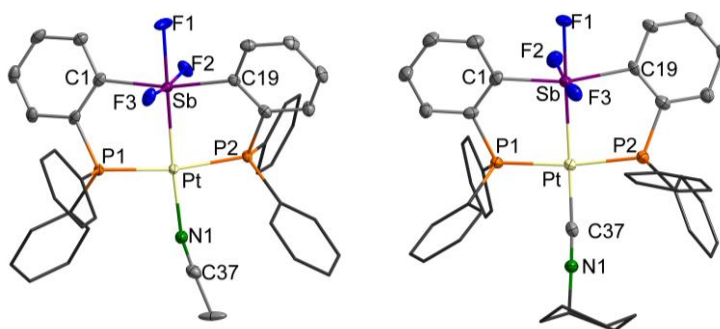


Figure 102. Solid state structure of **52** (left) and **53** (right). Thermal ellipsoids are drawn at the 50% probability level. Phenyl groups are drawn in wireframe. Hydrogen atoms and solvent molecules are omitted for clarity. Relevant metrical parameters can be found in the text or the experimental section.

Table 5. Selected bond lengths (Å) and angles (°) for complexes **52**-CH₃CN and **53** as determined crystallographically.

| Parameter | 52 | 53 |
|------------------|--------------|-------------|
| Sb-Pt | 2.57974(19)Å | 2.6215(11)Å |
| Pt-N1 (or C37) | 2.125(2)Å | 2.005(5)Å |
| F(1)-Sb-Pt | 178.65(6)° | 172.71(9)° |
| F(2)-Sb-F(3) | 172.33(6)° | 168.73(12)° |
| F(1)-Sb-Pt | 168.20(9)° | 166.03(17)° |
| Sb-Pt-N1(or C37) | 176.39(6) | 171.35(13) |
| P(1)-Pt-P(2) | 170.49(2) | 172.31(4) |

To achieve a better understanding of the Sb-Pt bonding in **52** and **53**, both structures have been studied computationally using DFT methods (Gaussian program, functional: BP86; mixed basis set: Sb/Pt: cc-pVTZ; P: 6-31g(d'); F: 6-31+g(d'); C/N/H: 6-31g). Optimization was first performed on both structures and yielded a good agreement between the optimized structures and experimental values (Experimental section). Frequency calculations further confirmed the accuracy of optimization, since no imaginary frequency was found. The optimized structures were then subjected to NBO analysis, which identified natural localized molecular orbitals (NLMO) for the Sb-Pt interaction in the two complexes. The NLMO of both complexes were shown to have a larger orbital contribution from platinum (Sb: 13.48%/Pt: 69.56% for **52**-CH₃CN; Sb: 34.96%/Pt: 55.01% for **52**-CNCy). The result is in contrast to the electron distribution found in complex **42**, which features a slightly larger orbital contribution from antimony than platinum (Sb: 49.09% / Pt: 45.12%). It can be concluded that the Sb-Pt bonding of complexes **52** and **53** is polarized towards platinum, indicating a more reduced platinum center, which is consistent with the high J_{Pt-P} coupling constant observed in

the ^{31}P NMR spectra. Based on formal oxidation state assignment, the complex could be described as $\text{Sb}^{\text{V}}\text{Pt}^0$, with the platinum center being stabilized by a $\text{Pt}\rightarrow\text{Sb}$ donor-acceptor interaction. This supported dative bonding depiction, involving an electron rich metal and a Lewis acidic site, resembles the dative bonds in Lewis base-Lewis acid adducts of general formula $(\text{PCy}_3)_2\text{Pt}\rightarrow\text{LA}$ (Figure 104). However, it is worthwhile to note that the platinum center in **52** and **53** displays a square planar geometry because of coordination of a donating ligand trans from the acidic antimony center. This differs from the T-shaped geometry encountered in the reported $(\text{PCy}_3)_2\text{Pt}\rightarrow\text{LA}$ examples. It is likely that the platinum center in **52** and **53** is less sterically encumbered than that in $(\text{PCy}_3)_2\text{Pt}\rightarrow\text{LA}$, making it well-suited for catalysis.

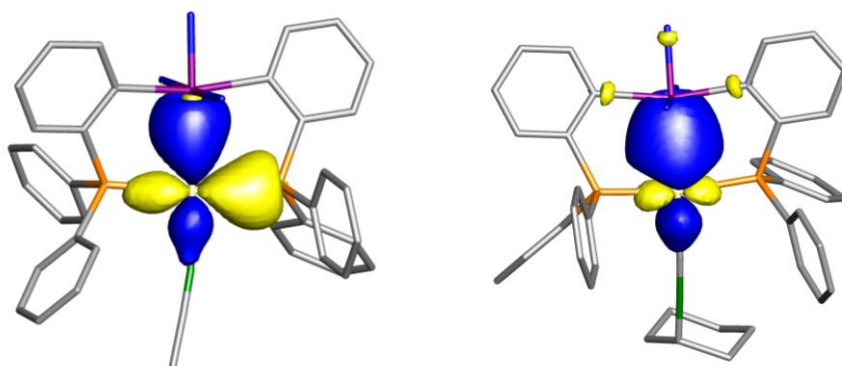


Figure 103. NBO plots of the major Sb-Pt bonding interactions in **52** (left) and **53** (right) (isodensity value = 0.04). Hydrogen atoms are omitted.

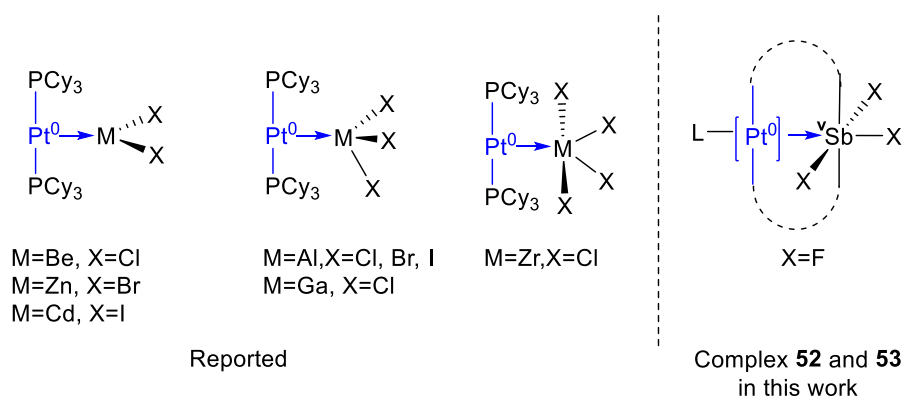


Figure 104. Reported examples showing a zero valent platinum center forms dative bonds with Lewis acids. Complex **52** and **53** features a similar dative bonding to the Lewis acidic antimony site.

5.3 Cationic monofluorostiboranyl platinum complexes

Noting the isoelectronic relationship of the platinum center in in **52** and **53** with the gold centers in $[\mathbf{C}]^+$ and $[\mathbf{D}]^+$, in which the gold features the formal oxidation state +I and forms a dative $\text{Au} \rightarrow \text{Z}$ -ligand bond, we decided to test if the Lewis acidic platinum center would be competent for electrophilic catalysis, such as hydroamination of alkynes or enyne cyclizations, a set of reactions that $[\mathbf{C}]^+$ and $[\mathbf{D}]^+$ were reported to be capable of catalyzing.

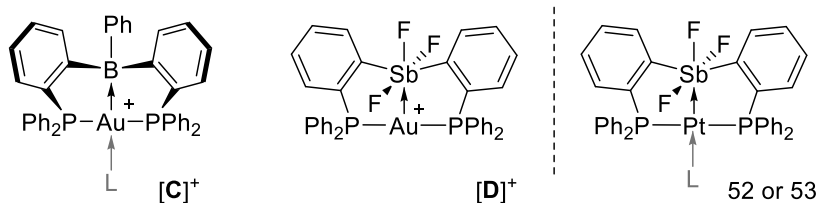


Figure 105. Side by side comparison showing complex **52** or **53** and recently reported $[\text{Au} \rightarrow \text{Z}]^+$ complexes of type $[\mathbf{C}]^+$ and $[\mathbf{D}]^+$.

However, we found that **52** and **53** were not active, presumably because the zero-valent platinum center is not Lewis acidic enough. This prompted us to search for strategies to enhance the Lewis acidity of the platinum center, while retaining its coordination environment.

With this in mind, we turned our attention to increase the σ -accepting ability of the antimony ligand, as means to increase the Pt \rightarrow Z-ligand interaction. While the Lewis acidity of antimony (III) center can be readily increased by oxidation to antimony (V), further increasing the Lewis acidity of antimony (V) is challenging. Inspired by the idea that remote Lewis acid binding to basic sites on the ligand framework can cause alteration to the metal electronics and reactivity,²⁷² we decided to try the acid binding to the three fluoride ligands using a Brønsted acid or a Lewis acid, as depicted in Figure 106.

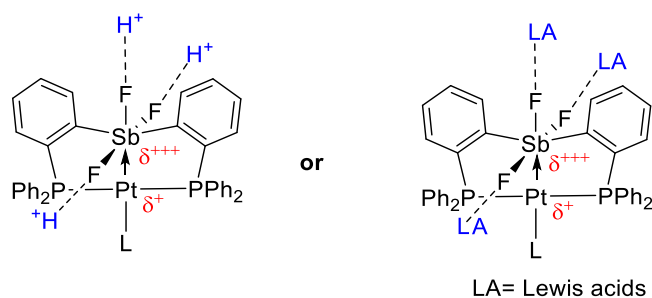


Figure 106. Hypothesized ligand post-synthetic modification through acid binding to the fluorine atoms, in order to enhance the Lewis acidity at the metal center.

In pursuit of this idea, we chose HBF_4 as the Brønsted acid, given that the non-coordinating counter anion BF_4^- is less likely to enter the primary coordination sphere. Reaction of complexes **52** and **53** with excess $\text{HBF}_4 \cdot \text{Et}_2\text{O}$ in CH_2Cl_2 did not show obvious changes in colour or precipitation. When the reaction was carried out in an NMR tube, a vigorous gas evolution was observed for about 5 mins. Sizable colourless crystals formed on the side of the NMR tube over the course of 12 h. These crystals were identified as new products **54** and **55** in 30-40% yield (Figure 107).

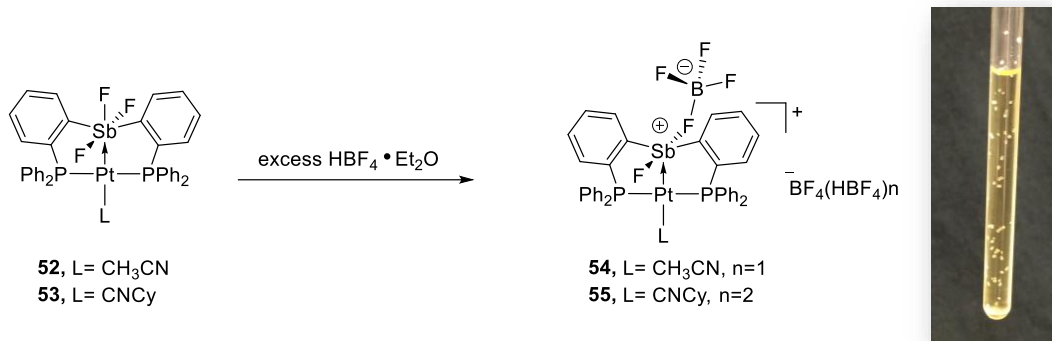


Figure 107. Reaction of complexes **52** and **53** with HBF_4 . The insert shows the crystals of **54**.

The single crystal structures of **54** and **55** showed that instead of obtaining fluorine-hydrogen bonding as expected, two fluorides were abstracted by HBF_4 , resulting in cationic complexes, as shown in Figure 108. Both of these complexes feature a square pyramidal antimony center, with two carbon atoms and two fluorine atoms defining the square plane. One of the fluorine atoms is associated with the BF_4^- unit. While this BF_4^- unit is interacting with antimony in the primary coordination sphere, another BF_4^- unit forms an extended chain with excess HBF_4 molecules by hydrogen bonding in the lattice, which could be formulated as $\text{BF}_4^-(\text{HBF}_4)_2$ and $\text{BF}_4^-(\text{HBF}_4)$ in **54** and **55**, respectively. Interestingly, excess HBF_4 did not protonate the platinum bound CH_3CN and CNCy ligands, leaving the platinum center in square planar geometry. This phenomenon suggests that the platinum center is more acidic than the proton of HBF_4 . Most importantly, the crystal structures reveal significant contractions of the Sb-Pt distances from 2.57974(19) Å in **52** to 2.4528(6) Å in **54** and from 2.6215(11) Å in **53** to 2.4861(5) Å in **55**. The shortened Sb-Pt distances are comparable to that observed in complex **42** (2.4408(5) Å) (Table 1 and Table 6). This fact indicates that the resulting

complexes may have similar redox states to that of complex **42**, which we described as a $\text{Sb}^{\text{IV}}\text{Pt}^{\text{I}}$ complex with a covalent Sb-Pt bond. While it was expected that fluoride abstraction should lead to the formation of a stibonium center (cationic antimony (V)) and afford a stronger donor-acceptor interaction $\text{Pt}(0)\rightarrow[\text{Sb}(\text{V})]^+$ interaction, the resulting $\text{Sb}^{\text{IV}}\text{Pt}^{\text{I}}$ core could be considered as an extreme case of the $\text{Pt}\rightarrow\text{Sb}$ interaction. That is, the stibonium center is highly Lewis acidic and pulls electron density towards itself, resulting in a reduced Sb^{IV} and an oxidized Pt^{I} center.

Structural information regarding the isolated crystalline products were also collected by multi-nuclear NMR. Crystalline product **54** showed two broad resonances at 59.3 ppm (75.5%, $J_{\text{Pt-P}}=2649$ Hz) and 50.8 ppm (24.5%, $J_{\text{Pt-P}}=2311$ Hz) in the ^{31}P NMR spectra. Similarly, isolated crystals of product **55** showed two set of signals at 48.5 ppm (60%, $J_{\text{Pt-P}}=2226.8\text{Hz}$) and 46.5 ppm (40%, $J_{\text{Pt-P}}=2230.3\text{Hz}$). When compared to complexes **52** and **53** (**52**: δ_{P} 75.9 ppm, $J_{\text{Pt-P}}$ 3462 Hz/**53**: 71.8 ppm, $J_{\text{Pt-P}}$ 3131 Hz), the chemical shifts of **54** and **55** appear to be notably upfield, and the coupling constants (2200-2700Hz) are significantly reduced. Such phenomena are typically observed for phosphine-platinum complexes upon oxidization. The observation of two signals in ^{31}P NMR spectra of these two complexes remains unexplained. Possibly it is the dynamic coordination of BF_4^- unit to the antimony center. This might also explain the broadened ^{31}P NMR signals of **54**. Two signals at -149.3ppm and -150.5 ppm in the ^{19}F NMR spectrum of **54**, and -147.3 and -149.2 ppm of **55** are diagnostic of the inner and outer sphere BF_4^- counter anion. The fluorine signals for the coordinated Sb-F are not observed.

To probe the electronic structure changes, NBO analysis were carried out on the optimized structures of **54** and **55** (Gaussian program, functional: BP86; mixed basis set: Sb/Pt:

cc-pVTZ; P: 6-31g(d'); F: 6-31+g(d'); C/N/H: 6-31g). As indicated by the NLMO of these two complexes, the Sb-Pt bond bears a slightly larger orbital contribution from antimony than platinum (Sb: 47.813%/ Pt: 45.690% for **54**; Sb: 46.686%/Pt: 45.943% for **55**), which are very close to that found in complex **42** (Sb: 49.09% / Pt: 45.12%). Therefore, the computational results suggest profound covalent character of the Sb-Pt bond in the cationic complexes, correlating strongly with the shortened bond distances found for these complexes. Taken collectively, the data corroborates the view that, as a consequence of fluoride abstraction, the electron density is pulled back towards antimony, leading to the re-formation of covalent bonding between antimony and platinum.

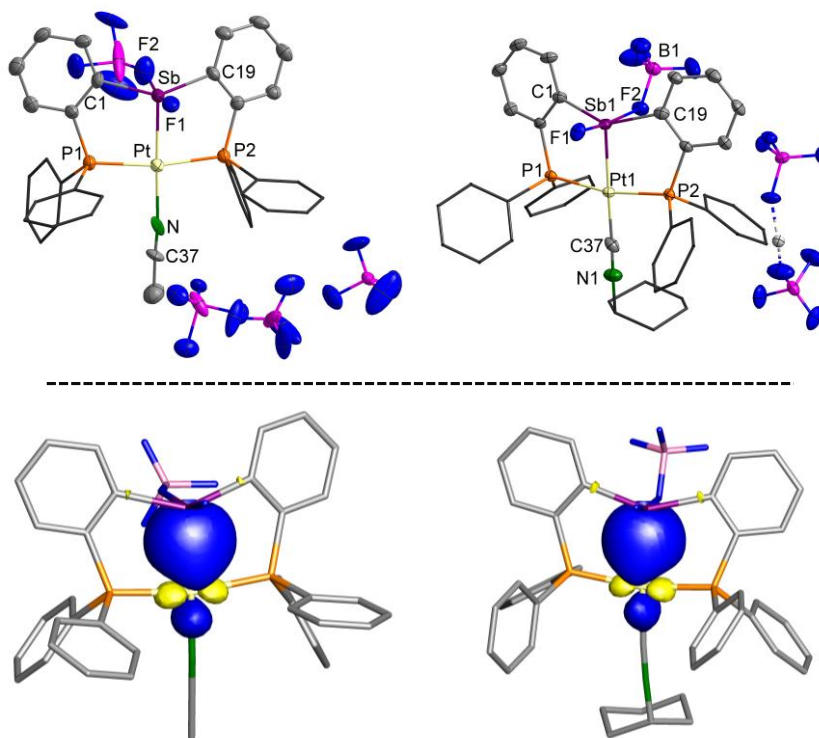


Figure 108. Top: Solid state structure of **54** (Top left) and **55** (Top right). Thermal ellipsoids are drawn at the 50% probability level. Phenyl groups are drawn in wireframe. Hydrogen atoms and solvent molecules are omitted for clarity. Relevant metrical parameters can be found in the experimental section. Bottom: NBO plots of the major Sb-Pt bonding interactions in **54** (Bottom left) and **55** (Bottom right). (isodensity value = 0.05). Hydrogen atoms are omitted.

Table 6. Selected bond lengths (Å) for complexes **54** and **55** as determined crystallographically.

| Parameter | 54 | 55 |
|----------------|------------|-------------|
| Sb-Pt | 2.4528(6) | 2.4861(5) |
| Pt-N1 (or C37) | 2.152(9) | 1.985(7) |
| Sb-F(1) | 1.972(7) | 1.947(4) |
| Sb-F(2) | 2.499(8) | 2.486(4) |
| F(1)-Sb-Pt | 98.61(16)° | 102.09(14)° |

Table 6 Continued.

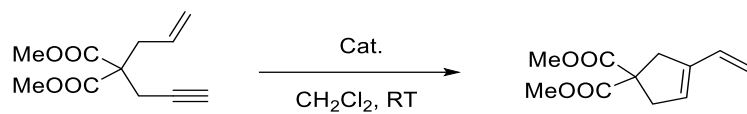
| Parameter | 54 | 55 |
|-------------------|-----------|-------------|
| F(1)-Sb-F(2) | 168.7(3)° | 175.31(17)° |
| F(2)-Sb-Pt | 92.4(2)° | 82.57(10)° |
| Sb-Pt-N1 (or C37) | 177.5(2) | 175.6(2) |
| P(1)-Pt-P(2) | 169.96(7) | 168.00(6) |

5.4 Catalytic properties of the cationic platinum complexes

We speculated that the metal centers in the two cationic complexes are highly Lewis acidic, and sought to use them as electrophilic catalysts for enyne cyclization reactions.²⁷³⁻²⁷⁸ As a powerful reaction to construct cyclic compounds, enyne cyclization reactions have been catalyzed by late transition metal complexes, including platinum complexes.²⁷⁹⁻²⁸⁰ Our model reactions were carried out using 1,6-enyne (dimethyl-2-allyl-2-(prop-2-ynyl)malonate) at room temperature in CH₂Cl₂, in the presence of 2% catalyst loading (Table 7). Catalysts were generated in situ, by reaction of complexes **52** and **53** with HBF₄, leading to full conversion of 1,6-enyne into vinylcyclopentene as the only product (entry 2).

In contrast, HBF_4 did not catalyze the reaction even after 12 hours (entry 1). For the purpose of proving the catalytic reactivity of the cationic platinum complexes, the isolated crystalline product of **54** was also used as catalyst, which showed comparable efficiency as the catalyst generated in situ (entry 4). While HBF_4 was considered to play the role of fluoride abstraction, other strongly Lewis acidic compounds were also used as additive to activate the precatalyst **52**. A notable Lewis acid $\text{B}(\text{C}_6\text{F}_5)_3$ was chosen for the test. Its stoichiometric reaction with the precatalyst **52** was monitored by ^{31}P NMR and ^{19}F NMR spectroscopy, which indicates the successful abstraction of fluoride and formation of cationic platinum complexes (Experimental section). For the same reason, a newly developed stiborane $\text{SbCat}^{\text{Cl}}(\text{C}_6\text{F}_5)_3$ Lewis acid was also used to abstract the fluoride (Experimental section). Under the same conditions, the combination of precatalyst **52** and Lewis acid additives gave similar results, supporting our hypothesis that Lewis acids can also abstract the fluorides and impart reactivity to the metal center (entry 3-4). To gather more information about the reactivity of the metal center, **55** was also tested as a catalyst for the same model reaction. After 12 hours, only 30 percent conversion was observed (entry 5). Given that the catalysis step necessitates the dissociation of the Pt-bound ligand, the reduced efficiency of catalyst **55** might be rationalized by considering the greater donicity of CNCy when compared to CH_3CN .

Table 7. 1,6-Enyne cyclization catalysis.



| Entry | Catalyst (mol%) | t | Conversion [%] |
|-------|--|------|----------------|
| 1 | HBF ₄ (4%) | 12 h | n.r. |
| 2 | 52 (2%) +HBF ₄ (4%) | 2h | 100% |
| 3 | 52 (2%) +B(C ₆ F ₅) ₃ (4%) | 2h | 100% |
| 4 | 52 (2%) +SbCat ^{Cl} (C ₆ F ₅) ₃ (2%) | 3h | 100% |
| 5 | 54 | 2h | 100% |
| 6 | 55 | 12h | 53% |

Conversion was determined by ¹H NMR spectroscopy. n.r.= no reaction. Information concerning the conversion was provided in the experimental section.

The results in Table 7 highlighted the ability of the cationic platinum complex **54** to activate alkynes towards nucleophilic attack. It is important to note that other Lewis acids-activated cationic catalyst analogues, although not structurally characterized, showed comparable catalytic reactivity. To further investigate the potential of **54** to catalyze other 1,6-enyne derivatives, (diethyl-2-allyl-2-(prop-2-ynyl)malonate, 3-(prop-2-yn-1-yloxy)prop-1-ene and N-allyl-4-methyl-N-(prop-2-yn-1-yl)benzenesulfonamide were also used for catalysis under the same conditions. However, only (diethyl-2-allyl-2-(prop-2-ynyl)malonate was shown to be converted into the desired product at similar rate. The other two substrates remain intact. Similarly, we also tested hydroamination and propargylic amide cyclization reactions. Although the reaction proceeded, only low conversion (4-20%) was observed, suggesting deactivation of the catalyst (Experimental section).

5.5 Conclusion

In this work, we demonstrated that the dichlorostiboranyl-platinum chloride complex $[\text{Cl}_2\text{R}_2\text{SbPtCl}]$ can be converted into trifluorostiborane-platinum complexes of general formula $[\text{F}_3\text{R}_2\text{SbPtL}]$. The driving force for this process likely originates from the preference of the Lewis acidic antimony center for harder anions, such as fluoride. As a consequence of this anion exchange event, internal redox reactions occurred, affording a more oxidized stiborane antimony center, and a more reduced platinum center. In response to the oxidation state changes, the Sb-Pt bond changes from a more covalent bonding interaction into a donor-acceptor interaction of $\text{Pt} \rightarrow \text{Sb(V)}$ character. While the trifluorostiborane possesses notable σ -

accepting ability to confer Lewis acidity to the adjoining metal, the inherently reduced platinum is not competent for electrophilic catalysis towards nucleophilic addition to alkyne.

The catalytic reactivity of the platinum center was turned on by reacting the neutral stiborane platinum complex with HBF₄ or Lewis acids, which afforded the cationic stiboranyl platinum complex. The conversion of the stiborane back to a different form of stiboranyl, illustrates the ligand-centered coordination non-innocence in an opposite way. Due to the cationic nature of the resulting complex, the platinum demonstrated considerable reactivity towards enyne cyclization. As a whole, this work highlighted the ability of the antimony ligand to exhibit reversible coordination non-innocent behavior. More importantly, the ligand-centered coordination non-innocence can significantly impact the electronic properties and reactivity of the metal, fitting the paradigm of ligand-mediated metal catalysis.

5.6 Experimental

General considerations. *cis*-PtCl₂(Et₂S)₂,¹⁷⁶ [(*o*-(Ph₂P)C₆H₄)₂SbCl] and complex **42** were prepared according to the reported procedures. Solvents were dried by passing through an alumina column (n-pentane and CH₂Cl₂) or by reflux under N₂ over Na/K (Et₂O and THF). All other solvents were used as received. Commercially available chemicals were purchased and used as provided (Commercial sources: Acros Organics for TIF, and Bu₄NF; Strem chemicals for CyNC). Ambient temperature NMR spectra were recorded on a Varian Unity Inova 500 FT NMR (499.42 MHz for ¹H, 125.58 MHz for ¹³C, 469.89 MHz for ¹⁹F, 202.16 MHz for ³¹P). Chemical shifts δ are given in ppm and are referenced against residual solvent

signals (^1H , ^{13}C) or external $\text{BF}_3\text{-Et}_2\text{O}$ (^{19}F) and 85% H_3PO_4 (^{31}P). IR spectra were recorded on a Mattson ATI Genesis FT-IR spectrometer using KBr pellets. Elemental analyses were performed at Atlantic Microlab (Norcross, GA).

Synthesis of 52. A CH_2Cl_2 solution (8 mL) of complex **42** (460 mg, 0.49 mmol) was mixed with 4 mL CH_3CN solvent. After the mixture was stirred for 30 min, solid TIF (330mg, 1.46 mmol) was added. The reaction mixture was stirred for 16 h. and resulted in pale yellow suspension. After filtration through celite, the solvent was reduced under vacuum, affording an oily residue. This residue was treated with Et_2O (10 mL) leading to the precipitation of **52** as a pale yellow solid. Compound **52** was dried under vacuum and obtained in a 56.2% yield (256 mg). Crystals of **52**-(CDCl_3) suitable for X-ray diffraction were obtained from slow evaporation of a CDCl_3 solution of **52**. ^1H NMR (499.42 MHz; CDCl_3): δ 7.01 (m, 2 H, *o*- $\text{P}(\text{Sb})\text{C}_6\text{H}_4$), 7.35 (t, 2 H, *o*- $\text{P}(\text{Sb})\text{C}_6\text{H}_4$, $^3J_{\text{H-H}} = 7.49$ Hz), 7.45–7.54 (m, 16 H), 7.64 (t, 2 H, *o*- $\text{P}(\text{Sb})\text{C}_6\text{H}_4$, $^3J_{\text{H-H}} = 7.49$ Hz), 7.86 (m, 4 H), 8.59 (d, 2 H, *o*- $\text{P}(\text{Sb})\text{C}_6\text{H}_4$, $^3J_{\text{H-H}} = 7.49$ Hz). $^{13}\text{C}\{^1\text{H}\}$ NMR (125.58 MHz; CDCl_3): δ 128.5 (q, $J_{\text{C-P}} = 28.9$ Hz), 129.3 (t, $J_{\text{C-P}} = 4.0$ Hz), 129.4 (t of d, $-\text{C}_6\text{H}_5$, CH, $J_{\text{C-P}} = 42.7$ Hz, $J = 5.9$ Hz), 131.9 (d, $-\text{C}_6\text{H}_5$, CH, $J_{\text{C-P}} = 4.9$ Hz), 132.7 (s), 133.5 (t, $J_{\text{C-P}} = 2.8$ Hz), 134.2 (t of d, $-\text{C}_6\text{H}_5$, CH, $J_{\text{C-P}} = 24.6$ Hz, $J = 7.2$ Hz), 135.3 (t, $J_{\text{C-P}} = 8.5$ Hz), 137.7 (t, $J_{\text{C-P}} = 29.1$ Hz), 149.3 (t, $J_{\text{C-P}} = 17.7$ Hz). $^{31}\text{P}\{^1\text{H}\}$ NMR (202.28 MHz; CDCl_3): δ 71.8 (d, $J_{\text{F-P}} = 11.7$ Hz, $J_{\text{Pt-P}} = 3462$ Hz), $^{19}\text{F}\{^1\text{H}\}$ NMR (470.2 MHz; CDCl_3): δ -83.8 (d, $2F_{\text{eq}}$, $J_{\text{Fa-Feq}} = 40.1$ Hz), -113.3 (t, $1F_{\text{a}}$, $J_{\text{Feq-Fa}} = 40.1$ Hz).

Synthesis of 53. CyNC (35 μL , 0.29 mmol) was added to a stirred CH_2Cl_2 (5 mL) solution of complex **1** (270 mg, 0.29 mmol). The solution turned from pale yellow to deep yellow

immediately. After the mixture was stirred for 30 min, solid TIF (195mg, 0.86 mmol) was quickly added. The reaction mixture was stirred for 16 h, which results in pale yellow suspension. After filtration through celite, the solvent was removed under vacuum, affording an oily residue. This residue was washed with 3 x 5 mL of Et₂O, leading to the precipitation of **53** as a pale yellow solid. Compound **53** was subsequently dried under vacuum and obtained in 58.6% yield (168 mg) as a pale yellow powder. Crystals of **53** suitable for X-ray diffraction were obtained by slow diffusion of Et₂O into a concentrated CH₂Cl₂ solution of **53** at room temperature. ¹H NMR (499.42 MHz; CDCl₃): δ 7.15 (q, 2 H, *o*-P(Sb)C₆H₄, ³J_{H-H} = 6.49 Hz), 7.51 (q, 6 H, ³J_{H-H} = 7.49 Hz), 7.60 (t, 4 H, ³J_{H-H} = 7.49 Hz), 7.64–7.66 (m, 12 H), 7.72 (t, 2 H, ³J_{H-H} = 7.99 Hz), 8.48 (d, 2 H, *o*-P(Sb)C₆H₄, ³J_{H-H} = 7.49 Hz). ¹³C{¹H} NMR (125.58 MHz; CDCl₃): δ 125.0 (t, J_{C-P} = 30.9 Hz), 125.8 (t, J_{C-P} = 30.1 Hz), 130.3 (t of d, -C₆H₅, CH, J_{C-P} = 37.7 Hz, J = 6.0 Hz), 131.1 (t, J_{C-P} = 4.5 Hz), 133.3 (s, -C₆H₅, CH), 133.6 (s), 133.9 (t, J_{C-P} = 4.2 Hz), 134.1 (t of d, -C₆H₅, CH, J_{C-P} = 27.9 Hz, J = 7.4 Hz), 135.3 (t, J_{C-P} = 7.8 Hz), 148.8 (t, J_{C-P} = 16.1 Hz). ³¹P{¹H} NMR (202.28 MHz; CD₂Cl₂): δ 75.9 ((d, J_{F-P} = 14.8 Hz, J_{Pt-P} = 3131 Hz), ¹⁹F{¹H} NMR (470.2 MHz; CD₂Cl₂): δ -85.1 (d, 2F_{eq}, J_{Fa-Feq} = 34.8 Hz), -112.5 (m, 1F_a, J_{Feq-Fa} = 34.8 Hz, J_{P-F} = 14.8 Hz).

General procedure for catalytic enyne cyclization reactions. Catalytic reactions were carried out in air. In a typical reaction, the enyne (~0.5 mmol) was dissolved in CH₂Cl₂ (2 mL). After addition of the catalyst (2 mol% loading), conversion was estimated using ¹H NMR spectroscopy.

Computational Details. Density functional theory (DFT) structural optimizations were carried with the Gaussian 09 suite of programs with effective core potentials on all heavy atoms (functional: BP86; mixed basis set: Sb/Au: cc-pVTZ-PP; P/Cl: 6-31g(d); C/O/H: 6-31g, F: 6-31+g(d')). The optimized structures, which are in good agreement with the solid state structures (Table 8, were subjected to a NBO analysis.²⁶⁰ The resulting NBOs were visualized and plotted using Jimp 2 program.¹⁷⁹

Crystallographic Measurements. The crystallographic measurements were performed at 110(2) K using a Bruker APEX-II CCD area detector diffractometer (Mo-K α radiation, $\lambda = 0.71069$ Å). In each case, a specimen of suitable size and quality was selected and mounted onto a nylon loop. The structures were solved by direct methods, which successfully located most of the non-hydrogen atoms. Semi-empirical absorption corrections were applied. Subsequent refinement on F² using the SHELXTL/PC package (version 6.1) allowed location of the remaining non-hydrogen atoms.

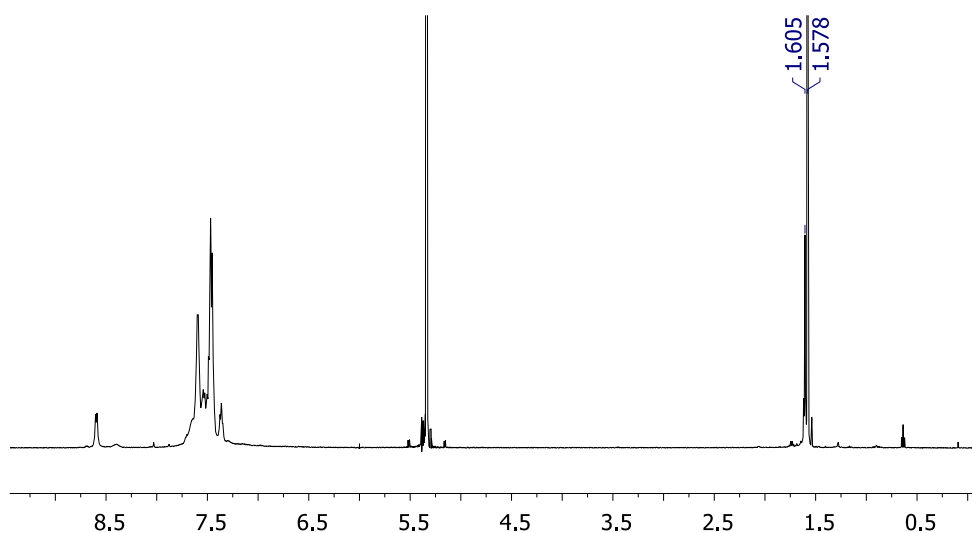


Figure 109. ¹H NMR spectrum of **52** in CD₂Cl₂.

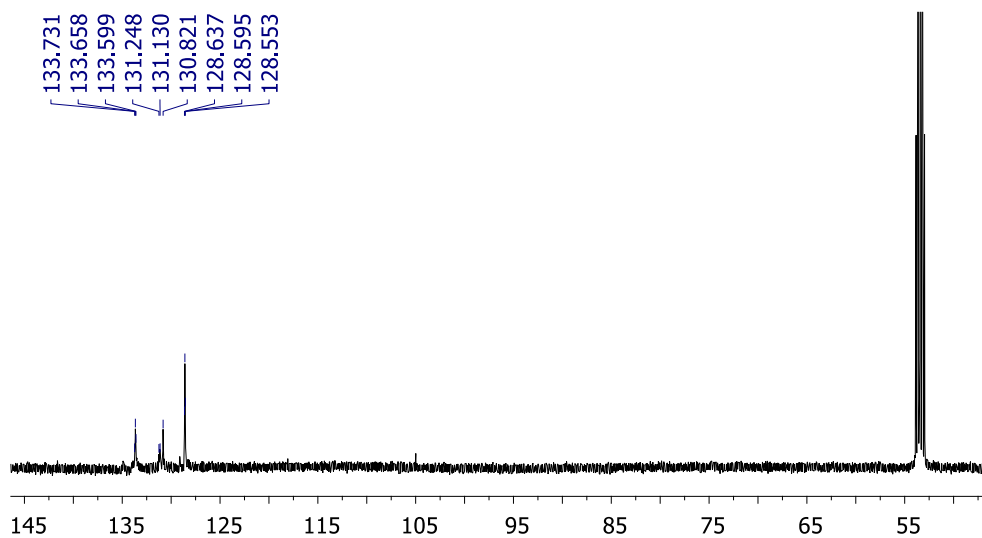


Figure 110. ^{13}C NMR spectrum of **52** in CD_2Cl_2 .

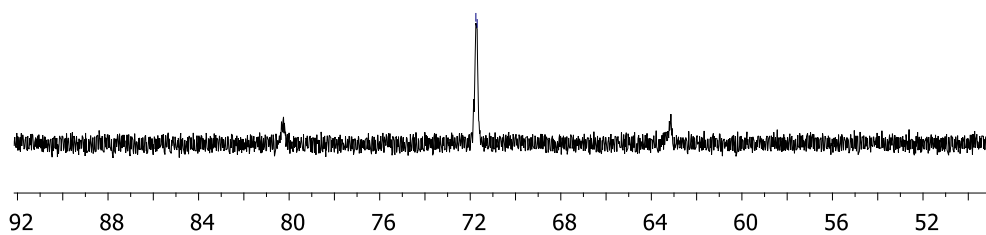


Figure 111. ^{31}P NMR spectrum of **52** in CD_2Cl_2 .

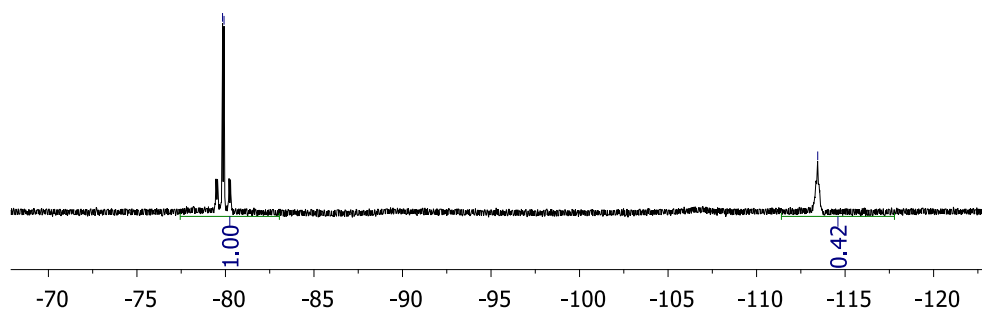


Figure 112. ^{19}F NMR spectrum of **52** in CD_2Cl_2 .

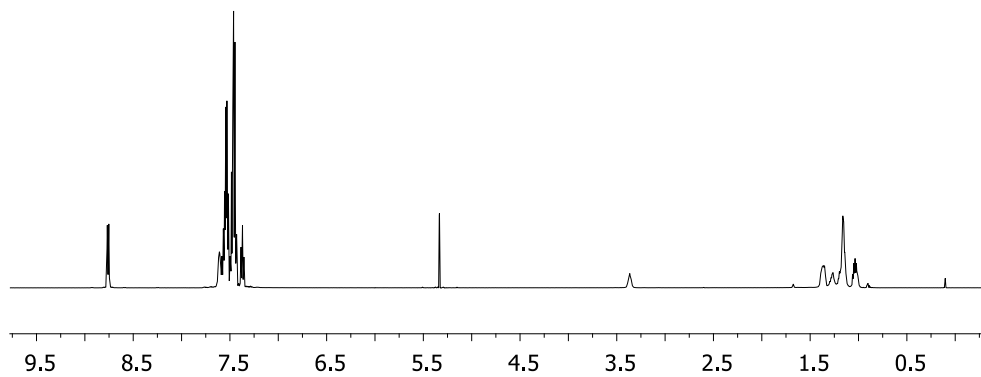


Figure 113. ^1H NMR spectrum of **53** in CD_2Cl_2 .

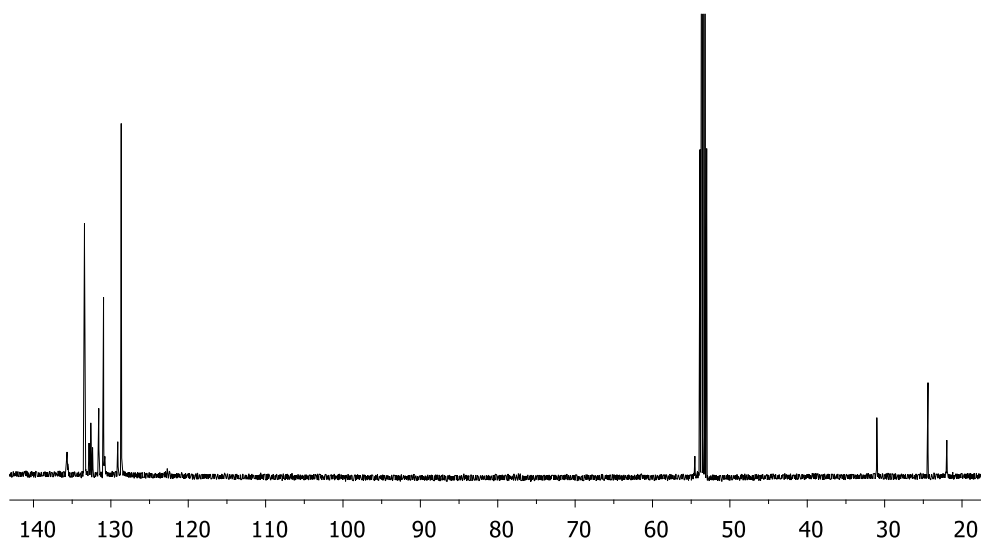


Figure 114. ^{13}C NMR spectrum of **53** in CD_2Cl_2 .

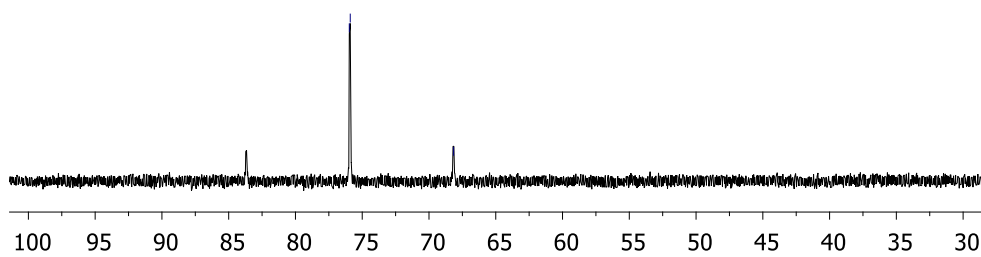


Figure 115. (above) ^{31}P NMR spectrum of **53** in CD_2Cl_2 . (below) Magnified spectrum corresponding to **53**.

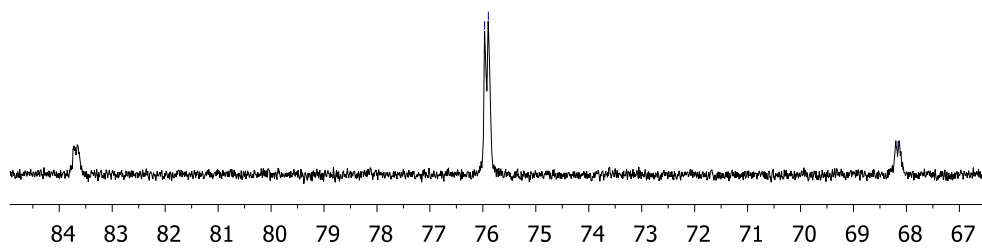


Figure 115. Continued

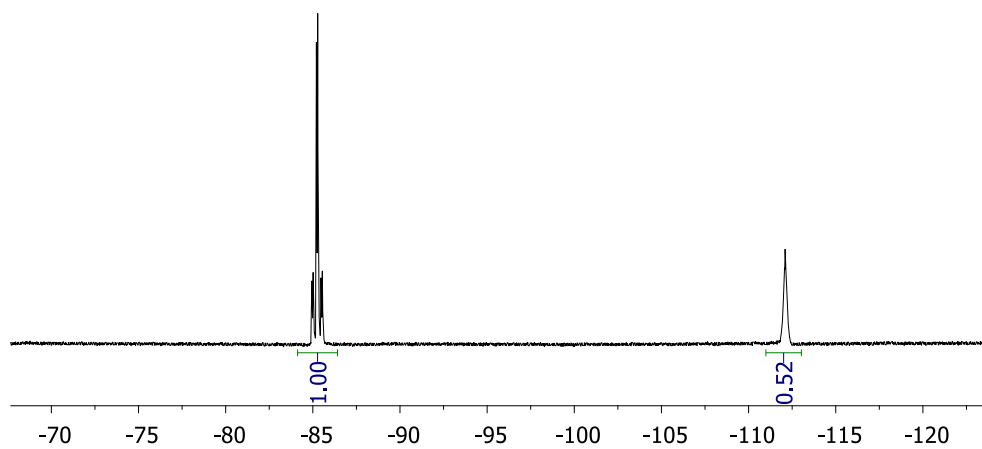


Figure 116. ^{19}F NMR spectrum of **53** in CD_2Cl_2 .

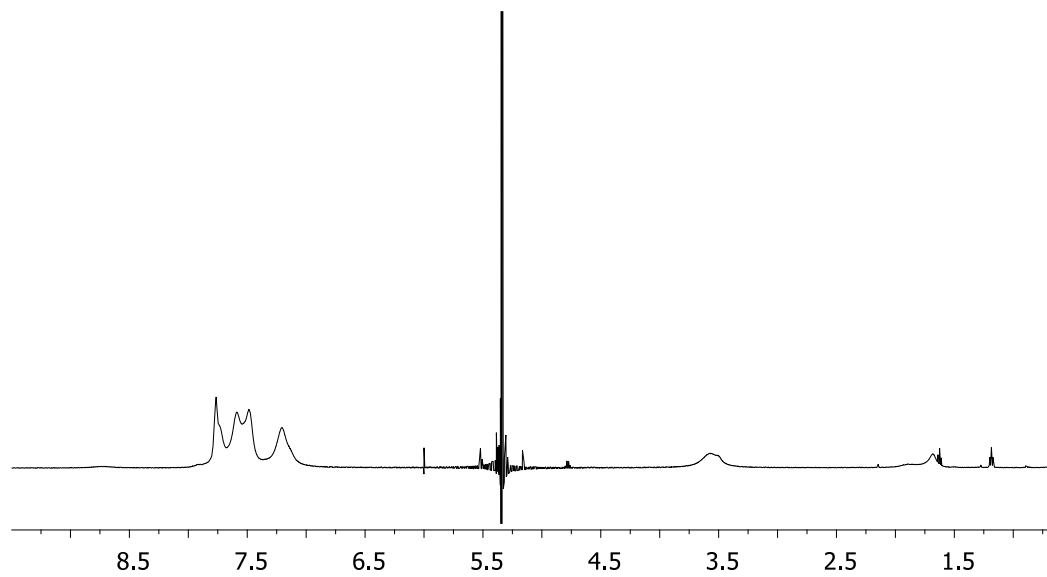


Figure 117. ^1H NMR spectrum of **54** in CD_2Cl_2 .

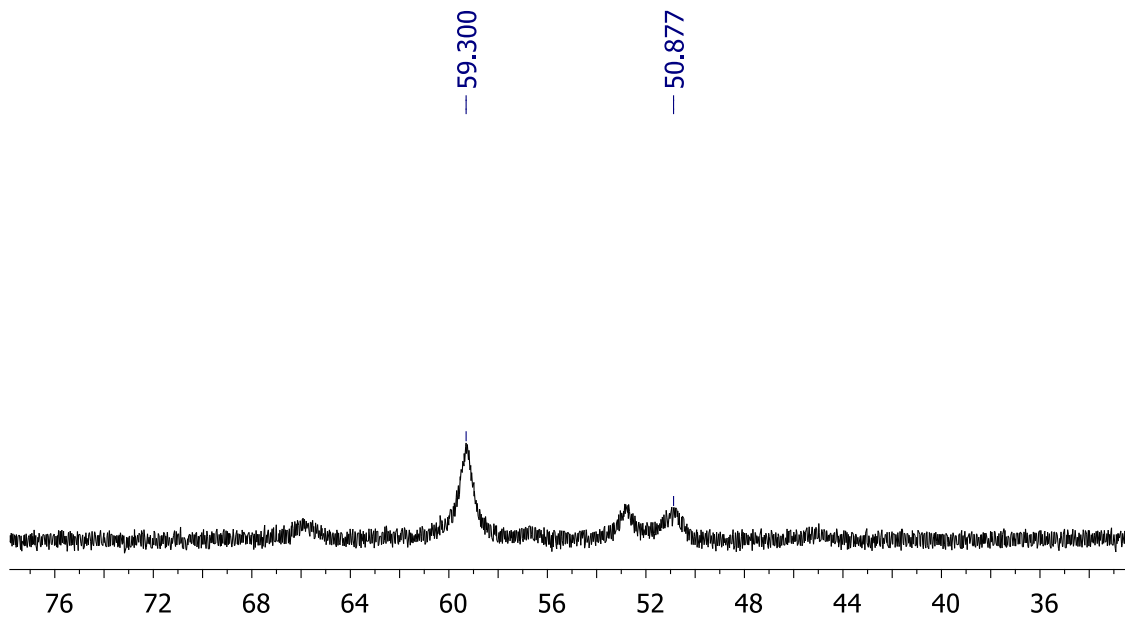


Figure 118. ^{31}P NMR spectrum of **54** in CD_2Cl_2 .

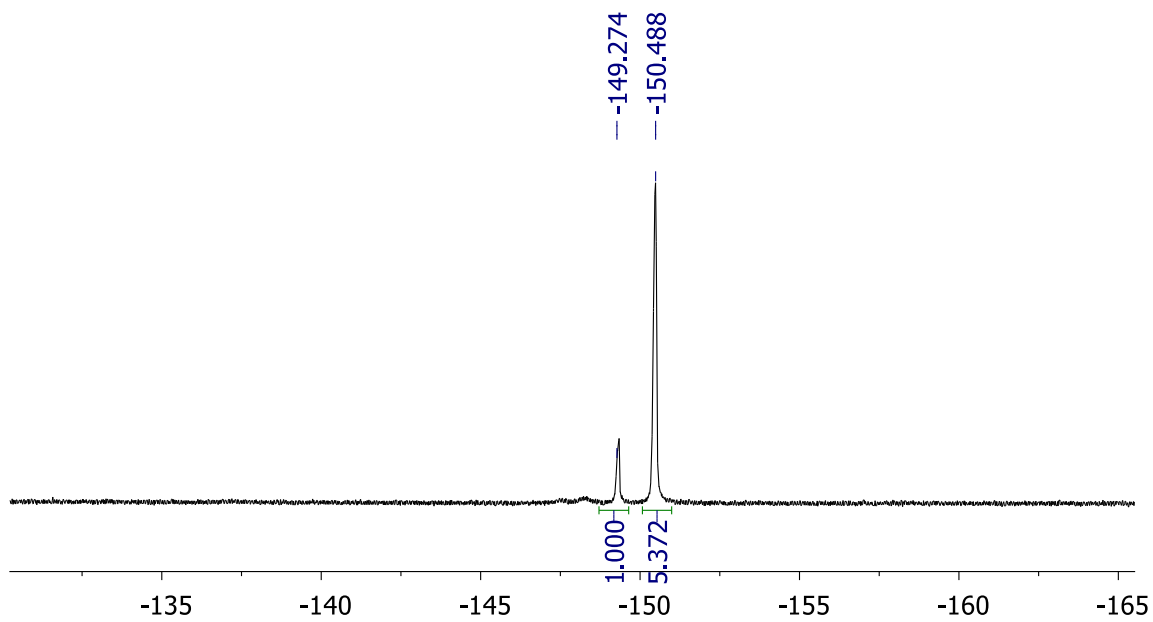


Figure 119. ^{19}F NMR spectrum of **54** in CD_2Cl_2 .

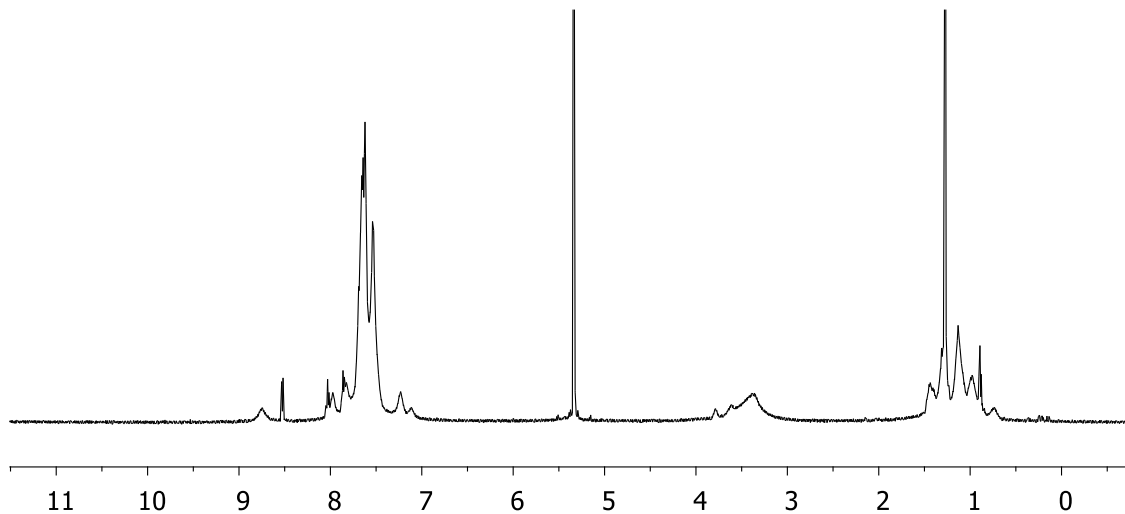


Figure 120. ^1H NMR spectrum of **55** in CD_2Cl_2 .

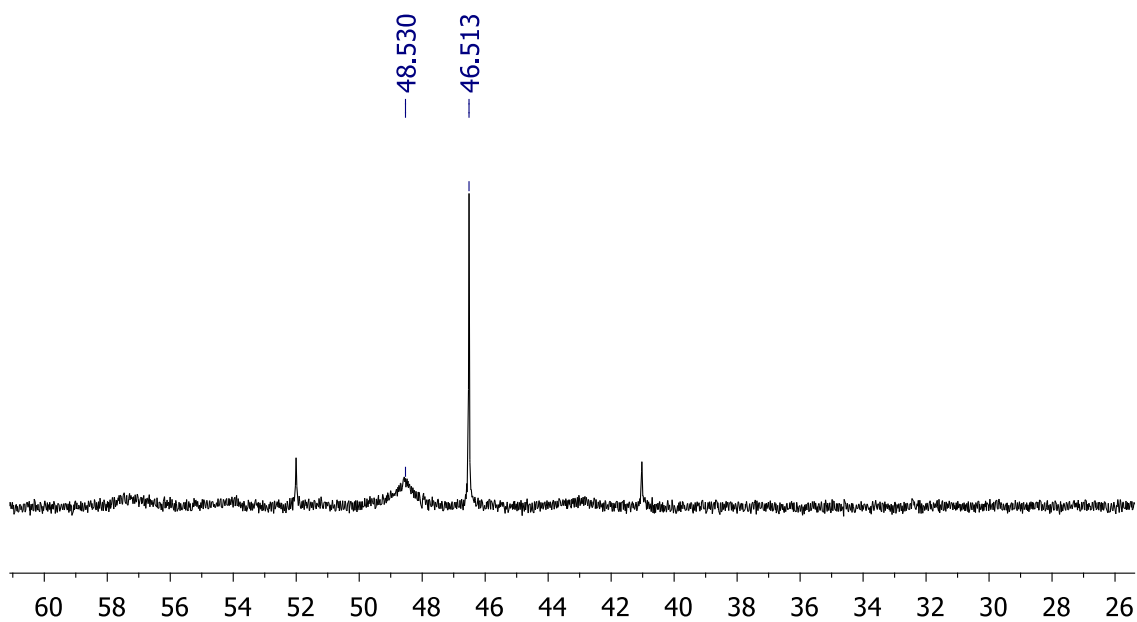


Figure 121. ^{31}P NMR spectrum of **55** in CD_2Cl_2 .

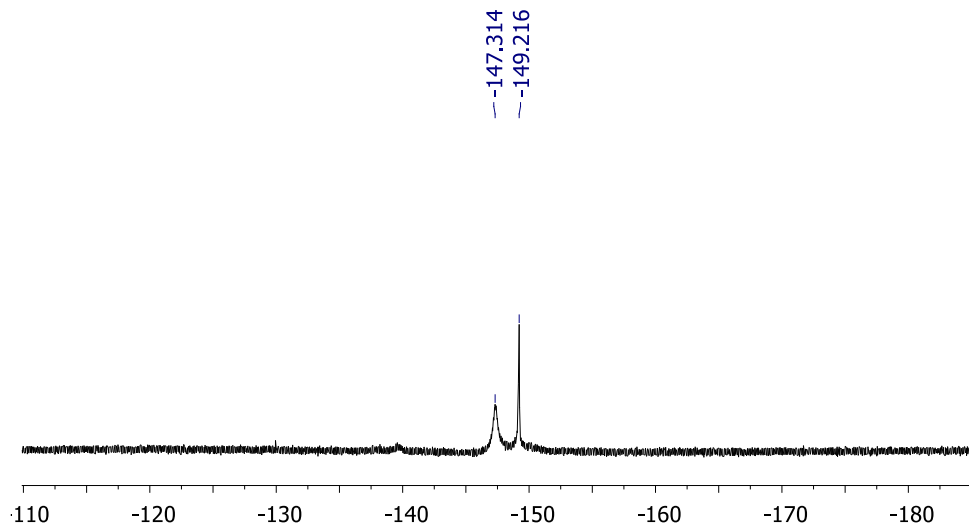


Figure 122. ^{19}F NMR spectrum of **55** in CD_2Cl_2 .

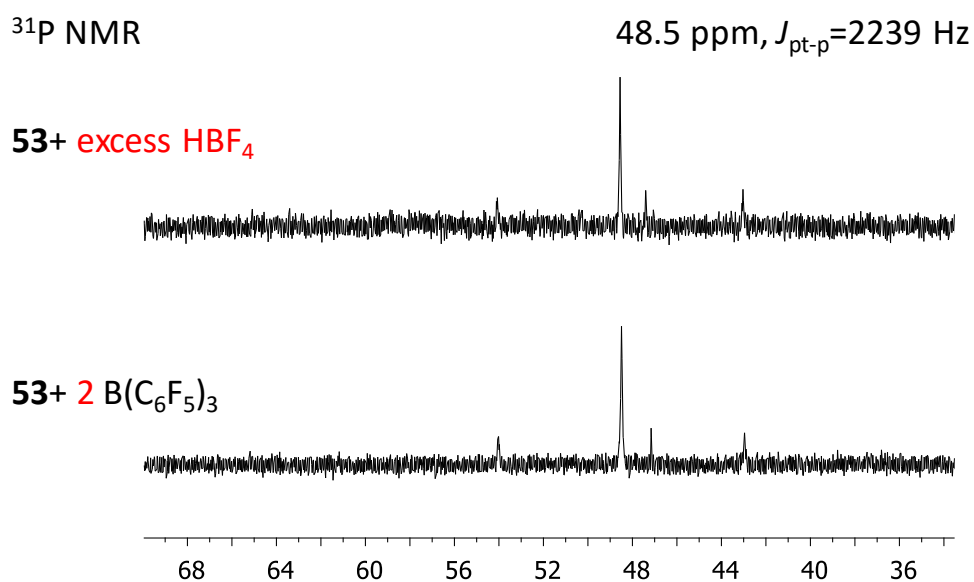


Figure 123. ^{31}P NMR spectra for reaction of **53** with excess HBF_4 or two equivalents of $\text{B}(\text{C}_6\text{F}_5)_3$ in CH_2Cl_2 , showing the same resonance at 48.5 ppm, $J_{\text{pt-p}} = 2239$ Hz.

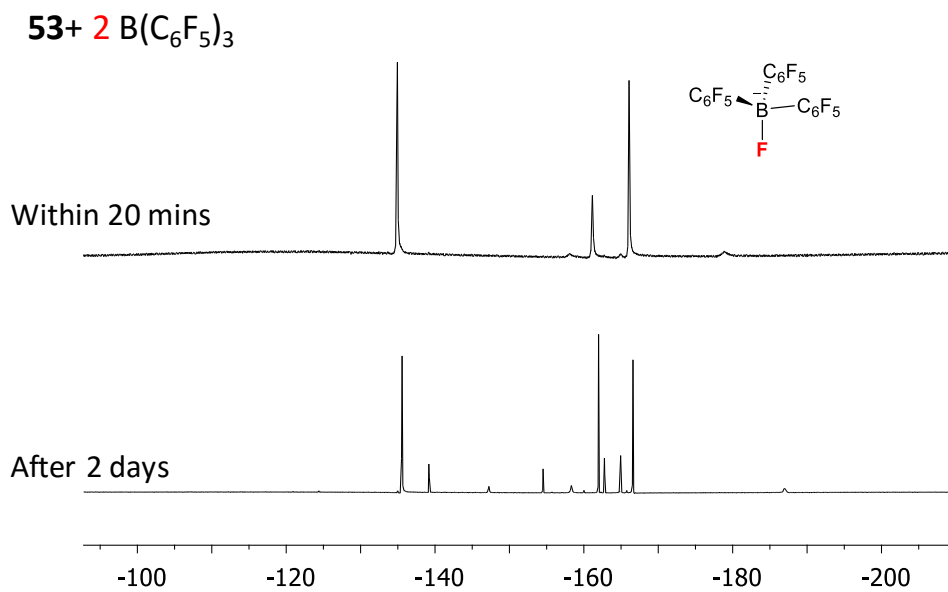


Figure 124. ¹⁹F NMR spectrum for reaction of **53** with two equivalents of B(C₆F₅)₃ in CH₂Cl₂, showing one set of signals corresponding to the formation of [FB(C₆F₅)₃]⁻.

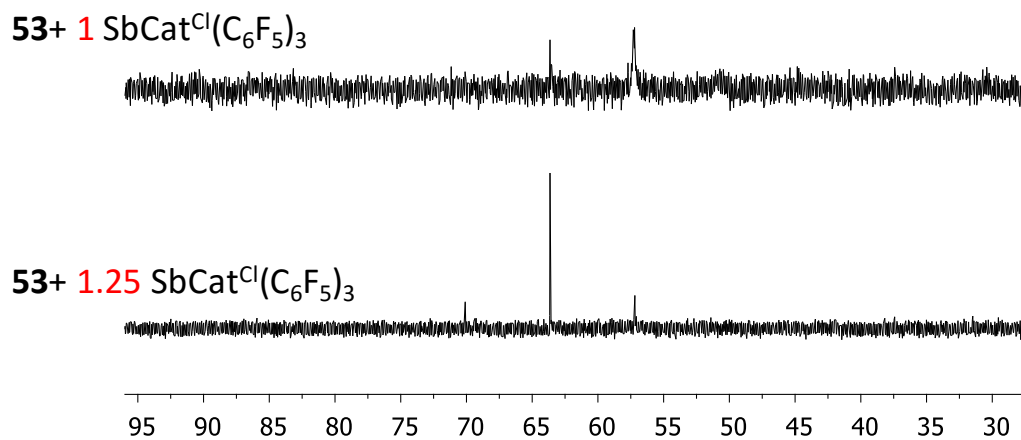


Figure 125. ³¹P NMR spectra for reaction of **53** with SbCat^{Cl}(C₆F₅)₃ in CH₂Cl₂. The addition of 1.25 equivalents of SbCat^{Cl}(C₆F₅)₃ results in one resonance at 63.7 ppm, *J*_{pt-p} = 2607 Hz.

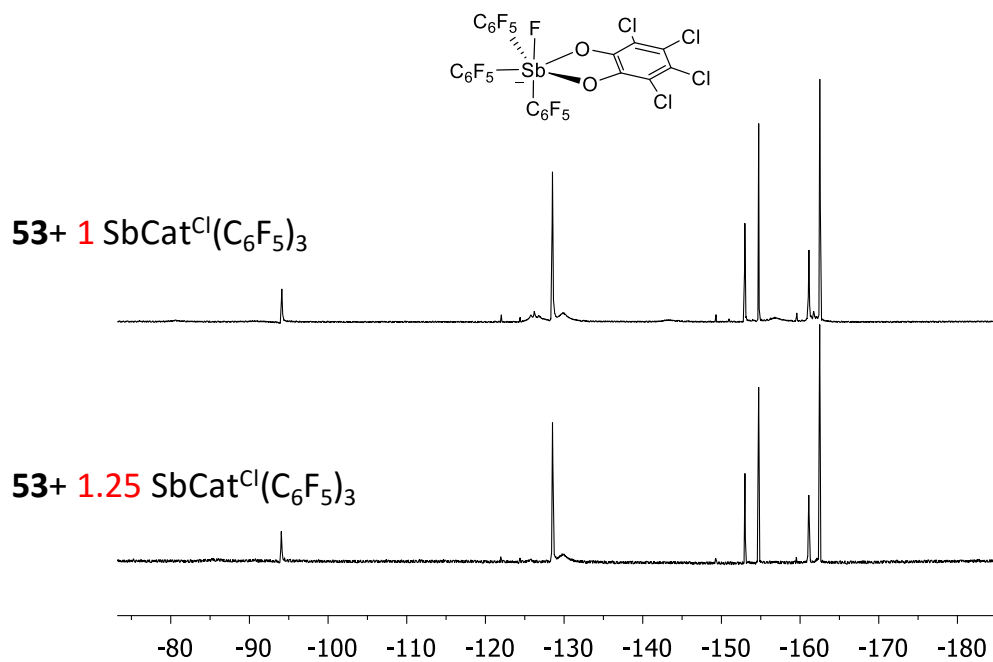


Figure 126. ^{19}F NMR spectra for reaction of **53** with $\text{SbCat}^{\text{Cl}}(\text{C}_6\text{F}_5)_3$ in CH_2Cl_2 . The addition of 1 or 1.25 equivalents of $\text{SbCat}^{\text{Cl}}(\text{C}_6\text{F}_5)_3$ result in the same signals corresponding to the formation of $[\text{SbFCat}^{\text{Cl}}(\text{C}_6\text{F}_5)_3]^+$.

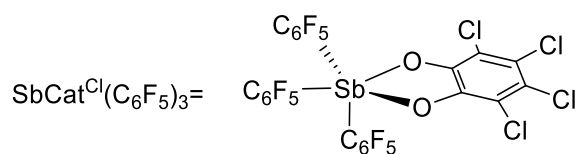
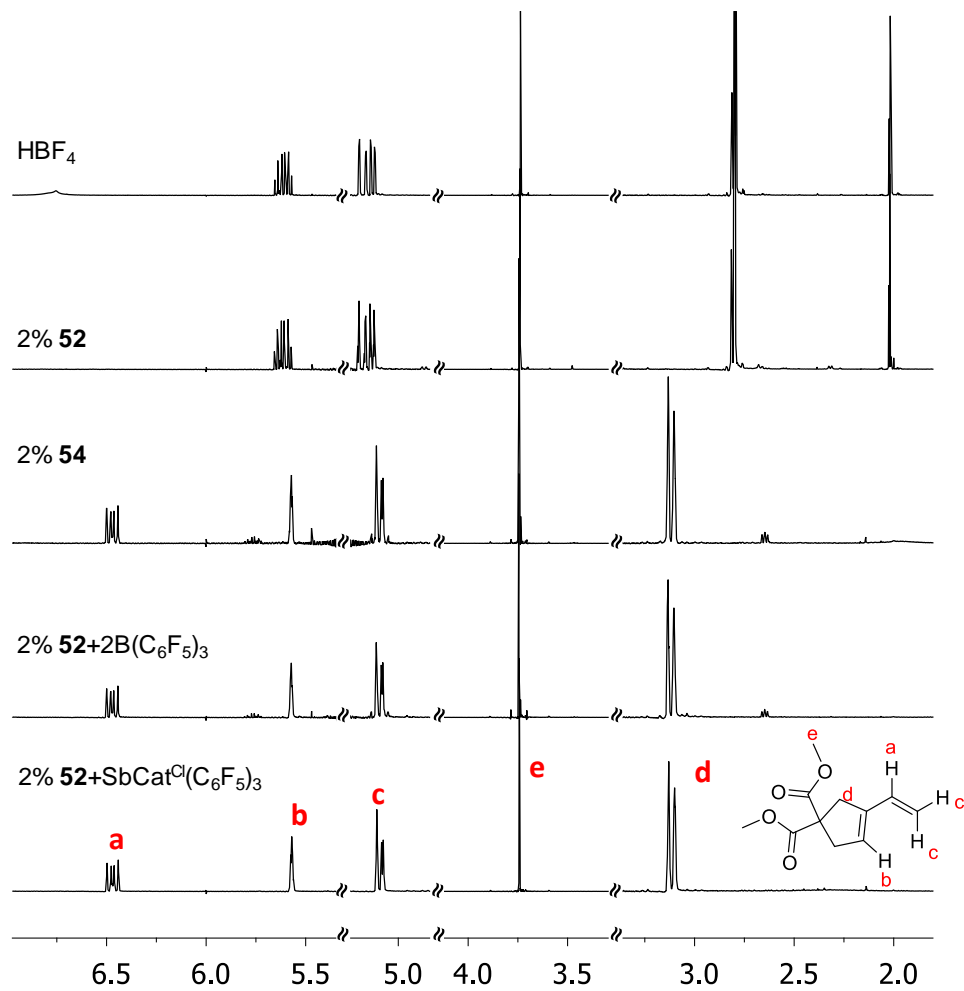


Figure 127. Comparative ^1H NMR spectra of enyne cyclization catalysis.

Table 8. Selected bond lengths (\AA) and angles ($^\circ$) for complexes **52** and **53** as determined crystallographically and optimized computationally.

| Parameter | 52 | | 53 | |
|-----------|-------------|--------|------------|--------|
| | X-ray | DFT | X-ray | DFT |
| Sb-Pt | 2.57974(19) | 2.6869 | 2.6215(11) | 2.7451 |

Table 8 Continued.

| Parameter | 52 | | 53 | |
|----------------------|------------|--------|-------------|--------|
| | X-ray | DFT | X-ray | DFT |
| Pt-N1 (or C37) | 2.125(2) | 2.1273 | 2.005(5) | 1.9806 |
| Sb-F1 | 1.9697(14) | 2.0160 | 1.981(3) | 2.0223 |
| Sb-F2 | 1.9922(13) | 2.0318 | 1.991(3) | 2.0295 |
| Sb-F3 | 1.9811(14) | 2.0185 | 1.988(3) | 2.0445 |
| Sb-C1 | 2.160(2) | 2.2002 | 2.179(5) | 2.2018 |
| Sb-C19 | 2.162(2) | 2.1972 | 2.180(4) | 2.2039 |
| Pt-P1 | 2.2918(6) | 2.3148 | 2.2881(15) | 2.3225 |
| Pt-P2 | 2.2816(6) | 2.3169 | 2.2914(15) | 2.3290 |
| F(1)-Sb-Pt | 178.65(6)° | 179.13 | 172.71(9)° | 175.06 |
| F(2)-Sb-F(3) | 172.33(6)° | 178.15 | 168.73(12)° | 179.67 |
| C(1)-Sb-C(19) | 168.20(9)° | 168.62 | 166.03(17)° | 166.41 |
| Sb-Pt-N1 (or C37) | 176.39(6)° | 174.16 | 171.35(13)° | 171.71 |
| P(1)-Pt-P(2) | 170.49(2)° | 171.39 | 172.31(4)° | 166.57 |

Table 9. Selected bond lengths (Å) and angles (°) for complexes **54** and **55** as determined crystallographically and optimized computationally.

| Parameter | 54 | | 55 | |
|-------------------|-----------|--------|-----------|--------|
| | X-ray | DFT | X-ray | DFT |
| Sb-Pt | 2.4528(6) | 2.4933 | 2.4861(5) | 2.5566 |
| Pt-N1 (or C37) | 2.152(9) | 2.0432 | 1.985(7) | 1.9767 |
| Sb-F1 | 1.972(7) | 1.9763 | 1.947(4) | 1.9827 |
| Sb-F2 | 2.499(8) | 2.3473 | 2.486(4) | 2.3488 |
| Sb-C1 | 2.104(8) | 2.1269 | 2.103(7) | 2.1371 |
| Sb-C19 | 2.106(8) | 2.1290 | 2.105(7) | 2.1326 |

Table 9 Continued.

| Parameter | 54 | | 55 | |
|----------------------|------------|--------|-------------|--------|
| | X-ray | DFT | X-ray | DFT |
| Pt-P1 | 2.312(2) | 2.3670 | 2.3073(17) | 2.3626 |
| Pt-P2 | 2.3049(19) | 2.3589 | 2.3117(17) | 2.3619 |
| F(1)-Sb-Pt | 98.61(16)° | 110.78 | 102.09(14)° | 107.75 |
| C(1)-Sb-C(19) | 142.3(4)° | 142.33 | 142.2(3)° | 146.49 |
| Sb-Pt-N1 (or C37) | 177.5(2)° | 170.81 | 175.6(2)° | 173.46 |
| P(1)-Pt-P(2) | 169.96(7)° | 167.81 | 168.00(6)° | 165.96 |

CHAPTER VI

CONCLUSION

6.1 Photochemical activation of M-X bond

In search of novel main group-based redox active platforms for solar fuel production, a pair of redox active antimony-platinum molecular platforms **42** $\text{Cl}_2\text{Sb}^{\text{IV}}\text{Pt}^{\text{I}}\text{Cl}_3(o\text{-dppp})_2$ and **43** have been synthesized. The reduced complex **42**, obtained from complexation of a platinum precursor *cis*- $\text{PtCl}_2(\text{Et}_2\text{S})_2$ by chlorostibine ligand, can be readily oxidized by PhICl_2 , giving rise to the thermally stable complex **43**. Complex **43**, featuring five chlorine atoms decorating the central core, undergoes efficient photo reductive elimination of Cl_2 . This photoreduction is very efficient, with a maximum quantum yield of 13.8% when carried out in a 4.4 M solution of 2,3-dimethyl-1,3-butadiene in CH_2Cl_2 . Remarkably, it also evolves chlorine when irradiated in the solid state under ambient conditions in the absence of a trap. DFT calculations support that this chlorine photoreductive elimination reaction is indeed endergonic.

6.2 Redox non-innocent behavior of a telluroether ligand

While Ph_2Te is oxidized into Ph_2TeCl_2 in the presence of $(\text{tht})\text{AuCl}$ (tht = tetrahydrothiophene), reaction of a telluroether ligand $(o\text{-(Ph}_2\text{P)C}_6\text{H}_4)_2\text{Te}$ (first developed by Dr. Lin), with the same gold reagent affords a stable telluroether gold complex **44**. The resulting complex features a $\text{Te}\rightarrow\text{Au}$ dative bond. Oxidation of it with H_2O_2 affords the corresponding telluroxide gold complex **46**. Natural Bond Orbital analysis shows that oxidation of **44** into **46** results in a umpolung of the Te-Au bond which switches from $\text{Te}\rightarrow\text{Au}$ in **44** to $\text{Au}\rightarrow\text{Te}$ in **46**. This result showed that the telluroxide moiety can act as a Z-type

ligand, which revealed the first time the redox non-innocent behavior of tellurium ligands in the coordination sphere of gold.

6.3 Activation of an electrophilic gold catalyst

In search of new platforms that support redox-controlled catalysis, the non-innocent behavior of chlorostibine ligands coordinated to gold was investigated. The gold chlorostibine complex ((*o*-(Ph₂P)C₆H₄)₂SbCl)AuCl (**47-Cl**) undergoes a clean oxidation reaction when treated with PhICl₂. This oxidation reaction affords the corresponding trichlorostiborane complex ((*o*-(Ph₂P)C₆H₄)₂SbCl₃)AuCl (**49-Cl**) which can be converted into the more tractable trifluoride analog ((*o*-(Ph₂P)C₆H₄)₂SbF₃)AuCl (**50-Cl**) by treatment with a fluoride source. As supported by experimental and computational results, these complexes possess a Au→Sb donor–acceptor interaction which is distinctly stronger in the oxidized complexes **49-Cl** and **50-Cl**. Both **47-Cl** and **50-Cl** undergo a clean chloride abstraction reaction to afford the corresponding cationic gold species [((*o*-(Ph₂P)C₆H₄)₂SbCl)Au]⁺ (**[47]⁺**) and [((*o*-(Ph₂P)C₆H₄)₂SbF₃)Au]⁺ (**[50]⁺**) which have been isolated as SbF₆[−] salts. As a result of a stronger Au→Sb interaction, cation **[50]⁺** features a more Lewis acidic gold center. It forms an isolable adducts with a variety of Lewis bases, including water, 4-dimethylaminopyridine, *p*-toluidine and THF. It also activates terminal alkynes toward hydroamination with arylamines. These results demonstrate that the redox state of non-innocent Z-ligands can be used to control the catalytic activity of the adjoining metal center.

6.4 Accessing a $\text{Sb}^{\text{V}}\text{Pt}^0$ and a cationic $\text{Sb}^{\text{IV}}\text{Pt}^{\text{I}}$ complexes

Ligand platforms amenable to post-synthetic modification has been pursued to activate the metal center towards catalysis. In this work, we investigated the coordination non-innocence behavior of a dihalogenated stiboranyl ligand, and a trifluorostiborane ligand in the coordination sphere of platinum. The previously reported dichlorostiboranyl platinum complex **42**, $\text{Cl}_2\text{Sb}^{\text{IV}}\text{Pt}^{\text{I}}\text{Cl}(\text{o-dppp})_2$, can be readily converted into a trifluorostiborane platinum complex **52** and **53** ($\text{F}_3\text{Sb}^{\text{V}}\text{Pt}^0\text{L}(\text{o-dppp})_2$, L= acetonitrile) by chloride-to-fluoride exchange. The anion exchange event caused internal redox reactions, with complex **52** and **53** being best described as $\text{Sb}^{\text{V}}\text{Pt}^0$. NBO analysis suggests that the zero valent platinum center is stabilized by the donor-acceptor interaction $\text{Pt}(0)\rightarrow\text{Sb}(\text{V})$, indicative of a Lewis acidic low-valent platinum center. Attempts to convert the coordinated stiborane to the cationic stibonium as a means to enhance the $\text{Pt}(0)\rightarrow[\text{Sb}(\text{V})]^+$ interaction, led to the isolation of cationic monofluorostibine platinum complex **54** and **55**, by reacting complexes **52** and **54** with HBF_4 , respectively. Complex **54** and **55** features a more oxidized and more Lewis acidic platinum center, which displays reactivity towards enyne cyclization catalysis. The results speak for the antimony-centered coordination non-innocence, highlighting the potential of halogenated antimony ligand to undergo post-synthetic anion coordination or dissociation, and tune the electronic properties and catalytic reactivity of the adjoining transition metal center.

6.5 Summary of halogenated antimony ligands

In search of strongly Lewis acidic antimony and tellurium ligands to enable new ligand-mediated catalysis, this dissertation presented my major work on halogen functionalized antimony ligands, and the reactivity of their late transition metal complexes. The chlorostibine

ligand, incorporated with supporting donors, proved to be a robust Z-type ligand. It can activate metal-halide bond or draw electron density from the adjoining metal upon complexation due to its Z-type ligand function, as shown in the formation of complex **42** and complex **47-Cl**. In particular, the dichlorostiboranyl ligand, derived from the chlorostibine ligand, was a redox responsive ligand platform, as evidenced by its dual function in facilitating the metal-centered oxidative addition and reductive elimination. Such potential originates from its inherent σ -donating ability, and Lewis acidity conferred by the electron-withdrawing chlorine atoms. This ligand-mediated redox chemistry allowed us to obtain the antimony-platinum complexes for photo reductive elimination of chlorine (Chapter II). Further, chlorostibine Z-type ligand showed its potential to sustain oxidation reactions in the coordination sphere of the coordinated metal, which enhances the M \rightarrow Z-ligand interaction, therefore activating the metal center for electrophilic catalysis. This antimony ligand-centered redox non-innocent behavior was investigated for the activation of a gold catalyst towards hydroamination (Chapter VI). In addition, the above-described dichlorostiboranyl ligand demonstrated its ability to facilitate chloride-to-fluoride exchange within the bimetallic core, which induces internal redox reactions and free the metal site for catalysis. Remarkably, the resulting fluoroantimony ligands, such as trifluorostiborane, possess a second pathway to tune the reactivity of the metal center, through F-H or F-Lewis acids interaction. This antimony ligand-centered coordination non-innocent behavior was explored for accessing an active platinum catalyst for enyne cyclization (Chapter V).

REFERENCES

1. Jørgensen, C. K., *Coord. Chem. Rev.* **1966**, *1* (1), 164-178.
2. Schrauzer, G. N.; Mayweg, V., *J. Am. Chem. Soc.* **1962**, *84* (16), 3221-3221.
3. Ray, K.; Petrenko, T.; Wiegardt, K.; Neese, F., *Dalton Trans.* **2007**, (16), 1552-1566.
4. Lyaskovskyy, V.; de Bruin, B., *ACS Catal.* **2012**, *2* (2), 270-279.
5. Bart, S. C.; Lobkovsky, E.; Chirik, P. J., *J. Am. Chem. Soc.* **2004**, *126* (42), 13794-13807.
6. Bart, S. C.; Chłopek, K.; Bill, E.; Bouwkamp, M. W.; Lobkovsky, E.; Neese, F.; Wiegardt, K.; Chirik, P. J., *J. Am. Chem. Soc.* **2006**, *128* (42), 13901-13912.
7. Nguyen, A. I.; Blackmore, K. J.; Carter, S. M.; Zarkesh, R. A.; Heyduk, A. F., *J. Am. Chem. Soc.* **2009**, *131* (9), 3307-3316.
8. Chirik, P. J.; Wiegardt, K., *Science* **2010**, *327* (5967), 794-795.
9. Dunn, T. J.; Ramogida, C. F.; Simmonds, C.; Paterson, A.; Wong, E. W. Y.; Chiang, L.; Shimazaki, Y.; Storr, T., *Inorg. Chem.* **2011**, *50* (14), 6746-6755.
10. Heyduk, A. F.; Zarkesh, R. A.; Nguyen, A. I., *Inorg. Chem.* **2011**, *50* (20), 9849-9863.
11. Myers, T. W.; Berben, L. A., *J. Am. Chem. Soc.* **2011**, *133* (31), 11865-11867.
12. Dunn, T. J.; Chiang, L.; Ramogida, C. F.; Webb, M. I.; Savard, D.; Sakaguchi, M.; Ogura, T.; Shimazaki, Y.; Storr, T., *Dalton Trans.* **2012**, *41* (26), 7905-7914.
13. Green, M. L. H., *J. Organomet. Chem.* **1995**, *500* (1-2), 127-148.
14. Amgoune, A.; Bourissou, D., *Chem. Commun.* **2011**, *47* (3), 859-871.
15. Werner, H., *Angew. Chem., Int. Ed. Engl.* **1983**, *22* (12), 927-949.
16. Muir, K. W.; Ibers, J. A., *Inorg. Chem.* **1969**, *8* (9), 1921-1928.
17. Burlitch, J. M.; Leonowicz, M. E.; Petersen, R. B.; Hughes, R. E., *Inorg. Chem.* **1979**, *18* (4), 1097-1105.
18. Braunschweig, H.; Gruss, K.; Radacki, K., *Angew. Chem., Int. Ed.* **2007**, *46* (41), 7782-7784.

19. Braunschweig, H.; Gruss, K.; Radacki, K., *Inorg. Chem.* **2008**, *47* (19), 8595-8597.
20. Bouhadir, G.; Bourissou, D., *Chem. Soc. Rev.* **2016**, *45* (4), 1065-1079.
21. Kameo, H.; Nakazawa, H., *Chem. Asian J.* **2013**, *8* (8), 1720-1734.
22. Devillard, M.; Bouhadir, G.; Bourissou, D., *Angew. Chem., Int. Ed.* **2015**, *54* (3), 730-732.
23. Fong, H.; Moret, M.-E.; Lee, Y.; Peters, J. C., *Organometallics* **2013**, *32* (10), 3053-3062.
24. Tsoureas, N.; Kuo, Y.-Y.; Haddow, M. F.; Owen, G. R., *Chem. Commun.* **2011**, *47* (1), 484-486.
25. Bonanno, J. B.; Henry, T. P.; Wolczanski, P. T.; Pierpont, A. W.; Cundari, T. R., *Inorg. Chem.* **2007**, *46* (4), 1222-1232.
26. Harman, W. H.; Peters, J. C., *J. Am. Chem. Soc.* **2012**, *134* (11), 5080-5082.
27. Devillard, M.; Nicolas, E.; Appelt, C.; Backs, J.; Mallet-Ladeira, S.; Bouhadir, G.; Sloopweg, J. C.; Uhl, W.; Bourissou, D., *Chem. Commun.* **2014**, *50* (94), 14805-14808.
28. Derrah, E. J.; Sircoglou, M.; Mercy, M.; Ladeira, S.; Bouhadir, G.; Miqueu, K.; Maron, L.; Bourissou, D., *Organometallics* **2011**, *30* (4), 657-660.
29. Sircoglou, M.; Bouhadir, G.; Saffon, N.; Miqueu, K.; Bourissou, D., *Organometallics* **2008**, *27* (8), 1675-1678.
30. Sircoglou, M.; Mercy, M.; Saffon, N.; Coppel, Y.; Bouhadir, G.; Maron, L.; Bourissou, D., *Angew. Chem., Int. Ed.* **2009**, *48* (19), 3454-3457.
31. Sircoglou, M.; Saffon, N.; Miqueu, K.; Bouhadir, G.; Bourissou, D., *Organometallics* **2013**, *32* (22), 6780-6784.
32. Inagaki, F.; Matsumoto, C.; Okada, Y.; Maruyama, N.; Mukai, C., *Angew. Chem., Int. Ed.* **2015**, *54* (3), 818-822.
33. Yi, W.; Tan, N., *Acta Crystallogr. Sect. E* **2011**, *67* (7), m917.
34. Ohkata, K.; Takemoto, S.; Ohnishi, M.; Akiba, K.-y., *Tetrahedron Lett.* **1989**, *30* (36), 4841-4844.
35. Althaus, H.; Breunig, H. J.; Lork, E., *Organometallics* **2001**, *20* (3), 586-589.

36. Copolovici, D.; Isaia, F.; Breunig, H. J.; Rat, C. I.; Silvestru, C., *RSC Adv.* **2014**, *4* (51), 26569-26576.
37. Gutmann, V., *Coord. Chem. Rev.* **1976**, *18* (2), 225-255.
38. Gutmann, V.; Hubacek, H.; Steininger, A., *Monatshefte für Chemie und verwandte Teile anderer Wissenschaften* **1964**, *95* (3), 678-686.
39. Hirai, M.; Gabbai, F. P., *Chem. Sci.* **2014**, *5* (5), 1886-1893.
40. Ke, I.-S.; Myahkostupov, M.; Castellano, F. N.; Gabbai, F. P., *J. Am. Chem. Soc.* **2012**, *134* (37), 15309-15311.
41. Pan, B.; Gabbai, F. P., *J. Am. Chem. Soc.* **2014**, *136* (27), 9564-9567.
42. Drabowicz, J.; Lewkowski, J.; Kudelska, W.; Girek, T., *Science of Synthesis*. Thieme Chemistry: 2008; Vol. 39, p 1112.
43. You, Y.; Ahsan, K.; Detty, M. R., *J. Am. Chem. Soc.* **2003**, *125* (16), 4918-4927.
44. Murphy, P. J., *Science of Synthesis*. Thieme Chemistry: 2001; Vol. 10, p 352.
45. Kirsch, G.; Goodman, M. M.; Knapp, F. F., *Organometallics* **1983**, *2* (3), 357-363.
46. Boese, R.; Haas, A.; Herkt, S.; Pryka, M., *Chemische Berichte* **1995**, *128* (4), 423-428.
47. Fujihara, H.; Takaguchi, Y.; Ninoi, T.; Erata, T.; Furukawa, N., *J. Chem. Soc., Perkin Trans. 1* **1992**, (20), 2583-2584.
48. Detty, M. R.; Frade, T. M., *Organometallics* **1993**, *12* (7), 2496-2504.
49. Carrera, E. I.; Lanterna, A. E.; Lough, A. J.; Scaiano, J. C.; Seferos, D. S., *J. Am. Chem. Soc.* **2016**, *138* (8), 2678-2689.
50. Carrera, E. I.; McCormick, T. M.; Kapp, M. J.; Lough, A. J.; Seferos, D. S., *Inorg. Chem.* **2013**, *52* (23), 13779-13790.
51. Carrera, E. I.; Seferos, D. S., *Dalton Trans.* **2015**, *44* (5), 2092-2096.
52. Sudha, N.; Singh, H. B., *Coord. Chem. Rev.* **1994**, *135*, 469-515.
53. Bukka, K.; Satchell, R. S., *J. Chem. Soc., Perkin Trans. 2* **1975**, (10), 1110-1112.
54. Naumann, D.; Tyrra, W.; Herrmann, R.; Pantenburg, I.; Wickleder, M. S., *Z. Anorg. Allg. Chem.* **2002**, *628* (4), 833-842.

55. Lobana, T. S.; Mbogo, S. A.; McWhinnie, W. R.; Patalinghug, W. C.; White, A. H., *J. Organomet. Chem.* **1990**, *390* (1), 29-34.
56. Champness, N. R.; Levason, W., *Coord. Chem. Rev.* **1994**, *133*, 115-217.
57. Black, J. R.; Levason, W.; Spicer, M. D.; Webster, M., *J. Chem. Soc., Dalton Trans.* **1993**, (20), 3129-3136.
58. Bowmaker, G. A.; Hart, R. D.; White, A. H., *Aust. J. Chem.* **1997**, *50* (6), 567-576.
59. Cavaglioni, A.; Cini, R., *Polyhedron* **1997**, *16* (23), 4045-4054.
60. Chand, S.; Coll, R. K.; McIndoe, J. S., *Polyhedron* **1998**, *17* (4), 507-511.
61. Cini, R.; Cavaglioni, A.; Tiezzi, E., *Polyhedron* **1999**, *18* (5), 669-678.
62. Dallmann, K.; Preetz, W., *Z. Anorg. Allg. Chem.* **1998**, *624* (2), 267-270.
63. Domasevitch, K. V.; Petkova, E. G.; Nazarenko, A. Y.; Ponomareva, V. V.; Sieler, J.; Dalley, N. K.; Rusanov, E. B., *Z. Naturforsch., B: Chem. Sci.* **1999**, *54* (7), 904-912.
64. F. Wendt, O.; I. Elding, L., *J. Chem. Soc., Dalton Trans.* **1997**, (24), 4725-4732.
65. Godfrey, S. M.; McAuliffe, C. A.; Pritchard, R. G., *J. Chem. Soc., Chem. Commun.* **1994**, (1), 45-46.
66. Hart, R. D.; Bowmaker, G. A.; Silva, E. N. D.; Skelton, B. W.; White, A. H., *Aust. J. Chem.* **1997**, *50* (6), 621-626.
67. Hill, A. M.; Levason, W.; Webster, M., *Inorg. Chem.* **1996**, *35* (11), 3428-3430.
68. Holmes, N. J.; Levason, W.; Webster, M., *J. Organomet. Chem.* **1998**, *568* (1-2), 213-223.
69. Liu, Y.; Leong, W. K.; Pomeroy, R. K., *Organometallics* **1998**, *17* (15), 3387-3389.
70. Menten, A.; Kemmitt, R. D. W.; Fawcett, J.; Russell, D. R., *J. Organomet. Chem.* **1997**, *528* (1-2), 59-63.
71. Srivastava, K. V.; Bhatt, D. S.; Shukla, S. R.; Bajaj, C. H.; Jasra, V. R., *React. Kinet. Catal. Lett.* **2005**, *85* (1), 3-9.
72. Wache, S.; Herrmann, W. A.; Artus, G.; Nuyken, O.; Wolf, D., *J. Organomet. Chem.* **1995**, *491* (1-2), 181-188.
73. Wendt, O. F.; Scodinu, A.; Elding, L. I., *Inorg. Chim. Acta* **1998**, *277* (2), 237-241.

74. Benjamin, S. L.; Levason, W.; Light, M. E.; Reid, G.; Rogers, S. M., *Organometallics* **2014**, *33* (11), 2693-2695.
75. Benjamin, S. L.; Levason, W.; Reid, G.; Warr, R. P., *Organometallics* **2012**, *31* (3), 1025-1034.
76. Higginson, B. R.; McAuliffe, C. A.; Venanzi, L. M., *Inorg. Chim. Acta* **1971**, *5*, 37-40.
77. Baracco, L.; McAuliffe, C. A., *J. Chem. Soc., Dalton Trans.* **1972**, (8-9), 948-951.
78. Breunig, H. J.; Ghesner, I., *Adv. Organomet. Chem.* **2003**, *49*, 95-132.
79. Burt, J.; Levason, W.; Reid, G., *Coord. Chem. Rev.* **2014**, *260*, 65-115.
80. Levason, W.; McAuliffe, C. A., *Acc. Chem. Res.* **1978**, *11* (9), 363-368.
81. Levason, W.; Reid, G., *Coord. Chem. Rev.* **2006**, *250* (19-20), 2565-2594.
82. Schulz, S., *Coord. Chem. Rev.* **2001**, *215* (1), 1-37.
83. Schulz, S., Synthesis, Structure and Reactivity of Group 13/15 Compounds Containing the Heavier Elements of Group 15, Sb and Bi. In *Group 13 Chemistry I: Fundamental New Developments*, Roesky, H. W.; Atwood, D. A., Eds. Springer Berlin Heidelberg: Berlin, Heidelberg, 2002; pp 117-166.
84. Werner, H., *Angew. Chem., Int. Ed.* **2004**, *43* (8), 938-954.
85. Wade, C. R.; Ke, I.-S.; Gabbai, F. P., *Angewandte Chemie* **2012**, *124* (2), 493-496.
86. Ke, I.-S.; Gabbai, F. P., *Inorg. Chem.* **2013**, *52* (12), 7145-7151.
87. Wade, C. R.; Gabbai, F. P., *Angew. Chem., Int. Ed.* **2011**, *50* (32), 7369-7372.
88. Jones, J. S.; Wade, C. R.; Gabbai, F. P., *Organometallics* **2015**, *34* (11), 2647-2654.
89. Jha, A.; Richards, B. D. O.; Jose, G.; Toney Fernandez, T.; Hill, C. J.; Lousteau, J.; Joshi, P., *Int. Mater. Rev.* **2012**, *57* (6), 357-382.
90. Ma, Y.; Hao, Q.; Poudel, B.; Lan, Y.; Yu, B.; Wang, D.; Chen, G.; Ren, Z., *Nano Letters* **2008**, *8* (8), 2580-2584.
91. Zhu, W.; Wang, W.; Xu, H.; Zhou, L.; Zhang, L.; Shi, J., *Cryst. Growth Des.* **2006**, *6* (12), 2804-2808.
92. Carrera, E. I.; Seferos, D. S., *Macromolecules* **2015**, *48* (2), 297-308.

93. Jahnke, A. A.; Djukic, B.; McCormick, T. M.; Buchaca Domingo, E.; Hellmann, C.; Lee, Y.; Seferos, D. S., *J. Am. Chem. Soc.* **2013**, *135* (3), 951-954.
94. Jahnke, A. A.; Seferos, D. S., *Macromol. Rapid Commun.* **2011**, *32* (13), 943-951.
95. Lee, W.-H.; Kyu Lee, S.; Suk Shin, W.; Moon, S.-J.; Kang, I.-N., *J. Polym. Sci., Part A: Polym. Chem.* **2013**, *51* (13), 2753-2758.
96. Park, Y. S.; Kale, T. S.; Nam, C. Y.; Choi, D.; Grubbs, R. B., *Chem. Commun.* **2014**, *50* (59), 7964-7967.
97. Takimiya, K.; Kunugi, Y.; Konda, Y.; Niihara, N.; Otsubo, T., *J. Am. Chem. Soc.* **2004**, *126* (16), 5084-5085.
98. Jung, E. H.; Bae, S.; Yoo, T. W.; Jo, W. H., *Polym. Chem.* **2014**, *5* (22), 6545-6550.
99. Mbogo, S. A.; McWhinnie, W. R.; Lobana, T. S., *Inorg. Chim. Acta* **1990**, *172* (2), 221-224.
100. Gardner, S. A., *J. Organomet. Chem.* **1980**, *190* (3), 289-296.
101. Das, D.; Singh, P.; Singh, A. K., *J. Organomet. Chem.* **2010**, *695* (7), 955-962.
102. Drake, J. E.; Bailey, J. H. E.; Singh, A. K.; Srivastava, V., *Acta Crystallogr. Sect. C* **1993**, *49* (4), 684-687.
103. Kirsten, L.; Schwade, V. D.; Selter, L.; Hagenbach, A.; Piquini, P. C.; Schulz Lang, E.; Abram, U., *Eur. J. Inorg. Chem.* **2015**, *2015* (22), 3748-3757.
104. Kumar, S.; Rao, G. K.; Kumar, A.; Singh, M. P.; Singh, A. K., *Dalton Trans.* **2013**, *42* (48), 16939-16948.
105. Paluru, D. K.; Dey, S.; Wadawale, A.; Maity, D. K.; Bhuvanesh, N.; Jain, V. K., *Eur. J. Inorg. Chem.* **2015**, *2015* (3), 397-407.
106. Singh, P.; Singh, A. K., *Organometallics* **2010**, *29* (23), 6433-6442.
107. Vigo, L.; Salin, P.; Oilunkaniemi, R.; Laitinen, R. S., *J. Organomet. Chem.* **2009**, *694* (19), 3134-3141.
108. Kaur, R.; Singh, H. B.; Butcher, R. J., *Organometallics* **1995**, *14* (10), 4755-4763.
109. Sharma, K. N.; Joshi, H.; Sharma, A. K.; Prakash, O.; Singh, A. K., *Chem. Commun.* **2013**, *49* (81), 9344-9346.
110. Nakayama, Y.; Watanabe, K.; Ueyama, N.; Nakamura, A.; Harada, A.; Okuda, J., *Organometallics* **2000**, *19* (13), 2498-2503.

111. Janzen, M. C.; Jennings, M. C.; Puddephatt, R. J., *Inorg. Chem.* **2003**, *42* (15), 4553-4558.
112. Jones, J. S.; Wade, C. R.; Gabbai, F. P., *Angewandte Chemie* **2014**, *126* (34), 9022-9025.
113. Ke, I.-S.; Jones, J. S.; Gabbai, F. P., *Angew. Chem., Int. Ed.* **2014**, *53* (10), 2633-2637.
114. Nocera, D. G., *Inorg. Chem.* **2009**, *48* (21), 10001-10017.
115. Hwang, S. J.; Powers, D. C.; Maher, A. G.; Nocera, D. G., *Chem. Sci.* **2015**, *6* (2), 917-922.
116. Lin, T.-P.; Gabbai, F. P., *J. Am. Chem. Soc.* **2012**, *134* (29), 12230-12238.
117. Perera, T. A.; Masjedi, M.; Sharp, P. R., *Inorg. Chem.* **2014**, *53* (14), 7608-7621.
118. Powers, D. C.; Anderson, B. L.; Nocera, D. G., *J. Am. Chem. Soc.* **2013**, *135* (50), 18876-18883.
119. Gray, H. B.; Maverick, A. W., *Science* **1981**, *214* (4526), 1201-1205.
120. Heyduk, A. F.; Nocera, D. G., *Science* **2001**, *293* (5535), 1639-1641.
121. Mann, K. R.; Lewis, N. S.; Miskowski, V. M.; Erwin, D. K.; Hammond, G. S.; Gray, H. B., *J. Am. Chem. Soc.* **1977**, *99* (16), 5525-5526.
122. Elgrishi, N.; Teets, T. S.; Chambers, M. B.; Nocera, D. G., *Chem. Commun.* **2012**, *48* (76), 9474-9476.
123. Powers, D. C.; Chambers, M. B.; Teets, T. S.; Elgrishi, N.; Anderson, B. L.; Nocera, D. G., *Chem. Sci.* **2013**, *4* (7), 2880-2885.
124. Cook, T. R.; Esswein, A. J.; Nocera, D. G., *J. Am. Chem. Soc.* **2007**, *129* (33), 10094-10095.
125. Cook, T. R.; Surendranath, Y.; Nocera, D. G., *J. Am. Chem. Soc.* **2009**, *131* (1), 28-29.
126. Teets, T. S.; Lutterman, D. A.; Nocera, D. G., *Inorganic Chemistry* **2010**, *49* (6), 3035-3043.
127. Jones, J. S.; Gabbai, F. P., *Acc. Chem. Res.* **2016**, *49* (5), 857-867.
128. Jones, J. S.; Gabbai, F. P., *Chem. Lett.* **2016**, *45* (4), 376-384.

129. Mann, K. R.; Bell, R. A.; Gray, H. B., *Inorg. Chem.* **1979**, *18* (10), 2671-2673.
130. Maverick, A. W.; Gray, H. B., *Pure Appl. Chem.* **1980**, *52* (10), 2339-2348.
131. Sigal, I. S.; Mann, K. R.; Gray, H. B., *J. Am. Chem. Soc.* **1980**, *102* (24), 7252-7256.
132. Mann, K. R.; Dipierro, M. J.; Gill, T. P., *J. Am. Chem. Soc.* **1980**, *102* (11), 3965-3967.
133. Gray, H. B.; Maverick, A. W., *Science* **1981**, *214* (4526), 1201-1205.
134. Eidem, P. K.; Maverick, A. W.; Gray, H. B., *Inorg. Chim. Acta* **1981**, *50* (1), 59-64.
135. Esswein, A. J.; Nocera, D. G., *Chem. Rev.* **2007**, *107* (10), 4022-4047.
136. Heyduk, A. F.; Macintosh, A. M.; Nocera, D. G., *J. Am. Chem. Soc.* **1999**, *121* (21), 5023-5032.
137. Cook, T. R.; Esswein, A. J.; Nocera, D. G., *J. Am. Chem. Soc.* **2007**, *129* (33), 10094-10095.
138. Teets, T. S.; Nocera, D. G., *J. Am. Chem. Soc.* **2009**, *131* (21), 7411-7420.
139. Teets, T. S.; Neumann, M. P.; Nocera, D. G., *Chem. Commun.* **2011**, *47* (5), 1485-1487.
140. Teets, T. S.; Cook, T. R.; McCarthy, B. D.; Nocera, D. G., *Inorg. Chem.* **2011**, *50* (11), 5223-5233.
141. Cook, T. R.; McCarthy, B. D.; Lutterman, D. A.; Nocera, D. G., *Inorg. Chem.* **2012**, *51* (9), 5152-5163.
142. Wickramasinghe, L. A.; Sharp, P. R., *Inorg. Chem.* **2014**, *53* (3), 1430-1442.
143. Karikachery, A. R.; Lee, H. B.; Masjedi, M.; Ross, A.; Moody, M. A.; Cai, X.; Chui, M.; Hoff, C. D.; Sharp, P. R., *Inorg. Chem.* **2013**, *52* (7), 4113-4119.
144. Wade, C. R.; Gabbai, F. P., *Angew. Chem. Int. Ed.* **2011**, *50*, 7369-7372.
145. Oberhauser, W.; Bachmann, C.; Stampfl, T.; Brüggeller, P., *Inorg. Chim. Acta* **1997**, *256* (2), 223-234.
146. Oberhauser, W.; Stampfl, T.; Bachmann, C.; Haid, R.; Langes, C.; Kopacka, H.; Ongania, K.-H.; Brüggeller, P., *Polyhedron* **2000**, *19* (8), 913-923.
147. Elding, L. I.; Gustafson, L., *Inorg. Chim. Acta* **1976**, *19* (0), 165-171.

148. Bondarenko, V. S.; Korniets, E. D.; Sokolenko, V. A.; Kovrova, N. B.; Kovtonyuk, N. P., *Zh. Neorg. Khim.* **1989**, *34* (6), 1541-3.
149. Bryan, S. A.; Dickson, M. K.; Roundhill, D. M., *Inorg. Chem.* **1987**, *26* (23), 3878-3886.
150. Levy, C. J.; Puddephatt, R. J., *J. Am. Chem. Soc.* **1997**, *119* (42), 10127-10136.
151. Perdew, J. P., *Phys. Rev. B* **1986**, *33*, 8822-8824.
152. Becke, A. D., *Physical Review A* **1988**, *38*, 3098-3100.
153. Peterson, K. A.; Figgen, D.; Goll, E.; Stoll, H.; Dolg, M., *J. Chem. Phys.* **2003**, *119* (21), 11113-11123.
154. Figgen, D.; Peterson, K. A.; Dolg, M.; Stoll, H., *J. Chem. Phys.* **2009**, *130* (16), 164108-12.
155. Parkin, G., *J. Chem. Educ.* **2006**, *83* (5), 791-799.
156. Shriver, D. F., *Acc. Chem. Res.* **1970**, *3* (7), 231-238.
157. Dammann, C. B.; Hughey, J. L.; Jicha, D. C.; Meyer, T. J.; Rakita, P. E.; Weaver, T. R., *Inorg. Chem.* **1973**, *12* (9), 2206-2209.
158. Chan, D. M. T.; Marder, T. B., *Angew. Chem., Int. Ed.* **1988**, *27* (3), 442-443.
159. Parkin, G., *Organometallics* **2006**, *25* (20), 4744-4747.
160. Hill, A. F., *Organometallics* **2006**, *25* (20), 4741-4743.
161. Fontaine, F.-G.; Boudreau, J.; Thibault, M.-H., *Eur. J. Inorg. Chem.* **2008**, *2008* (35), 5439-5454.
162. Braunschweig, H.; Dewhurst, R. D.; Schneider, A., *Chem. Rev.* **2010**, *110* (4), 3924-3957.
163. Bouhadir, G.; Amgoune, A.; Bourissou, D., *Adv. Organomet. Chem.* **2010**, *58*, 1-107.
164. Braunschweig, H.; Dewhurst, R. D., *Dalton Trans.* **2011**, *40*, 549-558.
165. Bauer, J.; Braunschweig, H.; Dewhurst, R. D., *Chem. Rev.* **2012**, *112* (8), 4329-4346.
166. Owen, G. R., *Chem. Soc. Rev.* **2012**, *41* (9), 3535-3546.
167. Mingos, D. M. P., *J. Organomet. Chem.* **2014**, *751* (0), 153-173.

168. Marenich, A. V.; Cramer, C. J.; Truhlar, D. G., *J. Phys. Chem. B* **2009**, *113* (18), 6378-6396.
169. Alfassi, Z. B.; Mosseri, S.; Neta, P., *J. Phys. Chem.* **1989**, *93* (4), 1380-1385.
170. Hatchard, C. G.; Parker, C. A., *Proc. R. Soc. London, Ser. A* **1956**, *235* (1203), 518-536.
171. Parker, C. A., *Proc. R. Soc. London, Ser. A* **1953**, *220* (1140), 104-116.
172. Kuhn, H. J.; Braslavsky, S. E.; Schmidt, R., *Pure Appl. Chem.* **2004**, *76* (12), 2105-2146.
173. Znakovskaya, I. V.; Sosedova, Y. A.; Glebov, E. M.; Grivin, V. P.; Plyusnin, V. F., *Photochem. Photobiol. Sci.* **2005**, *4* (11), 897-902.
174. Perera, T. A.; Masjedi, M.; Sharp, P. R., *Inorg. Chem.* **2014**, *53* (14), 7608-7621.
175. Higginson, B. R.; McAuliffe, C. A.; Venanzi, L. M., *Inorg. Chim. Acta* **1971**, *5* (1), 37-40.
176. De Crisci, A. G.; Lough, A. J.; Multani, K.; Fekl, U., *Organometallics* **2008**, *27* (8), 1765-1779.
177. Zhao, X.-F.; Zhang, C., *Synthesis* **2007**, (4), 551-557.
178. Hall, M. B.; Fenske, R. F., *Inorg. Chem.* **1972**, *11* (4), 768-775.
179. Manson, J.; Webster, C. E.; Pérez, L. M.; Hall, M. B., <http://www.chem.tamu.edu/jimp2/index.html>.
180. de Jonge, R. M., *J. Inorg. Nucl. Chem.* **1976**, *38* (10), 1821-1826.
181. Hatchard, C. G.; Parker, C. A., *Proc R Soc Lon Ser-A* **1956**, *235* (1203), 518-536.
182. Parker, C. A., *Proc R Soc Lon Ser-A* **1953**, *220* (1140), 104-116.
183. Kuhn, H. J.; Braslavsky, S. E.; Schmidt, R., *Pure Appl. Chem.* **2004**, *76* (12), 2105-2146.
184. Zhang, J.; Zhang, Y.; Richmond, W.; Wang, H.-p., *Int. J. Miner., Metall. Mater.* **2010**, *17*, 1-10.
185. Bonasia, P. J.; Gindelberger, D. E.; Arnold, J., *Inorg. Chem.* **1993**, *32* (23), 5126-5131.

186. Lang, E. S.; Maichle-Mössmer, C.; Strähle, J., *Z. Anorg. Allg. Chem.* **1994**, 620 (10), 1678-1685.
187. Smith, D. M.; Roof, L. C.; Ansari, M. A.; McConnachie, J. M.; Bollinger, J. C.; Pell, M. A.; Salm, R. J.; Ibers, J. A., *Inorg. Chem.* **1996**, 35 (17), 4999-5006.
188. Kirij, N. V.; Tyrre, W.; Naumann, D.; Yagupolskii, Y. L.; Pantenburg, I.; Schäfer, M., *J. Fluorine Chem.* **2004**, 125 (12), 1933-1938.
189. Bumbu, O.; Ceamanos, C.; Crespo, O.; Gimeno, M. C.; Laguna, A.; Silvestru, C.; Villacampa, M. D., *Inorg. Chem.* **2007**, 46 (26), 11457-11460.
190. Molter, A.; Mohr, F., *Coord. Chem. Rev.* **2010**, 254 (1-2), 19-45.
191. Angermaier, K.; Schmidbaur, H., *Z. Naturforsch., B: Chem. Sci.* **1996**, 51 (6), 879-882.
192. Murray, S. G.; Hartley, F. R., *Chem. Rev.* **1981**, 81 (4), 365-414.
193. Hope, E. G.; Levason, W., *Coord. Chem. Rev.* **1993**, 122 (1-2), 109-170.
194. Levason, W.; Orchard, S. D.; Reid, G., *Coord. Chem. Rev.* **2002**, 225 (1-2), 159-199.
195. Roulet, R.; Favez, R., *Chimia* **1975**, 29 (8), 346-8.
196. Jones, J. S.; Wade, C. R.; Gabbai, F. P., *Angew. Chem., Int. Ed.* **2014**, *Angewandte Chemie* **2014**, 126 (34), 9022-9025.
197. Yang, H.; Gabbai, F. P., *J. Am. Chem. Soc.* **2014**, 136 (31), 10866-10869.
198. Jones, C. H. W.; Sharma, R. D., *J. Organomet. Chem.* **1987**, 332 (1-2), 115-121.
199. Bailey, J. H. E.; Drake, J. E.; Wong, M. L. Y., *Can. J. Chem.* **1991**, 69 (12), 1948-1956.
200. Elemental tellurium is known to reduce gold(III) to metallic gold. See the following reference: Hall, R. D.; Lenher, V. *J. Am. Chem. Soc.* **1902**, 24, 918-927.
201. Apte, S. D.; Zade, S. S.; Singh, H. B.; Butcher, R. J., *Organometallics* **2003**, 22 (26), 5473-5477.
202. Kaur, R.; Menon, S. C.; Panda, S.; Singh, H. B.; Patel, R. P.; Butcher, R. J., *Organometallics* **2009**, 28 (8), 2363-2371.
203. Pyykkö, P.; Atsumi, M., *Chem.-Eur. J.* **2009**, 15 (1), 186-197.

204. Cordero, B.; Gomez, V.; Platero-Prats, A. E.; Reves, M.; Echeverria, J.; Cremades, E.; Barragan, F.; Alvarez, S., *Dalton Trans.* **2008**, (21), 2832-2838.
205. Hoshino, M.; Uekusa, H.; Sonoda, S.; Otsuka, T.; Kaizu, Y., *Dalton Trans.* **2009**, (16), 3085-3091.
206. Jones, P. G.; Sheldrick, G. M.; Muir, J. A.; Muir, M. M.; Pulgar, L. B., *J. Chem. Soc., Dalton Trans.* **1982**, (10), 2123-2125.
207. Frisch, M. J.; Trucks, G. W.; Schlegel, H. B.; Scuseria, G. E.; Robb, M. A.; Cheeseman, J. R.; Scalmani, G.; Barone, V.; Mennucci, B.; Petersson, G. A.; Nakatsuji, H.; Caricato, M.; Li, X.; Hratchian, H. P.; Izmaylov, A. F.; Bloino, J.; Zheng, G.; Sonnenberg, J. L.; Hada, M.; Ehara, M.; Toyota, K.; Fukuda, R.; Hasegawa, J.; Ishida, M.; Nakajima, T.; Honda, Y.; Kitao, O.; Nakai, H.; Vreven, T.; Montgomery, J., J. A.; ; Peralta, J. E.; Ogliaro, F.; Bearpark, M.; Heyd, J. J.; Brothers, E.; Kudin, K. N.; Staroverov, V. N.; Kobayashi, R.; Normand, J.; Raghavachari, K.; Rendell, A.; Burant, J. C.; Iyengar, S. S.; Tomasi, J.; Cossi, M.; Rega, N.; Millam, J. M.; Klene, M.; Knox, J. E.; Cross, J. B.; Bakken, V.; Adamo, C.; Jaramillo, J.; Gomperts, R.; Stratmann, R. E.; Yazyev, O.; Austin, A. J.; Cammi, R.; Pomelli, C.; Ochterski, J. W.; Martin, R. L.; Morokuma, K.; Zakrzewski, V. G.; Voth, G. A.; Salvador, P.; Dannenberg, J. J.; Dapprich, S.; Daniels, A. D.; Farkas, Ö.; Foresman, J. B.; Ortiz, J. V.; Cioslowski, J.; Fox, D. J., *Gaussian 09*, Revision B.01, Gaussian, Inc.: Wallingford, CT: 2009.
208. Figgen, D.; Rauhut, G.; Dolg, M.; Stoll, H., *Chem. Phys.* **2005**, *311* (1-2), 227-244.
209. Peterson, K. A.; Puzzarini, C., *Theor. Chem. Acc.* **2005**, *114* (4-5), 283-296.
210. Schmidbaur, H.; Schier, A., *Chem. Soc. Rev.* **2012**, *41* (1), 370-412.
211. Schmidbaur, H.; Schier, A., *Chem. Soc. Rev.* **2008**, *37* (9), 1931-1951.
212. Schmidbaur, H., *Gold Bulletin* **2000**, *33* (1), 3-10.
213. Glendening, E. D.; Badenhop, J. K.; Reed, A. E.; Carpenter, J. E.; Bohmann, J. A.; Morales, C. M.; Weinhold, F., *NBO 5.9*, Theoretical Chemistry Institute, University of Wisconsin, Madison, WI, 2011.
214. Suess, D. L. M.; Peters, J. C., *Organometallics* **2012**, *31* (15), 5213-5222.
215. Derrah, E. J.; Ladeira, S.; Bouhadir, G.; Miqueu, K.; Bourissou, D., *Chem. Commun.* **2011**, *47* (30), 8611-8613.
216. Derrah, E. J.; Martin, C.; Mallet-Ladeira, S.; Miqueu, K.; Bouhadir, G.; Bourissou, D., *Organometallics* **2013**, *32* (4), 1121-1128.
217. Takaguchi, Y.; Fujihara, H.; Furukawa, N., *Organometallics* **1996**, *15* (7), 1913-1919.

218. Alcock, N. W.; Harrison, W. D., *J. Chem. Soc., Dalton Trans.* **1982**, (2), 251-255.
219. Lin, T.-P.; Gabbai, F. P., *Angew. Chem., Int. Ed.* **2013**, 52 (14), 3864-3868.
220. Liaw, W.-F.; Chiou, S.-J.; Lee, G.-H.; Peng, S.-M., *Inorg. Chem.* **1998**, 37 (5), 1131-1134.
221. Uson, R.; Laguna, A.; Laguna, M., *Inorg. Synth.* **1989**, 26, 85-91.
222. Sheldrick, G. M., SADABS-2008/1, *Absorption Correction Program*, Bruker AXS, Madison, Wisconsin, USA 2008.
223. Sheldrick, G. M., SHELXTL-2008/4, *Structure Determination Software Suite*, Bruker AXS, Madison, Wisconsin, USA, 2008.
224. Silvestru, C.; Breunig, H. J.; Althaus, H., *Chem. Rev.* **1999**, 99 (11), 3277-3328.
225. Schulz, S., *Coord. Chem. Rev.* **2001**, 215, 1-37.
226. Schulz, S., *Struct. Bonding* **2002**, 103 (Group 13 Chemistry I), 117-166.
227. Breunig, H. J.; Ghesner, I., *Adv. Organomet. Chem.* **2003**, 49, 95-131.
228. Wade, C. R.; Ke, I.-S.; Gabbai, F. P., *Angew. Chem. Int. Ed.* **2012**, 51 (2), 478-481.
229. Anderson, J. S.; Rittle, J.; Peters, J. C., *Nature* **2013**, 501 (7465), 84-87.
230. Huang, L.; Arndt, M.; Gooßen, K.; Heydt, H.; Gooßen, L. J., *Chem. Rev.* **2015**, 115 (7), 2596-2697.
231. Mizushima, E.; Chatani, N.; Kakiuchi, F., *J. Organomet. Chem.* **2006**, 691 (26), 5739-5745.
232. Hahn, C.; Cruz, L.; Villalobos, A.; Garza, L.; Adeosun, S., *Dalton Trans.* **2014**, 43 (43), 16300-16309.
233. Wang, Y.; Wang, Z.; Li, Y.; Wu, G.; Cao, Z.; Zhang, L., *Nat. Commun.* **2014**, 5.
234. Anokhin, M. V.; Murashkina, A. V.; Averin, A. D.; Beletskaya, I. P., *Mendeleev Communications* **2014**, 24 (6), 332-333.
235. Malhotra, D.; Mashuta, M. S.; Hammond, G. B.; Xu, B., *Angew. Chem., Int. Ed.* **2014**, 53 (17), 4456-4459.
236. Gonell, S.; Poyatos, M.; Peris, E., *Angew. Chem., Int. Ed.* **2013**, 52 (27), 7009-7013.
237. Lavallo, V.; Wright, J. H.; Tham, F. S.; Quinlivan, S., *Angew. Chem., Int. Ed.* **2013**, 52 (11), 3172-3176.

238. Alvarado, E.; Badaj, A. C.; Larocque, T. G.; Lavoie, G. G., *Chem.-Eur. J.* **2012**, *18* (38), 12112-12121.
239. Dash, C.; Shaikh, M. M.; Butcher, R. J.; Ghosh, P., *Inorg. Chem.* **2010**, *49* (11), 4972-4983.
240. Leyva, A.; Corma, A., *Adv. Synth. Catal.* **2009**, *351* (17), 2876-2886.
241. Lavallo, V.; Frey, G. D.; Donnadiu, B.; Soleilhavoup, M.; Bertrand, G., *Angew. Chem. Int. Ed.* **2008**, *47* (28), 5224-5228.
242. Mizushima, E.; Hayashi, T.; Tanaka, M., *Org. Lett.* **2003**, *5* (18), 3349-3352.
243. Inagaki, F.; Matsumoto, C.; Okada, Y.; Maruyama, N.; Mukai, C., *Angewandte Chemie International Edition* **2014**, *54* (3), 818-22.
244. Slone, C. S.; Mirkin, C. A.; Yap, G. P. A.; Guzei, I. A.; Rheingold, A. L., *J. Am. Chem. Soc.* **1997**, *119* (44), 10743-10753.
245. Wang, X.; Thevenon, A.; Brosmer, J. L.; Yu, I.; Khan, S. I.; Mehrkhodavandi, P.; Diaconescu, P. L., *J. Am. Chem. Soc.* **2014**, *136* (32), 11264-11267.
246. Harman, W. H.; Peters, J. C., *J. Am. Chem. Soc.* **2012**, *134* (11), 5080-5082.
247. Sircoglou, M.; Bontemps, S.; Mercy, M.; Saffon, N.; Takahashi, M.; Bouhadir, G.; Maron, L.; Bourissou, D., *Angew. Chem. Int. Ed.* **2007**, *46* (45), 8583-8586.
248. Yang, H.; Gabbai, F. P., *J. Am. Chem. Soc.* **2014**, *136*, 10866-10869.
249. Tschersich, C.; Limberg, C.; Roggan, S.; Herwig, C.; Ernsting, N.; Kovalenko, S.; Mebs, S., *Angew. Chem., Int. Ed.* **2012**, *51* (20), 4989-4992.
250. Lin, T.-P.; Ke, I.-S.; Gabbai, F. P., *Angew. Chem. Int. Ed.* **2012**, *51*, 4985-4988.
251. Sircoglou, M.; Bontemps, S.; Bouhadir, G.; Saffon, N.; Miqueu, K.; Gu, W.; Mercy, M.; Chen, C.-H.; Foxman, B. M.; Maron, L.; Ozerov, O. V.; Bourissou, D., *J. Am. Chem. Soc.* **2008**, *130* (49), 16729-16738.
252. Lin, T.-P.; Wade, C. R.; Pérez, L. M.; Gabbai, F. P., *Angew. Chem., Int. Ed.* **2010**, *49* (36), 6357-6360.
253. Lin, T.-P.; Nelson, R. C.; Wu, T.; Miller, J. T.; Gabbai, F. P., *Chem. Sci.* **2012**, *3*, 1128-1136.
254. Wu, C.-Y.; Horibe, T.; Jacobsen, C. B.; Toste, F. D., *Nature* **2015**, *517* (7535), 449-454.

255. Alex, K.; Tillack, A.; Schwarz, N.; Beller, M., *ChemSusChem* **2008**, *1* (4), 333-338.
256. Chen, Q.; Lv, L.; Yu, M.; Shi, Y.; Li, Y.; Pang, G.; Cao, C., *RSC Adv.* **2013**, *3* (40), 18359-18366.
257. Hartung, C. G.; Tillack, A.; Trauthwein, H.; Beller, M., *J. Org. Chem.* **2001**, *66* (19), 6339-6343.
258. Klein, D. P.; Ellern, A.; Angelici, R. J., *Organometallics* **2004**, *23* (24), 5662-5670.
259. Tokunaga, M.; Eckert, M.; Wakatsuki, Y., *Angew. Chem., Int. Ed.* **1999**, *38* (21), 3222-3225.
260. E. D. Glendening, J. K. Badenhoop, A. E. Reed, J. E. Carpenter, J. A. Bohmann, C. M. Morales, F. Weinhold; *NBO 5.9*, Theoretical Chemistry Institute, University of Wisconsin, Madison, WI, 2011.
261. Mewald, M.; Fröhlich, R.; Oestreich, M., *Chem.-Eur. J.* **2011**, *17* (34), 9406-9414.
262. Blanchard, S.; Derat, E.; Desage-El Murr, M.; Fensterbank, L.; Malacria, M.; Mouriès-Mansuy, V., *Eur. J. Inorg. Chem.* **2012**, *2012* (3), 376-389.
263. Eisenberg, R.; Gray, H. B., *Inorg. Chem.* **2011**, *50* (20), 9741-9751.
264. Kiernicki, J. J.; Fanwick, P. E.; Bart, S. C., *Chem. Commun.* **2014**, *50* (60), 8189-8192.
265. Lewis, R. A.; MacLeod, K. C.; Mercado, B. Q.; Holland, P. L., *Chem. Commun.* **2014**, *50* (76), 11114-11117.
266. Yang, H.; Gabbai, F. P., *J. Am. Chem. Soc.* **2015**, *137* (41), 13425-13432.
267. Yang, H.; Lin, T.-P.; Gabbai, F. P., *Organometallics* **2014**, *33* (17), 4368-4373.
268. Yang, H.; Gabbai, F. P., *J. Am. Chem. Soc.* **2014**, *136* (31), 10866-10869.
269. Braunschweig, H.; Gruss, K.; Radacki, K., *Angew. Chem., Int. Ed.* **2009**, *48* (23), 4239-4241.
270. Braunschweig, H.; Radacki, K.; Schwab, K., *Chem. Commun.* **2010**, *46* (6), 913-915.
271. Ma, M.; Sidiropoulos, A.; Ralte, L.; Stasch, A.; Jones, C., *Chem. Commun.* **2013**, *49* (1), 48-50.
272. Horak, K. T.; VanderVelde, D. G.; Agapie, T., *Organometallics* **2015**, *34* (19), 4753-4765.

273. Lloyd-Jones, G. C., *Organic & Biomolecular Chemistry* **2003**, *1* (2), 215-236.
274. Tong, X.; Li, D.; Zhang, Z.; Zhang, X., *J. Am. Chem. Soc.* **2004**, *126* (24), 7601-7607.
275. Tong, X.; Zhang, Z.; Zhang, X., *J. Am. Chem. Soc.* **2003**, *125* (21), 6370-6371.
276. Aubert, C.; Buisine, O.; Malacria, M., *Chem. Rev.* **2002**, *102* (3), 813-834.
277. Ma, S.; Yu, S.; Gu, Z., *Angew. Chem., Int. Ed.* **2006**, *45* (2), 200-203.
278. Fairlamb, I. J. S., *Angew. Chem., Int. Ed.* **2004**, *43* (9), 1048-1052.
279. Chatani, N.; Furukawa, N.; Sakurai, H.; Murai, S., *Organometallics* **1996**, *15* (3), 901-903.
280. Fürstner, A.; Stelzer, F.; Szillat, H., *J. Am. Chem. Soc.* **2001**, *123* (48), 11863-11869.

APPENDIX TO CHAPTER IV

Structures provided in this section were Lewis acid-Lewis base adducts, involving the gold catalyst **[50][SbF₆]** and different Lewis basic molecules or anions, including 4-dimethylaminopyridine, *p*-toluidine, THF, and fluoride. Although these cationic complexes were not tested for carbophilic catalysis, they provide a better understanding the Lewis acidity of the active gold catalyst. The crystals were generally obtained by layering pentane on top of the concentrated CH₂Cl₂ solution of **[50][SbF₆]** and the Lewis bases. Detailed crystallization methods were provided in the following.

Crystallization of **[50-DMAP][SbF₆]**: To a CH₂Cl₂ solution (1 mL) of approx. 20mg of **[50][SbF₆]**, was slowly added a CH₂Cl₂ solution (0.5 mL) of 4-dimethylaminopyridine (5.4mg, 2.5 equiv.). The mixed CH₂Cl₂ solution was filtered into a clean NMR tube, which was then layered on top with an approx. 1mL of dry pentane. Sizable colorless crystals formed on the side of the NMR tube over the course of two days.

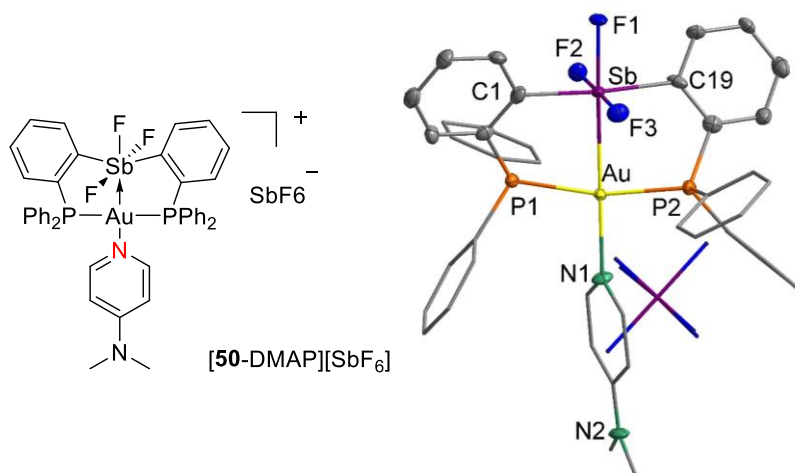


Figure 128. Structure of complex **[50-DMAP][SbF₆]**.

Table 10. Crystal data collection and refinement parameters for complex **[50-DMAP][SbF₆]**.

| | [50-DMAP][SbF₆] |
|--|---|
| chemical formula | C ₄₅ H ₄₂ Au Cl ₄ F ₉ N ₂ P ₂ Sb ₂ |
| crystal colour | colourless |
| <i>F</i> _w ; <i>F</i> (000) | 1426.01; 2744 |
| <i>T</i> (K) | 110(2) |
| wavelength (Å) | 0.71073 |
| space group | P 2 ₁ 2 ₁ 2 ₁ |
| <i>a</i> (Å) | 14.859(6) |
| <i>b</i> (Å) | 16.850(7) |
| <i>c</i> (Å) | 19.657(8) |
| α (deg) | 90.00 |
| β (deg) | 90.00 |
| γ (deg) | 90.00 |
| <i>Z</i> | 4 |
| <i>V</i> (Å ³) | 4921(3) |
| ρ_{calcd} (g·cm ⁻³) | 1.925 |
| μ (mm ⁻¹) | 4.415 |
| θ range (deg); completeness | 1.72 – 28.56; 0.998 |
| collected reflections; <i>R</i> _{σ} | 60538; 0.0495 |
| unique reflections; <i>R</i> _{int} | 60538; 0.0500 |
| <i>R</i> 1 ^a ; <i>wR</i> 2 ^b [<i>I</i> > 2 σ (<i>I</i>)] | 0.0669; 0.1712 |
| <i>R</i> 1; <i>wR</i> 2 [all data] | 0.0779; 0.1798 |
| GOF | 1.049 |
| largest diff peak and hole | 4.634 and -2.004 |

^a $R_1 = \sum(|F_o| - |F_c|) / \sum|F_o|$. ^b $wR_2 = \{\sum[w(F_o^2 - F_c^2)^2] / \sum[w(F_o^2)^2]\}^{1/2}$

Crystallization of **[50-*p*-toluidine][SbF₆]**: To a CH₂Cl₂ solution (1 mL) of approx. 20mg of **[50][SbF₆]**, was slowly added a CH₂Cl₂ solution (0.5 mL) of *p*-toluidine (4.0 mg, 2.1 equiv.). The mixed CH₂Cl₂ solution was filtered into a clean NMR tube, which was then layered on top with an approx. 1mL of dry pentane. Sizable colorless crystals formed on the side of the NMR tube over the course of two days.

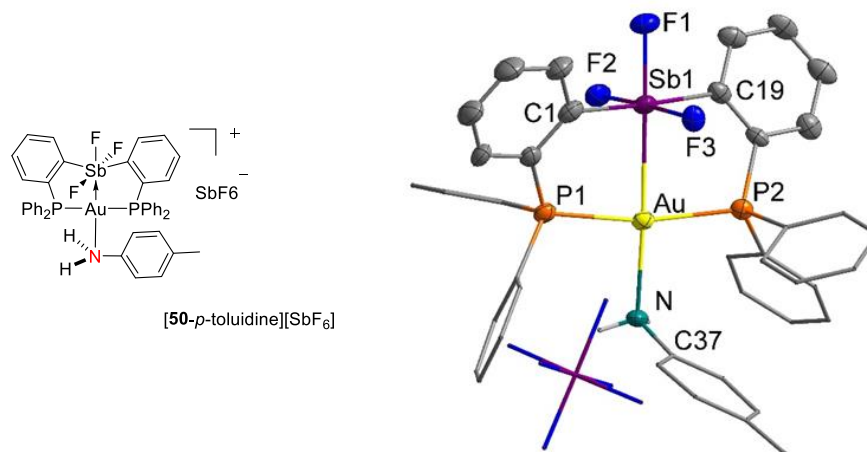


Figure 129. Structure of complex **[50-*p*-toluidine][SbF₆]**.

Table 11. Crystal data collection and refinement parameters for complex **[50-*p*-toluidine][SbF₆]**.

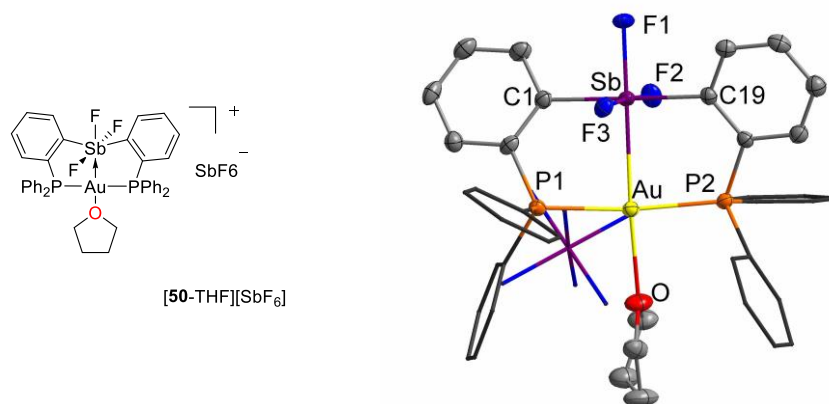
| | [50-<i>p</i>-toluidine][SbF₆] |
|--|--|
| chemical formula | C ₄₆ H ₃₇ Au Cl ₄ F ₉ N P ₂ Sb ₂ |
| crystal colour | colourless |
| Fw; F(000) | 1418.97; 2720 |
| T (K) | 110(2) |
| wavelength (Å) | 0.71073 |
| space group | P 2 ₁ /c |
| a (Å) | 15.525(4) |
| b (Å) | 17.213(4) |
| c (Å) | 18.875(5) |
| α (deg) | 90.00 |
| β (deg) | 108.060(3) |
| γ (deg) | 90.00 |
| Z | 4 |
| V (Å ³) | 4796(2) |
| ρ _{calcd} (g·cm ⁻³) | 1.965 |
| μ (mm ⁻¹) | 4.530 |
| θ range (deg); completeness | 1.64 – 28.62; 0.986 |
| collected reflections; R _σ | 57089; 0.1023 |

Table 11Continued.

| | |
|--------------------------------|------------------|
| unique reflections; Rint | 57089; 0.1168 |
| R1a; wR2b [$I > 2\sigma(I)$] | 0.0661; 0.1580 |
| R1; wR2 [all data] | 0.1128; 0.1823 |
| GOF | 1.027 |
| largest diff peak and hole | 3.713 and -1.920 |

$$^a R_1 = \frac{\sum(|F_o| - |F_c|)}{\sum|F_o|}, \quad ^b wR_2 = \left\{ \frac{\sum[w(F_o^2 - F_c^2)^2]}{\sum[w(F_o^2)]} \right\}^{1/2}$$

Crystallization of **[50-THF][SbF₆]**: To a CH₂Cl₂ solution (1 mL) of approx. 20mg of **[50][SbF₆]**, was slowly added a 0.1 mL of dry THF. The mixed solution was filtered into a clean NMR tube, which was then layered on top with an approx. 1mL of dry pentane. Sizable colorless crystals formed on the side of the NMR tube over the course of two days.

**Figure 130.** Structure of complex **[50-THF][SbF₆]**.**Table 12.** Crystal data collection and refinement parameters for complex **[50-THF][SbF₆]**.

| | [50-THF][SbF₆] |
|------------------|--|
| chemical formula | C ₄₁ H ₃₈ Au Cl ₂ F ₉ O P ₂ Sb ₂ |
| crystal colour | colourless |
| F_w ; $F(000)$ | 1291.02; 2472 |
| T (K) | 110(2) |

Table 12 Continued.

| | |
|---|---------------------|
| wavelength (Å) | 0.71073 |
| space group | P 2 ₁ /c |
| <i>a</i> (Å) | 11.876(4) |
| <i>b</i> (Å) | 17.644(6) |
| <i>c</i> (Å) | 21.382(7) |
| α (deg) | 90.00 |
| β (deg) | 102.376(4) |
| γ (deg) | 90.00 |
| <i>Z</i> | 4 |
| <i>V</i> (Å ³) | 4376(2) |
| ρ_{calcd} (g·cm ⁻³) | 1.960 |
| μ (mm ⁻¹) | 4.836 |
| θ range (deg); completeness | 1.76 – 28.56; 0.983 |
| collected reflections; R_{σ} | 50119; 0.0445 |
| unique reflections; R_{int} | 50119; 0.0537 |
| $R1^a$; $wR2^b$ [$I > 2\sigma(I)$] | 0.0367; 0.0795 |
| $R1$; $wR2$ [all data] | 0.0576; 0.0915 |
| GOF | 1.028 |
| largest diff peak and hole | 1.966 and -2.295 |

$$^a R_1 = \frac{\sum(|F_o| - |F_c|)}{\sum|F_o|} \quad ^b wR_2 = \left\{ \frac{\sum[w(F_o^2 - F_c^2)^2]}{\sum[w(F_o^2)^2]} \right\}^{1/2}$$

Synthesis and crystallization of **50-F**: A CH₂Cl₂ solution of TBAT (5.0 mg, 0.5 mL) was slowly added to a CH₂Cl₂ solution of [**50**][SbF₆] (10.6 mg, 0.5 mL). The mixed solution was filtered into a clean NMR tube, which was then layered on top with an approx. 1mL of dry pentane. Sizable colorless crystals formed on the side of the NMR tube over the course of two days.

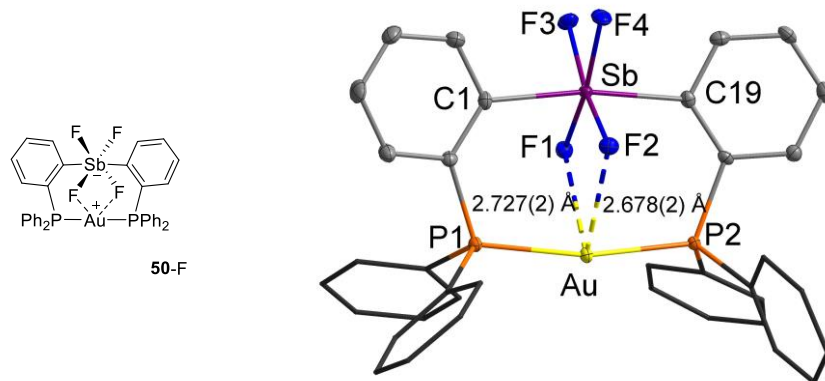


Figure 131. Structure of a zwitterionic complex **50-F**.

Table 13. Crystal data collection and refinement parameters for complex **50-F**.

| | 50-F |
|---|---|
| chemical formula | C ₃₆ H ₂₈ Au F ₄ P ₂ Sb |
| crystal colour | colourless |
| F_w ; $F(000)$ | 917.24; 1760 |
| T (K) | 110(2) |
| wavelength (Å) | 0.71073 |
| space group | P 2 ₁ /c |
| a (Å) | 14.623(3) |
| b (Å) | 12.134(3) |
| c (Å) | 17.882(4) |
| α (deg) | 90.00 |
| β (deg) | 108.580(2) |
| γ (deg) | 90.00 |
| Z | 4 |
| V (Å ³) | 3007.4(11) |
| ρ_{calcd} (g·cm ⁻³) | 2.026 |
| μ (mm ⁻¹) | 5.929 |
| θ range (deg); completeness | 2.06 – 28.46; 0.955 |
| collected reflections; R_σ | 34024; 0.0232 |
| unique reflections; R_{int} | 34024; 0.0284 |
| $R1^a$; $wR2^b$ [$I > 2\sigma(I)$] | 0.0204; 0.0450 |
| $R1$; $wR2$ [all data] | 0.0232; 0.0459 |
| GOF | 1.051 |
| largest diff peak and hole | 0.832 and -0.767 |

^a $R_1 = \Sigma(|F_o| - |F_c|) / \Sigma|F_o|$. ^b $wR_2 = \{\Sigma[w(F_o^2 - F_c^2)^2] / \Sigma[w(F_o^2)^2]\}^{1/2}$

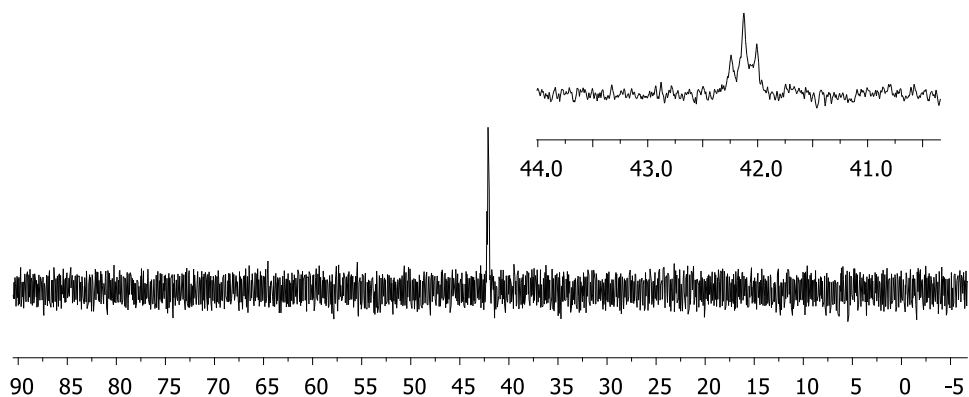


Figure 132. ^{31}P NMR spectrum of zwitterionic complex **50-F** in CH_2Cl_2 .

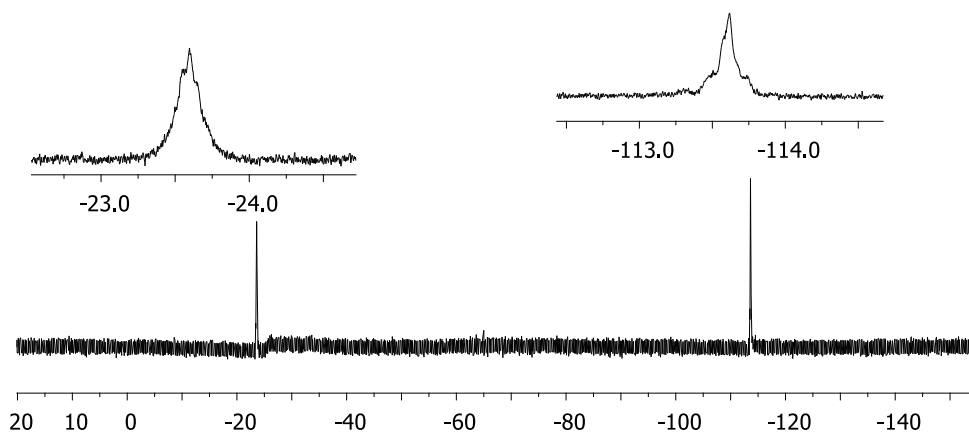


Figure 133. ^{19}F NMR spectrum of zwitterionic complex **50-F** in CH_2Cl_2 .

Crystallization of complex **56**: $[\mathbf{50}][\text{SbF}_6]$ (approx. 12 mg) was first dissolved in regular acetonitrile (1mL), which was filtered into a clean NMR tube. The acetonitrile solution was then layered on top with an approx. 1mL of pentane. Small amount of sizable, colorless crystals formed on the side of the NMR tube over the course of two days.

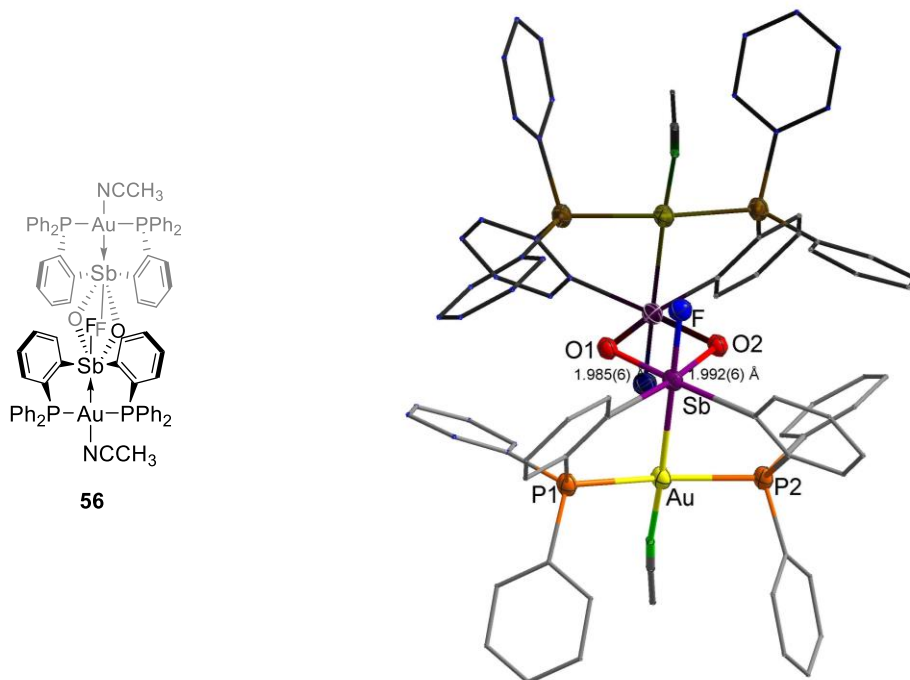


Figure 134. Structure of complex **56**.

Table 14. Crystal data collection and refinement parameters for complex **56**.

| | 56 |
|--|--|
| chemical formula | C ₃₇ H ₃₁ Au F ₉ N O P ₂ Sb ₂ |
| crystal colour | colourless |
| <i>F</i> _w ; <i>F</i> (000) | 1179.03; 1120 |
| <i>T</i> (K) | 110(2) |
| wavelength (Å) | 0.71073 |
| space group | P-1 |
| <i>a</i> (Å) | 12.671(3) |
| <i>b</i> (Å) | 14.242(4) |
| <i>c</i> (Å) | 14.892(7) |
| α (deg) | 109.511(4) |
| β (deg) | 108.753(4) |

Table 14 Continued.

| | |
|---|---------------------|
| γ (deg) | 104.232(3) |
| Z | 2 |
| V (\AA^3) | 2202.9(13) |
| ρ_{calcd} ($\text{g}\cdot\text{cm}^{-3}$) | 1.778 |
| μ (mm^{-1}) | 4.678 |
| θ range (deg); completeness | 1.71 – 28.41; 0.918 |
| collected reflections; R_{σ} | 24957; 0.0792 |
| unique reflections; R_{int} | 24957; 0.0520 |
| $R1^a$; $wR2^b$ [$I > 2\sigma(I)$] | 0.0498; 0.1105 |
| $R1$; $wR2$ [all data] | 0.0815; 0.1223 |
| GOF | 1.037 |
| largest diff peak and hole | 2.610 and -1.793 |

$$^a R_1 = \Sigma(|F_o| - |F_c|) / \Sigma|F_o|. \quad ^b wR_2 = \{ \Sigma[w(F_o^2 - F_c^2)^2] / \Sigma[w(F_o^2)^2] \}^{1/2}$$

APPENDIX TO CHAPTER V

Structures provided in this section were analogues to complex **52**, Chapter V.

Synthesis and crystallization of $[\mathbf{52-Cl}] \text{N}^n\text{Bu}_4$: A CH_2Cl_2 solution (4 mL) of TBAF (242 mg, 0.76 mmol) was slowly added to a CH_2Cl_2 solution (10 mL) of complex **42** (181.5 mg, 0.19 mmol). The solution turned from cloudy to clear, and was stirred for 16h. The reaction solution was concentrated. Crystals of $[\mathbf{52-Cl}] \text{N}^n\text{Bu}_4$ suitable for X-ray diffraction were obtained from slow evaporation of the CH_2Cl_2 solvent over the course of two weeks.

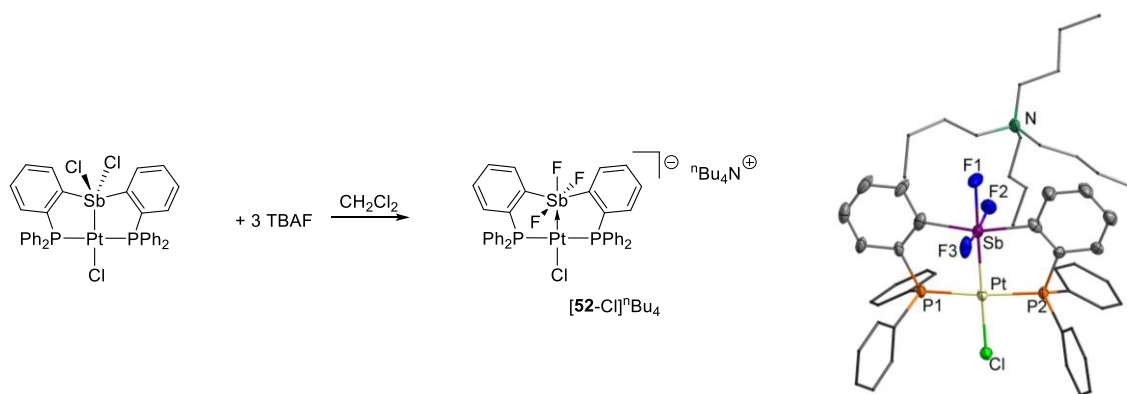


Figure 135. Synthesis and crystal structure of complex $[\mathbf{52-Cl}] \text{N}^n\text{Bu}_4$.

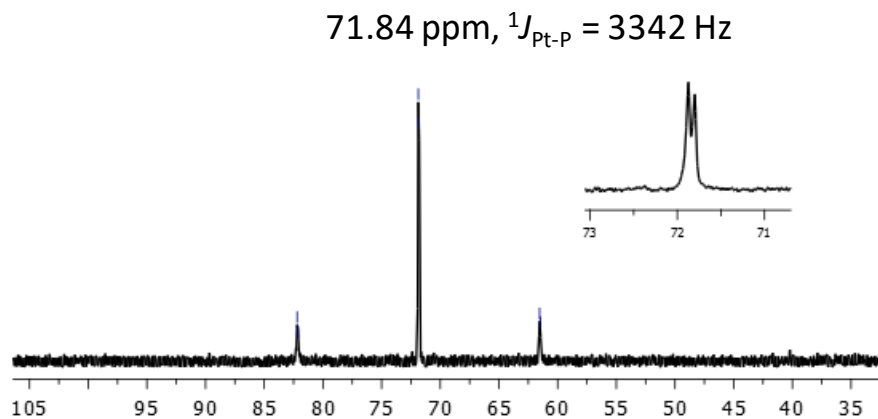


Figure 136. ^{31}P NMR spectrum of complex $[\mathbf{52-Cl}] \text{N}^n\text{Bu}_4$ in CH_2Cl_2 .

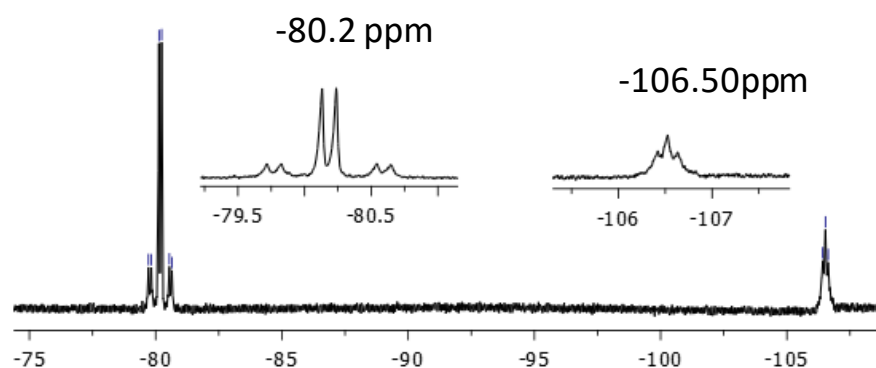


Figure 137. ^{19}F NMR spectrum of complex $[\mathbf{52}\text{-Cl}] \text{N}^n\text{Bu}_4$ in CH_2Cl_2 .

Table 15. Crystal data collection and refinement parameters for complex $[\mathbf{52}\text{-Cl}]\text{N}^n\text{Bu}_4$.

| | $[\mathbf{52}\text{-Cl}]\text{N}^n\text{Bu}_4$ |
|---|--|
| chemical formula | $\text{C}_{52} \text{H}_{64} \text{Cl} \text{F}_3 \text{N} \text{P}_2 \text{Pt} \text{Sb}$ |
| crystal colour | colourless |
| $F_w; F(000)$ | 1174.27; 1172 |
| T (K) | 110(2) |
| wavelength (\AA) | 0.71073 |
| space group | P -1 |
| a (\AA) | 11.307(5) |
| b (\AA) | 12.186(5) |
| c (\AA) | 18.702(8) |
| α (deg) | 100.725(5) |
| β (deg) | 92.241(5) |
| γ (deg) | 102.987(4) |
| Z | 2 |
| V (\AA^3) | 2458.3(18) |
| ρ_{calcd} ($\text{g}\cdot\text{cm}^{-3}$) | 1.586 |
| μ (mm^{-1}) | 3.558 |
| θ range (deg); completeness | 1.85 – 28.24; 0.958 |

Table 15 Continued.

| | |
|---------------------------------------|------------------|
| collected reflections; R_{σ} | 28321; 0.0960 |
| unique reflections; R_{int} | 28321; 0.0645 |
| $R1^a$; $wR2^b$ [$I > 2\sigma(I)$] | 0.0562; 0.1313 |
| $R1$; $wR2$ [all data] | 0.1007; 0.1507 |
| GOF | 1.022 |
| largest diff peak and hole | 3.363 and -2.502 |

$$^a R_1 = \frac{\sum(|F_o| - |F_c|)}{\sum|F_o|}, \quad ^b wR_2 = \left\{ \frac{\sum[w(F_o^2 - F_c^2)^2]}{\sum[w(F_o^2)^2]} \right\}^{1/2}$$

Synthesis and crystallization of $[\mathbf{52}\text{-Cl}]\text{Tl}$: A CH_2Cl_2 solution (6 mL) of complex **42** (75 mg, 0.079 mmol) was mixed with 2 mL of benzene solvent. After the mixture was stirred for 30 min, solid TlF (55 mg, 0.24 mmol) was added. The reaction mixture was stirred for 16 h. and resulted in pale yellow suspension. After filtration through celite, the solution was concentrated. Crystals of $[\mathbf{52}\text{-Cl}]\text{Tl}$ suitable for X-ray diffraction were obtained from slow diffusion of Et_2O into the concentrated solution. $^{31}\text{P}\{^1\text{H}\}$ NMR (202.28 MHz; CDCl_3): δ 71.4 (major, br, weak), δ 44.1 (minor impurity, s, weak). $^{19}\text{F}\{^1\text{H}\}$ NMR (470.2 MHz; CDCl_3): δ -74.8 (br weak, $2F_{\text{eq}}$), -103.1 (br, weak $1F_{\text{a}}$), -144.8 (impurity, s).

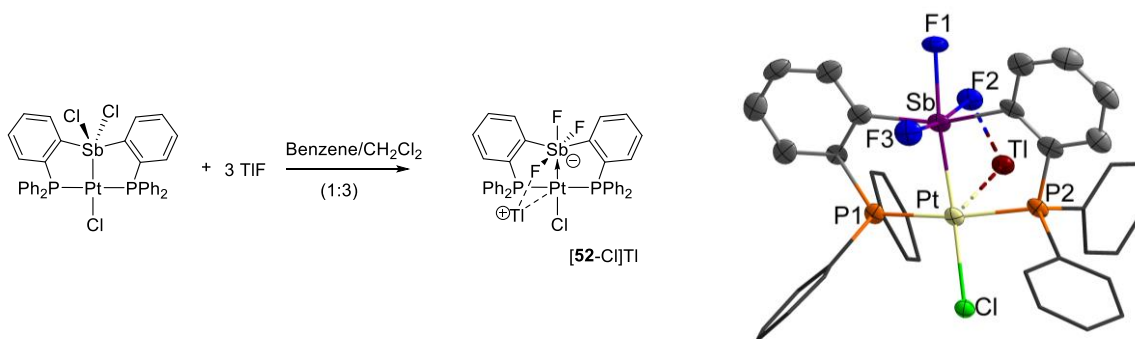


Figure 138. Synthesis and crystal structure of complex $[\mathbf{52}\text{-Cl}]\text{Tl}$.